

“You must be the change you want to see in the world.”
Mahatma Gandhi

University of Alberta

**Laser Ablation Laser Induced Fluorescence for Sensitive Detection of
Heavy Metals in Water**

by

Yogesh Godwal

A thesis submitted to the Faculty of Graduate Studies and Research
in partial fulfillment of the requirements for the degree of

Doctor of Philosophy

in

Photonics and Plasmas

Electrical and Computer Engineering

©Yogesh Godwal

Fall 2010

Edmonton, Alberta

Permission is hereby granted to the University of Alberta Libraries to reproduce single copies of this thesis and to lend or sell such copies for private, scholarly or scientific research purposes only. Where the thesis is converted to, or otherwise made available in digital form, the University of Alberta will advise potential users of the thesis of these terms.

The author reserves all other publication and other rights in association with the copyright in the thesis and, except as herein before provided, neither the thesis nor any substantial portion thereof may be printed or otherwise reproduced in any material form whatsoever without the author's prior written permission.

Examining Committee

Robert Fedosejevs, Electrical and Computer Engineering

Ying Tsui, Electrical and Computer Engineering

Abdul Elezabbi, Electrical and Computer Engineering

John Tulip, Electrical and Computer Engineering

Richard Marchand, Physics

Jagdish Singh, Mississippi State University

To my parents

Abstract

Laser Induced Breakdown Spectroscopy LIBS is a fast non-contact technique for the analysis of the elemental composition using spectral information of the emission from a laser-induced plasma. For the LIBS studies in this thesis the focus has been in using very low energy, microjoule pulses in order to give high spatial resolution and minimize the laser system requirements. This is a regime that we refer to as microLIBS. Under such conditions it is important to maximize the signal detected to give the lowest limit of detection LOD possible.

One technique to improve the signal to noise ratios is by coupling LIBS with Laser Induced Fluorescence. This is a technique where the first pulse creates a vapor plume and the second pulse tuned to a resonant absorption line of the species of interest re-excites the plume. We term this technique as Laser ablation Laser Induced Fluorescence LA-LIF. We have been investigating the performance of LA-LIF at low pulse energies (≤ 1 mJ for both pulses) for the detection of elemental contaminants in water. This technique allows reasonable performance compared to high energy single-pulse LIBS, but at a much reduced total energy expenditure. This allows LODs in the parts per billion range ppb range which typically cannot be obtained with low energy single pulse probing of the systems. This approach or exceeds the sensitivities which can be obtained with many shots using much larger energy systems. In this thesis we investigated the performance of LIBS at low pulse energies for the detection of Pb as a contaminant in water. An LOD of 70 ppb was obtained for an accumulation of 100 shots with the ablation laser pulse energy of 250 μ J and an excitation laser pulse energy of 8 μ J. A systematic study of the detector conditions was made for the system for the detection of Pb. Scaling laws for the LOD in terms of the pump and probe energies were measured and also the effect of detector gain, the gate delay and the gate width were studied.

In this thesis LIBS and LA-LIF were also used to analyze ultralow volumes of analyte in liquids in microfluidic geometries. LIBS was applied for the detection of Na in liquid droplets in a microfluidic system. The detection of Na as low as 360 femtograms was demonstrated for 100 shots integrated in this system. An LOD of 7 ppm for Pb for 100 shot accumulation was demonstrated using the LA-LIF technique on an 18 μm diameter microdroplet.

To study the laser interaction with the water targets the MEDUSA one dimensional hydrocode was used. The propagation of the shockwave and plume dynamics were studied using this modeling code. The expansion of the plume was studied and compared to experimentally measured values and to physical models for blast wave expansion and stagnation.

Two preconcentration techniques were also studied, one of which used a wood-chip as a substrate to absorb the analyte liquid and wick the salt on to the surface for analysis and the other used an electroplating technique to plate the analyte metal as a thin film on a substrate metal used as a cathode. The electroplating method for preconcentration was also studied using a microchip laser and a LOD of 6.4 ppb for Pb in water was obtained for an accumulation of 200,000 shots.

Acknowledgements

I wish to thank my supervisor Dr. Robert Fedosejevs for his guidance, encouragement and support throughout the entire course of the thesis. I admire his dedication and professionalism. I would also like to thank Dr. Ying Tsui for his valuable suggestions throughout this thesis. Early help and guidance from Dr. Siu-Lung Lui was extremely valuable and his contributions are acknowledged. I am thankful for the great technical support from Blair Harwood and Rick Conrad at numerous stages during the course of the thesis. Dr. Mike Taschuk, Dr. Sean Kirkwood, Dr. Matt Reid, Dr. Ilya Utkin, Dr. Sanjay Singh, Shyama Bannerjee, Lei Pan, Zhijiang Chen are some of the few people who I had the pleasure of working with at the Laser Plasma Labs.

Finally would like to thank my mother Madhuri Godwal and my father Dr. B.K. Godwal (my first physics teacher) for their endless support and encouragement in all my endeavors.

Contents

1	Introduction	1
1.1	The LIBS Process	2
1.2	LIBS Instrumentation	4
1.2.1	Lasers in LIBS	5
1.2.2	Optical Components in LIBS	6
1.2.3	Wavelength selecting elements in LIBS	7
1.2.4	Detectors for LIBS	10
1.3	Advantages and Limitations of LIBS	13
1.4	Dual-Pulse LIBS	14
1.5	Micro Laser Induced Breakdown Spectroscopy (μ LIBS)	18
1.6	Laser Ablation - Laser Induced Fluorescence (LA - LIF)	19
1.6.1	Excitation-Detection Schemes	20
1.7	LIBS and LA-LIF for drinking water monitoring	21
1.8	μ LIBS and LA-LIF for Microfluidics	23
1.8.1	Introduction	23
2	Principles of Laser Ablation - Laser Induced Fluorescence	26
2.1	Laser Matter Interaction	26
2.2	Laser Ablation	26
2.2.1	Ablation by nanosecond pulses	28
2.3	Growth of the Plasma	29
2.3.1	Plasma Shielding	29
2.3.2	Plasma Expansion	30
2.3.3	Interaction of the plume with the environment	31
2.4	Spectral Line Emission	32
2.4.1	Local Thermodynamic Equilibrium	33
2.4.2	Line Emission	35
2.5	Laser Plasma Modeling using MEDUSA Hydrocode	35
2.6	Laser Atomic Fluorescence	38
2.6.1	Case of a metastable level	40
3	Experimental Methodologies	44
3.1	Introduction	44
3.2	LALIF experimental setup	44
3.2.1	Energy Calibrations	47

3.2.2	Laser Focal Spot measurements	47
3.2.3	Wavelength Calibration	49
3.2.4	Detector Response	53
3.2.5	LIBS signal analysis	61
3.2.6	Detector parameter optimization for Single Pulse μ LIBS of Pb	62
3.3	μ LIBS of Microdroplets: Rapid Thermal Heater Approach	71
3.3.1	Microchip architecture and operating principle	71
3.3.2	Fabrication of Microheaters	71
3.3.3	Micromachining of PDMS Layer	73
3.3.4	Microdroplet Imaging Setup	73
3.3.5	μ LIBS microdroplets	74
3.3.6	Nucleation Process	74
3.3.7	Microdroplet Extrusion and Operation	76
3.4	μ LIBS of Monodisperse Microdroplets: Piezoelectric Approach	77
3.4.1	Optimization experiments for μ LIBS and LA-LIF of the microdroplets	78
3.4.2	Optimization of focusing conditions	79
4	μLIBS and LA-LIF studies on a waterjet system	83
4.1	Introduction	83
4.2	μ LIBS of Pb	83
4.3	LA-LIF of Pb	85
4.3.1	Selective Enhancement	85
4.3.2	Interpulse Separation ΔT	87
4.3.3	Detector Gate Width T_{width}	89
4.3.4	Calibration Curve	89
4.4	Towards a Water Quality Monitoring System	95
4.4.1	LA-LIF of Pb using a PMT and a Multi-Pixel Photon Counter	96
5	μLIBS on Microfluidic platform	101
5.1	μ LIBS and LA-LIF on Microdroplets: Piezoelectric Pulsed Approach	102
5.1.1	μ LIBS emission Intensity as a function of Gate Delay and Laser Pulse Energy	102
5.1.2	μ LIBS emission Intensity as a function of Microdroplet Size	103
5.2	LA-LIF of microdroplets	104
5.2.1	LA-LIF emission as a function of Microdroplet Size	105
5.2.2	Effect of Probe pulse energy on LA-LIF of Microdroplets	105
5.2.3	Comparison of LA-LIF of Microdroplets and LA-LIF for waterjet	107
5.3	Demonstration of μ LIBS on a Microfluidic Platform	109
6	Modelling of Laser Interaction	114
6.1	Introduction	114
6.2	Analytical Models for laser absorption and expansion	115
6.3	Blast wave theory	116
6.3.1	Dyer's Stagnation Model	117

6.3.2	Laser and Target Parameters	118
6.4	Simulation Results	119
6.5	Conclusion	121
7	Preliminary studies on preconcentration for μLIBS	131
7.1	Preconcentration for LIBS of Liquid Samples	131
7.2	Pb detection in water samples using LIBS of wood slice samples . . .	132
7.2.1	Sample Preparation	133
7.3	Results and Discussion	134
7.3.1	LIBS signal intensity as a function of Laser Pulse Energy . . .	134
7.3.2	SNR as a function of number of shots	138
7.3.3	Calibration Curves and L.O.D	138
7.4	Preconcentration using Electroplating	143
8	Conclusions	146
8.1	Summary of Thesis Results	146
8.2	Future Work: Outlook	148
8.2.1	μ LIBS Capabilities	148
8.2.2	LA-LIF Capabilities	149
8.3	LIBS Modelling and Physics	149
8.4	Conclusion	150
A	LA-LIF simulation using Mathcad	151
B	Medusa hydrocode parameter settings	163
C	Code for ICCD parameter optimization	170
D	Matlab Code for Microheater temperature simulation	173
	Bibliography	177

List of Tables

4.1	Comparison of our results with those published in the literature. All the LOD's are scaled to 100 shot LOD's to compare with our results.	84
4.2	Summary of the LODs from the Measurements Scaled to 10000 Shots Using a $N^{1/2}$ scaling with Number of Shots	93
4.3	Summary of the LODs reported for Pb from literature to our results scaled to 100 shot accumulation.	94
4.4	Comparison of three different detectors, ICCD, PMT and the MPPC on the basis of the 100 shot LOD's for 1 ppm Pb in water using different collection apertures. The photons detected represent the sum of the photoelectrons detected for 100 shots.	97
7.1	Pulses of three different wavelengths using a 100 shot accumulation from the calibration curves with sample concentrations ranging from 200 ppb and 50 ppm. Scaling of the 100 shot data to the expected LOD for the 1000 shot accumulation and the 1000 shot LODs were determined from Fig.7.5.	141

List of Figures

1.1	Layout of a typical LIBS setup.	2
1.2	Basic stages of plasma development in LIBS.	3
1.3	Pb emission spectra generated from a LIBS microplasma created by a 270 μ J, 7 ns, 266 nm laser pulse as it evolves in time in the spectral window 390 - 420 nm.	4
1.4	Illustration of an echelle spectrograph (a) Shows the echelle spectrograph and the bi-dimensional dispersion it produces. (b) Illustration of a intensified CCD with different parts labelled. (reprinted with permission from S.B.Q Sociedade Brasileira de Quimica (Brazilian Chemical Society)) [1]	9
1.5	Schematic representation of laser timing in single and dual pulse LIBS (a) Single pulse LIBS: the laser pulses are at a 5Hz repetition rate. (b) Dual Pulse LIBS: Two laser pulses temporally separated by ΔT and at 5 Hz repetition rate.	15
1.6	Geometric Configurations for Dual Pulse LIBS (a) Collinear (b) Orthogonal	16
1.7	Various excitation-detection schemes used in LA-LIF also LEAFS. (a) Resonant detection (b) Non-Resonant (Stokes) (c)Non- resonant (anti-stokes) (d) Collisionally assisted non-resonance (Stokes) (e) collisionally assisted double resonance fluorescence. The different energy levels indicate the energy levels in the atom. The thick arrows indicate the stimulated absorption due to the laser excitation and the narrow arrows indicate the fluorescence radiation.	21
1.8	A droplet extrusion system using either a thermal or a piezoelectric technique to eject sample droplets for analysis of chemical composition.	25

2.1	Simulation of the ionization fraction as a function of temperature for the three level Pb system for two different electron densities of $10^{18}m^{-3}$ and $10^{19} m^{-3}$	36
2.2	Simulation of population of the ground state as a function of temperature for the three level Pb system for two different electron densities of $10^{18}m^{-3}$ and $10^{19} m^{-3}$	36
2.3	Illustration of a three-level model of a Pb atom	39
2.4	Simulation of the fluorescence signal emitted for a 1 ppm Pb solution as a function of the probe pulse energy for a 238 μm diameter probe spot. A probe pulse duration of 5 ns has been assumed.	43
3.1	Schematic setup of the LA-LIF experiment. A frequency-quadrupled Nd:YAG laser (266 nm, ≈ 10 ns) at 170 μJ ablates the water jet. Pulse energy is controlled by a half-wave plate and Glan-Taylor polarizer. The pulse for re-excitation is a frequency-doubled dye laser pulse pumped by a XeCl excimer laser.	45
3.2	Simplified Grotrian diagram of Pb. The excitation and fluorescence transitions are indicated. The energies of the levels are in wavenumbers cm^{-1}	46
3.3	Energy calibration of a photodiode used to monitor the ablation laser beam energy. The calibration factor for this data set was $353 \pm 3 \mu\text{J}/\text{V}$	48
3.4	Energy calibration of a photodiode used to monitor the resonant probe laser beam energy. The calibration factor for this data set was $92 \pm 1 \mu\text{J}/\text{V}$	49
3.5	Measurement of the focal spot size of the ablation laser pulse using the knife edge technique in the horizontal direction. A gaussian fit indicates a beamwaist of $12 \pm 3 \mu\text{m}$	50
3.6	Measurement of the focal spot size of the ablation laser pulse using the knife edge technique in the vertical direction. A gaussian fit indicates a beamwaist of $8 \pm 2 \mu\text{m}$	50
3.7	Image of a calibrated scale each division on the scale is 0.005 inches which leads to each pixel being approximately 1.98 μm	51

3.8	The image and line profile of the resonant laser beam. The gaussian fit indicated a beamwaist of $238 \pm 5 \mu\text{m}$	51
3.9	The image and line profile of the resonant laser beam. The gaussian fit indicated a beamwaist of $238 \pm 5 \mu\text{m}$	52
3.10	Fig shows the line profile of the dye laser beam in the vertical direction. A gaussian fit to the line profile indicates a beam waist of $400 \pm 10 \mu$	52
3.11	Three emission lines from a Hg lamp 404.65 nm, 407.78 nm and 435.83 nm are shown. The spectrometer grating was 2400 l/mm and was centered at 418 nm. The 407.78 line has a much lower intensity compared to the other two lines.	53
3.12	The LIBS emission spectrum of an Al2024 Al alloy is shown. A 2400 l/mm grating was used and the grating was centered at 395 nm. The al doublets of 394/396 nm are observed.	54
3.13	The LIBS emission spectrum of Pb is shown (top). Three emission lines 280.19 nm, 282.31 nm and the resonant line for our scheme at 283.305 are observed. Scattered laser light at 266 nm from the ablation laser is also observed. The profile for the dye laser at 283.305 nm (bottom) is shown. A 2400 l/mm grating was used in both cases. The intensifier gain was set at minimum. For the emission spectrum the gate delay was set at 400 ns and the gate width was set to 500 ns.	55
3.14	Manufacturer data for the quantum efficiency as a function of the wavelength for the Andor DH720 ICCD's photocathode.	56
3.15	Calibration data for the ICCD used. The line is an exponential fit for a gain of less than 125. Above a gain of 125 a saturation in the detector gain is observed. The pixel readout time was 16 μs	56
3.16	Calibration data provided by manufacturer for the Andor ICCD. The line is an exponential fit for a gain of less than 125. Above a gain of 125 a saturation in the detector gain is observed.	57
3.17	PMT dynode array and the voltage-divider supply.	57

3.18	Schematic setup of the LA-LIF experiment. A frequency-quadrupled Nd:YAG laser (266 nm, ≈ 10 ns) at 170 μ J ablates the water jet. Pulse energy is controlled by a half-wave plate and Glan-Taylor prism. The pulse for re-excitation is a frequency-doubled dye laser pulse pumped by a XeCl excimer laser. The Pb emission is collected by a lens onto a filtered PMT with a 2 nm bandwidth interference filter.	58
3.19	Picture of a 100 pixel MPPC and a close up view showing each pixel of the device [2]. The pixel size is $100 \times 100 \mu\text{m}$ each.	59
3.20	Recovery time for the MPPC. The device was irradiated with two 5 ns laser pulses with the interpulse separation controlled by a digital delay generator. The recovery time was measured to be 130 ns.	60
3.21	Outline of the signal analysis technique. The integrated signal intensity is $\sum I(\lambda)$, $N_{channels}$ is the inetgrated width which is used to scale the noise. The noise region is the area used to estimate the variation in the background.	61
3.22	Background (top left), Noise(top right), Signal(bottom left), SNR (bottom right) of the emission spectra 100 accumalations from a LIBS plasma measured at different gate delay and gate width. The laser pulse energy was 260 μ J. The water sample contained 500 ppm of Pb. The gate delay (x-axis) was varied from 50 ns to 230 ns in steps of 20 ns and the gatewidth (y-axis) of the ICCD was 50 ns to 450 ns ,the slit width was fixed at 300 μm and the detector gain was set to zero. The legend shows the strength of the parameter (Background, Signal, Noise and SNR) being measured.	64

- 3.23 Background (top left), Noise(top right), Signal(bottom left), SNR (bottom right) of the emission spectra 100 accumalations from a LIBS plasma measured at different gate delay and gate width. The laser pulse energy was 260 μ J. The water sample contained 500 ppm of Pb. The gate delay (x-axis) was varied from 50 ns to 230 ns in steps of 20 ns and the gatewidth (y-axis) of the ICCD was 50 ns to 450 ns,the slit width was fixed at 300 μ m and the detector gain was set to 50. The legend shows the strength of the parameter (Background, Signal, Noise and SNR) being measured. 66
- 3.24 Background (top left), Noise(top right), Signal(bottom left), SNR (bottom right) of the emission spectra 100 accumalations from a LIBS plasma measured at different gate delay and gate width. The laser pulse energy was 260 μ J. The water sample contained 500 ppm of Pb. The gate delay (x-axis) was varied from 50 ns to 230 ns in steps of 20 ns and the gatewidth (y-axis) of the ICCD was 50 ns to 450 ns,the slit width was fixed at 300 μ m and the detector gain was set to 100. The legend shows the strength of the parameter (Background, Signal, Noise and SNR) being measured. 67
- 3.25 Background (top left), Noise(top right), Signal(bottom left), SNR (bottom right) of the emission spectra 100 accumalations from a LIBS plasma measured at different gate delay and gate width. The laser pulse energy was 260 μ J. The water sample contained 500 ppm of Pb.The gate delay (x-axis) was varied from 50 ns to 230 ns in steps of 20 ns and the gatewidth (y-axis) of the ICCD was 50 ns to 450 ns,the slit width was fixed at 300 μ m and the detector gain was set to 150. The legend shows the strength of the parameter (Background, Signal, Noise and SNR) being measured. 68

3.26	Background (top left), Noise(top right), Signal(bottom left), SNR (bottom right) of the emission spectra 100 accumalations from a LIBS plasma measured at different gate delay and gate width. The laser pulse energy was 260 μJ . The water sample contained 500 ppm of Pb. The gate delay (x-axis) was varied from 50 ns to 230 ns in steps of 20 ns and the gatewidth (y-axis) of the ICCD was 50 ns to 450 ns,the slit width was fixed at 300 μm and the detector gain was set to 200. The legend shows the strength of the parameter being (Background, Signal, Noise and SNR) measured.	69
3.27	Background (top left), Noise(top right), Signal(bottom left), SNR (bottom right) of the emission spectra 100 accumalations from a LIBS plasma measured at different gate delay and gate width. The laser pulse energy was 260 μJ . The water sample contained 500 ppm of Pb. The gate delay (x-axis) was varied from 50 ns to 230 ns in steps of 20 ns and the gatewidth (y-axis) of the ICCD was 50 ns to 450 ns,the slit width was fixed at 300 μm and the detector gain was set to 250. The legend shows the strength of the parameter (Background, Signal, Noise and SNR) being measured.	70
3.28	Conceptual diagram showing the integration of μLIBS on a microfluidic platform that extrudes droplets and, (b) Assembled microchip architecture for continuous flow elemental analysis.	72
3.29	LIBS experimental set-up consisting of a frequency quadrupled Nd:YAG laser producing pulses up to $\approx 260 \mu\text{J}$ to ablates the microdroplet target. LIBS emission is observed along the laser axis.	75
3.30	Microbubble nucleation in action during the application of short electrical pulses. Nucleation process of a heater activated with a 14V 15 μs pulse at different times, from left to right (a) $t = -5 \mu\text{s}$ (before the start of the heating pulse);(b) $t = 0 \mu\text{s}$; (c) 5 μs ; (d) 10 μs ; (e) 15 μs ; (f) 20 μs and (g) 25 μs	76

3.31	Droplet formation captured over a period of a 5 μ s. Sequence of droplet formation using a 13V 5 μ s pulse across a 60 Ω heater. The images were captured using the setup described in Fig. 3.29. Images from left to right show the bubble at (a) 1 μ s; (b) 2 μ s; (c) 3 μ s; (d) 4 μ s; and (e) 5 μ s. A reflection of the partially extruded microdroplet from the PDMS surface is seen in the top of each image.	77
3.32	A piezoelectric microdroplet dispenser is shown with the schematic of the voltage pulse is shown. An image of a 20 μ m microdroplet generated with a 30 Vpp voltage pulse with a 5 ns rise and fall time is shown.	78
3.33	LIBS and LA-LIF experimental set-up consisting of a frequency quadrupled Nd:YAG laser producing pulses up to \approx 200 μ J to ablate the microdroplet target. The plasma is re-excited after a fixed time delay by a frequency doubled dye laser at 283 nm to excite Pb. LIBS and LA-LIF emission is observed along the laser axis.	79
3.34	Optimization of axial focal position in laser ablation studies at a breakdown energy of \approx 92 μ J. Larger values of relative focal position focus further on front of the droplet.	80
3.35	Plasma images obtained at low fluence ablation of the microdroplets \approx 92 μ J. Even though the energy is not enough to completely ablate the microdroplet the microdroplet acts like a converging lens to focus the laser beam to the back to generate a higher intensity in images at (- 0.2 mm and -0.1 mm).	81
3.36	Plasma images captured at a higher ablation energy of \approx 192 μ J. As can be observed at the focal spot complete ablation of the microdroplet is achieved.	82
3.37	Focal spot scan done at a high ablation energy of 192 μ J is shown. The LIBS emission intensity obtained from using Na as a analyte is highest at the best focus position.	82

4.1	Pb emission spectra generated from single-pulse LIBS at different gate delays (50, 70, 110, 150 and 210 ns) in the spectral window 390–420 nm. Experimental conditions: laser pulse energy=260 μ J, gate width=100 ns, accumulation=100 events. The spectra were offset vertically by 1×10^4 counts each for ease of viewing	84
4.2	Comparison of the LOD obtained for μ LIBS to other reported results in literature as a function of energy used. All the results were scaled to 100 shot LOD's.	85
4.3	Selective enhancement of lead using LA-LIF. The sample contains aluminum and lead as analyte. The spectra were obtained by (a) LIBS and (b) the LA-LIF scheme. Only Pb atoms were excited by the LA-LIF technique. The number of events accumulated for each spectrum was 100. A grating of 600 lines/mm was used in order to observe both Al and Pb emission lines.	86
4.4	Pb emission spectra obtained by using LA-LIF with two different ΔT . The second pulse re-excited the plasma at (a) $\Delta T = 50$ ns and (b) $\Delta T = 3000$ ns. The background was extremely high in case (a) whereas the signal became too weak in case (b). Each spectrum was an accumulation of 1000 events. The concentration of Pb was 50 ppm by weight.	87
4.5	Intensity of the Pb 405.8 nm line (solid circles), the background noise (open squares, $\times 500$), and the S/N (open diamonds) at different probe times ΔT . For each ΔT the probe position was centered at 36 μ m in front of the water surface.	88
4.6	Time-resolved Pb emission signal obtained from the LALIF scheme. The detector gate width was 10 ns and moved in 10 ns steps. The Pb concentration was 500 ppm, and the probe time delay was set at $\Delta T = 700$ ns. The number of events accumulated for each data point was 100.	90
4.7	1σ background noise (open squares) and SNR (solid circles) vs detection gate width. Signals were obtained for Pb at 50 ppm and a probe time of $\Delta T = 300$ ns and ablation pulse energy of 170 μ J.	91

4.8	Single-shot Pb spectrum at gate widths of (a) 20 and (b) 200 ns. The result indicates that a longer gate window accumulates more noise spikes. Signals were taken for Pb at 50 ppm concentration and a probe time of $\Delta T=300\text{ns}$	92
4.9	Calibration plot for Pb using the LA-LIF scheme with (a) 100 and (b) 1000 shot accumulations. The Pb signal (solid circles) and the 3σ background noise signal (open squares) are plotted against the Pb concentration. The intersection of the two lines gives the 3σ LOD. For the 100 shot case, the signal can be fit by $I = 2257C_{Pb}$, where I is the intensity and C_{Pb} is the concentration in ppm. The average 3σ noise is 798 ± 40 counts. For case b, the linear fit is $I = 24005C_{Pb}$, and the average 3σ noise is 2789 ± 200 counts.	92
4.10	Pb 405.8 nm emission line obtained using the LA-LIF scheme with a 10000 shot accumulation for a sample with a concentration of 166 ppb as verified by ICP analysis. The SNR is 11.7.	93
4.11	Relationship between number of accumulated shots and the S/N. Data were taken for a Pb concentration of 5 ppm and $\Delta T=300$ ns. The line is a least-squares fit to an $N_{shot}^{-1/2}$ slope scaling law.	94
4.12	Comparison of our LA-LIF LOD for Pb in water to other results reported in literature. The LOD's are plotted with respect to the ablation laser pulse energy used.	95
4.13	Pb emission signal measure using a PMT for an accumulation of 100 shots. The ablation laser energy was 260 μJ the probe laser energy was 8 μJ .The interpulse separation was 300 ns.	97
4.14	Pb emission signal measure using a MPPC for an accumulation of 100 shots. The ablation laser energy was 260 μJ the probe laser energy was 8 μJ . The interpulse separation was 300 ns.	98

4.15	A comparison of the theoretical (closed squares) to the experimentally (open squares)determined values for the fluorescence signal emitted. The concentration of Pb was 1 ppm and the ablation pulse energy was 260 μJ the excitation pulse energy was varied. The theoretical results presented are for a sum of 1000 shots assuming a temperature of 0.2 eV and atomic density of 10^{21} m^{-3} and a 30% overlap factor between the probe pulse and the plasma (i.e) assuming the probe beam only samples 30 % of the plasma plume. The delay between the two pulses was 300 ns. The detector gain was 200. Details of the calculation are given in Appendix A.	100
5.1	LIBS emission intensity as a function of detector gate delay for different laser pulse energy . The size of the microdroplet was constant at $\approx 20 \mu\text{m}$. The gate delay was varied from 80 ns to 10 μs . The laser pulse energy was varied from 50 μJ to 470 μJ . Each data point is an average of 100 laser shots. The detector gain was set at 200 and the gatewidth was 1 μs	103
5.2	LIBS emission intensity as a function of laser energy for different sizes of the microdroplet for different gate delays. The laser pulse energy was varied from 50 - 450 μJ . The size of the microdroplets was varied from 8-23 μm . The detector gate delay was set at 100 ns and the gate width was 1 μs . The gain of the detector was set to 200 and the slit width of the spectrometer was 300 μm	104
5.3	(a)Figure shows the variation of the μLIBS signal and SNR as a function of the size of the microdroplet. (b) Is the variation of the LA-LIF emission signal and the SNR as a function of the size of the microdroplet for a 100 ppm sample of Pb. In both the experimenst the ablation pulse energy was 130 μJ the gate delay was set to 300 ns and the gate width was 50 ns. For the LA-LIF case the energy of the probe pulse was 8 μJ . All data shown is an accumulation of 200 shots. . . .	106

5.4	(a) Shows the 10 shot accumulation of μ LIBS emission from 20 μ m droplets. (b) Shows the 10 shot accumulation of LA-LIF emission from the microdroplet. The LA-LIF emission appears brighter indicating the resonant re-excitation of the plume. The ablation energy used in both cases was 195 μ J and the probe pulse energy in the LA-LIF case was 10 μ J. The inter-pulse separation was 300 ns and the gate width was 100 ns.	107
5.5	A comparison of the spectral emission for Pb obtained with μ LIBS and with LA-LIF. The μ LIBS laser pulse energy is 130 μ J the gate delay was set at 300 ns and the detector gate width was 50 ns the spectrometer slit width is 300 μ m the size of the microdroplet is 18 μ m the detector gain was set at maximum the concentration of Pb in the solution was 100 ppm. For the LA-LIF case the experimental conditions were the same, the energy of the resonant laser pulse was 8 μ J and the delay between the two pulses was 300 ns. The Pb emission is not visible for the μ LIBS case as it is below the detection limit of the system but the Pb emission at 405 nm is clearly visible for the LA-LIF case. Both spectra represent a 100 shot accumulation.	108
5.6	LA-LIF signal emission intensity and SNR as a function of the probe pulse energy. The ablation laser energy was 130 μ J the probe pulse was varied from 2-8 μ J. The delay between the two pulses was 300 ns. The detector gate delay was set at 300 ns and the integration time was set to 50 ns. The spectrometer was centered at 405 nm, the grating used was a 2400 l/mm and the slit width was 300 μ m.	109
5.7	The signal distribution for 1000 shots for the LA-LIF emission for a 20 μ m microdroplet.	110
5.8	Comparison of the fluctuation in data of Na μ LIBS emission for 1000 shots for a waterjet target and a 20 μ m microdroplet target for a laser energy of 170 μ J. As can be observed the relative signal fluctuation is almost the same for both the microdroplet and the waterjet.	111

5.9	Single shot LIBS spectra on a micro-droplet. The pulse energy for ablation was 200 μJ , and the spectra were obtained at a gate width of 1 μs with gate delay varied: (a) 100 ns; (b) 200 ns; (c) 500 ns; and (d) 800 ns. The corresponding SNR are 11, 4, 2, and 0 respectively. . . .	112
5.10	Multiple shot accumulation μLIBS spectra on microdroplets. 100 shot accumulation μLIBS spectra on micro-droplet. The gate delay was set at 100 ns.	113
6.1	The temporal profile of the laser pulse as simulated by MED103 hydrocode.	120
6.2	The spatial variation of the density profiles at different instances in time. The microdroplet is 40 μm in diameter.	123
6.3	The spatial variation of the electron temperature profiles at different instances in time. The microdroplet is 40 μm in diameter.	124
6.4	The spatial variation of the ion temperature profiles at different instances in time. The microdroplet is 40 μm in diameter.	125
6.5	The spatial variation of the density, electron and ion temperature profiles 50 ns. The microdroplet is 40 μm in diameter.	126
6.6	The spatial variation of the density, electron and ion temperature profiles at 100 ns. The microdroplet is 40 μm in diameter.	127
6.7	The spatial variation of the density, electron and ion temperature profiles at 200 ns. The microdroplet is 40 μm in diameter.	128
6.8	The radius of the shockwave as predicted by ideal blast wave theory (squares) into ambient 1 atm nitrogen and by the Medusa103 hydrocode (circles) for an absorbed energy of 300 mJ. The microdroplet is 40 μm in diameter.	129
6.9	Emission signal versus the resonant excitation probe position as a function of distance from the waterjet surface. The probe beam (2nd beam) is 238 μm in diameter. Three different ΔT are compared: 200 ns, 500 ns, and 2000 ns.	129
6.10	The radius of the shock wave as a function of time calculated using the ideal blast wave theory for an absorbed energy of 260 μJ	130

7.1	Illustration of our experimental setup. Only one of the three wavelengths (1064, 532, or 266 nm) was used at a time.	133
7.2	Detected Pb emission signal intensity at 405.7 nm as a function of detector gate delay. Three different wavelengths of laser pulses were used: 266 nm 1.8 mJ (open circles), 532 nm 3.46 mJ (filled triangles), 1064 nm 4 mJ (open squares). The detector gate delay was varied from 0.5 to 3 μ s, the gate width was set at 3 μ s, the detector gain setting was 100, the grating used was 2400 l/mm, centered at 405.7 nm and the slit width of the spectrometer was 100 μ m.	135
7.3	Detected Pb emission signal intensity at 405.7 nm as a function of detector gate delay. Three different wavelengths of laser pulses were used: 266 nm (open circles), 532 nm (filled triangles), 1064 nm (open squares). The detector gate delay was 500 ns, the gate width was set at 3 μ s, the detector gain setting was 100, the grating used was 2400 l/mm, centered at 405.7 nm and the slit width of the spectrometer was 100 μ m. The inset shows the magnification of the regime of 266 nm close to the ablation threshold.	136
7.4	RSD of signal intensity versus pulse energies for three wavelengths: (a) 266 nm, (b) 532 nm, (c) 1064 nm. The RSD of each data point was measured based on five sets of signals with an accumulation of 100 shots in each set. The curves are visual fits to guide the eye.	137
7.5	Relation between the SNR and the number of shots for pulses of three different wavelengths: (a) 266 nm, (b) 532 nm, (c) 1064nm for accumulations of 10 to 1000 shots on a wood slice sample preconcentrated for a 20 ppm concentration of Pb in water.	139
7.6	Calibration curves for pulses of three different wavelengths: (a) 266 nm, (b) 532 nm, (c) 1064 nm, with lead solutions with concentrations from 200 ppb to 50ppm. The error bars are based on the standard deviation of ten sets of measurements for 100 shots/measurement. Laser energies of 1.8, 3.5, and 4:0mJ were used for irradiation wavelengths of 266, 532, and 1064 nm, respectively.	140

7.7	Measurement of the background emission of 10 different runs (grey line) and the emission from the wood substrate that has been dipped in 200 ppb lead solution (solid back line) by 100 shots accumulation with 532 nm pulses at an average energy of 3.5 mJ. The average of background signal is given by the black dashed line. An SNR of 6 is obtained	142
7.8	Experimental setup of the μ LIBS setup using electrolytic preconcentration. The microchip laser at 1064nm , 4 μ J is shown in the diagram.	143
7.9	Pb spectra for two different concentrations, 0 ppb and 30 ppb. The spectra were obtained using the microchip LIBS setup described earlier. The concentrations were verified using ICPMS.	145
A.1	Definitions of physical constants in mathcad.	152
A.2	Partition function matrix for PbI from NIST tables.	153
A.3	Partition function matrix for PbII from NIST atomic energy level tables.	154
A.4	Calculation of the Debye length and Saha equation for Pb.	155
A.5	Reduction in ionization energies.	155
A.6	Approximation for partition function of PbI.	155
A.7	Approximation for partition function of PbII.	156
A.8	Probability that PbI or PbII are in ground state.	156
A.9	Calculation of degree of ionization.	157
A.10	Plot of degree of ionization for PbI from 0-1 ev at number densities of 10^{20} and $10^{21} m^{-3}$	157
A.11	Plot of fractional ground state population for PbI from 0-1 ev at number densities of 10^{20} and $10^{21} m^{-3}$	158
A.12	Initial conditions and physical constants definitions. The energy of the probe laser beam was 10 μ J.	159
A.13	Calculating the number of Pb atoms available based on the ablation laser spot size and concentration of the solution.	160
A.14	Calculating the number of atoms available in the ground state based on the ionization fraction and fractional ground state population from above.	161

A.15	Calculation of the number of emitted photons.	161
A.16	Calculation of the number of photons collected by the f/4 imaging system.	162
A.17	Calculation of the number of counts observed using an f/4 collection system with an intensified CCD.	162
B.1	An example of a MEDUSA 103 input file is shown. Details of the logical switches and the variables are explained in the text.	164
D.1	Simulation of surface temperature profile for the Pt microheater for a 12 V 5 μ s pulse on the surface and 2 and 5 μ m above the surface. . .	176
D.2	Simulation of surface temperature profile for the Pt microheater for a 14 V 5 μ s pulse on the surface and 2 and 5 μ m above the surface. . .	176

Glossary

AL Action Level.

AMS Atomic Mass Spectroscopy.

AOTF Acousto-Optical Tunable Filter.

APD Avalanche Photodiode.

CCD Charge Coupled Device.

CTE Complete Thermodynamic Equilibrium.

DLF Direct Line Fluorescence.

EBCCD Electron Bombardment Charge Coupled Device.

EHD Electrohydrodynamic.

EMCCD Electron Multiplication Charge Coupled Device.

EPA Environmental Protection Agency.

FWHM Full Width at Half Maximum.

GPDA Geiger Photodiode Array.

ICCD Intensified Charge Coupled Device.

ICP-AES Inductively Coupled Plasma - Atomic Emission Spectroscopy.

ICPMS Inductively Coupled Plasma Mass Spectrometry.

IPDA Intensified Photodiode Array.

LA-LEAFS Laser Ablation - Laser Excited Atomic Fluorescence Spectroscopy.

LA-LIF Laser Ablation - Laser Induced Fluorescence.

LCR Lead Copper Rule.

LCTF Acousto-Optical Tunable Filter.

LIBS Laser Induced Breakdown Spectroscopy.

LOC Lab on a chip.

LOD Limit of Detection.

LTE Local Thermodynamic Equilibrium.

MCP Microchannel Plate.

MPPC Multi Pixel Photon Counter.

PDA Photodiode Array.

PDMS Polydimethylsiloxane.

PMT Photomultiplier Tube.

ppb parts per billion.

ppm parts per million.

R-LIBS Remote - Laser Induced Breakdown Spectroscopy.

RF Resonance Fluorescence.

RF Root Mean Square.

RSD Relative Standard Deviation.

SNR Signal to Noise Ratio.

Chapter 1

Introduction

Atomic spectroscopy is based on the concept that when atoms are sufficiently energized they may re-emit the absorbed energy as electromagnetic radiation having frequencies characteristic of the radiating species, the intensity is proportional to the number of atoms responsible for the emission. With these two properties qualitative and quantitative spectroscopy can be carried out. The effect of focusing a laser beam on a material which excites the material into a state of optical emission is called LIBS Laser Induced Breakdown Spectroscopy and is one of the methods for the direct chemical analysis of materials. The basic motivation for LIBS is that it has capabilities in many fields: as a method for local analysis, as a micro chemical method, and as a method for distribution analysis in a solid. LIBS has the versatility of being able to work under different experimental conditions like atmospheric pressure, in different gaseous environments, in high vacuum conditions, and coupled with other methods. As LIBS causes the removal of material by melting and vaporization, it offers several attractive features for chemical analysis of surfaces such as local micro-analysis of surfaces with a micrometer-level lateral and depth resolution together with multielemental detection capability. Depth profiling and two-dimensional mapping can be combined for a three-dimensional analysis of the material. With the major advancements made in the field of microfluidics LIBS can be combined with fluorescence spectroscopy for very promising applications in the medical industry . The basic components of an emission spectroscopy apparatus include the excitation source, wavelength selector, and radiant power detector. The excitation source is required to produce free atoms and ions from any sample and to transform these atoms

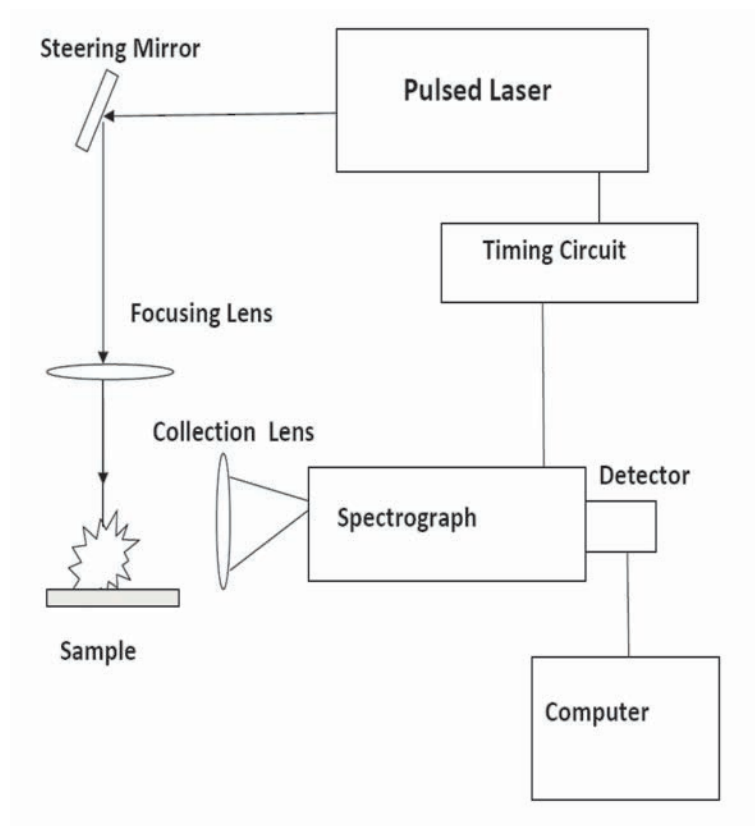


Figure 1.1: Layout of a typical LIBS setup.

and ions into excited species. The wavelength selector is needed to provide a specific frequency to the detector. The radiant power detector is capable of quantifying the intensity of electromagnetic radiation emitted from the excited atoms at a given frequency determined by the wavelength selector. A block diagram of a typical LIBS setup is shown in Fig. 1.1.

1.1 The LIBS Process

Soon after the development of the ruby laser, it was realized that when the laser radiation was focused, the intense light beam was capable of vaporizing and exciting solid material into a plasma. Brech and Cross first demonstrated the possibility of using lasers as excitation sources in atomic emission spectroscopy in 1962 [3]. LIBS is based on a concept that when a nanosecond laser pulse of high energy density strikes the surface of any material, the surface temperature is instantly increased beyond the vaporization temperature. The coupling of the pulse energy occurs through several

zone in the post- plasma plume. The decay typically ends with the formation of condensed clusters, which usually occurs within hundreds of microseconds after the plasma has been ignited. For analytical purposes, the emitted radiation (integrated over the first tens of microseconds) is spectrally resolved, and the emitting species in the laser-induced plasma are identified and quantified by their unique spectral wavelengths and line intensities of the emission change with respect to time as shown in Fig. 1.3

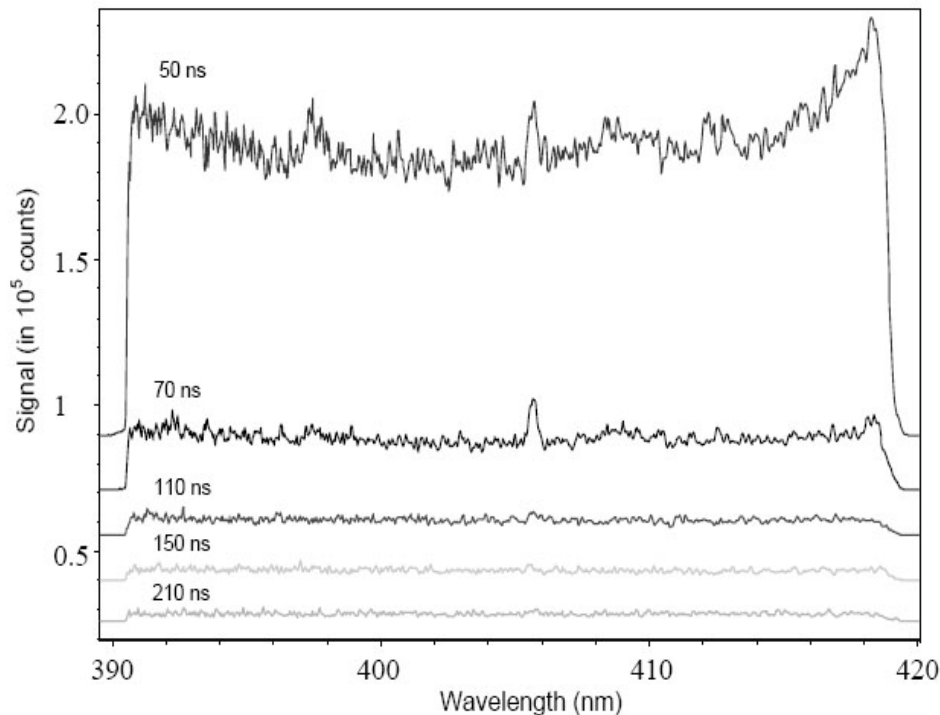


Figure 1.3: Pb emission spectra generated from a LIBS microplasma created by a 270 μJ , 7 ns, 266 nm laser pulse as it evolves in time in the spectral window 390 - 420 nm.

1.2 LIBS Instrumentation

A typical gated LIBS experimental setup is shown in Fig.1.1. To perform a LIBS analysis, the basic components include a high-powered, pulsed laser system, focusing optics (i.e., plasma-forming optics), optics to collect the signal, a monochromator or spectrograph to spectrally disperse the light, a gated detector, and a computer for data storage. The function of each component is discussed in more detail below.

1.2.1 Lasers in LIBS

The amount of laser power needed to produce a laser-induced plasma depends on many factors including: properties of the laser pulse (i.e., energy, mode quality, wavelength and pulse length), the focusing optics, as well as the type of sample or matrix under investigation [5]. For nanosecond pulses the typical power density requirements range from 10^6 to 10^{11} W/cm^2 [6,7]. In general, less power is required to form a plasma from solid substrates with more power required for liquid samples and gases, which require the most power. The most common laser system used for LIBS measurements is the Q-switched Neodymium Yttrium Aluminum Garnett (Nd:YAG) laser [6]. Typically the Nd:YAG is a 4 to 10 nanosecond (ns) pulsed solid state laser capable of providing reliable, powerful laser pulses at the fundamental and four harmonic wavelengths spanning from the near-infrared to the ultraviolet (1064 nm, 532nm, 355nm, 266nm, 215 nm). Other laser systems commonly used for LIBS measurements include gas lasers (e.g., CO_2 and excimer), and Nd:YAG or flashlamp pumped dye lasers [6]. In the late 90's there was an increase in the use of UV laser wavelengths in LIBS, which have been shown to have more efficient coupling to most metals [8–10]. The developments made in the generation and amplification of ultrashort laser pulses (≤ 1 ps) [11] opened up many applications in laser–matter interaction. High peak Laser intensities can be easily achieved with low pulse energies due to the very short laser pulsewidths. For example, a laser pulse with a pulsewidth of 100 fs (10^{-13} s) and a pulse energy of 330 μ J has a peak intensity of 10^{15} W/cm^2 when focused to a 20 μ m diameter spot. A 10-ns-long laser pulse would have to have 100 J in the pulse to reach the same intensity. As a femtosecond laser pulse deposits all of its energy into the material before any is transferred to the surrounding lattice [11,12] the material rapidly gets converted to an ionized gas. Also, due to the instantaneous energy deposition the laser does not interact with the plasma. On the other hand, a nanosecond pulse interacts with several transient states of matter. Therefore the use of femtosecond pulses leads to lower ablation thresholds, higher efficiencies of ablation, and ablation craters with less surrounding thermal and mechanical damage (i.e. less heat affected zone) [13,14]. Due to the lower amount of mechanical and thermal damage which occurs, more precise machining can be obtained [15–19]. The advantages of femtosecond

pulses for ablation are also desirable for certain LIBS experiments [20]. Several studies have been performed in order to characterize the properties and performance of femtosecond LIBS. The majority of these experiments have been performed on metallic surfaces: copper, brass, aluminum, etc. [13, 14, 21, 22]. Other studies have used femtosecond pulses for LIBS analysis of bacterial samples organic coatings [23, 24] and mapping of latent fingerprints [25]. Two key advantages associated with femtosecond LIBS have been identified: negligible effect of surrounding air and reduced background continuum emission [22]. Remote LIBS R-LIBS with pico- and femto-second laser systems was demonstrated by Rohwetter et al. [26]. They showed that using a container-integrated mobile terawatt femtosecond laser, together with the detection system (telescope, spectrometer, ICCD camera), it is possible to remotely induce and detect LIBS signals with signal to noise ratios allowing for analytical applications. They performed a systematic study with metallic samples (copper and aluminium) at a distance of 25 m to characterise the R-LIBS signal in the picosecond and femtosecond regimes. They also studied the dependences of the R-LIBS signal on the pulse energy and pulse chirp.

1.2.2 Optical Components in LIBS

A LIBS instrument requires optical components to direct the laser radiation onto the sample surface and to collect the radiation emitted by the plasma and direct it into the wavelength selector. A very common LIBS configurations is to have the laser output directed perpendicularly to the sample surface, a lens to focus the laser radiation and another lens, which is tilted at an angle to the laser axis, collects the emitted radiation and focuses it onto the entrance of the wavelength selection device usually a spectrometer [27]. Often a dichroic mirror, or prisms, are used to redirect the laser beam to the sample surface [28]. The use of a microscope objective lens as a focusing element is also very common [29]. This allows a more precise focus and a smaller spot size on the sample which in turn leads to a higher spatial resolution. Collection of the emitted radiation also can be made on the same axis as that propagating the laser beam by using a pierced mirror or using a beam splitter [30]. In the pierced mirror configuration the laser beam passes through a hole at the center of the mirror, while the reflective face of the mirror collects the emitted radiation

and redirects it to a collection lens and then onto a spectrometer [31]. For remote analysis telescopes are used to focus the laser beam and collect the radiation emitted by the sample which is placed meters away from the instrument [26]. Optical fibers in LIBS have been employed by several research groups either for directing the laser or collecting the radiation emitted by the plasma, or for both [32]. To make remote measurements in hostile or hard to access environments more feasible, fiber-optics have been incorporated to both deliver the laser pulse to the sample and collect the resulting plasma emission [33].

1.2.3 Wavelength selecting elements in LIBS

The LIBS technique generates a complex spectrum, with many emission lines. Often these lines are very close to each other in terms of wavelengths ranging from vacuum ultraviolet to infrared. Thus an ideal wavelength selector for LIBS should have the capability of covering large wavelength ranges simultaneously and with high resolution. Diffraction gratings, mirror and lenses are commonly used in spectrographs for example the Czerny Turner and Paschen Runge designs, have been extensively used in LIBS for many years [34, 35]. One drawback of these wavelength selectors is that they can either cover a short wavelength range with high resolution, decreasing the capability of multielement detection, or cover a wide wavelength range with lower resolution, sometimes resulting in problems of detection of specific emission lines due to their overlapping with other lines. In order to overcome these limitations and to avoid more expensive instrumentation, Body et al [36] employed up to four grating-based spectrographs, simultaneously covering different spectral regions with high resolution, to analyze the radiation emitted by the plasma. In spite of the limitations, grating spectrographs are still important as instruments with relatively low cost. Neuhauser et al. [37] described such an instrument using a Paschen Runge design in a Rowland circle type spectrograph. Another important feature is the capability to develop miniaturized devices coupled to detecting systems composed of a linear array of sensors. These kinds of spectrometers, available commercially, have been used in many studies [29, 38]. A spectrograph already used in other atomic emission spectroscopic techniques since the 1990s [39, 40] called an echelle spectrograph, which comprises of a coarse resolution grating operating in high order is being increasingly used in

LIBS. It is also compact and, associated with appropriate detectors, constitutes a spectrometer covering a wide range of wavelengths, typically from 200 to 1000 nm, with a high resolving power. The echelle technology has been developed since about early 1950 [41, 42] and the first applications of echelle spectrographs in LIBS date from the late 1990s [43, 44]. The echelle spectrograph employs a grating containing grooves having a step like profile with one highly reflecting facet for each groove. The angle between the facet perpendicular and the grating perpendicular is called the blaze angle and the largest efficiency for diffraction by an echelle grating is obtained at wavelengths satisfying the condition for reflection from the groove facets. In a simplified way, when an incident beam of radiation is diffracted by an echelle grating, a linear dispersion of high resolution is produced in the focal plane, which is constituted by several continuous wavelength ranges (called spectral orders) superimposed on each other. Therefore, in each direction containing emerging beams from the diffraction grating, there could be radiation of several wavelengths, each from a different spectral order. This means that the spectral images of several wavelengths coincide in the focal plane. To avoid this, an echelle spectrograph normally also employs a cross dispersing element (also called the order sorter). This element is either a second grating or a prism placed at 90° in relation to the echelle grating, in order to separate the different orders by shifting them orthogonally to the dispersion direction of the echelle grating. This generates a high resolution bi-dimensional dispersion of wavelengths versus spectral orders Fig. 1.4 [1]. Therefore, the echelle spectrographs must be used with detecting devices composed of a bi-dimensional array of sensors (discussed later), placed at the focal plane of the bi-dimensional dispersion.

The emission signals are acquired, compiled and the rows of the different orders are linked together into a linear spectrum. Reference [45] provided a good explanation of the basic principles related to echelle spectrographs. Modern echelle spectrographs are capable of generating a dispersion with a high diffraction efficiency in all orders and with a practically constant spectral resolution over the whole wavelength range. Sabsabi et al. [46] described a comparison between two commercial echelle spectrometers (ESA 3000 from LLA Instruments and Mechelle 7500 from Multichannel Instruments) in terms of detectivity and precision for determination of Be, Mg, Si, Mn, Fe and Cu in Al alloy samples, concluding that both presented similar performances.

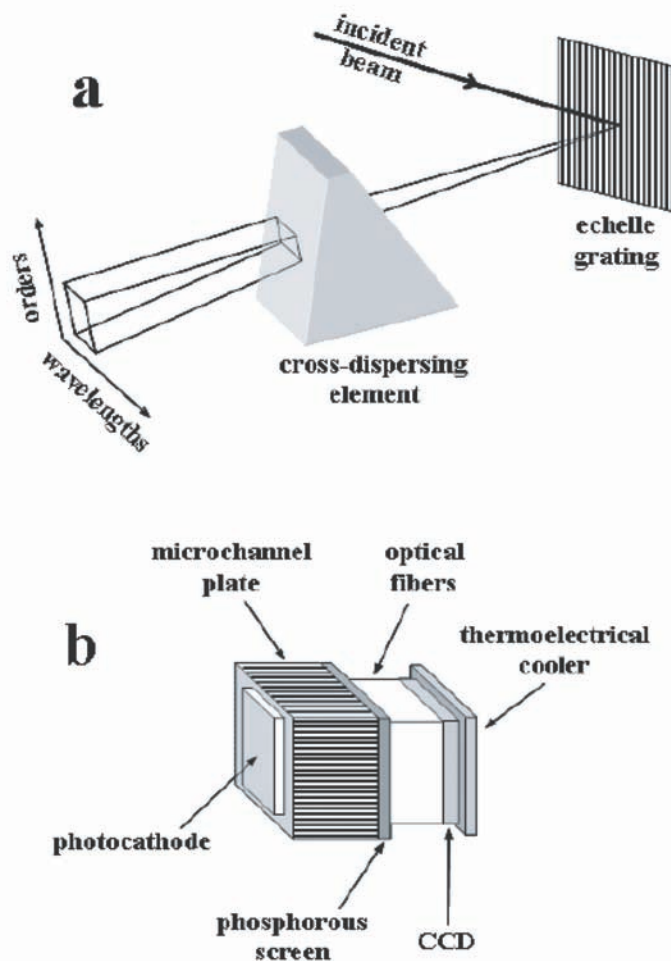


Figure 1.4: Illustration of an echelle spectrograph (a) Shows the echelle spectrograph and the bi-dimensional dispersion it produces. (b) Illustration of a intensified CCD with different parts labelled. (reprinted with permission from S.B.Q Sociedade Brasileira de Quimica (Brazilian Chemical Society)) [1]

Unlike the dispersive spectrographs, optical filters are less employed as wavelength selectors in LIBS. This is mainly because of their lower resolution and the selection of only one wavelength at their exit. This limits the number of emission lines that can be simultaneously detected to one line per filter and, therefore, reducing the capability of multielement detection. However, due to the higher throughput of optical filters (there is no slit) in relation to dispersive spectrographs, modern tunable filters, such as acousto-optical tunable filters AOTF, have been used in LIBS for plasma imaging, at a particular line emission wavelength, using bi-dimensional detecting systems [47, 48]. An AOTF is an optical band pass filter based on a diffraction of the

radiation by an acoustic wave, whose frequency determines the selected wavelength, propagating through an isotropic or anisotropic crystal medium (depending on the wavelength range of the AOTF). Another type of tunable filter, called liquid crystal tunable filter LCTF, has also been employed for plasma imaging [47]. The LCTF is a birefringent filter based on the constructive interference of theoretically just one wavelength, which is transmitted through the device, and destructive interferences of all others by different phase retardation between the ordinary and the extraordinary radiation rays passing through a liquid crystal. A comparison was made between an AOTF and a LCTF for plasma imaging. Both filters are capable of rapid wavelength selection with microsecond to millisecond tuning speeds while preserving imaging integrity. A higher background interference in the images generated was reported using the LCTF and a higher interference of strong atomic emission lines out of the tuning range was observed using the AOTF [47, 48]. Multiple images were also acquired at different wavelengths (for different laser pulses) around certain atomic emission lines using both filters, which were integrated in order to generate rough emission spectra, demonstrating higher resolution for the LCTF.

1.2.4 Detectors for LIBS

The two most common types of detectors used for LIBS measurements are intensified photodiode arrays IPDA, and intensified charge coupled devices ICCD [5, 7]. These detectors allow simultaneous collection of a complete laser-induced breakdown spectrum. Detectors having one sensor such as photomultiplier tubes PMT have not been used much in recent years. Even though using a PMT restricts the number of emission lines that can be measured simultaneously the advantage the PMT's present is of high detectivity in the visible spectral region there have been a number of publications with good results using PMT's [37, 49–51]. The development of high-quality solid state detectors made up of a combination of several sensors (also called pixels) in one device has provided a huge impetus to LIBS. These sensors allow the simultaneous acquisition of emission lines along a wide range of wavelengths. The PDA is made up of a linear array of up to 4096 photodiodes with a common n-type silicon as substrate while the CCD is made of linear or bi-dimensional configurations of several sensors, each made up of three electrodes over a common substrate of p-type silicon. In a

bi-dimensional configuration, they are also called CCD cameras [52, 53]. Typically the CCD's and PDA's are used with conventional spectrographs while bi-dimensional CCD's are employed with echelle spectrographs, due to the characteristic bidimensional dispersion generated by the echelle spectrograph. The higher the number of sensors present in a PDA or CCD, the higher the resolution of the acquired emission spectrum for the same wavelength range. In one of the first uses of a CCD camera in conjunction with an echelle spectrograph, the CCD area (due to its limited number of pixels) was smaller than the area of the focal plane of the echelle spectrograph, so that only one third of the total spectrum could be measured at one time to achieve a good resolution [43]. The PDA's or CCD's in the linear or bi-dimensional configurations employing an intensifier for signal enhancement and are referred to as intensified PDA and intensified CCD (IPDA and ICCD). A UV sensitizer is a scintillating coating applied directly onto their sensitive surfaces in order to convert UV radiation into visible radiation, making them more sensitive in the UV spectral region, where the PDA and CCD are relatively insensitive [45]. The intensifier used is generally based on a microchannel plate MCP, which also employs a photocathode and a phosphorous screen. Briefly, the incoming photons are converted to electrons by means of the photocathode, which are accelerated and multiplied in the MCP by application of a voltage, and then backconverted to photons when reaching the phosphorous screen. These photons are guided by a fiber optic taper or by a lens to the sensitive surface of the detecting device [54, 55]. The acceleration voltage applied to the MCP is variable, defining the gain of the intensifier, and its ability for fast switching allows gating of the optical detection on a nanosecond time scale (down to few nanoseconds). An illustration of a bi-dimensional ICCD is shown in Fig.1.4. Modern CCD's also include gating capabilities even without employing any intensifier, called gated CCD, but with higher gating times (generally down to hundreds of nanoseconds) [38, 45, 56]. The very fast gating capability is quite important since it allows a delay in starting detection in relation to application of the laser pulse, called delay time, removing from the detector signal the high intensity background continuum emission present in the early moments of plasma formation. In addition, it is used to optimize the detection for different decay rates between the plasma background continuum and the atomic emission for a given element. Gating detection, using IPDA, ICCD or

gated CCD, provides control of not only the delay time, but also the time for signal integration after the detection begins, called integration time gate, improving the analytical signal. It also permits averaging of multiple spectra for a series of laser pulses, one spectrum for each laser pulse, to compensate for pulse-to-pulse variations, frequently seen in LIBS [57]. The delay time is controlled by the electronics already present in the detecting devices or by a separate delay generator [37]. In both cases, counting of the delay time is initiated by a trigger pulse generated either by the laser source or by an additional detector, such as a fast photodiode, disposed to detect the laser radiation [26, 58] or the initial plasma formation. Yamasaki et al. described the development of a gated integrator suitable for gating control in LIBS, allowing the control of the delay time and the integration time gate down to 200 ns and 25 ns, respectively [59]. In addition to providing the acquisition of emission spectra, CCD cameras have also been used in LIBS applications for plasma imaging or sample imaging, in order to monitor plasma formation [47, 60, 61] or to adjust the sample position and the optical alignment in space resolved applications [28, 62], respectively. Studies of the temporal evolution of the plasma and the laser pulse are also carried out using fast photodiodes and PMT's connected to oscilloscopes [29, 63]. The acoustic emission associated with the laser ablation process can be measured using microphones connected to an oscilloscope [58] or a standard microcomputer sound card. The variation of acoustic emission as a function of the laser energy can be used to calculate the ablation threshold energy, or the minimum energy needed to start the ablation process, for a given sample. In comparison to PDA, CCD present a higher detectivity at lower radiation levels (such as those related to laser induced plasmas), the possibility of being used with echelle spectrographs (when using CCD cameras) and the possibility of gated detection even when a signal intensifier is not employed. That is why CCDs have been more frequently used in LIBS in recent years, in spite of their higher costs, although some examples of recent uses of PDA in LIBS can be cited [31, 32]. Recent papers dealing with comparisons between detecting systems employing ICCD and a non-intensified CCD for LIBS reported better performances for the ICCD in terms of temporal resolution, dynamic range and detectivity, even with the intensifier gains adjusted to their minimum values [38, 56]. Carranza et al. [56] observed an increase in the signal to noise ratio SNR of the ICCD in relation to the

CCD system from 2.8 to 25-fold for the 393.37 nm calcium emission line measured in calcium-based aerosols. Sabsabi et al. [38] observed an increase in the LOD of the ICCD in relation to the CCD system from 1 to 2 orders of magnitude from analytical detection for Cu, Mn, Mg and Be in aluminum alloy samples and Ni, Fe and Ag in copper alloy samples. On the other hand, although the use of ICCDs is becoming almost universal in LIBS (especially for quantitative applications), they present some drawbacks in relation to modern non-intensified CCD's. Some of the drawbacks are: much higher cost, lower resolution due to slight overlapping between the electrons of adjacent microchannels in the MCP, and a restriction of the upper wavelength range to about 850 nm depending on the photocathode. In addition, non-intensified CCDs can be more easily integrated into portable instruments due to their smaller dimensions. Recent advances in PDA and CCD technologies have introduced new devices with great potential for being employed in detecting systems for LIBS, such as the geiger PDA (GPDA), the electron bombardment CCD (EBCCD) and the electron multiplication CCD (EMCCD) [38, 55, 64]. The geiger photodiode is a photodiode operated under reverse polarization using a voltage above the breakdown voltage of the p-n junction (which is much lower than the voltage needed for the operation of a PMT), resulting in a high internal signal gain by impact ionization without any additional external amplification or detection cooling [64] (as for ICCD) .

1.3 Advantages and Limitations of LIBS

LIBS has a number of advantages over other forms of atomic spectroscopy. Much of this is due to the fact that a laser-induced plasma can be formed on virtually any type of sample, including solids, liquids, and gases, with no sample preparation required [5–7,65]. The sample needs to be only optically accessible as long as the laser power is high enough to obtain dielectric breakdown of the medium. Other advantages of LIBS include simultaneous multi-element analysis, small sample size (typically μg to pg per pulse), and the ability to perform a spatially resolved analysis. These advantages make LIBS ideally suited for remote on online analyses in cases where either a rapid analysis is needed, or sample handling needs to be minimized to prevent contamination and human exposure. Although it is relatively simple to form a laser-

induced plasma, the processes involved in laser-induced plasma formation are quite complex and difficult to reproduce [6, 7, 65]. As a result, LIBS is limited analytically compared to other laboratory-based techniques such as inductively coupled plasma atomic emission spectroscopy ICP-AES, or flame atomic spectroscopy. Specifically, LIBS detection limits are typically in the part per million ppm range as opposed to the part per billion ppb levels commonly achieved by ICP-AES [65]. The precision of this technique is also poor with the typical relative standard deviations as high as 10% [65]. These disadvantages stem from the non-linear sample ablation processes, shot to shot variations and sample matrix effects [65]. Despite these problems LIBS is still an attractive technique with applications spanning the environmental, medical, and industrial fields [8, 66–68]. The main impetus for the development of the LIBS technique is due to the need for rapid and direct determination of trace metals in various types of trace metals in various types of matrices from polluted air to paint, without complicated sample preparation. Many studies have investigated the use of LIBS for in-situ measurements in field deployable instruments, and online detection where a continuous monitoring of a certain analyte is desired. Thus there is continued interest in the development and application of LIBS as a sensitive technique with particular benefits gained in spatial and depth resolved analyses, remote sensing, operation in hostile environments and field-based applications. Improvements to the precision of the measurement, and detection limits are hoped to be achieved through continued fundamental studies, which aim to gain a better understanding of the factors that affect the LIBS signal.

1.4 Dual-Pulse LIBS

To address the sensitivity and reproducibility of LIBS some research groups have investigated the use of dual-laser pulses for plasma formation. Dual-pulse laser-induced breakdown spectroscopy also known as double-pulse excitation, is very similar to single pulse LIBS except that two or more laser pulses are used to form the LIBS plasma [69]. As illustrated in Figure 1.5 instead of a single laser pulse, a pair of laser pulses, which are typically delayed from each other by microseconds, are used to form the plasma. Fig.1.5 shows the difference between single and dual pulse LIBS

timing. In some cases it has been shown that the use of dual-laser pulses, can lead to lower detection limits [67]. The double pulse approach was first suggested by Piep-

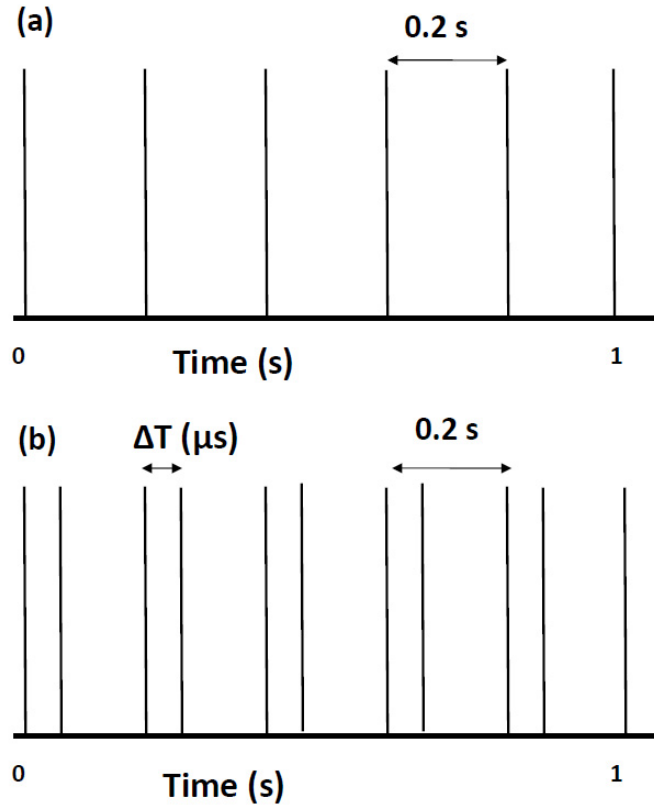


Figure 1.5: Schematic representation of laser timing in single and dual pulse LIBS (a) Single pulse LIBS: the laser pulses are at a 5Hz repetition rate. (b) Dual Pulse LIBS: Two laser pulses temporally separated by ΔT and at 5 Hz repetition rate.

meier and Malmstadt in 1969 [70] and Scott and Strasheim in 1970 [71] (they used aluminium alloy samples in air). They suggested that, because a large portion of laser energy is absorbed by the plasma plume, the second laser pulse could lead to further excitation of species in the plasma. In 1984, Cremers et al [72] performed a detailed study of the possible applications of the laser double pulse technique for analytical purposes. In this work they demonstrated the greatly increased emission intensities of elements during the bulk analysis of transparent liquids. Two main geometric configurations for the two laser beams have been realised for Double pulse LIBS as shown in Fig.1.6, collinear and orthogonal [73–75]. In the collinear case, both pulses have the same axis of propagation and are directed orthogonal to the sample

surface. The LIBS applications of collinear configuration demonstrate increases in the intensity of emission lines ranging from a factor of 2 up to a factor of 100 [76]. In the case of orthogonal pre-ablation, the first laser pulse irradiates perpendicular to the target surface generating a laser induced plasma above the target, and the second ablative pulse is directed orthogonal to the target surface. For the orthogonal re-heating mode, the first pulse irradiates the sample and the second re-heating pulse propagates parallel to the target surface. From the practical point of view, the collinear configuration is the simplest approach for the realization of the double pulse technique. Currently, it represents the only geometric configuration for stand-off double pulse LIBS applications. A combination of femtosecond (fs) and nanosecond (ns) laser pulses in orthogonal configurations was investigated by Pearman et al. [77]. A 30-fold enhancement for copper and 80-fold enhancement for aluminium was observed when fs (800 nm) and ns (1064 nm) pulses were combined in the re-heating configuration. For the studied wavelengths and pulse energies, it was found that a ns pulse is much more effective in the re-heating mode. It was also reported [78] that there was an enhancement of both material removal and emission intensity in the double pulse orthogonal configuration with a femtosecond pre-spark pulse and a nanosecond ablation pulse. This orthogonal combination yielded eight-fold and ten-fold increases of material removal for brass and aluminium, respectively. The observed increase in the emission enhancement factor was 3 to 4 times. In the double pulse configuration both the laser pulses used are mostly of the same wavelength; however, employing a double pulse scheme with pulses of different wavelength may lead to increased LIBS sensitivity. The combination of a UV pulse (ablation) and an IR pulse (reheating) was suggested by St. Onge et al. [79]. Lasers producing ultraviolet radiation are more effective for material ablation because of reduced plasma shielding. Thus, a UV pulse can be used for ablation with a second near-infrared pulse for effective re-heating of the plasma. It was found that sequential UV (266 nm)-NIR (1064 nm) double pulses on a Al target under certain conditions moderately improve LIBS sensitivity over that of NIR-NIR double pulses [79]. The effect of pulse energies in the collinear configuration was studied for different interpulse delays by Benedetti et al. [80]. In their case a substantial improvement of the LIBS signal was observed when the energy of the first pulse was equal to one third of the energy of the second pulse. Rai

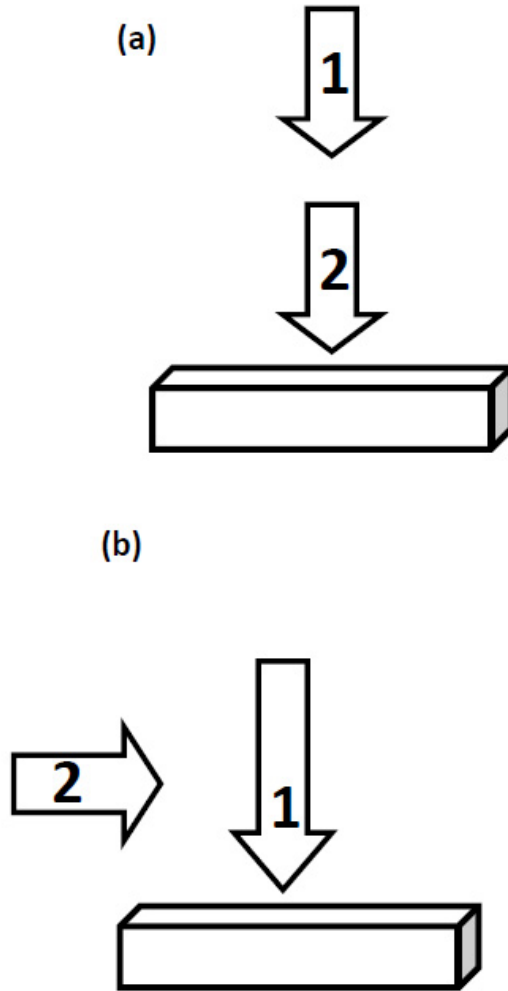


Figure 1.6: Geometric Configurations for Dual Pulse LIBS (a) Collinear (b) Orthogonal .

et al. [81] obtained the maximum emission intensity at approximately equal pulse energies for a liquid sample in the collinear mode. The variation of energy of the first pulse was conducted with the energy of the second pulse kept constant. Increasing the energy of the second pulse reveals a saturation effect [81]. Another double pulse approach was demonstrated by Chan and Cheung [82] based on resonance enhanced laser induced plasma spectroscopy. Because of the small time window between vaporization and thermal breakdown, the use of the double laser pulse procedure was suggested to increase the effectiveness of resonance-enhanced plasma spectroscopy. In this approach, the first intense 532 nm laser pre-pulse produced a hot plasma from

KIO₃ pellets containing traces of sodium. After 30 ns, a second 404.4 nm pulse was used for resonant photoionization of K atoms. As a result, a significant enhancement was observed for 589 nm emission of atomic sodium. The detection limit for Na was nearly 5 times lower with the suggested dual scheme compared to the single laser pulse technique. The ambient gas effect (air, N₂, He, Ar, Xe) and the influence of pressure on the performance of this configuration were analyzed by Lui et al. [83].

1.5 Micro Laser Induced Breakdown Spectroscopy (μ LIBS)

Traditionally LIBS employs lasers with pulse energies in the hundreds of millijoules range. During the mid- 1990^s several groups started applying μ J pulses to LIBS for different applications [25, 28, 62, 84–88]. This extension to the LIBS technique allows the probing of smaller sample spots for microanalysis applications, and would be compatible with fiber or microchip lasers which currently produce pulse energies in the range of 1 to several hundreds of microjoules. μ LIBS will assist in the development of both affordable and portable LIBS systems and thereby improve the utility of the LIBS technique for a number of industrial applications. The characterization of μ LIBS for microanalysis has been reported in a number of publications by our group [25, 62, 85, 86]. Rieger et al. [62] studied the scaling of LOD with energy, demonstrating LOD's comparable to high energy LIBS experiments. Cravetchi et al. [85] demonstrated single-shot classification of aluminum alloy precipitates, followed by the acquisition of a two-dimensional (2D) surface map of an aluminum alloy sample [86]. Taschuk et al. [25] demonstrated μ LIBS detection and mapping of latent fingerprints using 130 fs, 85 μ J pulses at 400 nm. The μ LIBS technique allows us to probe much smaller spots thus leading to a much higher spatial resolution for 2D scans of materials and also it allows the use of multi-KHz repetition rate fiber or microchip lasers which allow averaging of thousands of shots in a second and also are compact and portable.

1.6 Laser Ablation - Laser Induced Fluorescence (LA - LIF)

In Laser Ablation - Laser Induced Fluorescence LA-LIF, a focused laser beam is used to ablate a sample and after a delay time, a second laser, which is tuned to the resonant wavelength of the analyte atoms of interest, excites the atoms in the ablation plume and the fluorescence signal is detected. The advantages of laser ablation sampling include : (1) solid sampling, for which minimal sample dissolution and contamination is encountered; (2) suitability for both conducting and non-conducting samples; (3) localized analysis for which the ablation laser beam can be focused down to several micrometers to conduct local analysis; (4) depth profiling where analyte from different depths can be investigated; (5) suitability for both atmospheric and reduced pressures; and (6) close matching between the volume occupied by the sample atoms and the volume probed by the laser. This combination of LIBS and LIF was first investigated by Kwong and Measures [89]. As a demonstration of its application, Telle et al. [90] studied the Al, Cr, Fe, and Si content in steel. Kortenbrucka et al. [91] used LIBS - LIF to check for heavy metals in soil. Pesklak et al. [92] studied the temporal and spatial distribution of atomic species in a laser microprobe plume using non-resonance atomic fluorescence to provide three-dimensional resolution. The laser microprobe plume favors extended lifetimes of free atoms, which allows for increased observation time. However, matrix effects are pronounced without the use of internal standards, which must be used to improve precision. Gornushkin et al. [93] used laser ablation laser excited atomic fluorescence spectroscopy LA-LEAFS to study cobalt in solid sample matrices: soil, graphite and steel. Cobalt atoms, which were excited from a low-lying thermally excited state, yielded a better SNR than excitation from the ground state. The optimal time interval between the ablation laser and the probe laser was found to be in the microsecond range with an ablation laser power density of several GW cm^{-2} . Detection limits in the ppb to ppm range and linearity over four orders of magnitudes were obtained in a soil standard. They also studied lead in metallic reference materials by LA-LEAFS . A UV laser was used to ablate metallic samples, and a dye laser that was tuned to the resonant excitation wavelength of lead, 283.3 nm, was used to probe the lead atoms in the sample plume. Calibration

curves were constructed from various metallic samples that contained a wide range of concentration of lead from 0.15 to 750 $\mu\text{g g}^{-1}$. The amount of sample ablated by each laser pulse was estimated to be 20 ng. The optimal time interval between the ablation laser and the probe laser was found to be 100 μs and integration time of 200 μs was used to improve precision. When an atom is excited by a light source many physical and chemical processes occur, which include spontaneous emission and stimulated emission. Atomic fluorescence is included in the category of spontaneous emission of radiation. When the energy density of the light source is relatively low, the fluorescence signal is linearly proportional to the source energy density, since the de-excitation rate of an atom is faster than the excitation rate. As a result most of the atoms are in the ground state ready to be pumped to an excited state. As the energy density of the light source increases, the fluorescence signal becomes independent of the source energy density. Ultimately, LA-LIF is only limited in sensitivity by the onset of saturation of the atomic levels (i.e all atoms have absorbed a photon and have been raised to the excited state), at which point the signal is no longer proportional to the laser irradiance. The laser irradiance is typically set at or above the point of saturation, because this minimizes both quenching and the effects of fluctuations in laser irradiance.

1.6.1 Excitation-Detection Schemes

Several different excitation-detection schemes are commonly used as shown in Fig.1.7. The most suitable choice of excitation-detection scheme is dictated by the atomic structure of the element and also the possible interferences at various detection wavelengths.

The resonance detection scheme is shown in Fig.1.7(a) the fluorescence wavelength is the same as the excitation wavelength. This scheme is usually avoided if possible due to high levels of background noise from the scattered laser light. The non-resonant Stokes or the collisionally assisted non-resonant Stokes detection schemes in Fig.1.7 (b) and (d) are widely used for elements like Tl, Pb, Au [94] since they both yield high sensitivity and high rejection of stray and scattered light. Due to efficient collisional mixing between two nearby levels, the collisionally assisted detection schemes can be as efficient detection schemes where the upper laser connected level is identical to the

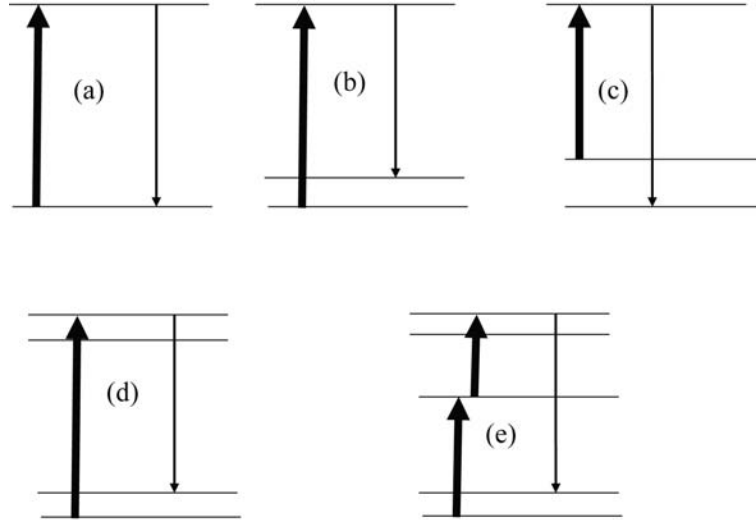


Figure 1.7: Various excitation-detection schemes used in LA-LIF also LEAFS. (a) Resonant detection (b) Non-Resonant (Stokes) (c) Non-resonant (anti-stokes) (d) Collisionally assisted non-resonance (Stokes) (e) collisionally assisted double resonance fluorescence. The different energy levels indicate the energy levels in the atom. The thick arrows indicate the stimulated absorption due to the laser excitation and the narrow arrows indicate the fluorescence radiation.

upper fluorescence level [94]. The non-resonant anti-stokes detection scheme as shown in Fig.1.7 (c) can yield a better signal-to-noise ratio and thus a better sensitivity, compared to the stokes detection scheme. This scheme is used with elements with a rather small energy difference between the ground state and the first excited state an example of which is Ga [94]. The double resonance excitation-detection scheme, where the atoms are excited by absorption of laser light in two steps is shown in Fig.1.7(e). It can be used in cases where the detection limit with other excitation-detection schemes is limited.

1.7 LIBS and LA-LIF for drinking water monitoring

One potential application of LIBS is the on-line real-time monitoring of hazardous contaminants such as lead in drinking water. Excessive ingestion of lead can result in physical or mental development delays for children and high blood pressure and kidney problems for adults [95]. According to the lead and copper rule LCR of the United State Environmental Protection Agency, the action level AL of lead in drinking water

is 15 ppb by weight [96]. When more than 10% of tap water samples collected during any monitoring period is greater than the AL, then actions like installing corrosion control treatment or replacing lead service lines must be taken. General practice for measuring the lead content is by inductively coupled plasma mass spectrometry ICPMS or graphite furnace atomic absorption spectrometry, which allows a sensitivity ranging from 0.01 to 0.1 ppb. However, the testing can only be conducted in a laboratory. Conversely, LIBS is potentially a portable technique. However, the limit of detection LOD for lead in water with conventional LIBS demonstrated to date is only 12.5 ppm [97]. There are other hyphenated techniques in which the sensitivity of LIBS can be further improved. Vander Wal et al. first deposited the lead solution sample onto carbon planchet and then evaporated the water. The residue left was probed by LIBS, and a sensitivity of 2 ppm for lead was obtained [98]. Ho and Cheung demonstrated a sensitivity of 0.25 ppb for lead in colloid form, which propagated slower in the plume thus resulting in a more concentrated region in the expansion plume. This volume was then re-excited by a 193 nm ArF laser [99]. The sensitivity of LIBS has to be addressed in order to compete with the aforementioned more sensitive non-LIBS techniques if it is to be used for testing of drinking water. However, many applications of industrial effluent monitoring require monitoring threshold levels which are much higher than the safe drinking standards due to the significant dilution factor allowed when effluent is discharged into a flowing river. These standards for lead emission are normally specified as 5 ppm [100]. However, this required sensitivity is still lower than that which can be achieved with traditional LIBS. The goal of this thesis was to improve the sensitivity of μ LIBS to the range required for analysis of water quality. This report presents a study to optimize conditions to obtain a very sensitive LOD using μ LIBS in combination with LIF. A laser pulse on the order of 200 μ J is used to create a microplasma. A second pulse is then tuned to resonantly excite the lead atoms inside the plasma. The ultrahigh sensitivity obtained reveals the possibility of building a cost-efficient and portable system for on-line monitoring of lead in drinking water or industrial effluents. In the following sections, the experimental setup and excitation scheme are first described. The optimization of the system and probe parameters are discussed next. Finally, the LOD is reported and possible methods to further improve the sensitivity are considered.

1.8 μ LIBS and LA-LIF for Microfluidics

1.8.1 Introduction

There is great merit in integrating sensitive analytical technologies onto microfluidic platforms for portability to perform testing at remote locations. Analytical detection techniques can broadly be classified as labeled and non-labeled. Labeled detection methods such as fluorescence detection [101] have already been adapted to microfluidic platforms. However, these techniques require that the samples of interest be tagged with particles such as organic dyes or quantum dots. For applications that require a large number of samples (and tests), such as elemental analysis for water quality assessment, labeling can be problematic requiring sample preparation steps that are expensive due to the tags and labor costs. Furthermore, although the sensitivity of these labeling methods is at the single-molecule level, they are typically limited by the lifetime of the fluorescent tags. Recently, there have been a few demonstrations of LIBS based detection (large volume and not on microfluidic chips) to various biomedical applications such as the detection of bacteria, spores and bioagents [102–104], and also cancer cells [105]. Another potential application of LIBS is the detection of low concentration elemental species in fluids either for simple chemical analysis or for analysis of cell contents in a fluidic stream which have thus far not been explored. The feasibility of detecting and quantifying sodium and potassium in single human red blood cells using LIBS has been reported earlier [106]. Though impressive, this demonstration makes use of a fluidic jet as a sample source, which we believe is suitable for use in a laboratory rather than a portable setting. Droplet dispensers using the microfluidic chip format have recently found applicability to several fields [107] but have not yet been applied to LIBS. Using μ LIBS to analyze the content of a monodispersed droplet allows us to retrieve both qualitative and quantitative information of a sample while requiring low laser energies. An important implication of making use of μ LIBS on monodispersed droplets emanating from microfluidic chips is the possibility of integration of several analytical techniques that have already been demonstrated within microfluidic platforms and eventually direct this work towards life-science technologies. There are several microelectromechanical (MEMS)-based droplet dispensing technologies applied for various applications, e.g. resistive

heaters [108,109], piezoelectric [110,111] and electrohydrodynamic EHD [112] methods. Of these, we believe that the resistive metal thin film heating is appropriate for use here due to its relatively low power consumption and ease in manufacturability. Furthermore, integrating thin film (platinum) resistive heaters within microfluidic chips is now a standard procedure using standard lab-on-a-chip LOC microfabrication technologies. There have been similar demonstrations of integration of droplets and analytical detection technologies, but none with LIBS-based techniques. Leonard et al. [107] demonstrated the use of a commercial thermal ink-jet based printer head to enable the rapid and reliable deposition of biological samples onto membranes for subsequent luminescence detection. Sung et al. [112] fabricated an EHD-based device for delivering ≈ 4 pL volumes of analyte, which can potentially be connected to a biosensing unit, such as atomic mass spectrometry AMS, mass spectrometry (MS) or protein microarray-type biochips. However, we believe that the integration of LIBS-based techniques with microfluidics will be highly suitable for a sensitive and a truly portable yet inexpensive analysis platform. To demonstrate the applicability of this μ LIBS-microfluidics integration, we perform sensitive detection of sodium by sampling hemispherical partially extruded monodispersed microdroplets generated by thermal actuation using a platinum resistive element within a microfluidic chip. We also performed μ LIBS studies using Na dissolved in water as a analyte on monodisperse microdroplets generated using a standalone piezoelectric dispenser and also LA-LIF studies on the microdroplet using Pb dissolved in water as a analyte. This integration is a significant technological advancement for LIBS. Such applications would allow the development of Lab on a Chip (LOAC) or micro-Total Analytic Systems (μ TAS) for the analysis of very small fluid samples. A conceptual layout of such a device is shown in Fig.1.8. Such sampling systems could potentially be operated at high sampling frequencies of the order of 100 – 1000 Hz. Experiments to characterize this technique and determine the potential sensitivity are described in chapter 5 of this thesis.

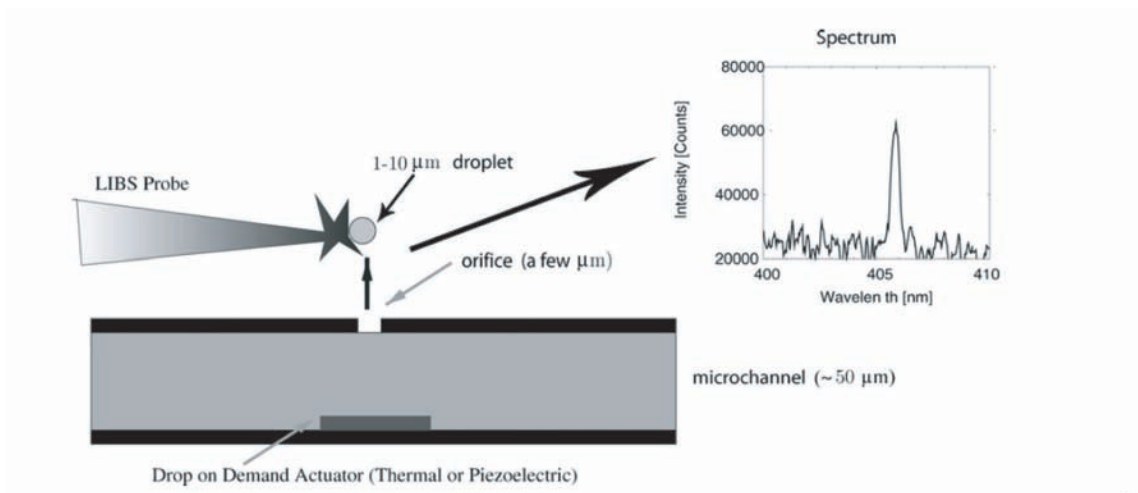


Figure 1.8: A droplet extrusion system using either a thermal or a piezoelectric technique to eject sample droplets for analysis of chemical composition.

Chapter 2

Principles of Laser Ablation - Laser Induced Fluorescence

2.1 Laser Matter Interaction

When a high-power laser is focused onto a material target the intensity in the focal spot produces rapid local heating and intense evaporation followed by plasma formation. Various factors affect the ablation process which include the properties of the laser as well as the target material. The evolution of the plasma depends on the intensity of the laser its wavelength, size of the focal spot, target composition, ambient gas and pressure. In this chapter the important physical processes related to plasma formation and plasma evolution will be discussed in detail.

2.2 Laser Ablation

When a high intensity laser pulse irradiates a sample, an extremely high-density excitation is produced on the surface of the sample [113]. The laser pulse energy is coupled with the electrons directly via acceleration in the oscillating electromagnetic field and then to the solid lattice through electron-phonon and electron-ion collisions. Ablation occurs when the energy deposited exceeds the critical temperature for phase transformation from a solid/liquid state to gaseous state, and the sample surface instantaneously vaporizes. As the surface rapidly heats ionization occurs forming a plasma plume. In the presence of ambient gas, the expanding plasma acts as a piston and compresses the surrounding gas. The gas is heated in the external shock wave which in turn decelerates the plasma expansion. Meanwhile, the gas temperature is

raised due to the collisions with the plume particles. Therefore, a significant part of the plume energy becomes thermal.

When a low fluence laser pulse irradiates a sample, atoms may detach from the surface without detectable surface damage. This phenomenon is called laser-induced desorption. While desorption can occur at a perfect surface site, it is more likely to occur at a surface site with defects or subsurface excitations that help localize the energy. Typical laser fluence to initiate desorption is in the range of 10^6 to 10^9 $W\ cm^{-2}$. Too high a fluence may lead to electron heating. Laser photons are first absorbed at the surface and free electrons or ions or atoms are excited. The laser energy is transformed into kinetics energy (for electrons) or electronic and vibrational energy (for atoms, ions, and molecule). When the energy absorption is strong enough, a breakdown of lattice bonds is possible. This is when desorption occurs [113]. However, in many cases, the photo-excitation is not localized. The absorbed energy is delocalized and the neighbouring atoms or molecules are vibrationally excited. Upon relaxation, the vibrational energy will be dissipated as thermal energy of the system. When the laser fluence further increases, the sample reaches its melting threshold. Some of the particles in the uppermost layer of the molten material have enough energy to transfer into the vapor phase. The ablation threshold is given by the term in the parantheses :

$$F \geq \left(\frac{\rho h \Omega}{\alpha}\right) \exp(\alpha z) \left(\frac{J}{cm^2}\right) \quad (2.1)$$

where F is the fluence for ablation, α (cm^{-1}) is the absorption coefficient, ρ ($\frac{atoms}{cm^3}$) is the density of the sample, h is the Planck's constant (Js), Ω is the phonon frequency for evaporation (Hz), the thermodynamic properties of a solid are directly related to its phonon structure. The phonon density of states determines the heat capacity of a crystal and the phonon frequency of evaporation is the frequency of the phonon vibrations at melting temperature, and z is the penetration depth of the radiation [113]. The depth of penetration of heat at time t (s) is the depth within which the energy of the of the heated material falls of to $1/e$ of the surface value.

$$D = (4kt)^{\frac{1}{2}}(cm) \quad (2.2)$$

where k ($\frac{cm^2}{s}$) is the thermal diffusivity. When a nanosecond laser is used for ablation considerable melting can be observed because of a large D .

On the other hand, the non-vaporized materials will be redistributed near the sample surface by diffusion. Diffusivity ranges from 10^{-5} to 10^{-4} cm^2/s in molten metals. Calculation of the particle diffusion is similar to that of diffusion of heat, except different species will have their own diffusivities. To calculate the final distribution of the elemental species, one can assume that the total volume occupied by the participating species remains unchanged. With this assumption, a single diffusivity can be used as the inter-diffusion of two elements, and the distribution of the melted species can be obtained [114].

2.2.1 Ablation by nanosecond pulses

When the pulse duration is of the order of a few nanoseconds and laser irradiance is in the range of 10^7 - 10^{11} W/cm^2 , some of the mechanisms involved in ablation are melting, sublimation, vaporization, ionization. The temperature at the target rises during the laser pulse and the temperature distribution can be calculated using the heat conduction equation [115]

$$\frac{\delta T(x, t)}{\delta t} = \frac{\delta}{\delta x} \left[\left(\frac{\kappa}{C_p \rho_s} \right) \frac{\delta T(x, t)}{\delta x} \right] + \frac{\alpha}{C_p \rho_s} I(x, t) \quad (2.3)$$

where T represents the temperature inside the target in K, x is the position from the surface, κ , C_p , ρ_s and α denote the thermal conductivity ($\frac{W}{m^{-1}K^{-1}}$), heat capacity ($\frac{J}{gK}$), mass density ($\frac{g}{cm^3}$) and absorption coefficient (cm^{-1}) of the solid target material, respectively Eq.2.3. The thermal evaporation rate J_ν is the function of the surface temperature [116]. Assuming thermal equilibrium,

$$J_\nu = 1.06 \times 10^6 \exp\left(\frac{-L_\nu}{K_B} \left(\frac{1}{T_s} - \frac{1}{T_B}\right)\right) \sqrt{\frac{M}{2\pi K_B T_s}} \left(\frac{atoms}{s^{-1}}\right) \quad (2.4)$$

where L_ν is the heat of vaporization and M is the atomic mass of the vapor. K_B ($\frac{J}{K}$) is the Boltzmann constant. T_B and T_s are the boiling temperature and surface temperature of the sample material, respectively in K. Vaporized mass can be ionized by the incoming laser beam forming the plasma. Laser radiation is absorbed primarily by inverse Bremsstrahlung, which involves the absorption of a photon by free electrons during the collision with heavy particles (ions and atoms). Free electrons play an

important role in inverse Bremsstrahlung heating. The electrons transfer the energy gained from the irradiating electromagnetic wave to other particles through collisions. The inverse bremsstrahlung absorption coefficient is given by [116]:

$$\alpha_{IB} = [QN_eN_0 + \frac{4e^6\lambda^3N_eZ^2N_i}{3hc^4m_e} \times (\frac{2\pi}{3m_eK_B T_e})^{1/2}] \times [1 - \exp(\frac{-hc}{\lambda K_B T_e})] \quad (2.5)$$

where Q is the absorption cross section for the absorption of a photon by an electron during collision with atoms, c is the speed of light, h is the Planck's constant and Z is the charge on the ions. N_e , N_i , N_0 are the number density of the electrons, ions and atoms respectively. T_e is the electron temperature. The first term on the right hand side of equation Eq.2.5 is the interaction of electrons and atoms and the second term is due to the electron ion interaction.

2.3 Growth of the Plasma

After the end of the laser pulse, the plasma induced by the interaction continues to expand into the surrounding atmosphere. The electron number density and temperature of the plasma change as the plasma expands. The expansion of the plasma is dependent on the amount and the properties of the ablated material the spot size of the laser beam and the surrounding ambient gas properties. Typically a LIBS spectrum is recorded on the order of one to a few microseconds after the laser pulse, hence a good understanding of how the plasma expands and what processes take place is very important in the optimization of LIBS measurements.

2.3.1 Plasma Shielding

Plasma shielding essentially occurs when a shield forms over the surface of the sample which influences the ablation process. It is formed when the gaseous particles surrounding the sample breakdown, or from the expanding plasma generated by the ablation itself. The effect on the ablation process results from absorption of part of the laser energy irradiating the sample which causes a reduction in the material removal so the shield interacts with the sample surface itself and causes material removal by the plasma. When the laser pulse duration is in the nanosecond regime the later part of the pulse is absorbed by the plasma. In the picosecond and femtosecond

regime the laser pulse is too short to be strongly absorbed by the plasma. However an air plasma can form during picosecond time period due to seed electrons from the target surface; this air plasma can absorb part of the picosecond pulse [117]. With femtosecond pulses plasma shielding can be neglected [117].

2.3.2 Plasma Expansion

Hot electrons, mass in the form of atoms and ions leave the sample after the laser pulse ends and the plasma expands. The expansion of the plasma is described by the following time-dependent Euler equations of the mass density, momentum, and energy conservation:

$$\frac{\delta \rho}{\delta t} = -\frac{\delta}{\delta x}(\rho \nu) \quad (2.6)$$

$$\frac{\delta}{\delta t}(\rho \nu) = -\frac{\delta}{\delta x}[p + \rho \nu^2] \quad (2.7)$$

$$\frac{\delta}{\delta t}[\rho(E + \frac{\nu^2}{2})] + \frac{\delta}{\delta x}[\rho \nu(E + \frac{p}{\rho} + \frac{\nu^2}{2})] = \alpha_{IB} I_{laser} - \epsilon_{rad} \quad (2.8)$$

where ρ , ν and P are the mass density, flow speed and local pressure respectively. E is the energy per unit mass, while α_{IB} is the absorption coefficient of Inverse Bremsstrahlung heating. When the expansion plasma reacts with the incoming laser beam (I_{laser}), the local laser energy absorption ($I_{laser} \alpha_{IB}$) and the energy radiating from the vapor (ϵ_{rad}) need to be considered too they represent non-linear terms, because they depend on the electron and ion densities, which in turn depend on the vapor density. Moreover, the vapor density can show large variations as a function of position, from near solid density till vacuum. This large discontinuity can give rise to shock waves. In order to accurately reflect this shock formation, an appropriate solution method needs to be used to solve the three conservation equations. Bogaerts et al. [115] used a finite difference method, based on finite difference schemes introduced by several researchers which describe the shock wave as a series of analytically solvable mini-shocks [118, 119].

2.3.3 Interaction of the plume with the environment

The expanding plasma interacts with the surrounding gas in three ways. First, the ambient molecules collide and cool the plume. Second, the molecules confine the plume, and slow the plasma from free expansion. Third, the exploding plume generates a shock wave in the ambient gas, which acts back to re-excite the plume atoms and ions. The conventional thermal conductivity measures the heat removal rate from a hot immobile surface under a temperature gradient. This is quite unlike the heat exchange among the mobile species in a hot plasma. The energy transfer between the plume and the ambient molecules may be better modeled by a simple two-body collision. The efficiency of energy transferred, η , can be expressed as [119]:

$$\eta \propto Nn\left(\frac{m_l}{m_h}\right) \quad (2.9)$$

where N is the number of excitable energy modes of the gas molecule, n is the number density related to the collision frequency, and m_l and m_h are the lighter mass and heavier mass of the particles in the collision, respectively. Since many collisions take place between the various particles, the plasma can be considered in local thermal equilibrium LTE. This means that in a sufficiently small region of the plume, thermal equilibrium is established between the electrons, ions and neutrals,

When η is high, the plasma temperature drops quickly. Concurrently, the ambient gas in contact with the surface of the plasma may be excited and ionized through the collisions. The plume expansion may be modeled as a spherical blast wave. The theory of shock waves and expansion plumes generated by lasers has been studied by many groups [120–122]. The value of the hydrodynamic quantities as a function of the expansion time, the stagnation distance of the expansion plume are two important parameters studied. Their models maybe used to predict the pressure, density and velocity for regions behind the shock front. If we combine this with the assumption of an ideal gas the temperature, pressure, density for all the regions behind the shock front can be estimated which in turn can be used to model the plasma emission. In the case of a strong shock, the background gas does not affect the propagation of the shockwave [120]. Taylor and Sedov used self-similarity to derive the shockwave relations for the spherical case. In the spherical geometry, the radius of the shock

front can be described by the relation

$$R(t) = s(\gamma)t^{2/5}E^{1/5}\rho^{-1/5} \quad (2.10)$$

$R(t)$ is the radius of the shock front, E is the energy deposited in the plume, s is a function of the γ the ratio of the specific heats of the background gas and ρ is the mass density of the ambient gas. An acoustic wave may be produced in the ambient gas under the expansion and compression of the plasma. Collisions with the background gas may initially transform high kinetic energy of the plume into the internal electronic energy of the background gas. When a supersonic spherical shock wave is induced, it exerts a pressure back on the plasma and re-excites the plume. This reheating is usually reflected by the rhythmic temperature variation of the plume. An attempt was made to study the propagation of a shockwave as described by Sir Geoffrey Taylor [120] in his work published in 1950. The plume stagnation distance has been studied by Dyer and Sidhu [122] for ablation studies using pulsed lasers. They developed an empirical relation for the length of the plume, L along the normal to the target when a pellet is irradiated with a KrF laser pulses of different intensities with low pressure oxygen gas as background. For an adiabatic expansion of the plasma with a conical expansion geometry the stagnation distance was reported to be

$$L = A[(\gamma - 1)E]^{1/3\gamma}P_o^{-1/3\gamma}V_i^{(\gamma-1)/3\gamma} \quad (2.11)$$

Here A is a geometric factor which depends on the expansion geometry of the plume. In the case of the study the plume has been assumed to expand as a cone with an angle θ which is capped with a hemispherical tip.

$$A = (1 + 1/\tan\theta)[3\tan\theta/(\pi + 2\pi\tan\theta)]^{1/3} \quad (2.12)$$

2.4 Spectral Line Emission

The spectral emissions from the laser-induced plasma reveal the composition of the sample. The origin of the emission signal may be explained by the electron transitions between energy levels.

2.4.1 Local Thermodynamic Equilibrium

When a gas with number density n is left sufficiently long in a thermally isolated box of volume V at absolute temperature T , the gas particles will come into equilibrium with each other and with the walls of the box. The whole system (gas and the box) is said to be one thermodynamic system. If dissociation and ionization occur in the gas, there will be different chemical species of specific number density. This system is said to be in the state of complete thermodynamic equilibrium CTE. When a plasma is in CTE condition, its radiation follows Kirchoff's Law [123], Planck's Law [124], and Stefan-Boltzmann's Law [125]. For all plasma particles, the laws that govern the distribution of kinetic energy, dissociation, and ionization are the Maxwell-Boltzmann distribution; the Guldberg-Waage equation [126], and the Saha-Eggert equation [127], respectively. The excited particles are populated over discrete energy states according to the Boltzmann distribution [125]. However, CTE condition only exists under very special conditions like stellar bodies, where the temperature and electron density are very high. In practice, a plasma usually has a cool outer part and a hot core, so a thermodynamic temperature does not exist. However, there exist many types of plasma in which some microscopic elements satisfy all the thermodynamic distribution laws in CTE condition. These plasmas are said to be in local thermodynamic equilibrium LTE condition. In such plasmas, the problems mentioned above can be solved due to a sufficiently high electron density. The reexcitation of a particle can be achieved by electron impacts. Electron collisions are also responsible for de-excitation, ionizations, and recombination within the plasma. All conditions (which will be discussed later), except the Planck's radiation law, that are satisfied under CTE are also fulfilled in LTE. However, radiation now plays an important role in LTE of low electron density. For a plasma to sustain spectral emissions under LTE, the localized electron impact excitation of the atom has to be faster than the radiative decay of the atom. Three equations can be established to describe the LTE condition [128]:

Maxwell-Boltzmann Distribution

When a plasma is in LTE, its free electrons obey a Maxwellian velocity distribution at plasma temperature T [125]:

$$f_M(\bar{v}) = \left(\frac{m_e}{2\pi K_B T}\right)^{3/2} e^{-m_e v^2 / 2K_B T} \quad (2.13)$$

Boltzmann Distribution of Energy States:

The bound electrons are populated over the discrete energy levels according to a Boltzmann distribution [125]:

$$\frac{N(m)}{N(n)} = \frac{g(m)}{g(n)} \exp\left[-\frac{E_m - E_n}{K_B T}\right] \quad (2.14)$$

Saha's Law:

The free electron and ion densities follow the Saha relation [129]:

$$\frac{N(Z, 0)n_e}{N(Z-1, 0)} = 2 \frac{g(Z, 0)}{g(Z-1, 0)} \left(\frac{m_e K_B T}{2\pi\hbar^2}\right)^{3/2} \exp\left[\frac{-\chi_i(Z-1, 0)}{K_B T}\right] \quad (2.15)$$

where $N(Z, 0)$ is the ground state population density with designated ionic charge Z . For example, $N(1, 0)$ is the population density of singly ionized atom in ground state. $\chi_i(Z, 0)$ is the ionization energy; and similarly, $\chi_i(Z-1, 0)$ is the ionization energy of particles of charge $(Z-1)$ in their ground state. The ratio of the emissivity $\epsilon(\omega)$ to the absorption coefficient $\alpha(\omega)$ of the atomic species can be expressed [128] as

$$\frac{\epsilon(\omega)}{\alpha(\omega)} \equiv \frac{\hbar\omega^3}{4\pi^3 c^2} \frac{1}{(e^{\hbar\omega/K_B T} - 1)} \quad (2.16)$$

For LTE to hold, the electronic collision processes must be extremely fast and must dominate the plasma rate equation. Using Eq. 2.9 to 2.12, it can be shown that the condition of LTE will only be approached at sufficiently high electron density [130]:

$$n_e \geq 1.4 \times 10^{14} T^{1/2} \chi^3(m, n) cm^{-3} \quad (2.17)$$

where $\chi(m, n)$ is the energy difference between levels m and n involved in the transition.

2.4.2 Line Emission

When an electron of an atom descends from an upper quantum level to a lower quantum level within the atom a spectral line emission is observed. During this bound-bound transition, a photon, which acts as a fingerprint of the atom, is emitted. The emissivity of this spectral line per unit length is characterized by the number of atoms in the upper state (N_{upp}), the transition probability (Einstein A coefficient), the emitted energy of the photon ($h\nu$) and the lineshape function [131]

$$I_{bb}(\lambda, n_e, T) = \frac{A}{4\pi} h\nu \times N_{upp} L(\lambda, n_e, T) W m^{-3} sr^{-1} snm^{-1} \quad (2.18)$$

The lineshape function is determined by line broadening which is dependent on n_e and T. The parameter N_{upp} is also dependent on n_e and T. It can be calculated using

$$N_{upp} = (1 - \alpha) N P_{upp} \quad (2.19)$$

N is the total number of neutral atoms, P_{upp} is the probability that an atom is in the excited state and α is the ionization fraction or the degree of ionization.

The ionization fraction for Pb was simulated in Mathcad for two different electron densities as a function of temperature. The details of the simulation are given in Appendix A and screen captures of the Mathcad code are given in Appendix A. Fig.2.1 shows a simulation of the ionization fraction as a function of temperature of the plasma. Thus we can also calculate the fraction of Pb atoms in the ground state versus the ionized state. For our case these are the number of atoms available for reexcitation with the resonant pulse. Fig.2.2 shows the number of Pb atoms in the ground state as a function of temperature.

2.5 Laser Plasma Modeling using MEDUSA Hydrocode

The computer program MEDUSA [132] calculates the 1-dimensional hydrodynamic and thermodynamic behaviour of a plasma irradiated by an intense laser beam. In MEDUSA the plasma is defined by four main dependent variables ρ , u , T_i , T_e representing the density, velocity, ion temperature and electron temperature respectively.

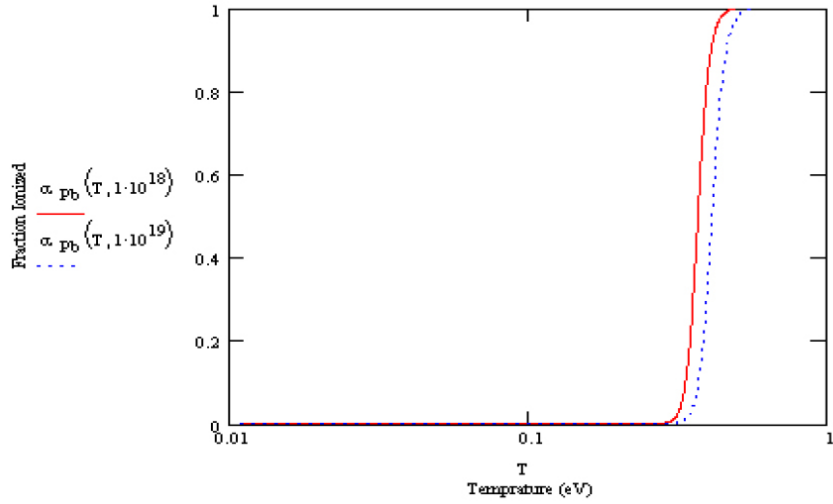


Figure 2.1: Simulation of the ionization fraction as a function of temperature for the three level Pb system for two different electron densities of $10^{18}m^{-3}$ and $10^{19} m^{-3}$

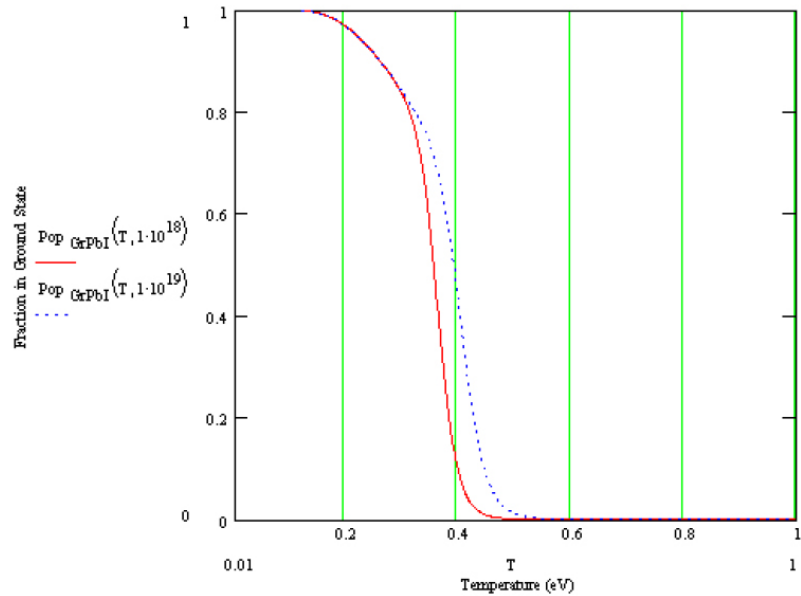


Figure 2.2: Simulation of population of the ground state as a function of temperature for the three level Pb system for two different electron densities of $10^{18}m^{-3}$ and $10^{19} m^{-3}$

Each of the variables is a function of a single space coordinate Each variable is a function of a single space coordinate r which can be chosen to correspond to slab, cylindrical or spherical geometry as required. The plasma is assumed to consist of charge-neutral electrons and various species of ions and atoms or molecules which

are collectively referred to as ions. The thermodynamics of MEDUSA treats the electrons as one subsystem with internal energy U_e per unit mass, temperature T_e , pressure p_e and specific heat ratio γ_e and the ions are another similar subsystem with their own set of equations. Charge neutrality requires that the subsystems have a common velocity, u . Electric fields are neglected in MEDUSA and the electron and ion subsystems are coupled by this common velocity and by the exchange of energy through electron-ion collisions or electron-atom collisions. The local electron density n_e only changes with time because of the hydrodynamic expansion and contraction of the moving fluid element. The exchange of energy between ions and electrons per second occurs at the rate [133]

$$\omega = \frac{M^{-1}Z^2e^4n_i\log\Lambda m_e^{1/2}}{32\sqrt{2\pi\epsilon_0^2m_H}}(kT_e)^{-3/2} \quad (2.20)$$

Where M is the average mass number and Z is the average charge number, m_e is the electron mass, m_H is the proton mass, the local ion density is n_i , $\log\Lambda$ is the coulomb logarithm [134] given by

$$\Lambda = \frac{1.24 \times 10^6 T_e^{3/2} n_e^{-1/2}}{Z} \quad (2.21)$$

The Bremsstrahlung radiation emitted by the electrons is represented by J is assumed to be escaping from the plasma and is thus an energy loss. In MEDUSA J is adapted from [133] for a Maxwellian gas

$$J = -\frac{\overline{Z^2e^6n_e\bar{v}_e}}{24\pi\epsilon_0^3c^3m_em_HMh} \quad (2.22)$$

The absorption of laser light is assumed to occur via inverse Bremsstrahlung at densities below the critical density [135]

$$\rho_c = \frac{\epsilon_0 M m_H m_e}{Z e^2} \omega_L^2 K g / m^3 \quad (2.23)$$

At critical density the plasma frequency equals the frequency of the laser light. The absorption coefficient is given by [135]

$$\alpha = 13.51\lambda^{-2}\beta^2(1-\beta)^{-1/2}T_e^{-3/2} \times (5.05 + \log\lambda T_e)\overline{Z^2}m^{-1} \quad (2.24)$$

where $\beta = \frac{\rho}{\rho_c} \leq 1$ and λ (m) is the wavelength of the laser light and T_e is in kelvins.

2.6 Laser Atomic Fluorescence

Consider a three-level model of an atom shown in Fig.2.3. Direct Line Fluorescence (DLF) can be realized in a three-level scheme - when the excitation takes place from level 1 to level 3 and fluorescence is recorded at the frequency of the 3-2 transition. Such a regime is by far preferable to resonance fluorescence (RF) when emission occurs on the 3 to 1 transition because it avoids the nonselective scattering of the powerful exciting radiation. The full realization of the advantages of the DLF can be reached only in the case of a source with a narrow line spectrum. From this viewpoint, a laser with such radiation spectrum differs advantageously from "classical" sources such as hollow cathode lamps or electrodeless discharge tubes-which give a rich spectrum of characteristic lines. In a three-level scheme, however, there exists a distinguishing characteristic which can considerably influence the fluorescence signal under laser excitation. The point is that, if optical transitions between 1-2 and 2-3 levels are allowed, the transition 3-1 is parity-forbidden, i.e. the level 3 can decay either due to radiationless collisions or due to magnetic-dipole and quadrupole radiation. Rather typical is the situation when all the above mentioned decay rates are small and level 3 is metastable (Just like in the case of Pb). Thus, at sufficient power and duration of the excitation laser pulse, a considerable portion of atoms can accumulate at level 3. In the case of RF, each atom can absorb and radiate many times during the laser pulse, but in the case of DLF, the atom transferred to level 3 is blocked from further interaction.

The rate equations for a 3-level system are

$$\frac{dN_1}{dt} = -N_1(R_{12} + R_{13}) + N_2R_{21} + N_3R_{31} \quad (2.25)$$

$$\frac{dN_2}{dt} = N_1R_{12} - N_2(R_{21} + R_{23}) + N_3R_{32} \quad (2.26)$$

$$\frac{dN_3}{dt} = N_1R_{13} + N_2R_{23} - N_3(R_{31} + R_{32}) \quad (2.27)$$

where R_{ij} are the total rates of excitation and deactivation of the appropriate levels including radiative and collisional processes. The system of equations Eq.2.25-

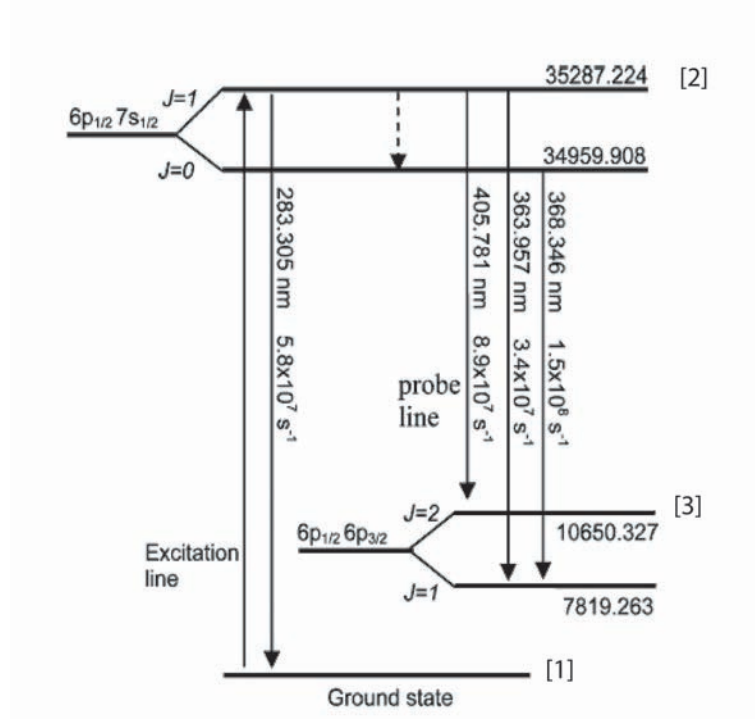


Figure 2.3: Illustration of a three-level model of a Pb atom

Eq.2.27 can be solved analytically. Consider the three level model of an atom as shown in Fig.2.3. If the laser frequency is set for level transition 1-3 the constants in Eq.2.25- Eq.2.27 become

$$R_{12} = R_{23} = 0, R_{31} = A_{31} + \rho B_{31} + Z_{31}, \quad (2.28)$$

$$R_{13} = \rho B_{13}, R_{21} = Z_2, R_{32} = A_{32} + Z_{32}$$

where ρ ($J.Hz^{-1}.m^{-3}$) is the spectral density of the laser radiation, B_{13} and B_{31} ($J_{-1}m^3Hzs^{-1}$) are the Einstein coefficients of induced absorption and emission, A_{31} and A_{32} (s^{-1}) are the Einstein coefficients for spontaneous radiation, Z_{21} , Z_{31}, Z_{32} (s^{-1}) are the rates of collisional deactivation of the appropriate levels. The solution of the system of equations Eq.2.25- Eq.2.27 with initial conditions $N_1(0) = N_0$; $N_2(0) = N_3(0) = 0$ with the above designations is [136]:

$$N_1(t) = N_0 \frac{R_{13}}{\xi_2 - \xi_1} \left[-\left(1 - \frac{R_{21} + R_{32}}{\xi_1}\right) \exp(-\xi_1 t) + \left(1 - \frac{R_{21} + R_{32}}{\xi_2}\right) \exp(-\xi_2 t) \right] + N_0 \frac{R_{21}(R_{31} + R_{32})}{\xi_1 \xi_2} \quad (2.29)$$

$$N_2(t) = N_0 \frac{R_{13}R_{32}}{\xi_2 - \xi_1} \left(-\frac{1}{\xi_1} \exp(-\xi_1 t) + \frac{1}{\xi_2} \exp(-\xi_2 t) \right) + N_0 \frac{R_{13}R_{32}}{\xi_1 \xi_2} \quad (2.30)$$

$$\begin{aligned}
N_3(t) = & N_0 \frac{R_{13}}{\xi_2 - \xi_1} \left[\left(1 - \frac{-R_{21}}{\xi_1}\right) \exp(-\xi_1 t) - \left(1 - \frac{R_{21}}{\xi_2}\right) \exp(-\xi_2 t) \right] \\
& + N_0 \frac{R_{13} R_{21}}{\xi_1 \xi_2}
\end{aligned} \tag{2.31}$$

where R_{ij} are determined using Eq.2.28 and values of ξ_1 and ξ_2 are determined by

$$\begin{aligned}
\xi_{1,2} = & \frac{X + R_{21}}{2} \mp \left[\left(\frac{X - R_{21}}{2} \right)^2 - R_{13} R_{32} \right]^{1/2} \\
X = & R_{13} + R_{31} + R_{32}
\end{aligned} \tag{2.32}$$

In the system being analyzed the transition between levels 1 and 2 is parity forbidden and so level 2 might decay due to non-radiative collisional processes. Analysis will be done for the case where level 2 is a metastable level so $R_{21} = 0$.

2.6.1 Case of a metastable level

Consider the case of Pb where the three atomic levels are 1,2 and 3. When Pb atoms are excited from the ground state to the $7s_{1/2}$ ($\lambda = 283.31$ nm) and fluorescence is recorded when the atoms decay to $6p_{3/2}$ ($\lambda = 405.78$ nm). At atmospheric pressure of Ar the lifetime of the level $6p_{3/2}$ is 1.8×10^{-5} s [136] which corresponds to the value $R_{21} = 5 \times 10^4 s^{-1}$. The values of A_{31} and A_{32} equal respectively $0.6 \times 10^8 s^{-1}$ and $3 \times 10^8 s^{-1}$ so the relationship $R_{21} \leq A_{31}, A_{32}$ is valid. In this case we can assume $R_{21} = 0$ and the solution to equations Eq.2.29 - Eq.2.31 is simplified. Steady state values of the populations are $N_1(\infty) = N_3(\infty) = 0$ this means that when the laser is switched on at $t=0$ all the atoms from the ground state follow the cycle 1-3-2 and accumulate at the metastable level. The temporal behaviour of the upper level population is determined from Eq.2.29 - Eq.2.31

$$N_3(t) = N_0 \frac{R_{13}}{\xi_2 - \xi_1} [\exp(-\xi_1 t) - \exp(-\xi_2 t)] \tag{2.33}$$

For ease of further calculation an assumption that the laser pulse is rectangular can be made. Let's assume the amplitude of the laser pulse is ρ and duration τ . The photons are recorded at a frequency ν_{32} which corresponds to the 3-2 transition. If the recording system integrates the fluorescence radiation over a time interval from

t_1 to t_2 . thus the fluorescence signal value is the total number of photons with the frequency ν_{32} radiated by a unit volume of the atomic cloud within the time interval $t_2 - t_1$

$$N_f = \int_{t_1}^{t_2} A_{32}N_3(t)dt \quad (2.34)$$

The choice of the beginning and the duration of the integration interval ($t_2 - t_1$) may have a considerable influence on the experimentally determined dependence of the fluorescence signal on the value ρ . If t_1 coincides with the start of the laser pulse and t_2 coincides with the end so that the signal is being integrated during the laser pulse the value of N_f can be determined from Eq.2.33

$$N_f = N_0 \frac{A_{32}}{A_{32} + Z_{32}} \left(1 - \frac{\xi_2 \exp(-\xi_1 \tau) - \xi_1 \exp(-\xi_2 \tau)}{\xi_2 - \xi_1}\right) \quad (2.35)$$

We can express the values $\xi_{1,2}$ in terms of the rates of radiative and collisional transitions. For our case ($R_{21}=0$) from Eq.2.32 the expressions for $\xi_{1,2}$ are:

$$\begin{aligned} \xi_1 &\approx \frac{R_{13}R_{32}}{X} = \frac{\rho B_{13}(A_{32} + Z_{32})}{A_{31} + Z_{31} + A_{32} + Z_{32} + \rho B_{13}(1 + g_1/g_3)} \\ \xi_2 &\approx X = A_{31} + Z_{31} + A_{32} + Z_{32} + \rho B_{13}(1 + g_1/g_3) \end{aligned} \quad (2.36)$$

from Eq.2.36 we can see that $\xi_2 \geq \xi_1$. For a representative value of ρ as $10^{-9}(\text{J.Hz}^{-1}.\text{m}^{-3})$ and $B_{13} = B_{12} = 1.4919 \cdot 10^{21} (\text{J}_{-1}\text{m}^3\text{Hzs}^{-1})$ and $A_{32} = 8.9 \times 10^7 \text{ s}^{-1}$, $A_{31} = 5.8 \times 10^7 \text{ s}^{-1}$ and substituting the values in equation Eq.2.36 we can calculate the values of $\xi_1 = 6.6 \times 10^5$ and $\xi_2 = 1.98 \times 10^{12}$. Once we substitute the values in Eq.2.35 N_f can be determined within an accuracy of $\leq 5 \%$ if

$$\xi_1 \tau \geq 5 \quad (2.37)$$

is fulfilled the expression for N_f becomes

$$N_f = N_0 \frac{A_{32}}{A_{32} + Z_{32}} \quad (2.38)$$

The equation Eq.2.38, for a large ρ and τ , shows that during time τ all the atoms will follow the cycle 1-3-2 and accumulate at the metastable level and in this case the total number of fluorescent photons will be determined by the quantum efficiency of fluorescence in the channel 3-2 [$A_{32}/(A_{32} + Z_{32})$]. The rates A_{31} and Z_{31} do not influence the value of N_f since all the atoms which have returned from the upper level

to the ground state will be excited again by the field into the level 3 and finally they will be at the metastable level 2. The condition Eq.2.37 can be rewritten as

$$\frac{\tau \rho B_{13}(A_{32} + Z_{32})}{A + Z + \rho B_{13}g} \geq 5 \quad (2.39)$$

where the notations $A = A_{31} + A_{32}$, $Z = Z_{31} + Z_{32}$ and $g = 1 + g_1/g_3$ have been introduced. If the energy density of the laser is large enough such that

$$\rho B_{13}g \geq A + Z \quad (2.40)$$

is achieved the condition Eq.2.38 is fulfilled with the duration of the laser pulse. The accumulation rate of particles at level 3 is determined by the rate of induced absorption 1-3 and by the ratio of decay probabilities of level 3 in the channels 3-1 and 3-2. For Pb atoms in inert gas with a laser pulse duration of $\tau = 5 \times 10^{-9}$ s the approximation $\xi_1\tau \leq 1$ and $\xi_2\tau \geq 1$ is valid if ρ is sufficient enough. In this case we can neglect $\exp(-\xi\tau)$ in Eq.2.35 and retain the first two terms in the expansion of $\exp-\xi_1\tau$ we obtain

$$\begin{aligned} N_f &= N_0 \frac{A_{32}}{A_{32} + Z_{32}} \left(1 - \frac{\xi_2(1 - \xi_1\tau)}{\xi_2 - \xi_1}\right) \approx N_0 \frac{A_{32}}{A_{32} + Z_{32}} \xi_1\tau \\ &= N_0 \frac{\rho B_{13}A_{32}\tau}{A + Z + \rho B_{13}g} \end{aligned} \quad (2.41)$$

The physical sense of this result indicates that when a metastable level is available atoms follow the cycle 1-3-2 only once within time τ and when quenching occurs ($Z_{32} \neq 0$) only a part of these atoms will radiate photons of frequency ν_{32} . Based on Eq.2.41 we can calculate the appropriate value of ρ that saturates the transition and compare it to the experimentally determined value.

Using the number of ground state atoms as $N_0 = 4.25 \times 10^3$ corresponding to 0.4 eV from Fig.2.2 for a starting atomic number density of $n = 10^{21}m^{-3}$ from appendix A. We can simulate the number of fluorescence atoms emitted for a 1 ppm Pb solution. The net signal for 1000 accumulated shots can then be calculated for an Intensified CCD camera ICCD. Fig.2.4 shows the calculated fluorescence signal as a function of the energy of the resonant laser pulse. In this case a focal spot diameter for the probe pulse of 238 μm has been assumed and corrections for the optical efficiencies of all elements as described in Chapter 3 have been included. We can see that the

theoretical estimation for the saturation of the transition is at an energy of $\approx 8 \mu\text{J}$. This is compared to an experimentally determined value later in this report.

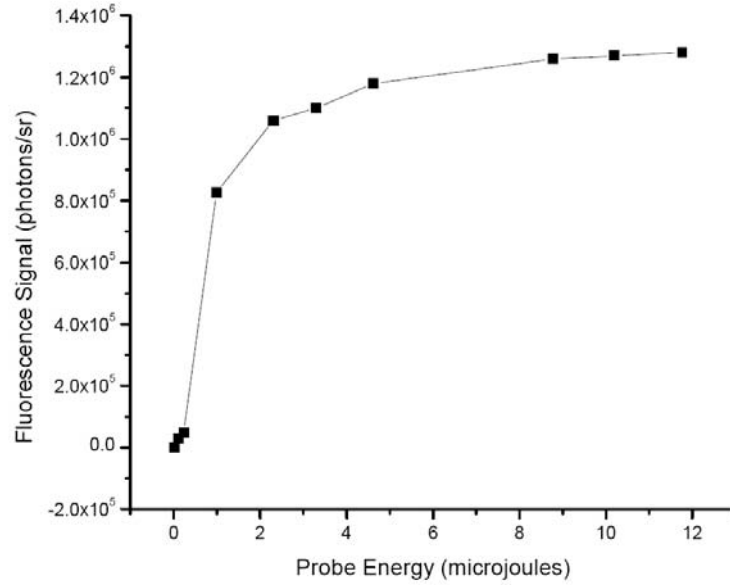


Figure 2.4: Simulation of the fluorescence signal emitted for a 1 ppm Pb solution as a function of the probe pulse energy for a $238 \mu\text{m}$ diameter probe spot. A probe pulse duration of 5 ns has been assumed.

Chapter 3

Experimental Methodologies

3.1 Introduction

This chapter gives an introduction to the various equipment and experimental techniques used in the course of this thesis. Details of spectrographs and detectors used and their calibration and response functions are described. Calibration procedures for laser energy and laser spot size determination are explained. A detailed study of detector settings is carried out. The methods used for signal analysis of the data will be outlined. Calibration procedures for target focal positions are also described.

3.2 LALIF experimental setup

The instrumental setup is shown in Fig. 3.1 The sample containing lead as analyte in the form of lead nitrate dissolved in water was delivered to a 1 mm nozzle by a peristaltic pump to form a liquid jet. The concentrations given throughout are in parts-per-million ppm or parts-per-billion ppb by weight of lead in the water. To prepare low concentration samples containing the analyte of interest first a higher concentration (for example 500 ppm of Pb in distilled water) solution was prepared. Then the high concentration solution was diluted by adding distilled water to the higher concentration solutions. Several samples and blank samples were sent for Inductively Coupled Mass Spectroscopy ICPMS analysis in a lab to verify their concentration and also to keep a check on contamination issues during sample preparation.

The first pulse for ablation was generated from a frequency-quadrupled flash lamp pumped Q-switched Nd:YAG laser (Big Sky Ultra CFR) at 266 nm with a pulse width

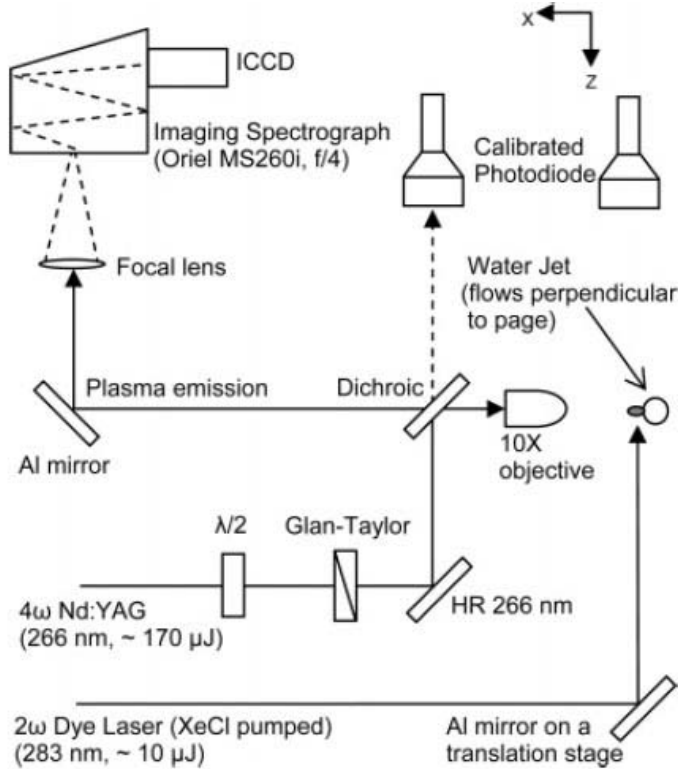


Figure 3.1: Schematic setup of the LA-LIF experiment. A frequency-quadrupled Nd:YAG laser (266 nm, ≈ 10 ns) at $170 \mu\text{J}$ ablates the water jet. Pulse energy is controlled by a half-wave plate and Glan-Taylor polarizer. The pulse for re-excitation is a frequency-doubled dye laser pulse pumped by a XeCl excimer laser.

of 10 ns. The laser pulse was focused by a microscope objective lens (Optics For Research, $10\times$, 15 mm working distance, $\text{NA} \approx 0.25$) to an approximately $12 \pm 3 \mu\text{m} \times 8 \pm 2 \mu\text{m}$ spot on the water jet surface. The objective was protected by a microscope coverslip, and it was found that only after a very large number of shots, on the order of 20,000 shots, the coverslip became foggy and required cleaning. The second pulse was a frequency-doubled XeCl-pumped dye laser (Lumonics HD-500, rhodamine 575), with a pulse width of ≈ 9 ns and a spot size of $\approx 238 \mu\text{m}$ (see section on laser focal spot size). The second pulse re-excited the plasma transversely (z -direction), and the intersection point was finely controlled by a translation stage. In the experiment, the second pulse was tuned to 283.3 nm (see section on wavelength calibration) such that the lead atoms were excited from the ground state to the $7s_{1/2}$ state as shown in Fig.3.2. The excited atoms decay to the $6p_{3/2}$ state emitting 405.8 nm photons. The spectral emission was imaged by a 20 cm focal length plano-convex quartz lens onto

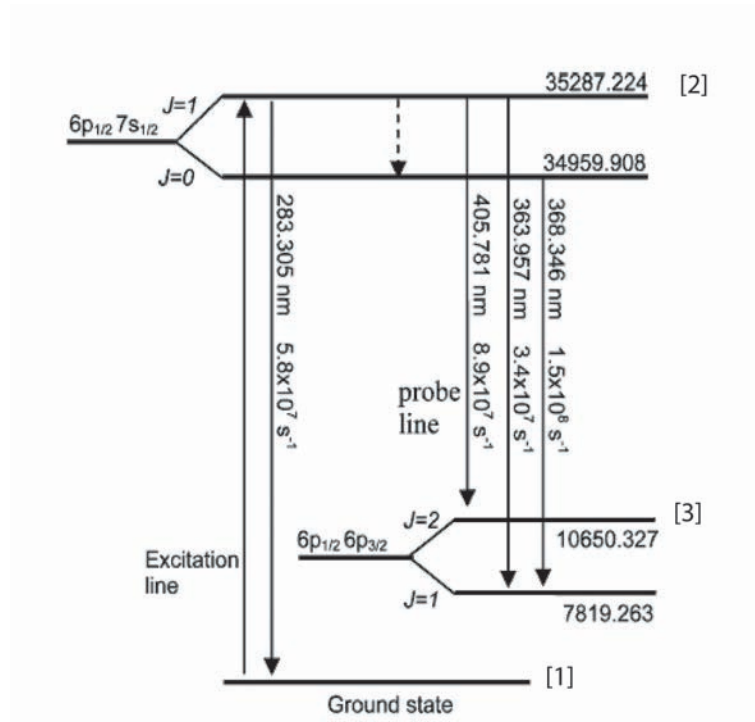


Figure 3.2: Simplified Grotrian diagram of Pb. The excitation and fluorescence transitions are indicated. The energies of the levels are in wavenumbers cm^{-1}

the entrance slit of a 0.25 m f/3.9 imaging spectrometer (Oriel MS260i) equipped with an intensified CCD (Andor iStar DH720). A grating of 2400 line mm^{-1} was used, and the slit width was 300 μm , yielding a spectral resolution of 0.45 nm. The intensifier on the ICCD was typically operated at the highest gain setting. Both laser systems were operated at 10 Hz. The temporal separation (ΔT) between the laser pulses was controlled by a delay generator (Stanford DG535). Unless stated otherwise, the energies of the first and second pulses were 170 μJ and 10 μJ respectively, and were monitored by two calibrated photodiodes (Hamamatsu R1193U). To obtain a spectrum, the delay generator triggered the first laser to fire and ablate the water jet. Then the second laser was triggered, and after a delay ΔT the beam intercepted the plasma. The emission from the plasma was then imaged onto the detector and recorded within an adjustable duration gate window. Each data set was an accumulation of a 100 spectra to improve the signal-to-noise ratio SNR and reduce the effect of signal fluctuation due to variations in laser pulse energies. The SNR is used as an indicator to quantify the signal strength. The signal is defined as the normalized in-

tensity under the full width of the Pb 405.8 nm line with the background subtracted. The noise was determined from the standard deviation of the background spectral density in individual channels scaled by the square root of the number of channels used to measure the peak line emission intensity. The noise was also scaled to take into account correlation in noise between neighboring output channels as determined from calibration measurements on the data acquisition system. The LOD is defined as the point at which the signal strength is 3 times the root mean square noise level.

3.2.1 Energy Calibrations

The energy delivered to the target is a very important parameter for LIBS [137,138]. As shown in Fig. 3.1 an online energy monitor measures the leakage light from the dichroic mirror. To calibrate the energy at the target a calibrated calorimeter is placed at the target location. The energy delivered to the target can then be compared directly to the energy monitor signal. Two photodiodes were used to monitor the pulse energies of the two laser beams namely the ablation pulse which was the 266 nm laser pulse and the resonant laser pulse at 283 nm. Fig.3.3 shows the calibration measurement for the 266 nm laser energy monitor and Fig.3.4 shows the energy calibration for the 283 nm energy monitor. The calorimeters used in these measurements were calibrated against a lab standard (Gentec ED-200). The lab standard is calibrated by the manufacturer against a NIST calibrated standard and has an accuracy of 5 %. The resultant accuracy of the experimental laser pulse energies was estimated to be $\pm 9\%$.

3.2.2 Laser Focal Spot measurements

One of the major applications of μ LIBS is in the scanning microanalysis of materials. To achieve high spatial resolution and very small ablation depths, very low energies and small focal spot sizes are desired. The smallest spot size gives a higher power density at the target which leads to higher signal strengths. A knowledge of the focal spot size at the target is important also for theoretical studies of the various laser-induced plasma properties. In this work a knife edge technique was used to measure the ablation laser beam profile. A a knife-edge monted on a piezo driven motorized stage was scanned through the beam and a measurement was made using

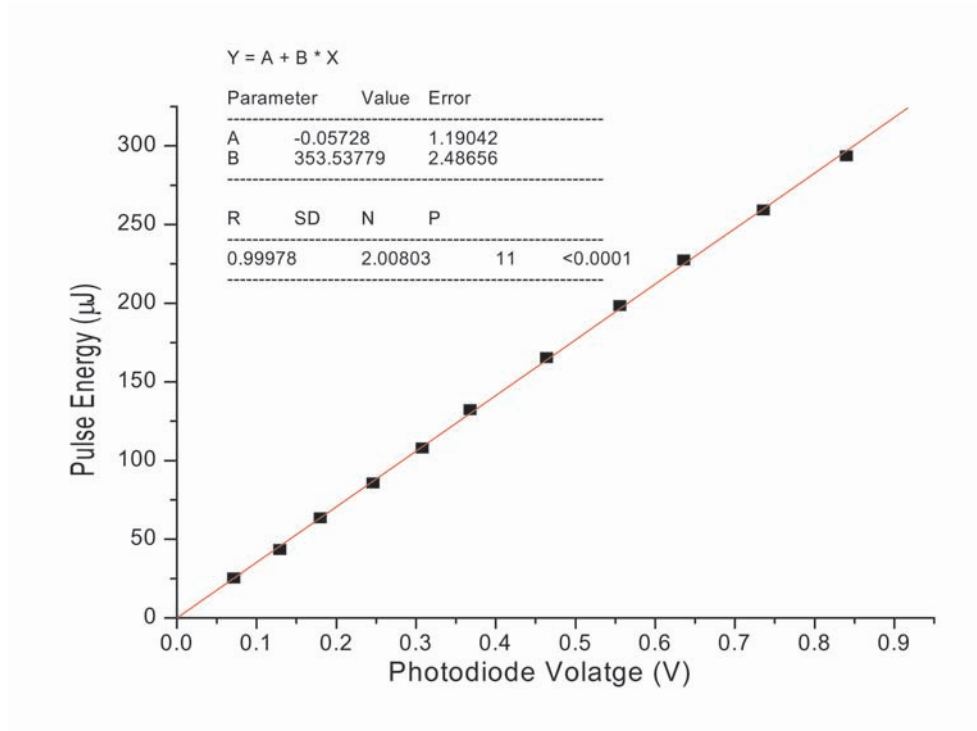


Figure 3.3: Energy calibration of a photodiode used to monitor the ablation laser beam energy. The calibration factor for this data set was $353 \pm 3 \mu\text{J}/\text{V}$

a photodetector behind the knife edge. The resolution, which is limited by diffraction from the scanning edge, is on the order of the wavelength of the beam. Knife-edge profilometers have a resolution as fine as 100 nm. As the blade moves across the beam, the detected signal decreases to zero and the measurement is differentiated to obtain the profile of the beam. The beam profile obtained at the focus of the 266 nm laser is shown in Fig .3.5 for the horizontal direction and Fig.3.6 for the vertical direction. The beam waist in the horizontal and vertical directions obtained using this measurement was $12 \pm 3 \mu\text{m} \times 8 \pm 2 \mu\text{m}$. This was the focal spot size used for the entire course of this work.

The spot size of the resonant laser pulse was also measured. A calibrated CCD camera (COHU 6612 progressive scan camera) was used to measure the spot size of the resonant laser pulse. Fig.3.7 shows the image of a calibrated scale using the camera. Each division on the scale is 0.005 inches which is 0.127 mm, the number of pixels between two divisions is 64 which corresponds to each pixel being $1.98 \mu\text{m} \pm 2 \%$. Using the same setup the resonant beam was imaged using the camera and a

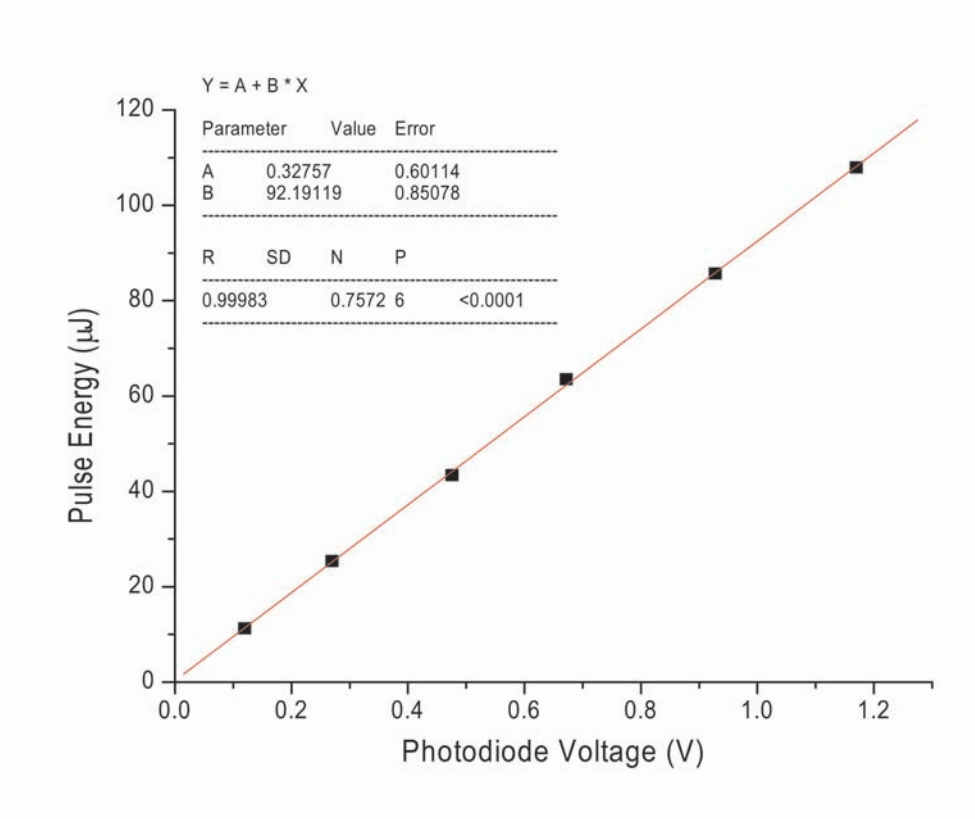


Figure 3.4: Energy calibration of a photodiode used to monitor the resonant probe laser beam energy. The calibration factor for this data set was $92 \pm 1 \mu\text{J}/\text{V}$

line profile across the beam was taken and a gaussian function was fitted which led to a beam waist of $238 \pm 5 \mu\text{m}$ in the horizontal direction and a waist of $\approx 400 \pm 10 \mu$. Fig.3.9 and Fig.3.10 show the spot image and the profile and the gaussian fit in the horizontal and vertical direction respectively. The resonant laser beam was not focused tightly on to the plasma, the idea is to excite every Pb atom in the plasma in the largest possible spot so that it emits a photon to maximize the fluorescence signal.

3.2.3 Wavelength Calibration

In order to obtain useful LIBS data the calibration of the spectrometer used to measure the spectra should be accurate. The imaging spectrometer's (Oriel MS260i) 2400 l/mm grating mentioned in the experimental section was calibrated using a Hg lamp (Oriel 6035). The calibration technique and procedure was similar to the one used by Reader et al. [139] and Sansonetti et al. [140] who used standard Hg emission

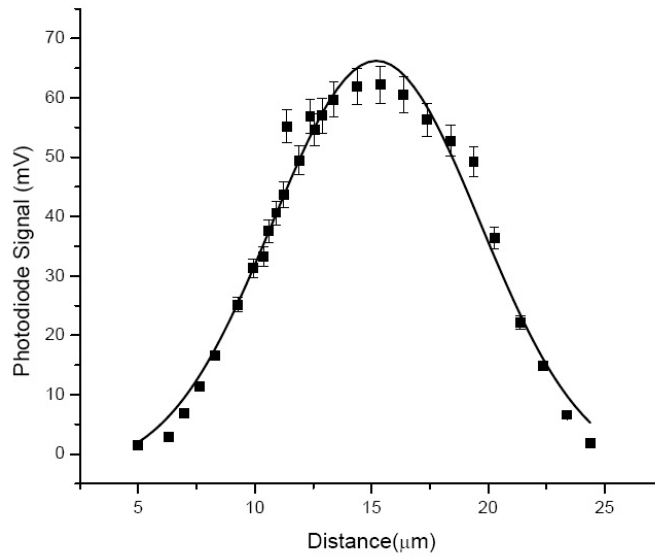


Figure 3.5: Measurement of the focal spot size of the ablation laser pulse using the knife edge technique in the horizontal direction. A gaussian fit indicates a beamwaist of $12 \pm 3 \mu\text{m}$

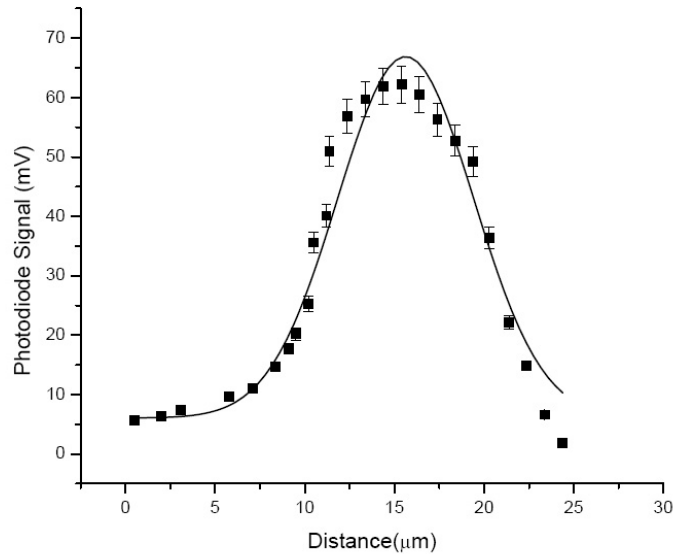


Figure 3.6: Measurement of the focal spot size of the ablation laser pulse using the knife edge technique in the vertical direction. A gaussian fit indicates a beamwaist of $8 \pm 2 \mu\text{m}$

lines from Hg pencil lamps. The other sources used throughout the thesis were the emission lines from the LIBS plasma of known metals such as Al and Pb. Sample data for a calibration of a 2400 1/mm grating set at a central position of 418 nm is

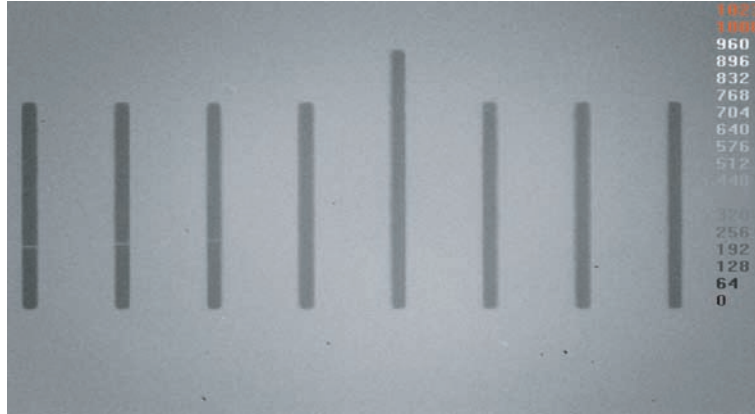


Figure 3.7: Image of a calibrated scale each division on the scale is 0.005 inches which leads to each pixel being approximately 1.98 μm .

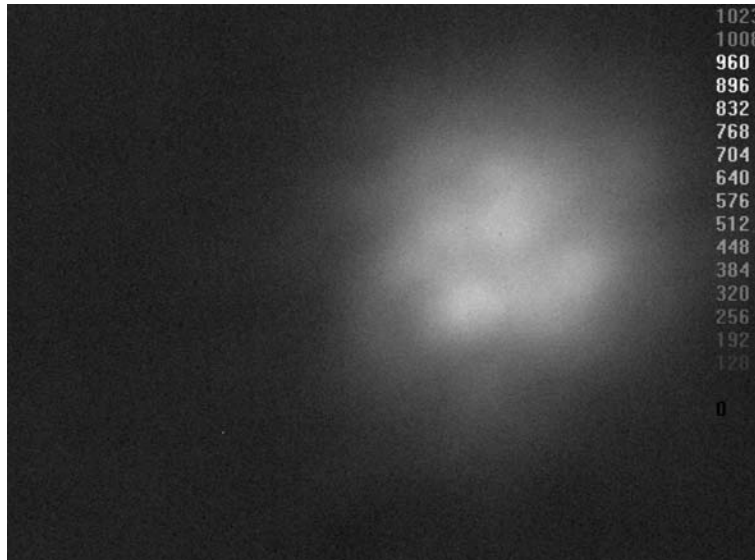


Figure 3.8: The image and line profile of the resonant laser beam. The gaussian fit indicated a beamwaist of $238 \pm 5 \mu\text{m}$.

shown in Fig.3.11 using the Hg lamp. In this case, 3 Hg lines, 404.65 nm, 407.78 nm and 435.83 nm are visible in the acquisition period. The grating was then moved to a center wavelength of 395 nm and an Al2024 alloy was tested for the known Al emission doublet lines at 394 nm and 396 nm as shown in Fig.3.12. This calibration technique was maintained for all the data presented using this grating during the course of this thesis. For the LA-LIF experiment, to verify if the dye laser wavelength was at the resonant 283.3 nm for Pb, a simple procedure was used. Fig .3.13 shows two spectra the top spectrum is the LIBS emission from Pb. The 280.19 nm, 282.31 nm and the

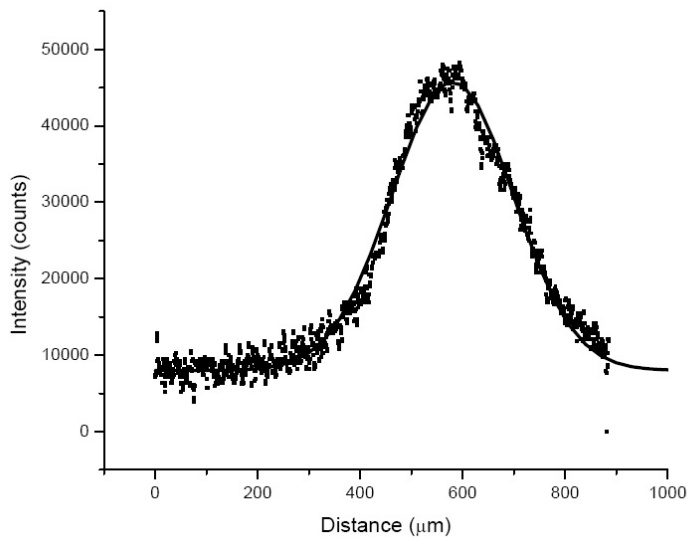


Figure 3.9: The image and line profile of the resonant laser beam. The gaussian fit indicated a beamwaist of $238 \pm 5 \mu\text{m}$.

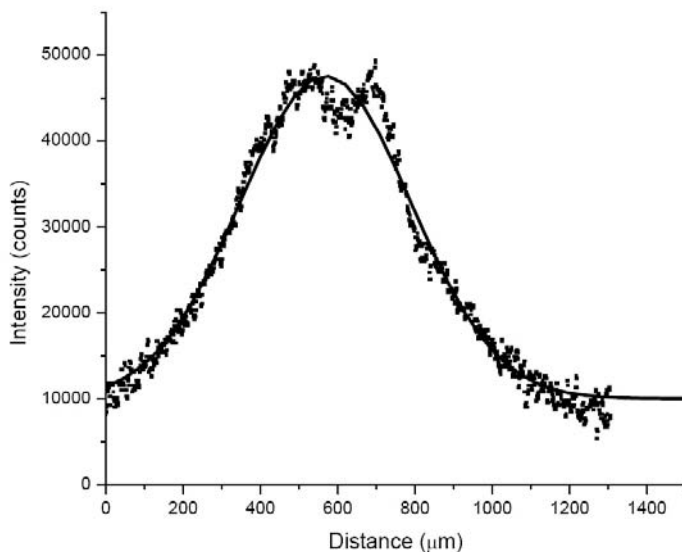


Figure 3.10: Fig shows the line profile of the dye laser beam in the vertical direction. A gaussian fit to the line profile indicates a beam waist of $400 \pm 10 \mu$

resonant line for our scheme at 283.305 nm are visible. Then the dye laser was tuned to overlap the 283 nm line. The dye laser line obtained is indicated in the bottom of Fig.3.13

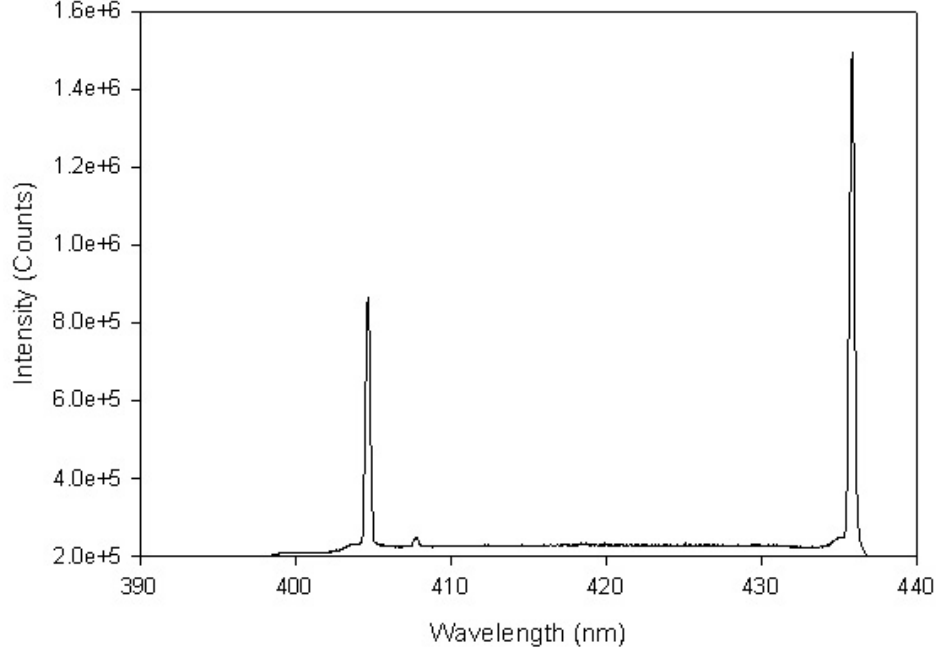


Figure 3.11: Three emission lines from a Hg lamp 404.65 nm, 407.78 nm and 435.83 nm are shown. The spectrometer grating was 2400 l/mm and was centered at 418 nm. The 407.78 line has a much lower intensity compared to the other two lines.

3.2.4 Detector Response

To measure the response of the ICCD detector a line emission technique [141] was used. A lambertian emitter was used to scatter laser radiation to a spectrometer's entrance slit or a PMT's photocathode. Light scattered by a lambertian source has a emission pattern given by [142]

$$E = \frac{E_{input}}{\pi} \cos\phi \quad (3.1)$$

The scattered light varies in intensity based on the emission angles. The number of counts expected as a function of the angle is given by

$$N_{count} = \frac{GN_{\gamma}\Omega_{slit}T(\lambda)\eta(\lambda)\cos\phi}{\pi} \quad (3.2)$$

where N_{γ} is the number of photons scattered from the barium sulphate plate, Ω_{slit} is the solid angle observed by the slit of the spectrometer, $T(\lambda)$ is the spectrometer transmission, $\eta(\lambda)$ is the quantum efficiency of the photocathode and G is the gain

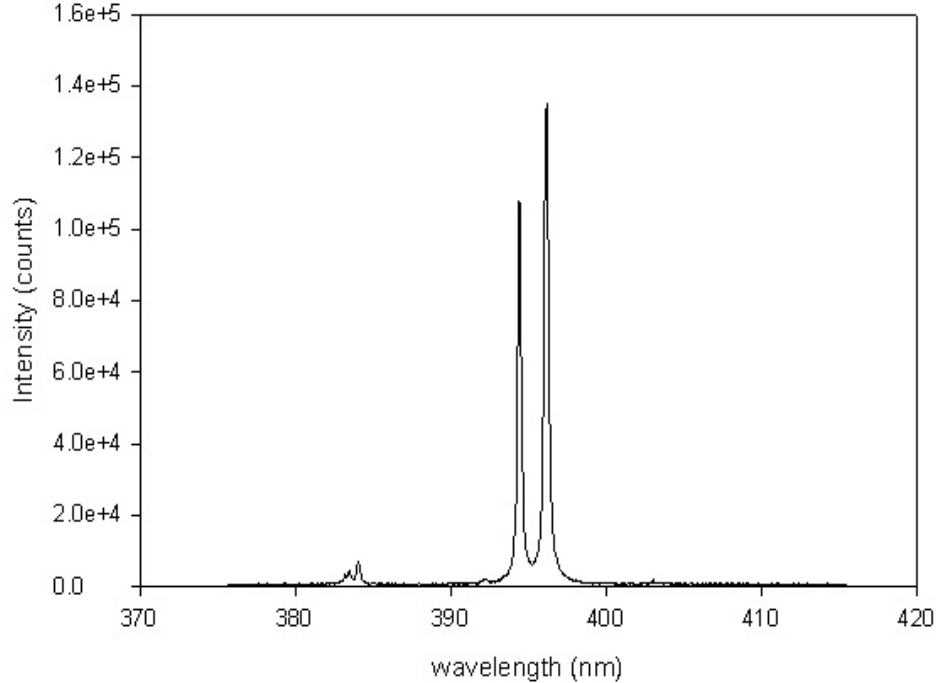


Figure 3.12: The LIBS emission spectrum of an Al2024 Al alloy is shown. A 2400 l/mm grating was used and the grating was centered at 395 nm. The al doublets of 394/396 nm are observed.

setting of the ICCD intensifier. The quantum efficiency of the photocathode was taken from the data provided by the manufacturer as shown in Fig.3.14

The result of the calibration of the ICCD using the lambertian emitter [141] is shown in Fig.3.15. The calibration given by the manufacturer is shown in Fig.3.16 for comparison.

Two other detectors were tested for suitability for LA-LIF in this thesis a PMT and a Multi Pixel Photon counter MPPC. A PMT is sensitive detector of optical radiation that makes use of the photoelectric effect to convert incident photons to photoelectrons. These electrons are accelerated through a chain of dynodes held at decreasing voltages. At each dynode, due to secondary emission more electrons are generated, which are in turn accelerated to the next dynode. In this fashion, the initial few photoelectrons which are a directly proportional to the incoming optical radiation are amplified. A diagram of the PMT dynode array is shown in a PMT is given in Fig.3.17, along with the first few amplification stages. The key characteristics

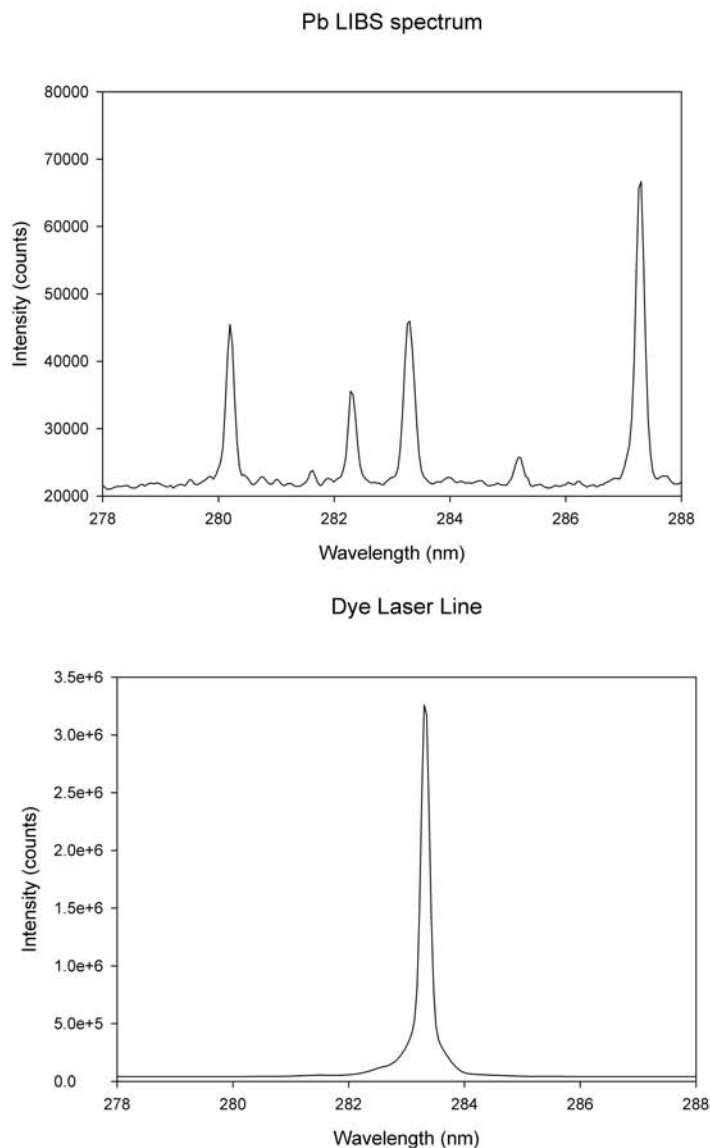


Figure 3.13: The LIBS emission spectrum of Pb is shown (top). Three emission lines 280.19 nm, 282.31 nm and the resonant line for our scheme at 283.305 are observed. Scattered laser light at 266 nm from the ablation laser is also observed. The profile for the dye laser at 283.305 nm (bottom) is shown. A 2400 l/mm grating was used in both cases. The intensifier gain was set at minimum. For the emission spectrum the gate delay was set at 400 ns and the gate width was set to 500 ns.

of a PMT are the quantum efficiency and the gain. The quantum efficiency, η is the number of photoelectrons emitted per incident photons. The gain of the PMT is the number of electrons collected at the output per photoelectron generated at the input.

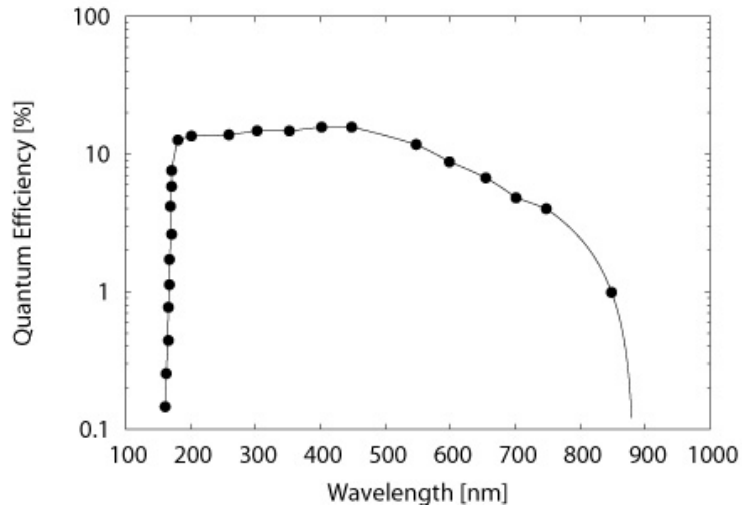


Figure 3.14: Manufacturer data for the quantum efficiency as a function of the wavelength for the Andor DH720 ICCD's photocathode.

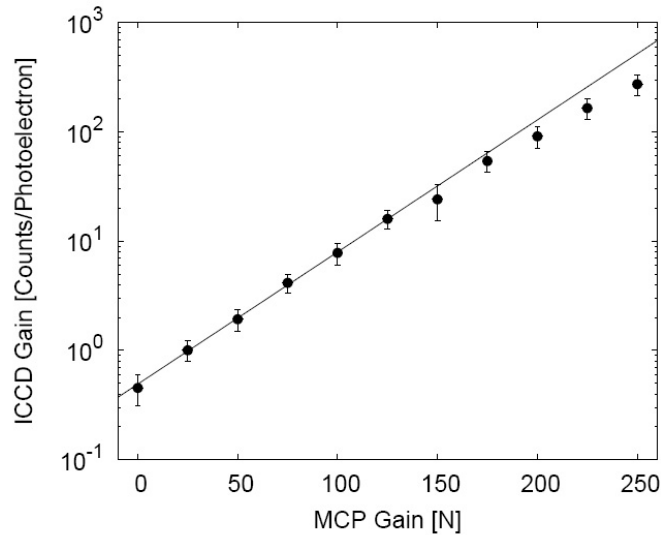


Figure 3.15: Calibration data for the ICCD used. The line is an exponential fit for a gain of less than 125. Above a gain of 125 a saturation in the detector gain is observed. The pixel readout time was 16 μ s.

A more detailed description can be found in [143]. The PMT used for this thesis was a Hamamatsu R7518 with a spectral response range from 185nm to 730 nm. The quantum efficiency of the photocathode given by the manufacturer is 28 % at 400 nm and the gain of the PMT is 10^7 at a bias voltage of 1 KV. The PMT was used

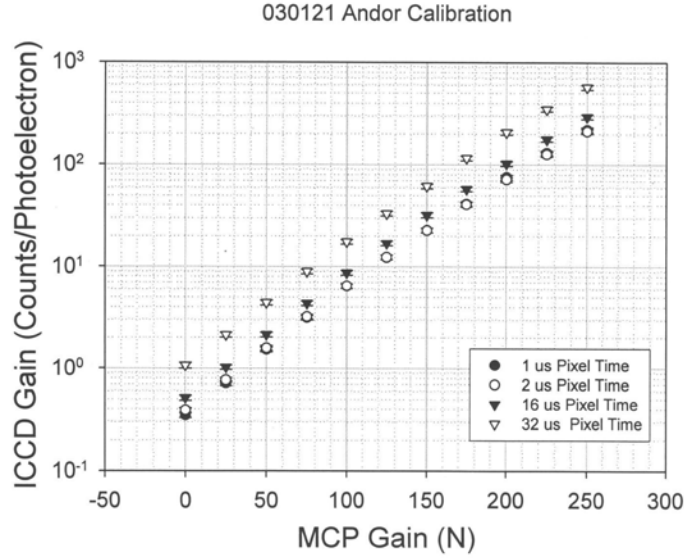


Figure 3.16: Calibration data provided by manufacturer for the Andor ICCD. The line is an exponential fit for a gain of less than 125. Above a gain of 125 a saturation in the detector gain is observed.

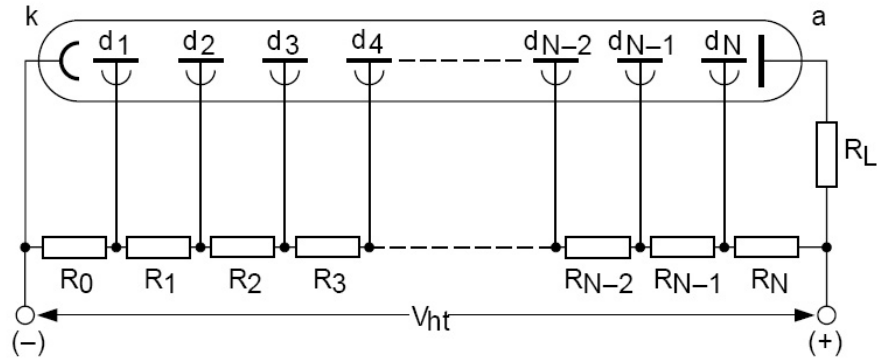


Figure 3.17: PMT dynode array and the voltage-divider supply.

to detect the fluorescence emission from the Pb atoms at a wavelength of 405.7 nm, an interference filter centered at 405 nm and having a spectral bandwidth of 2 nm was used. The setup diagram for the LA-LIF experiment using the PMT is shown in Fig.3.18. This setup is similar to the one shown in Fig.3.1 the difference being in the use of a filtered PMT for detection instead of the spectrometer and ICCD. In order to increase the number of collected fluorescence photons and thus the sensitivity of our setup. A lens with a focal length (f) of 4.6 mm and a 7 mm diameter is placed 4.6

mm away from the plasma orthogonal to both the 266 nm and 283 nm input beams. The plasma act as an object placed at f for the lens thus producing a parallel beam going into the interference filter and the PMT. The use of a PMT and a collection lens gives us the advantage of increasing the number of photons collected and a large sensitive aperture thus leading to a higher sensitivity. Care has to be taken though to make the PMT light tight to prevent stray photons from entering the PMT.

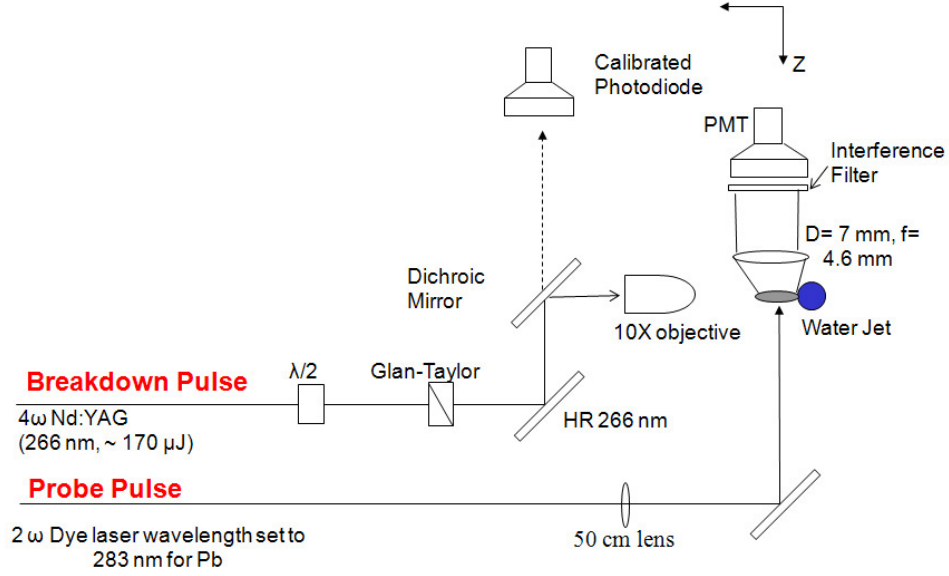


Figure 3.18: Schematic setup of the LA-LIF experiment. A frequency-quadrupled Nd:YAG laser (266 nm, ≈ 10 ns) at 170 μ J ablates the water jet. Pulse energy is controlled by a half-wave plate and Glan-Taylor prism. The pulse for re-excitation is a frequency-doubled dye laser pulse pumped by a XeCl excimer laser. The Pb emission is collected by a lens onto a filtered PMT with a 2 nm bandwidth interference filter.

The number of photoelectrons produced, N_{count} at the PMT cathode due to the LA-LIF emission for one event is given by

$$N_{count} = \frac{N_{fl}\Omega_c T(\lambda)\eta(\lambda)}{4\pi} \quad (3.3)$$

where N_{fl} is the number of fluorescence photons emitted Ω_c is the solid angle of collection of the optical system, $T(\lambda)$ is the transmission of the narrow-band interference filter and $\eta(\lambda)$ is the quantum efficiency of the detector. The multi-pixel photon counter MPPC is a relatively new photodetector developed by Hamamatsu Photonics, Japan [2]. An MPPC consists of many (100 to 1600) small avalanche photodiodes

APD's in an area of typically 1 mm^2 . An MPPC is shown in Fig.3.19 with 100 pixels.



Figure 3.19: Picture of a 100 pixel MPPC and a close up view showing each pixel of the device [2]. The pixel size is $100 \times 100 \text{ }\mu\text{m}$ each.

Each APD micropixel independently works in limited Geiger mode with an applied voltage a few volts above the breakdown voltage (V_{bd}). When a photoelectron is produced, it induces a Geiger avalanche. The avalanche is passively quenched by a resistor integral to each pixel. The output charge Q from a single pixel is independent of the number of produced photoelectrons within the pixel, and can be written as

$$Q_o = C(V - V_{bd}) \quad (3.4)$$

where V is the applied voltage and C is the capacitance of the pixel. Combining the output from all the pixels, the total charge from an MPPC is quantized to multiples of Q_o and proportional to the number of pixels that underwent discharge. The number of fired pixels is proportional to the number of injected photons if the number of photons is small compared to the total number of pixels. Thus, the MPPC has an excellent photon counting capability. For the MPPC, the operation voltage V is a few volts above the breakdown voltage typically 70 V. The pixel capacitance C is on the order of 10 –100 fF, giving a gain of 10^5 – 10^6 . These features enable us to read out the signal from the MPPC with simple electronics. In addition, because the thickness of the amplification region is a few μm , it is insensitive to an applied magnetic field and the response is fast. Because of these great advantages, several particle physics experiments are planning to use the MPPC.

To compare the performance and feasibility of using a MPPC for measuring Pb in water using LA-LIF compared to a PMT or ICCD we tested the S10362-100U MPPC from Hamamatsu. This particular device has a 100 pixels each $100 \mu\text{m}^2$ in area. The active area of the entire device was 1 mm^2 . The advantage of using the MPPC over the PMT is its high quantum efficiency $\approx 55 \%$ at 405 nm [3] as opposed to 10% of the PMT. Firstly we measured the recovery time of the MPPC as shown in Fig.3.20 by irradiating the MPPC by two 7 ns duration laser pulses from two separate lasers which were controlled by a digital delay generator. We measured the recovery time to be 130 ns as shown in Fig.3.20 which was in agreement with the manufacturer's specifications of $100\text{-}200 \text{ ns}$ [144]. Since our re-excitation pulse is timed at 300 ns after the ablation pulse the MPPC is fully ready to measure the fluorescence signal in our case though this may not be the case for traditional LIBS experiments where the high background continuum lasts for several μs and the MPPC might be saturated and would be unable to measure the atomic emission.

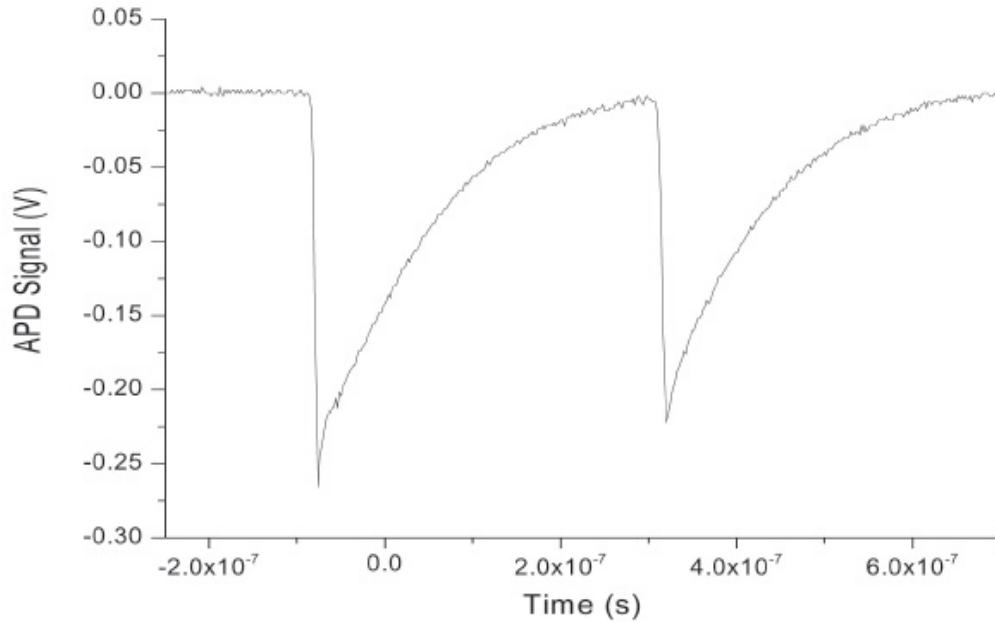


Figure 3.20: Recovery time for the MPPC. The device was irradiated with two 5 ns laser pulses with the interpulse separation controlled by a digital delay generator. The recovery time was measured to be 130 ns .

3.2.5 LIBS signal analysis

Once the LIBS spectrum is obtained, analysis is performed to give signal to noise ratio SNR which gives quantitative information about the experiment. A simple technique was used for removal of detector background from the signal. For a particular line of interest regions on either side are used to evaluate the background. In our case, the background is usually entirely devoid of other signals, or flat as a function of channel number, a simple average can be used to remove the background. Spectral regions which are used to calculate background noise with no visible spectral line emission are selected by inspection, especially in our case because our target is well known. In other cases, the standard deviation of each channel is calculated for 1000 shots and regions of flat minima with no visible spectral line emission were used to calculate the standard deviation .

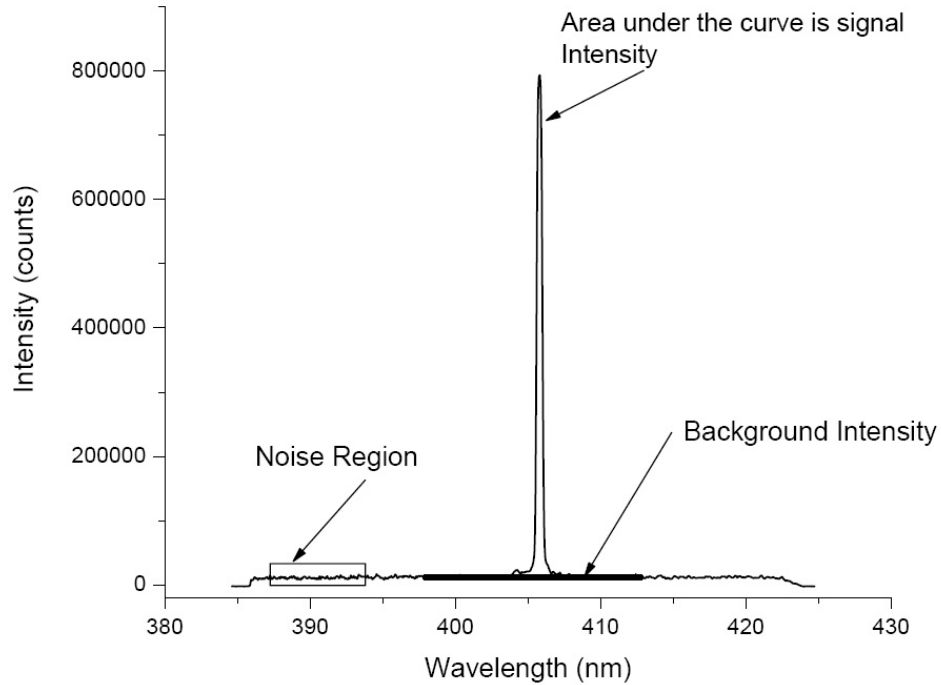


Figure 3.21: Outline of the signal analysis technique. The integrated signal intensity is $\sum I(\lambda)$, $N_{channels}$ is the integrated width which is used to scale the noise. The noise region is the area used to estimate the variation in the background.

The SNR is defined as

$$SNR = \frac{\sum I(\lambda)}{\sigma_{background} \sqrt{N_{channels}}} \quad (3.5)$$

where $\sum I(\lambda)$ is the integrated intensity after background correction for the signal of interest, $\sigma_{background}$ is the single pixel standard deviation measured in the spectrally quiet region away from the peak, and $N_{channels}$ is the number of channels over which the signal is integrated. The limit of Detection (LOD) is then defined as the point at which the signal strength is 3 times the root mean square noise level ($3\text{-}\sigma$). All the LOD's reported in the thesis are $3\text{-}\sigma$ LOD's. Over the course of this research work it was found that since one photocathode spike or a single noise emission photon illuminates more than one pixel there is a correlation between neighbouring pixels. This can be observed when we correlate the blank noise data with the blank noise data shifted by 1 pixel or 2 pixels we find that there is still a large net correlation. In order to determine the real effective noise value 16 samples of 28 point signals distributed between channels 380 to 620 were observed from a sample blanks spectra of 10,000 shots. The standard deviation in these values was also calculated and then these values were compared to the values determined from the single pixel RF in the same regions. It was observed that the real standard deviation for the random 28 point blanks is on average 1.73 ± 0.2 times larger than extrapolated from the single pixel standard deviation divided by 5.29 (the square root of 28). Specifically for the raw data it was found that the average 28pt Standard deviation from the single pixel values are 544 counts while the average standard deviation from the 28 pt direct samples was 919 cts or 1.69 times higher. Also the same test was run on average background subtracted data. It was found that the average 28 point standard deviation from the single pixel values is 411 counts while the average standard deviation from the 28 point direct samples was 726 counts or 1.77 times higher. Thus a correction factor of 1.73 was applied to the final LOD's presented for the data reported in Chapter 4. A similar approach was carried out every time for calculating the signal to noise ratio of a particular spectral line.

3.2.6 Detector parameter optimization for Single Pulse μ LIBS of Pb

The experimental setup used is as shown in Fig.3.1. The ablation pulse used was a 266 nm, frequency-quadrupled Q-switched Nd:YAG laser with an energy of approximately 260 μ J and pulse width of 10 ns FWHM. The pulse was focused with a 10 \times objective

to form an approximately 10 μ diameter spot on the water jet. The sample contained 500 ppm by weight of lead as analyte. The LIBS emission spectrum has temporal characteristics depending on the species of interest in the LIBS plasma. Thus a parametric survey of the detector in terms of the gate delay (when to turn it on) and the gate width (integration time of the camera) and also the gain setting of the intensifier was performed. A software analysis routine based on the commercial software provided by Andor was developed to analyse the data. The gain of the intensifier was varied from the minimum setting of 0 to the maximum value of 250 in steps of 50. For each value of the gain the gate delay of the ICCD was varied from 50 ns to 230 ns in steps of 20 ns and the gate width for each gate delay was varied from 50 ns to 450 ns in steps of 50 ns. Fig.3.22 shows the variation of the background, signal intensity the noise and the SNR of the LIBS emission spectrum for 500 ppm Pb in water accumulated for 100 laser shots as a function of the gate widths and the gate delays for a gain of 0. From 0 to 60 ns the background emission is large because its largely dominated by brehmasstrahlung emission from the plasam. As the plasma cools down we can observe the signal emission from the plasma signal emission from the plasma lasts upto \approx 100 ns. When the intensifier gain setting is 0 the likelihood of intensifier noise spikes is low and thus the RF noise levels is low except when the integration time is large. The highest SNR obtained is 9.

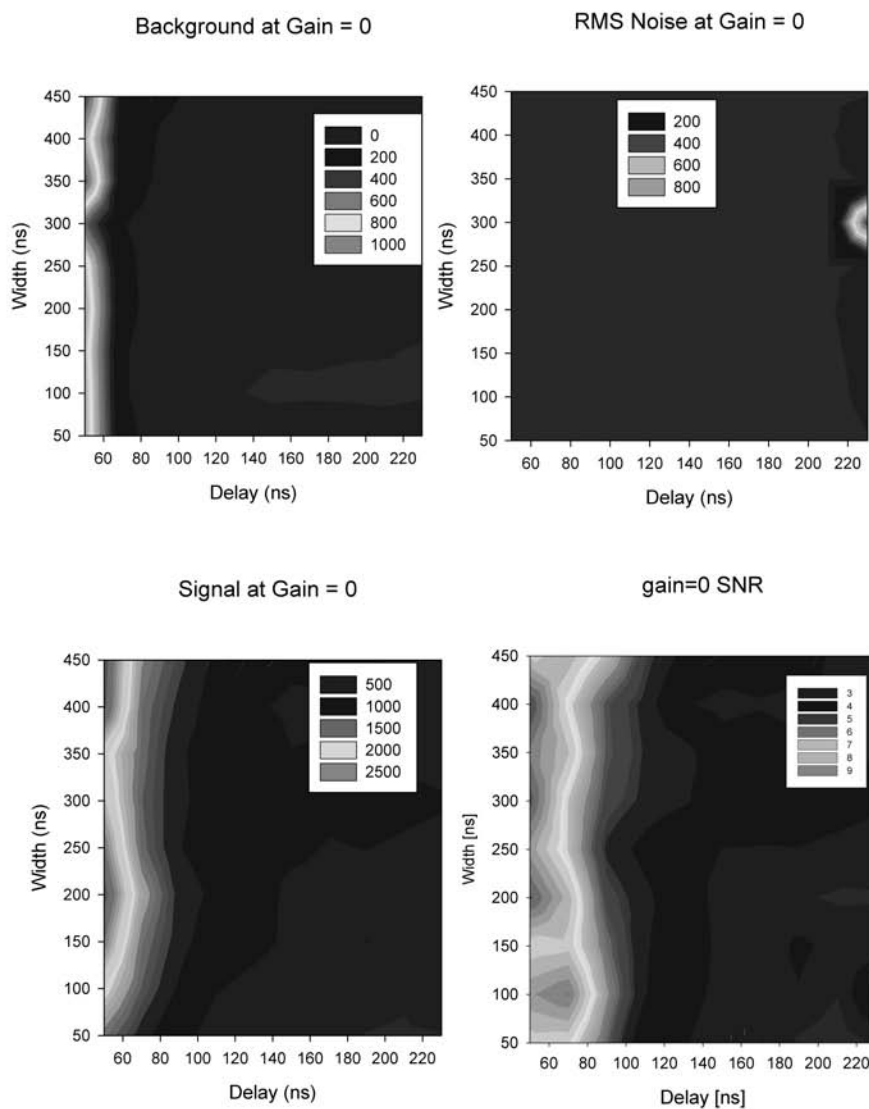


Figure 3.22: Background (top left), Noise(top right), Signal(bottom left), SNR (bottom right) of the emission spectra 100 accumulations from a LIBS plasma measured at different gate delay and gate width. The laser pulse energy was $260 \mu\text{J}$. The water sample contained 500 ppm of Pb. The gate delay (x-axis) was varied from 50 ns to 230 ns in steps of 20 ns and the gatewidth (y-axis) of the ICCD was 50 ns to 450 ns, the slit width was fixed at $300 \mu\text{m}$ and the detector gain was set to zero. The legend shows the strength of the parameter (Background, Signal, Noise and SNR) being measured.

For increasing intensifier gain settings of 50, 100 and 150 we observe an increase in

the number of signal counts due to the increasing number of counts per photoelectron from the increased gain. We also observe an increase in the RF noise levels Figs.3.23 - 3.25. Figs.3.26 - 3.27 show the signal and the RF noise for the high gain settings. A high number of intensifier noise spikes are observed at shorter gate delays.

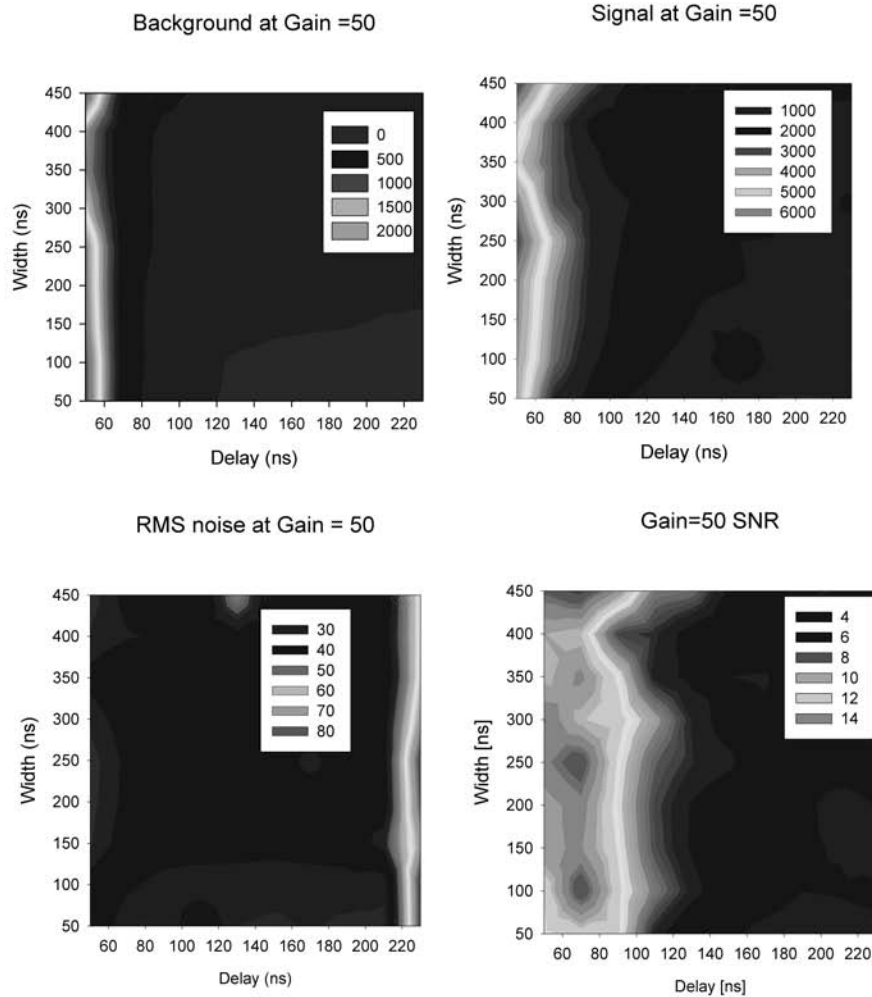


Figure 3.23: Background (top left), Noise(top right), Signal(bottom left), SNR (bottom right) of the emission spectra 100 accumulations from a LIBS plasma measured at different gate delay and gate width. The laser pulse energy was $260 \mu\text{J}$. The water sample contained 500 ppm of Pb. The gate delay (x-axis) was varied from 50 ns to 230 ns in steps of 20 ns and the gate width (y-axis) of the ICCD was 50 ns to 450 ns, the slit width was fixed at $300 \mu\text{m}$ and the detector gain was set to 50. The legend shows the strength of the parameter (Background, Signal, Noise and SNR) being measured.

A few conclusions can be drawn from the parametric study, the highest gain setting of the ICCD can be detrimental to the experiment, even though one does observe an

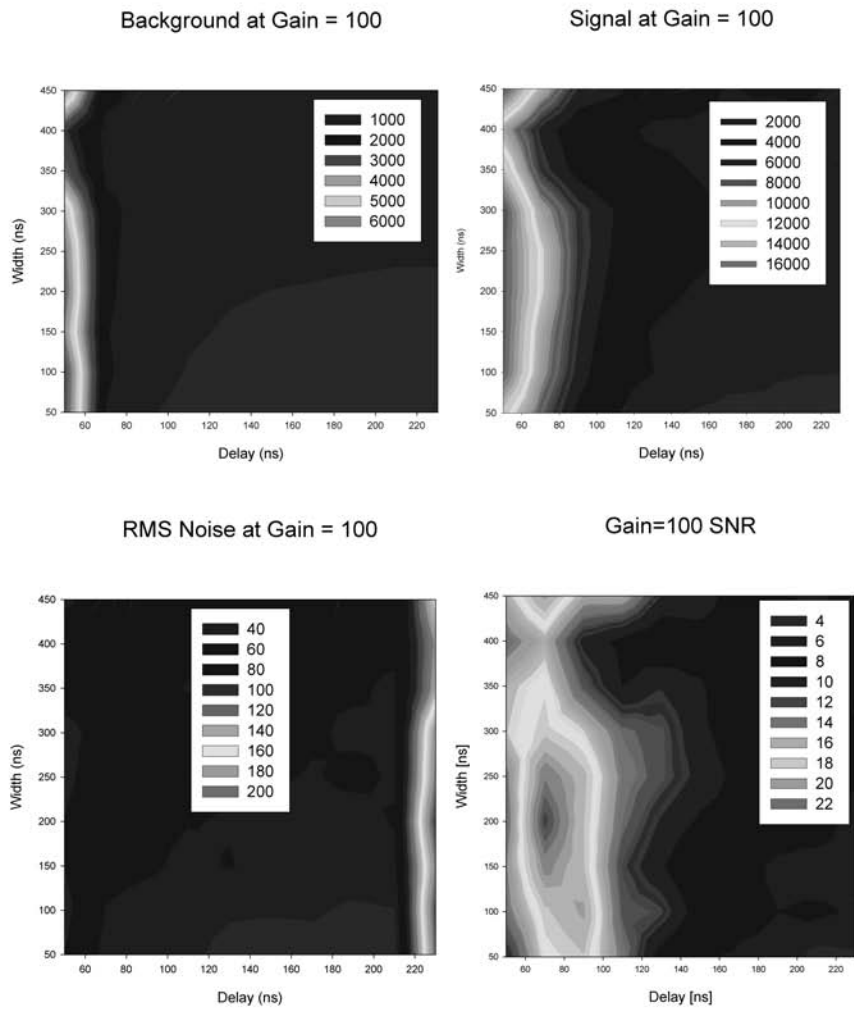


Figure 3.24: Background (top left), Noise(top right), Signal(bottom left), SNR (bottom right) of the emission spectra 100 accumulations from a LIBS plasma measured at different gate delay and gate width. The laser pulse energy was $260 \mu\text{J}$. The water sample contained 500 ppm of Pb. The gate delay (x-axis) was varied from 50 ns to 230 ns in steps of 20 ns and the gate width (y-axis) of the ICCD was 50 ns to 450 ns, the slit width was fixed at $300 \mu\text{m}$ and the detector gain was set to 100. The legend shows the strength of the parameter (Background, Signal, Noise and SNR) being measured.

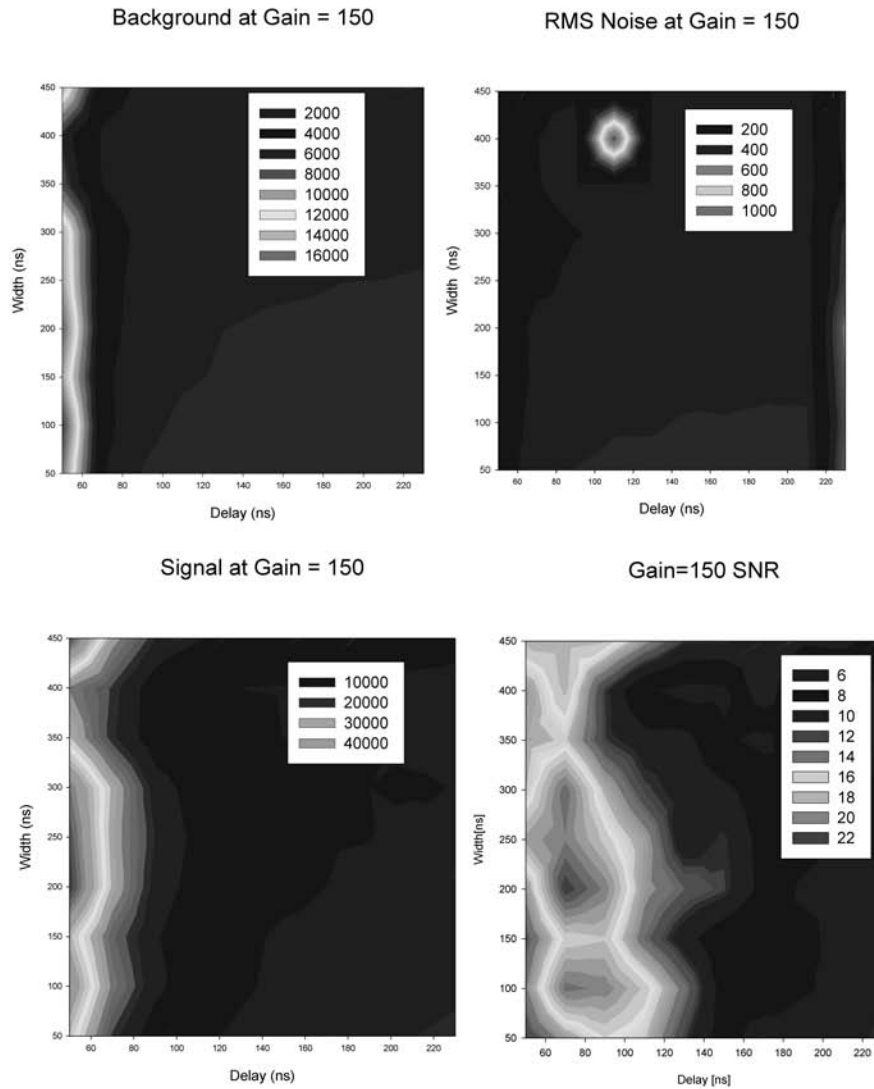


Figure 3.25: Background (top left), Noise(top right), Signal(bottom left), SNR (bottom right) of the emission spectra 100 accumulations from a LIBS plasma measured at different gate delay and gate width. The laser pulse energy was $260 \mu\text{J}$. The water sample contained 500 ppm of Pb. The gate delay (x-axis) was varied from 50 ns to 230 ns in steps of 20 ns and the gate width (y-axis) of the ICCD was 50 ns to 450 ns, the slit width was fixed at $300 \mu\text{m}$ and the detector gain was set to 150. The legend shows the strength of the parameter (Background, Signal, Noise and SNR) being measured.

increase in signal counts but the noise is more prominent at high gain levels. The higher gain settings should thus be avoided unless operating at extremely low photon

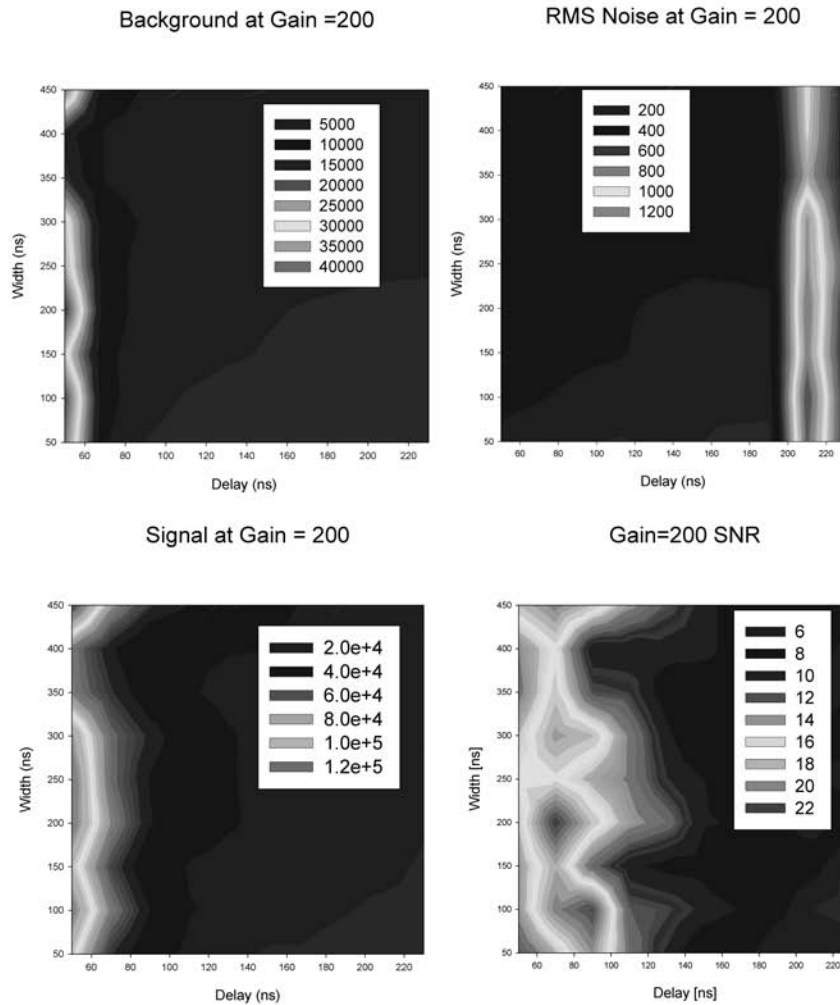


Figure 3.26: Background (top left), Noise(top right), Signal(bottom left), SNR (bottom right) of the emission spectra 100 accumulations from a LIBS plasma measured at different gate delay and gate width. The laser pulse energy was $260 \mu\text{J}$. The water sample contained 500 ppm of Pb. The gate delay (x-axis) was varied from 50 ns to 230 ns in steps of 20 ns and the gatewidth (y-axis) of the ICCD was 50 ns to 450 ns, the slit width was fixed at $300 \mu\text{m}$ and the detector gain was set to 200. The legend shows the strength of the parameter being (Background, Signal, Noise and SNR) measured.

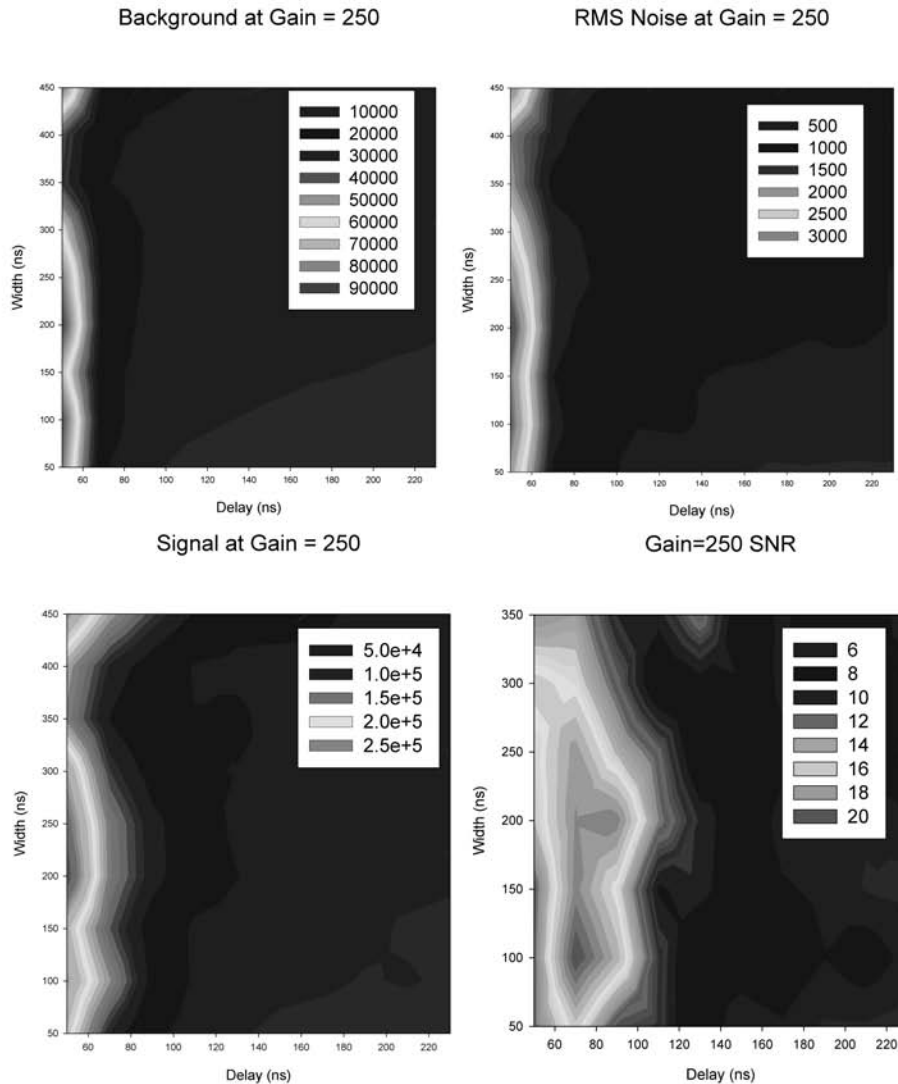


Figure 3.27: Background (top left), Noise(top right), Signal(bottom left), SNR (bottom right) of the emission spectra 100 accumulations from a LIBS plasma measured at different gate delay and gate width. The laser pulse energy was $260 \mu\text{J}$. The water sample contained 500 ppm of Pb. The gate delay (x-axis) was varied from 50 ns to 230 ns in steps of 20 ns and the gate width (y-axis) of the ICCD was 50 ns to 450 ns, the slit width was fixed at $300 \mu\text{m}$ and the detector gain was set to 250. The legend shows the strength of the parameter (Background, Signal, Noise and SNR) being measured.

levels. The best LOD obtained using the optimal detector settings are reported in Chapter 4.

3.3 μ LIBS of Microdroplets: Rapid Thermal Heater Approach

In this section we will first discuss the microfluidic chip and the different steps involved in the fabrication of the microfluidic chip. The fabrication of the microheaters was carried out by Govind Kaigala a member of Professor Chris Backhouse's research group in the ECE department here at the University of Alberta. The μ LIBS setup will be discussed next and then the bubble nucleation studies will be discussed.

3.3.1 Microchip architecture and operating principle

The microchip consists of two layers Fig.3.28, the bottom layer is a 1.1 mm thick borofloat glass (Paragon Optical Company, PA, USA) on which platinum (200 nm) (with a titanium adhesion layer (20 nm)) is patterned as microheaters (details in [145]), while the top layer is made of pre-cast polydimethylsiloxane, PDMS (HT-6135, Bisco Silicons, Elk Grove, IL, USA). The thickness of the PDMS layer is 0.254 mm and microchannels are patterned using a laser to form the fluidic channel, reservoir and an orifice. The PDMS and glass are irreversibly bonded by exposing the PDMS in a custom-built UV/Ozone cleaner for 6 min and then applying the PDMS on a clean glass surface [146]. To create a micro-droplet, the sample chamber is first loaded with sample solution. A microsecond pulse of tens of volts (section 3.1) is then applied across the platinum heater. The heater super-heats and vaporizes the surrounding solution instantaneously, forming a microbubble that partially extrudes a small volume of fluid in the form of a droplet through the orifice in the PDMS layer. Subsequently μ LIBS probing was done while the droplet was well localized at the exit of the orifice.

3.3.2 Fabrication of Microheaters

The microchip was designed in L-Edit v3.0 (MEMS Pro 8, MEMS CAP, CA, USA) and transferred to a mask wafer using a pattern generator (DWL 200, Heidelberg

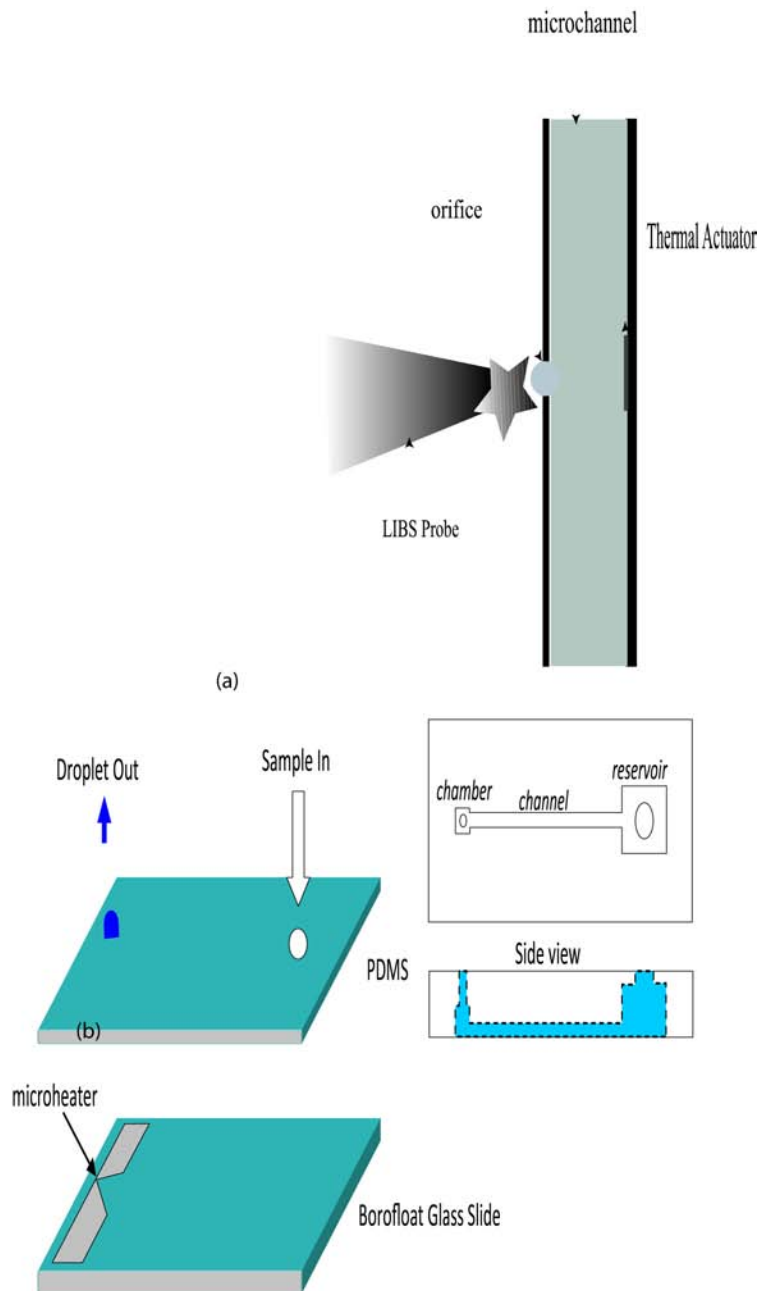


Figure 3.28: Conceptual diagram showing the integration of μ LIBS on a microfluidic platform that extrudes droplets and, (b) Assembled microchip architecture for continuous flow elemental analysis.

Instruments, CA, USA). The 4" \times 4" borofloat glass substrate was cleaned in hot Piranha etch (3:1 of $H_2SO_4:H_2O_2$). The glass substrate was sputter coated with 20 nm of Cr. The substrate was then spin-coated with AZ 4620 photoresist and soft baked (100°C for 90 s). The heater patterns were photolithographically transferred

using a mask aligner (ABM Inc., CA, USA). The UV–exposed regions of photoresist on the substrate (14 s, 356 nm and with intensity of $19.2 \text{ mW}/\text{cm}^2$) were then removed using an AZ developer. The Cr in the exposed regions was then removed by a Cr etchant. The wafer subsequently was sputtered with Ti (20 nm) /Pt (200 nm). Next, a lift-off process was performed by immersing this wafer in an ultrasonic bath filled with acetone. The remaining Cr layer was then removed by immersing the wafer in chrome etchant, leaving the patterned resistive thin-films of Ti (20 nm)/Pt (200 nm). The substrate was then diced and the individual heater element chips were bonded with laser patterned PDMS.

3.3.3 Micromachining of PDMS Layer

The microchannel, sample chamber, reservoir and orifice on the PDMS were laser micromachined in our lab using a micromachining setup developed by an MSc. student Michael Argument. Details about the laser drilling setup and hole characteristics can be found in [147]. Briefly, the laser source used was a Nd:YAG laser (Big Sky, Ultra CFR, Montana, USA) at its 4th harmonic at $700 \mu\text{J}$ per pulse running at 20 Hz. The laser was focused down to a $50 \mu\text{m}$ spot size on the PDMS surface using a 12.5 cm focal length aberration corrected triplet lens. The dimension of the reservoir in the PDMS that was formed by laser ablation is $100 \times 100 \mu\text{m}$ with a depth of $40 \mu\text{m}$ (PDMS membrane thickness $254 \mu\text{m}$). The width of the channel was $50 \mu\text{m}$ and the depth was $20 \mu\text{m}$. To form the PDMS channel, the laser fluence was $\approx 4 \text{ J}/\text{cm}^2$ and the PDMS membrane was moved using an automated stage at a speed of $10 \mu\text{m}/\text{s}$. The orifice with a diameter of $\approx 25 \mu\text{m}$ on the PDMS was drilled by 500 laser shots on a given spot using the same fluence. The debris deposited on the orifice and the channel surfaces were removed by a high pressure air jet. The PDMS membrane used here has a protective layer (as supplied by the manufacturer) that was retained during micromachining, and thus, debris landing on this protective layer was removed prior to PDMS/glass bonding.

3.3.4 Microdroplet Imaging Setup

The experimental setup for imaging the formation of a microbubble is based on a stroboscopic system as the nucleation process occurs on the microsecond time scale. A

delay pulse generator (Stanford DG535, Rhode and Schwarz, Munich, Germany) was used to control the delay between the heater electrical pulse (for droplet extrusion), the illumination system, and the imaging system. A Nd:YAG laser (Big Sky, Ultra CFR, Montana, USA) at 532 nm with a pulse width of 10 ns was used as the illumination source. This pulse of 10 ns was sufficiently short to capture the nucleation process. The imaging system equipped with a $10 \times$ objective lens gave a resolution in the micron range, thus assisting in estimating the size of the droplet. By adjusting the delay of the probe pulse, the image of the nucleation process could be observed.

3.3.5 μ LIBS microdroplets

The experimental setup used for LIBS analysis of the hemispherical microdroplets is shown in Fig.3.29. The ablation pulse used was generated from a frequency-quadrupled Q-switch Nd:YAG laser (Big Sky, Ultra CFR, Montana, USA) at 266 nm with a pulse width of 10 ns. The pulse energy was 200 μ J and was monitored using a calibrated photodiode (Hamamatsu, R1193U-52, Bridgewater, NJ, USA). Pulse energy was controlled using a combination of a half-wave plate and a Glan-Taylor polarizer. The beam was focused by a $10\times$ objective lens (Optics For Research, $10 \times$, 15 mm working distance, NA = 0.25) to form an $\approx 10 \mu\text{m}$ spot on the target (the hemispherical microdroplet). By adjusting the delay between the heater pulse and the laser, the droplet was ablated when it was half exposed on top of the orifice. The plasma created was imaged in the x-y plane through the same $10 \mu\text{m}$ objective lens (in the direction perpendicular to the microchip surface) and projected onto the entrance slit of a 1/4 m, f/3.9 imaging spectrometer (Oriel MS260i, Newport, California, USA) equipped with an intensified charge coupled device (ICCD) camera (Andor iStar DH720, Andor, Belfast, Northern Ireland). A grating with 2400 lines mm^{-1} was employed for spectral dispersion in the spectrometer. A slit width of 300 μm and effective spectral resolution of 0.45 nm were used for this measurement.

3.3.6 Nucleation Process

There are several factors that contribute to the formation of the microbubbles, we found in the literature that there are two main types of microbubble generation mechanisms [97]. We believe that the bubbles here are generated due to a combination

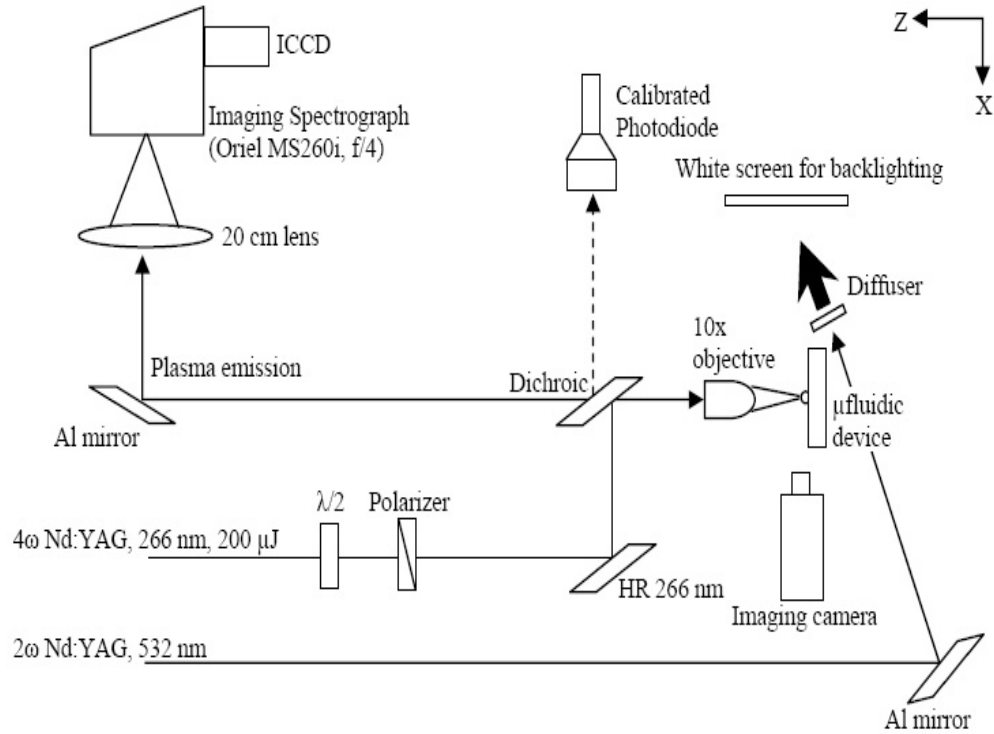


Figure 3.29: LIBS experimental set-up consisting of a frequency quadrupled Nd:YAG laser producing pulses up to $\approx 260 \mu\text{J}$ to ablates the microdroplet target. LIBS emission is observed along the laser axis.

of mechanisms. One mechanism is the spontaneous nucleation that can occur due to fluctuations in the temperature as the sample is heated, which causes a vapor film to grow due to superheating of the liquid. The other mechanism is homogeneous nucleation wherein the gas trapped on the surface of the heater material may expand and grow. In our set-up a square wave pulse of 14 V amplitude and 15 μs duration was applied across a 90 μm wide folded stripline heater (50 Ω) with geometry as shown in Fig.3.30. A series of images were captured to study the nucleation process is shown in Fig. 3.30. After 5 μs , nucleation was first observed in the close vicinity of the heater regions. The bubbles grew rapidly for the next 5 μs and merged together into a bigger bubble. The bubble expanded until the electrical pulse was turned off and collapsed within the next 10 μs .

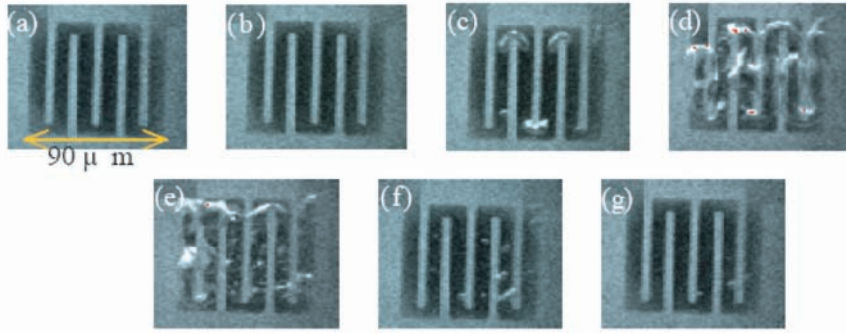


Figure 3.30: Microbubble nucleation in action during the application of short electrical pulses. Nucleation process of a heater activated with a 14V 15 μs pulse at different times, from left to right (a) $t = -5 \mu\text{s}$ (before the start of the heating pulse); (b) $t = 0 \mu\text{s}$; (c) 5 μs ; (d) 10 μs ; (e) 15 μs ; (f) 20 μs and (g) 25 μs .

3.3.7 Microdroplet Extrusion and Operation

To create a microdroplet, the sample liquid was first introduced into the reservoir by a syringe through a 0.2 μm pore size particle filter. Then, the liquid was directed to the sample chamber through the microfluidic channel by applying external positive pressure. Inside the chamber, the sample was heated by the microheater and liquid was extruded from the orifice on the top of the chamber. The initial nucleation and growth of the bubble pushes the liquid out from the orifice, creating a droplet (Fig.3.31) As another heater with a resistance of 60 Ω and a line width of 50 μm was used in this experiment, the amplitude and the width of the heater pulse were readjusted to 13 V and 5 μs , (established empirically). In a particular example presented here liquid was extruded from the chamber of the microfluidic chip in the form of a hemispherical droplet during the first few microseconds and grew up to $\approx 28 \mu\text{m}$ in diameter while staying attached to the surface of the orifice, which corresponds to a volume of $\approx 6 \text{ pL}$ for the hemispherical droplet. It was found that the size and extrusion speed of the droplet could vary by 15 %, making it difficult to adjust the spatial and temporal settings for ablation. Thus, the ablation beam was aligned normal to the device surface and focused right above the orifice where the sample is extruded. The laser beam was focused such that there was no damage to the orifice of the microfluidic device. It could be that the variation in droplet formation is due

to details of the nucleation of the vapor bubble by the heater which could vary from pulse to pulse.

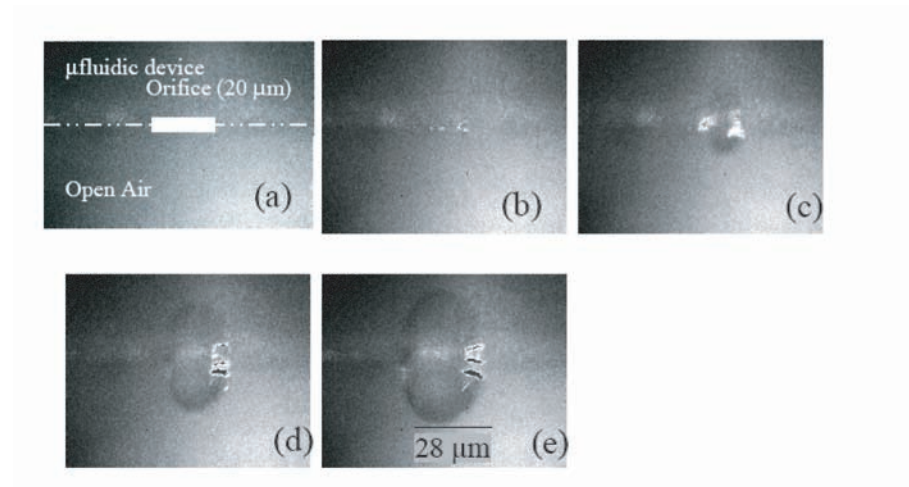


Figure 3.31: Droplet formation captured over a period of a 5 μ s. Sequence of droplet formation using a 13V 5 μ s pulse across a 60 Ω heater. The images were captured using the setup described in Fig. 3.29. Images from left to right show the bubble at (a) 1 μ s; (b) 2 μ s; (c) 3 μ s; (d) 4 μ s; and (e) 5 μ s. A reflection of the partially extruded microdroplet from the PDMS surface is seen in the top of each image.

3.4 μ LIBS of Monodisperse Microdroplets: Piezoelectric Approach

In order to use μ LIBS and subsequently LA-LIF for the analysis of monodispersed microdroplets a stand-alone piezoelectric droplet dispenser was used to generate microdroplets of different sizes. A commercial piezoelectric droplet dispenser manufactured by Microfab technologies was used. Fig.3.32 shows the microdroplet dispenser and the voltage pulse characteristics for the dispenser. A piezoelectric actuator requires a high-voltage driver capable of delivering hundred of volts, peak-to-peak. Since a typical actuator looks like virtually a pure capacitance to the driving amplifier, almost all the power dissipation becomes the burden of the driving amplifier. In order to generate droplets of varying diameters the rise and fall times of the pulse have to be very carefully controlled. To observe the microdroplet the same pulsed probe method as described earlier in the microfluidic chip technique was used. As shown in Fig.3.32 a 20 μ m microdroplet was generated using a 30 V peak to peak pulse with a 5 ns rise

and fall time.

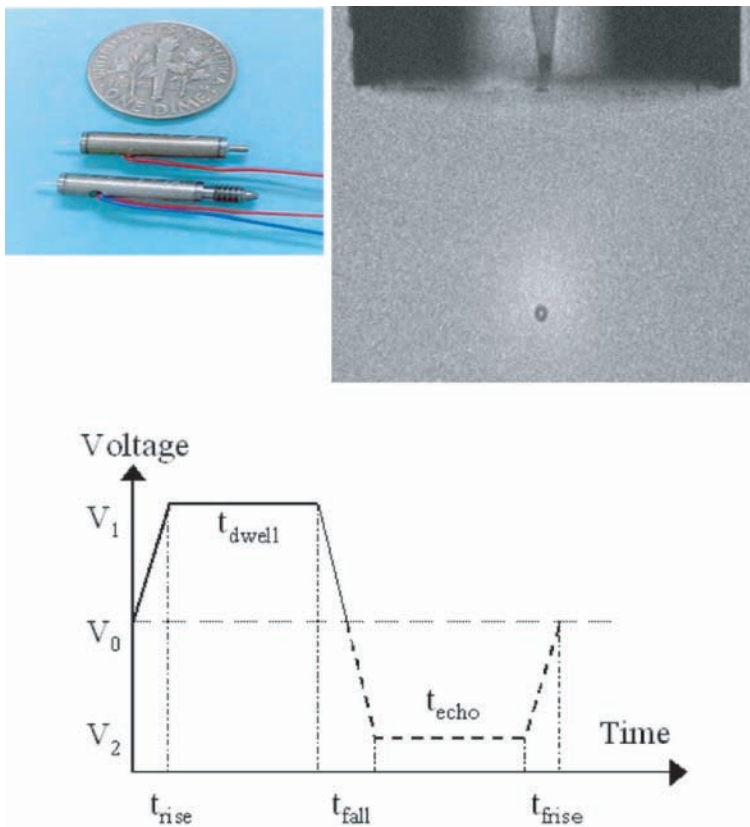


Figure 3.32: A piezoelectric microdroplet dispenser is shown with the schematic of the voltage pulse is shown. An image of a $20\ \mu\text{m}$ microdroplet generated with a 30 Vpp voltage pulse with a 5 ns rise and fall time is shown.

3.4.1 Optimization experiments for μLIBS and LA-LIF of the microdroplets

Fig.3.33 shows the schematic of the experiment for μLIBS and LA-LIF of the microdroplet. The experimental setup is similar to the one in the microfluidic setup for μLIBS case . A 100 ppm Na solution was used as an analyte to optimize the various parameters of the setup namely the droplet position in space and time to achieve complete ablation of the droplet. The laser focal spot size was $12\ \mu\text{m}$. A complete parametric study was done of the focusing conditions and microdroplet position in order to obtain the best ablation of the microdroplet. For LA-LIF studies on the microdroplet a similar setup was used. The analyte in this case was Pb and the same resonant excitation scheme as described earlier was used. Pb was used here in

particular to study the signal scaling of the LA-LIF technique when we moved from a bulk system like a waterjet to a microdroplet ablation system and study the factors that affect the emission processes for LA-LIF of a microdroplet.

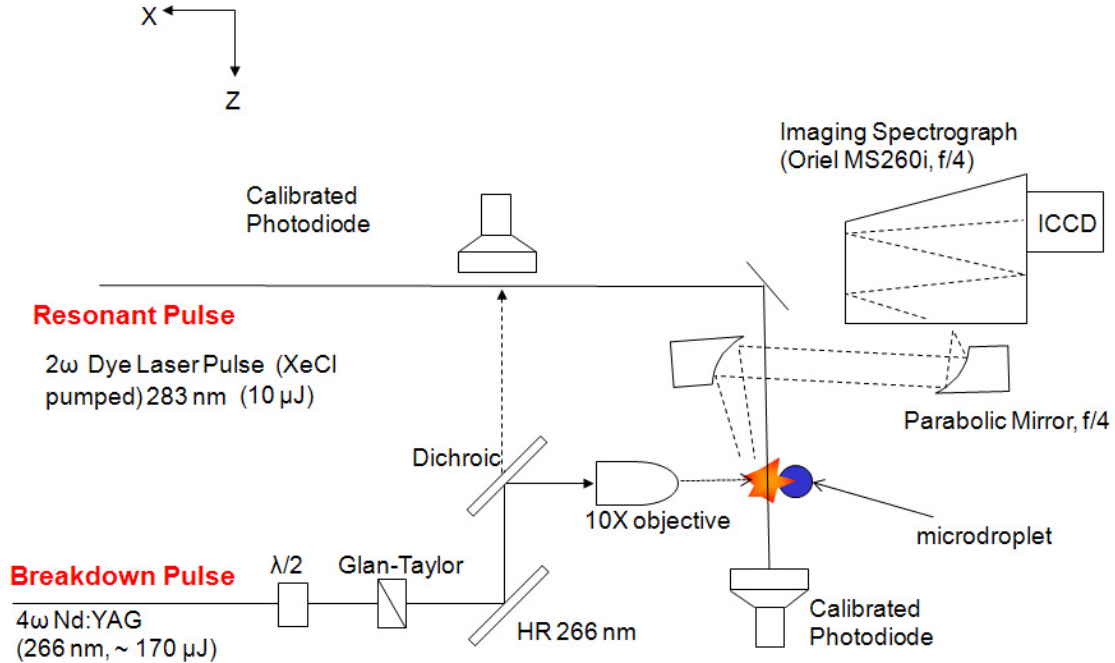


Figure 3.33: LIBS and LA-LIF experimental set-up consisting of a frequency quadrupled Nd:YAG laser producing pulses up to $\approx 200 \mu\text{J}$ to ablate the microdroplet target. The plasma is re-excited after a fixed time delay by a frequency doubled dye laser at 283 nm to excite Pb. LIBS and LA-LIF emission is observed along the laser axis.

3.4.2 Optimization of focusing conditions

In order to have a complete ablation of the microdroplet the laser pulse focal spot has to be optimized and the droplet position has to be exactly at the laser pulse focal spot. Two different sets of measurements were carried out to study the ablation conditions of the microdroplet based on a series of plasma images to observe the ablation of the microdroplet. Fig.3.34 shows the Na signal vs the relative position of the laser focal spot at a low laser pulse energy of $92 \mu\text{J}$. Fig.3.35 shows the ablation images captured of the laser interacting with the microdroplet at each of those focal conditions.

When the droplet is not at the focal spot of the laser pulse as can be seen from the ablation images that the fluence was not high enough to ablate the droplet. Yet, the droplet itself acted as a converging lens and focuses the beam to the back of

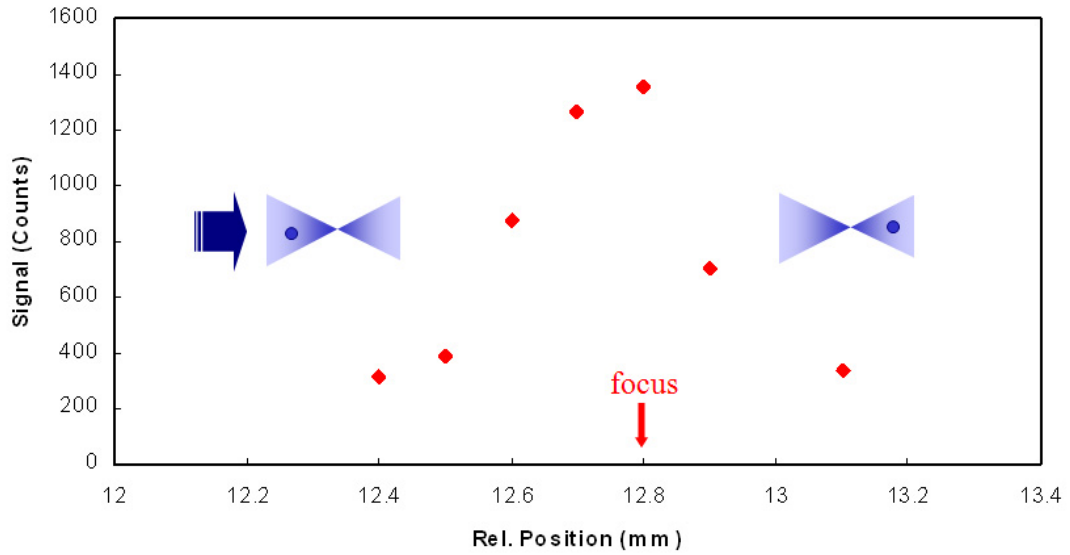


Figure 3.34: Optimization of axial focal position in laser ablation studies at a breakdown energy of $\approx 92 \mu\text{J}$. Larger values of relative focal position focus further on front of the droplet.

the droplet, creating localized breakdown. In order to obtain complete breakdown of the microdroplet at the focal position the energy was increased to $192 \mu\text{J}$. Fig.3.36 shows the ablation images at a high fluence. The $192 \mu\text{J}$ was also chosen to compare the results of LIBS emission from a microdroplet ablation to the waterjet ablation. Fig.3.37 shows the focal scan done at an energy of $192 \mu\text{J}$ for the $20 \mu\text{m}$ droplet where the Na emission was observed. The focal scan shows a similar behaviour to the low energy scan except that at $192 \mu\text{J}$ complete ablation of the microdroplet is observed. After the focusing conditions were set precisely a detailed study was made of the LIBS emission intensity with respect to droplet size and also a detailed study of the gate delay was carried out for the μLIBS case to obtain the best LOD for Na these results are presented in detail in the next chapter. The same focusing conditions were maintained for the LA-LIF experiments on the microdroplets. A parametric study of the LA-LIF detection of Pb in microdroplets was carried out in order to compare with the LA-LIF study on the waterjet target for Pb. A study of the LA-LIF signal as a function of the droplet size and probe pulse energy was carried out and these results are presented in the following chapter.

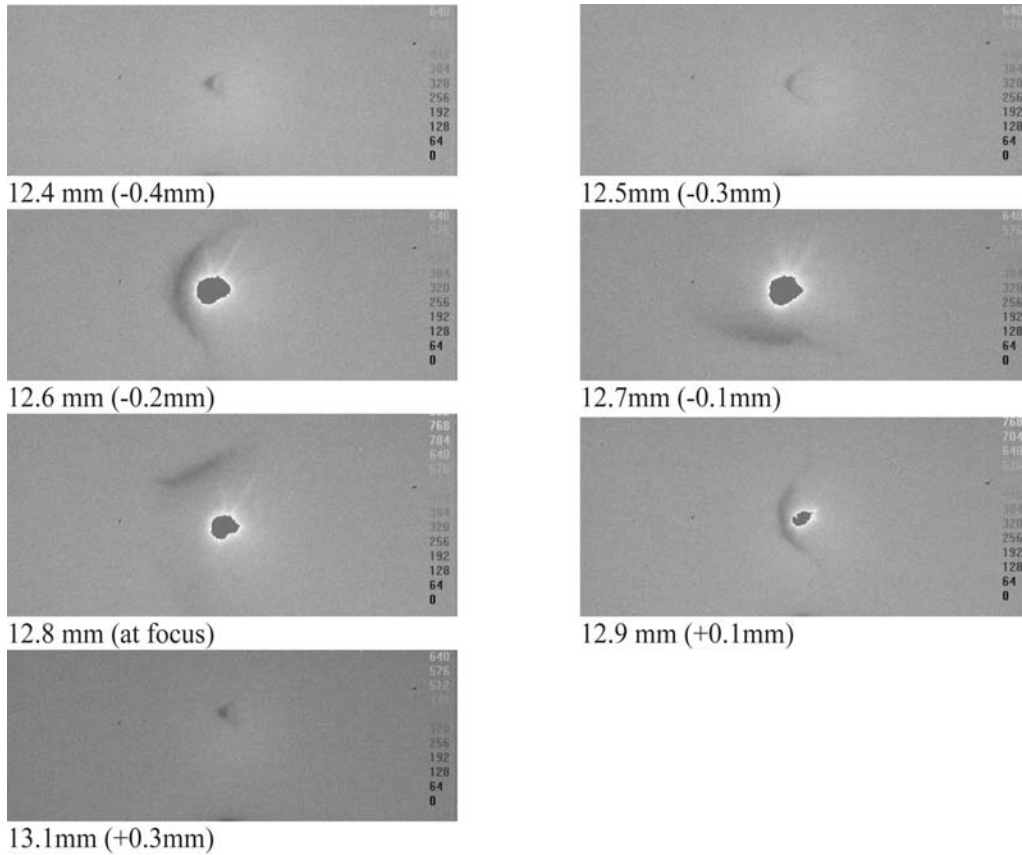


Figure 3.35: Plasma images obtained at low fluence ablation of the microdroplets $\approx 92 \mu\text{J}$. Even though the energy is not enough to completely ablate the microdroplet the microdroplet acts like a converging lens to focus the laser beam to the back to generate a higher intensity in images at (- 0.2 mm and -0.1 mm).

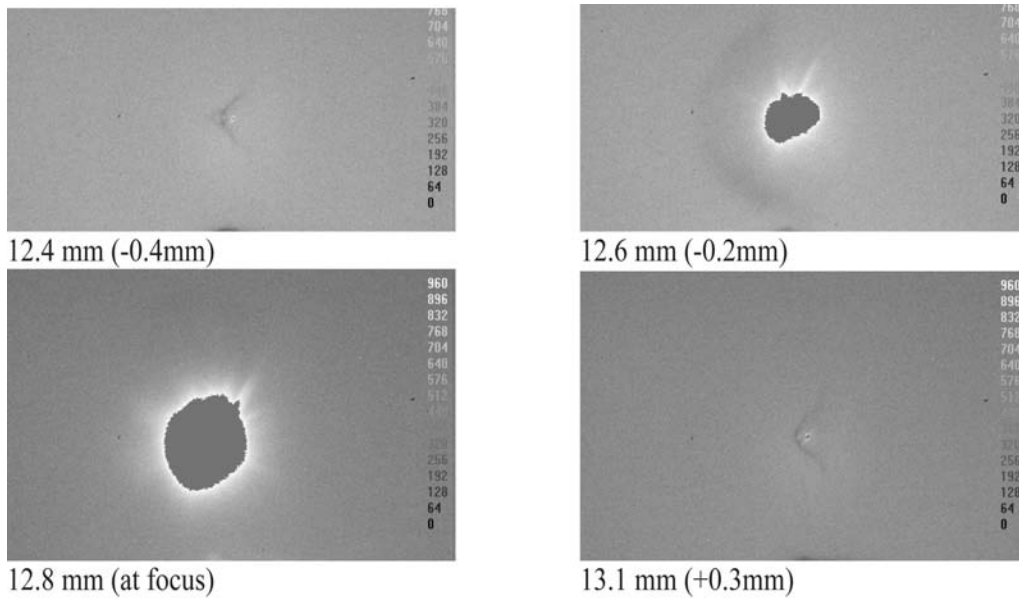


Figure 3.36: Plasma images captured at a higher ablation energy of $\approx 192 \mu\text{J}$. As can be observed at the focal spot complete ablation of the microdroplet is achieved.

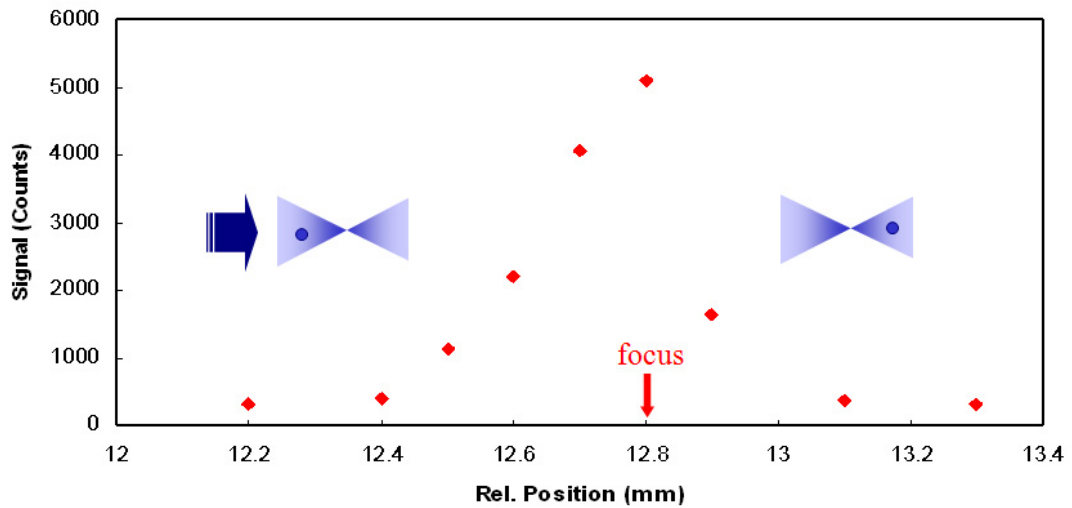


Figure 3.37: Focal spot scan done at a high ablation energy of $192 \mu\text{J}$ is shown. The LIBS emission intensity obtained from using Na as an analyte is highest at the best focus position.

Chapter 4

μ LIBS and LA-LIF studies on a waterjet system

4.1 Introduction

In this chapter the key results obtained are presented in detail. Initially the results of applying μ LIBS for detecting Pb using a waterjet sample are presented. Then, a parametric study of the μ LIBS and LA-LIF emission was carried out. Key instrumental parameters, for example the temporal separation of the two pulses ΔT and detector gate width T_{width} , were also explored. The LODs based on the optimized settings found are presented. Finally a comparison of different types of detectors is presented for moving towards a drinking water monitoring system having ultra-high sensitivity for measurement of Pb. Most of the results presented in this chapter have been published in references [30, 148, 149]

4.2 μ LIBS of Pb

In order to obtain the best SNR which would lead to the best LOD for the detection of Pb a survey of the camera conditions was carried out as presented in Section 3.2.6. Examples of emission signals are shown in Fig.4.1. These show that the Pb signal is already too weak to be detected at a gate delay of 210 ns.

From the results presented earlier, the highest SNR is 20 with a gate width of 100 ns and a gate delay of 70 ns for a solution containing 500 ppm of Pb in water. This corresponds to a LOD of 75 ppm for an average of 100 shots using a pulse energy of 260 μ J per pulse [30]. Table 4.1 and Fig.4.2 show a comparison of our

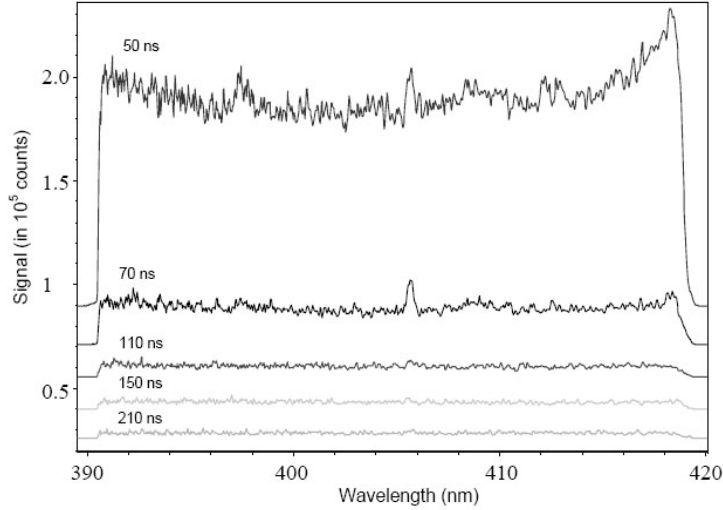


Figure 4.1: Pb emission spectra generated from single-pulse LIBS at different gate delays (50, 70, 110, 150 and 210 ns) in the spectral window 390–420 nm. Experimental conditions: laser pulse energy=260 μ J, gate width= 100 ns, accumulation=100 events. The spectra were offset vertically by 1×10^4 counts each for ease of viewing

”present result” with those reported in literature for the LIBS of Pb. This is to be compared to an LOD of 13 ppm obtained by Knopp et al. [97] using 22 mJ laser pulses and 0.3 ppm obtained by Lo et al. [150] using 27 mJ pulses. The increased sensitivity in their cases compared to ours can be explained because of the much higher laser pulse energies and the addition of an absorbing agent in the latter case. These results indicate that a comparable sensitivity can be achieved using μ LIBS with two orders of magnitude reduction in the laser pulse energy.

Group	LOD	Laser Energy	Reference
Current Result	75 ppm	260 μ J	[30]
Knopp	13 ppm	27 mJ	[97]
Arca	100 ppm	500 mJ	[151]
Lo	0.894 ppm	16 mJ	[150]

Table 4.1: Comparison of our results with those published in the literature. All the LOD’s are scaled to 100 shot LOD’s to compare with our results.

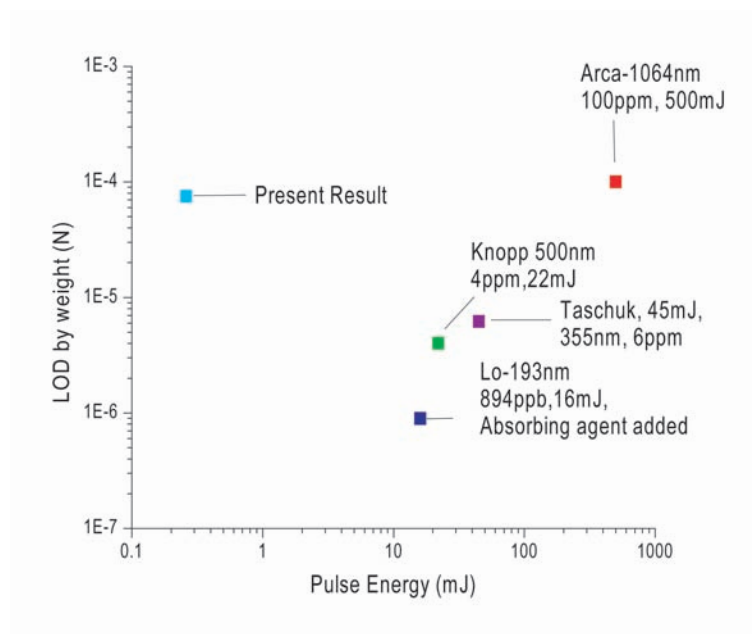


Figure 4.2: Comparison of the LOD obtained for μ LIBS to other reported results in literature as a function of energy used. All the results were scaled to 100 shot LOD's.

4.3 LA-LIF of Pb

In order to significantly improve the sensitivity of μ LIBS a dual pulse technique probing a resonant emission line of Pb in water was studied. A detailed summary of the results obtained is given below.

4.3.1 Selective Enhancement

One key advantage of LIF is that only the selected element is excited, and thus interferences from other contaminants in the sample are minimized. To demonstrate the selectivity of LIF, a sample solution which contained 150 ppm of aluminum and 10 ppm of lead was prepared in the forms of aluminum sulfate and lead nitrate dissolved in water. The intensifier of the detector was gated on at 300 ns after the ablation with a width of 100 ns. The first excited energy level for aluminum is 25347 cm^{-1} ($4^2S_{1/2}$), whereas for lead it is significantly higher at 35287 cm^{-1} . Thus by 300 ns the plasma plume had cooled sufficiently that only the easier to excite aluminum lines were excited leading to radiation of emission at 394.4 and 396.2 nm as shown in Fig.4.3(a). Direct excitation of the lead species was very weak at this time, and no

significant lead signal could be observed. However, when a 283 nm pulse re-excited the plasma at 300 ns after the first pulse, the lead signal was enhanced. At the same time, the intensity of the Al 394/396 nm doublet remains constant Fig.4.3(b).

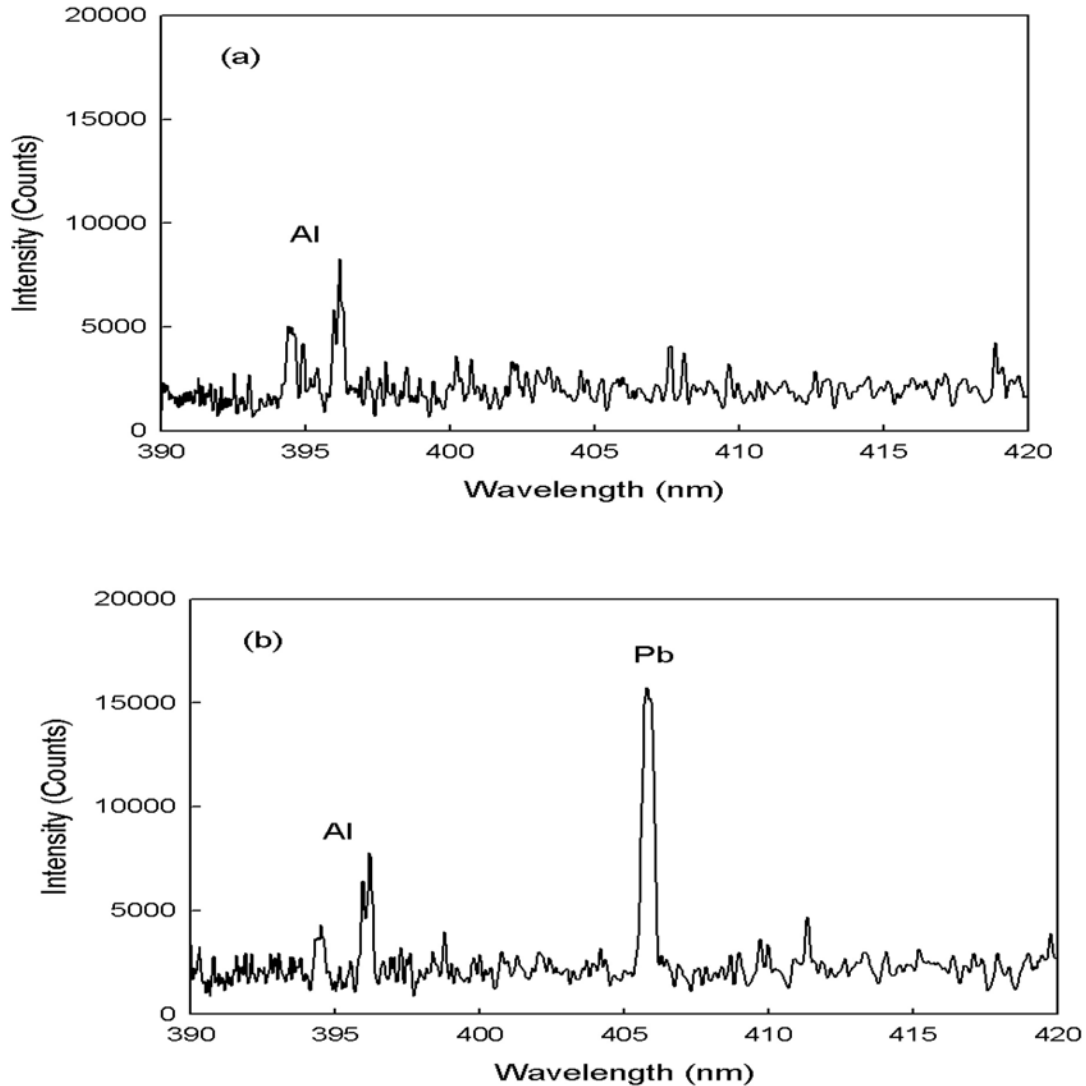


Figure 4.3: Selective enhancement of lead using LA-LIF. The sample contains aluminum and lead as analyte. The spectra were obtained by (a) LIBS and (b) the LA-LIF scheme. Only Pb atoms were excited by the LA-LIF technique. The number of events accumulated for each spectrum was 100. A grating of 600 lines/mm was used in order to observe both Al and Pb emission lines.

Given that the aluminum species has a smaller upper level energy than lead, this result demonstrates that the enhanced lead signal was purely a resonance effect, while the thermal reheating of the plasma was insignificant.

4.3.2 Interpulse Separation ΔT

The temporal separation between the pulses (ΔT) had to be optimized for the best LOD. Fig.4.4 shows two extreme cases when the plasma was re-excited too early and after a long delay. When the second pulse intercepted the plasma too early, only a

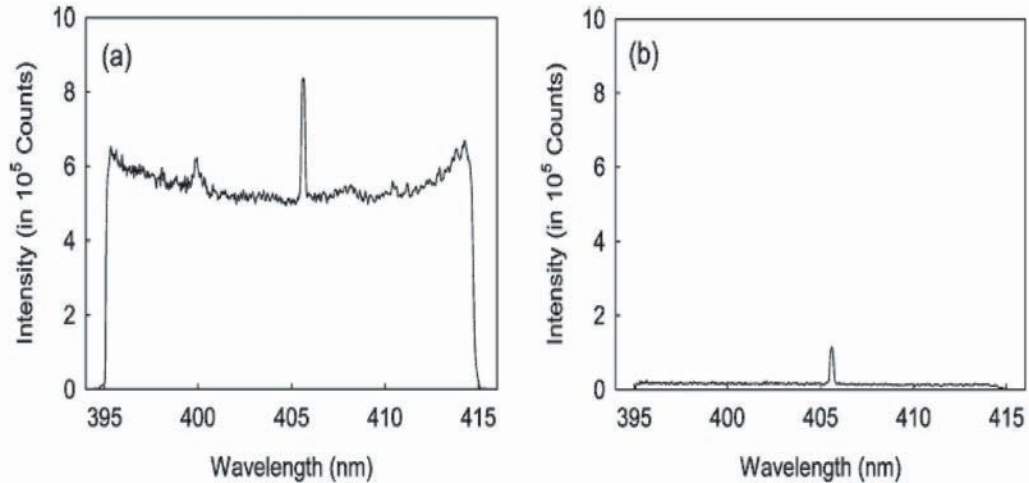


Figure 4.4: Pb emission spectra obtained by using LA-LIF with two different ΔT . The second pulse re-excited the plasma at (a) $\Delta T = 50$ ns and (b) $\Delta T = 3000$ ns. The background was extremely high in case (a) whereas the signal became too weak in case (b). Each spectrum was an accumulation of 1000 events. The concentration of Pb was 50 ppm by weight.

small portion of the analyte could be excited, as most atoms in the hot plasma were either in their ionized or excited state. In addition, the strong background continuum masked the enhanced signal. When the atoms were re-excited too late, the plasma has expanded and thinned out. Also some of the atoms may have combined to form molecules or condense into nanodroplets which no longer would be excited by the probe pulse. Thus, an optimum probe time exists, after the intense continuum subsides and before expansion and chemical reactions deplete the atomic species being probed. To obtain the best timing for plasma re-excitation, ΔT was varied over the range of 50-3000 ns. The detector gate was switched on for 100 ns at the time when the plasma was re-excited. This duration was long enough to record the complete LIF signal (refer to the next section). The dependences of the signal and the background continuum on the probe time are plotted in Fig.4.5. The background at

different ΔT could be regarded as background due to initial ablation pulse at various times, as it was shown in Fig.4.3 that thermal reheating of the expansion plume by the second pulse is minimal. The background dropped rapidly for the first 300 ns. At the same time the signal increased initially reaching a maximum at a ΔT of ≈ 300 ns. The drop of signal at longer ΔT was due to the loss of the Pb atoms during the continued plasma expansion and subsequent condensation and molecular reactions reducing the atomic number density in the plume. It is expected that the plasma plume will stagnate and does not expand for an extended period of time. It is also expected that the optimum ΔT will also change with changes in the first pulse energy. A stronger first pulse will create a hotter plasma which in turn requires a longer ΔT to reach optimum probe conditions. To simplify the optimization process, the first pulse energy was fixed at $170 \mu\text{J}$ throughout the experiment.

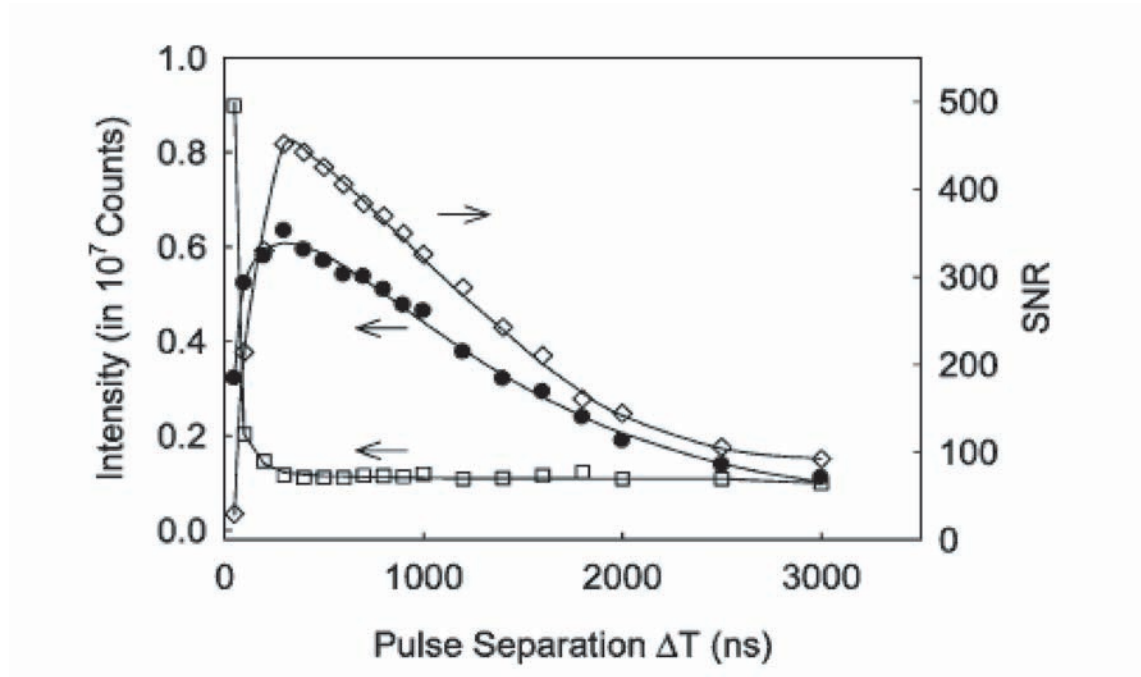


Figure 4.5: Intensity of the Pb 405.8 nm line (solid circles), the background noise (open squares, $\times 500$), and the S/N (open diamonds) at different probe times ΔT . For each ΔT the probe position was centered at $36 \mu\text{m}$ in front of the water surface.

4.3.3 Detector Gate Width T_{width}

In general, a long detector gate time is good for signal integration as long as the plasma is emitting. However, the longer the gate time the more noise is integrated. In the present case, the excitation of the emission occurs over a very short period, on the order of 10 ns, the lifetime of the excited state is also less than 10 ns, and thus, a short signal accumulation time can be used. An optimized gate width (T_{width}) can be employed such that the detection window opens only when the re-excited Pb atoms emit. Fig.4.6 is a time resolved plot of the Pb signal using the two-pulse scheme. T_{width} was 10 ns in order to obtain the instantaneous signal at each point in time. A sample of 500 ppm and a first pulse energy of 260 μ J were used for these studies. ΔT had to be extended to 700 ns for better SNR with the center of the probe beam located 40 μ m away from the water jet surface. Signal enhancement was only observed at the instance when the plasma was re-excited. The lifetime of the signal was so short that it only lasted for 20 ns. This agrees with the excitation probe pulse duration of 10 ns and the lifetime of the upper state of the 405.8 nm transition, which is of the order of 10 ns. As the fluorescence signal is short-lived, the detector gate width, T_{width} , could be shortened to exclude unwanted detector noise. The SNR and the noise level are plotted against T_{width} in Fig.4.7. As shown, a longer gate width increased the noise level, which resulted in a drop in SNR. The best SNR was obtained for the shortest gate width of $T_{width} \approx 20$ ns. The single-shot Pb spectra with a very short (20 ns) and a longer (200 ns) gate width are displayed in Fig.4.8. It was observed that the background noise appears primarily in the form of intensifier noise spikes. The intensifier noise spikes appeared much more frequently when a longer gate time was used and contributed to both the background and the noise level in an accumulated data series.

4.3.4 Calibration Curve

A calibration plot was generated with the optimum ΔT of 300 ns and T_{width} of 20 ns found above. To ensure clean starting conditions, the system was flushed with distilled water before the experiment until no Pb signal was observed. All necessary precautions were also taken while handling equipment and samples to prevent un-

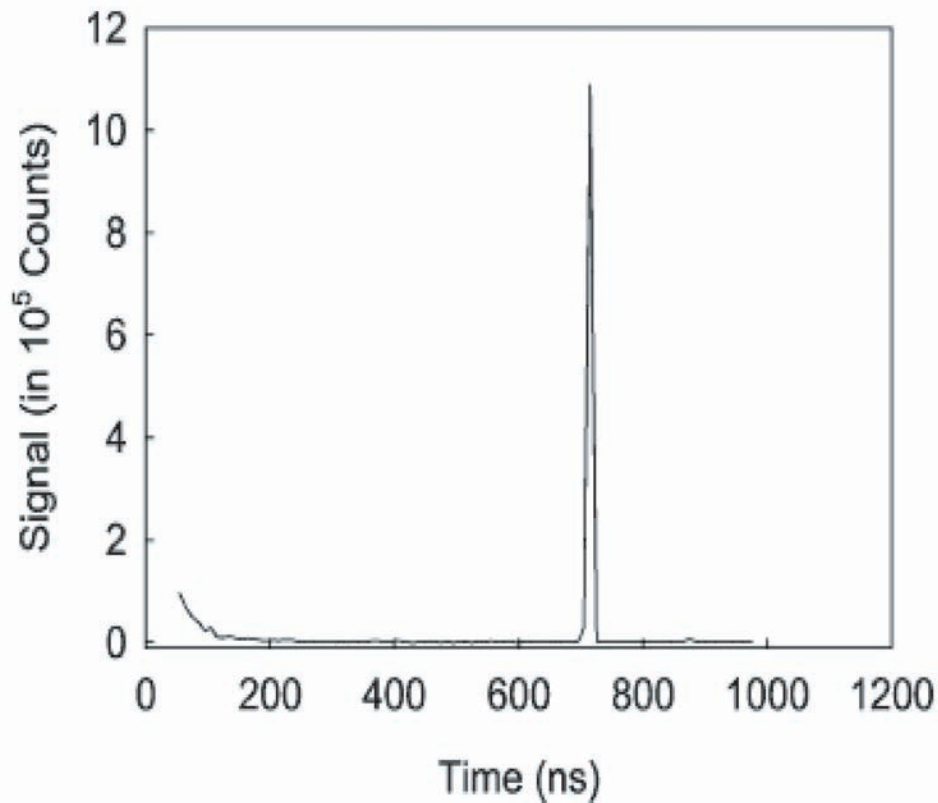


Figure 4.6: Time-resolved Pb emission signal obtained from the LALIF scheme. The detector gate width was 10 ns and moved in 10 ns steps. The Pb concentration was 500 ppm, and the probe time delay was set at $\Delta T = 700$ ns. The number of events accumulated for each data point was 100.

wanted contamination by lead. Lower concentration sample data were acquired first to prevent contamination by a more concentrated sample. In order to compare with other published results, only a hundred data sets were accumulated per measurement. The results are shown in Fig.4.9(a). It is expected at these low concentrations that the observed emission should scale linearly with the concentration. A least-squares fit of such a linear dependency to the data is also shown in Fig.4.9(a), and a good fit is observed.

From this fit, the 3σ LOD was found to be at an equivalent level of 353 ± 60 ppb. When the number of shots was increased to 1000, the acquisition time was extended from 10 to 100 s for our present shot rate of 10 Hz. A good fit to a linear dependency on concentration was again observed. The LOD in this case has improved to 116 ± 20

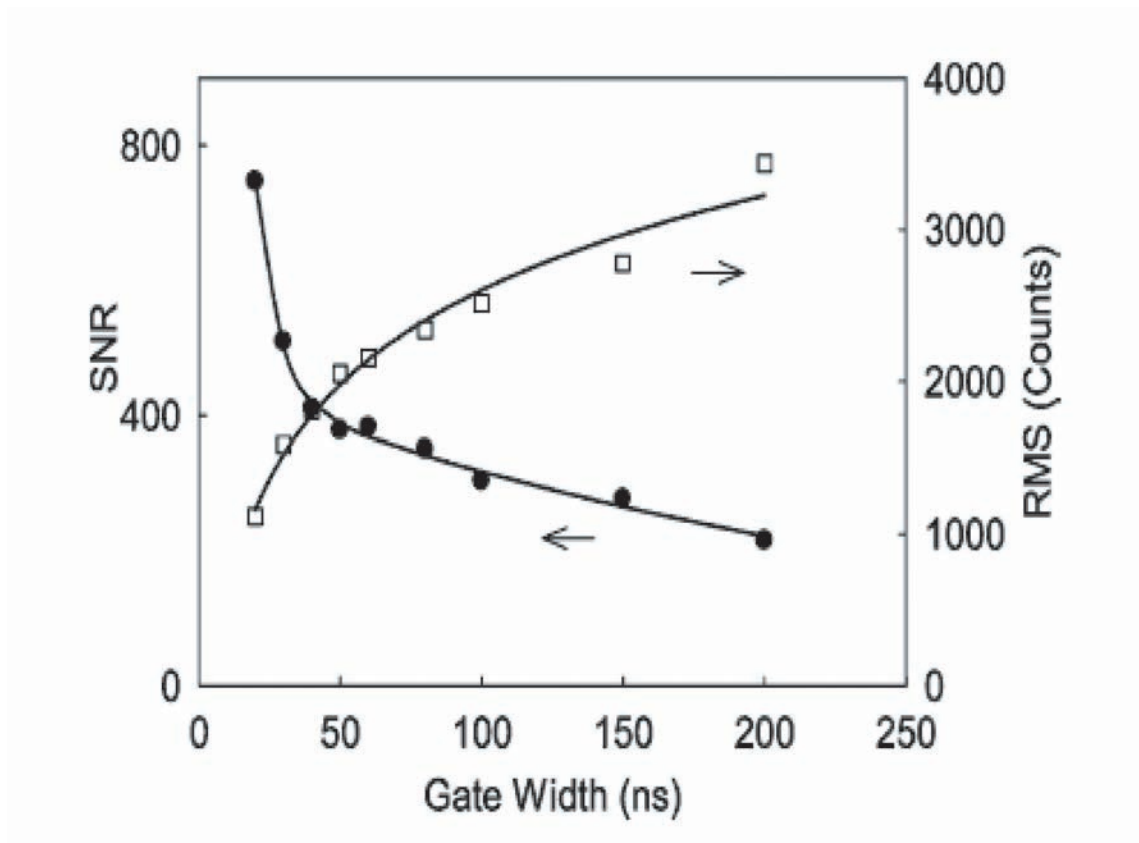


Figure 4.7: 1σ background noise (open squares) and SNR (solid circles) vs detection gate width. Signals were obtained for Pb at 50 ppm and a probe time of $\Delta T = 300$ ns and ablation pulse energy of $170 \mu\text{J}$.

ppb as shown in Fig.4.9(b), which is consistent with a $N_{shot}^{\frac{1}{2}}$ scaling, where N_{shot} is the number of shots. It is clear that the sensitivity can be further improved by integrating more shots taking advantage of the $N^{\frac{1}{2}}$ scaling for the LOD. A spectrum taken with an accumulation of 10000 shots for a 166 ppb sample is given in Fig.4.10. The concentration is verified by Inductively coupled Plasma Mass Spectrometry ICPMS, and the Pb 405.8 nm line is very clearly visible. Fig.4.11 shows the improvement of the SNR with the accumulation of more shots.

For comparison a least-squares fit of an $N_{shot}^{1/2}$ scaling is shown, and it is seen that this trend is followed quite closely. The scaling of LOD with the number of shots is given by $\text{LOD} = (3470 \pm 700) N_{shot}^{1/2}$ ppb leading to an LOD of 35 ± 7 ppb for 10000 shots.

The results from the above series of measurements are summarized in Table.4.2. They

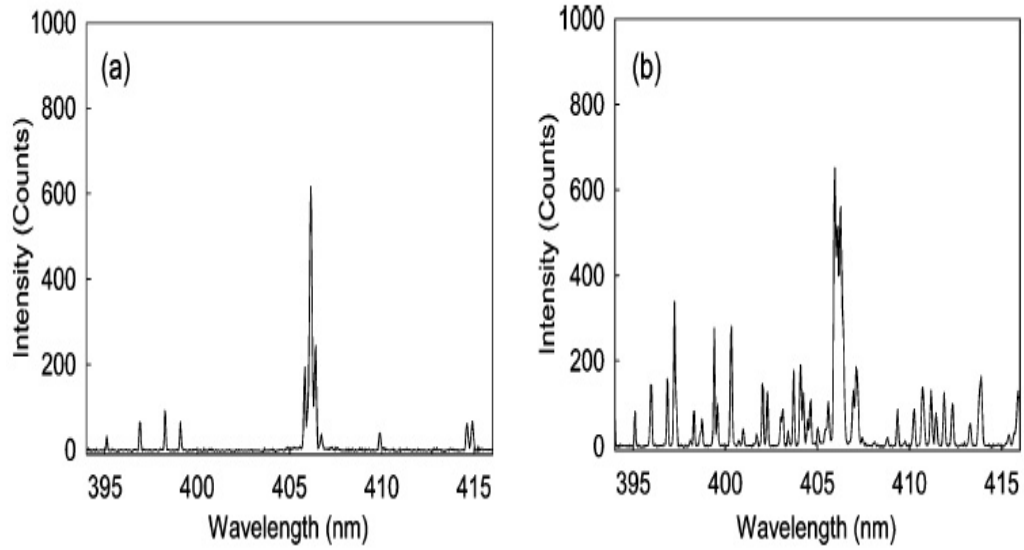


Figure 4.8: Single-shot Pb spectrum at gate widths of (a) 20 and (b) 200 ns. The result indicates that a longer gate window accumulates more noise spikes. Signals were taken for Pb at 50 ppm concentration and a probe time of $\Delta T=300\text{ns}$

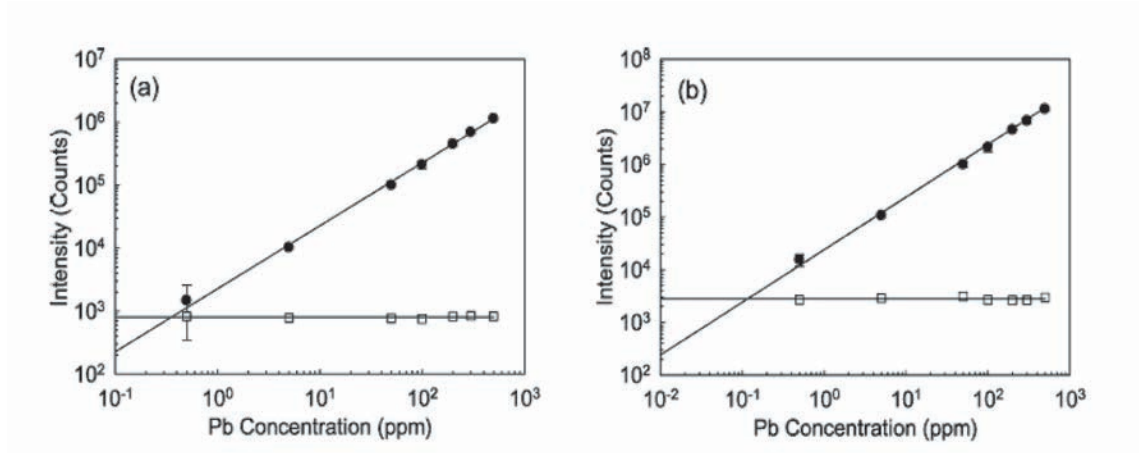


Figure 4.9: Calibration plot for Pb using the LA-LIF scheme with (a) 100 and (b) 1000 shot accumulations. The Pb signal (solid circles) and the 3σ background noise signal (open squares) are plotted against the Pb concentration. The intersection of the two lines gives the 3σ LOD. For the 100 shot case, the signal can be fit by $I = 2257C_{Pb}$, where I is the intensity and C_{Pb} is the concentration in ppm. The average 3σ noise is 798 ± 40 counts. For case b, the linear fit is $I = 24005C_{Pb}$, and the average 3σ noise is 2789 ± 200 counts.

have all been scaled to an equivalent LOD for 10 000 shots using the $N^{1/2}$ scaling law. It is observed that both the LODs determined by varying the concentration given in

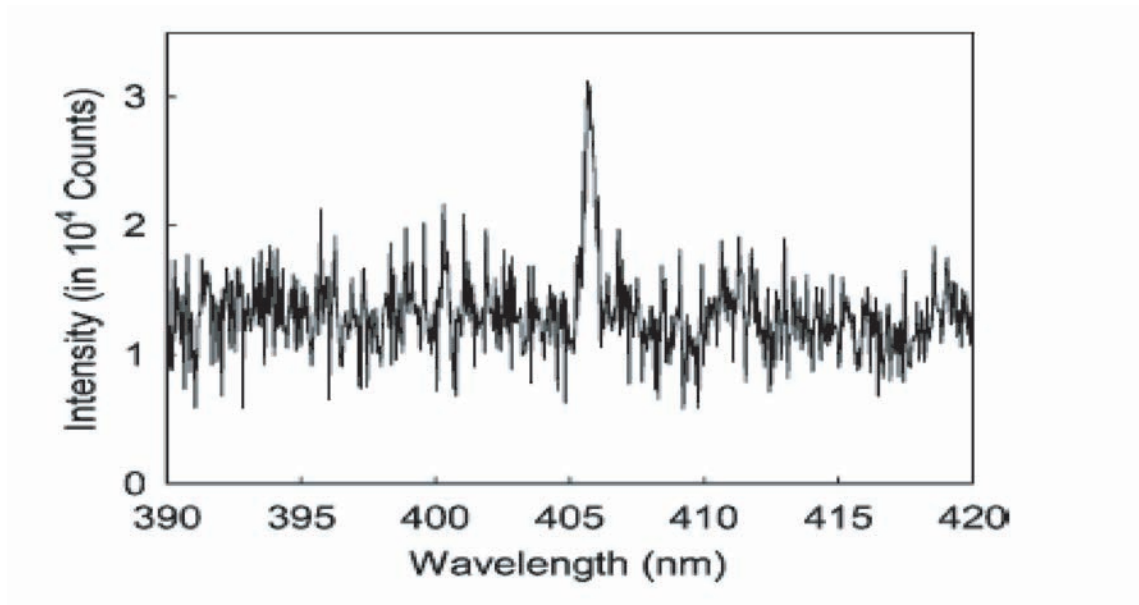


Figure 4.10: Pb 405.8 nm emission line obtained using the LA-LIF scheme with a 10000 shot accumulation for a sample with a concentration of 166 ppb as verified by ICP analysis. The SNR is 11.7.

Fig.4.9 and the LOD determined by varying the shot number Fig.4.11 lead to very similar results. The average of the measurements gives a scaling law for the LOD as a function of the number of shots given by Eq.4.1

$$LOD(N) = (3545 \pm 400)N_{shot}^{1/2}ppb \quad (4.1)$$

This scaling law is specifically for the irradiation conditions used in the present experiment but can serve as a basis for assessing microjoule irradiation experiments.

Measurement Series	LOD (N=10000)(ppb)
100 shot data	35 ± 7
1000 shot data	36 ± 7
Scaling with $N_{shot}^{1/2}$	35 ± 8
Average	35 ± 7

Table 4.2: Summary of the LODs from the Measurements Scaled to 10000 Shots Using a $N^{1/2}$ scaling with Number of Shots

To compare our present LOD for Pb in water with some of the other reported results we have compared them based on LOD and energy of Laser pulse or pulses

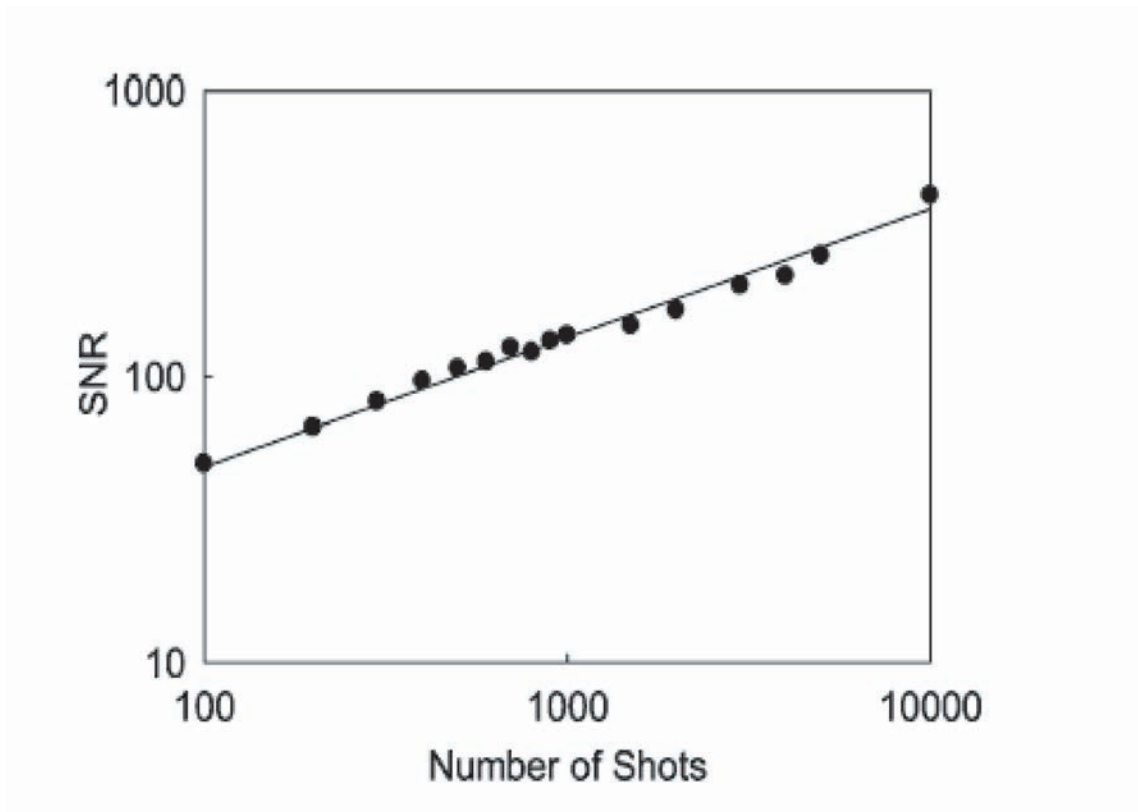


Figure 4.11: Relationship between number of accumulated shots and the S/N. Data were taken for a Pb concentration of 5 ppm and $\Delta T=300$ ns. The line is a least-squares fit to an $N_{shot}^{-1/2}$ slope scaling law.

used. Table.4.3 shows the comparison of the best LOD's reported for the detection of Pb in water for LIBS and double pulse LIBS. Fig.4.12 shows the same results plotted out.

Group	LOD	Laser Pulse Energy	Technique	Reference
Our Group	75 ppm	260 μ J	μ LIBS	[30]
Knopp	13 ppm	27 mJ	LIBS	[97]
Taschuk	6 ppm	45 mJ	LIBS	[152]
Arca	100 ppm	500 mJ	LIBS	[151]
Lo	0.894 ppm	16 mJ	LIBS	[150]
Pu	0.304 ppm	18 mJ + 56 mJ	Double Pulse LIBS	[153]
Our Group	0.353 ppm	260 μ J + 10 μ J	LA-LIF	[149]

Table 4.3: Summary of the LODs reported for Pb from literature to our results scaled to 100 shot accumulation.

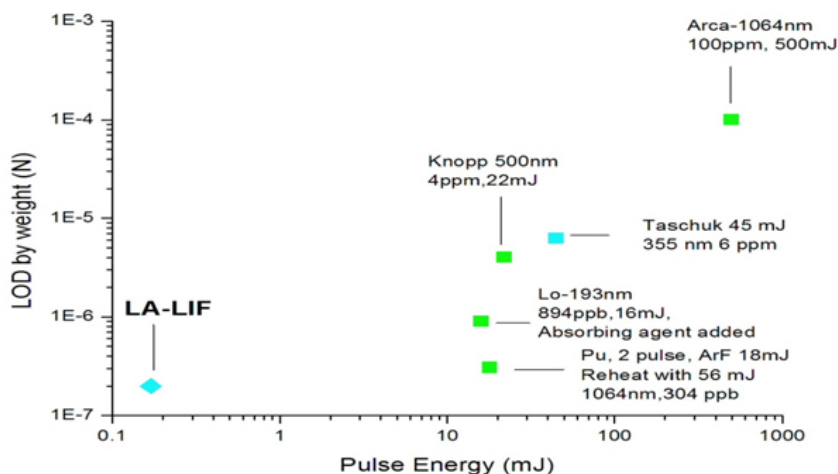


Figure 4.12: Comparison of our LA-LIF LOD for Pb in water to other results reported in literature. The LOD's are plotted with respect to the ablation laser pulse energy used.

4.4 Towards a Water Quality Monitoring System

To be able to measure water quality for comparison to the EPA standard, the sensitivity of LA-LIF has to be at least a factor of 3 better than the allowed limit. There are several means which can be pursued to improve the limiting LOD in order to achieve the required LOD of 5 ppb to monitor drinking water safety from lead contamination. Some possible methods to improve the sensitivity are by using a larger f-number light collection system, using a detector with higher quantum efficiency, using higher energy pulses, using longer duration fluorescence excitation pulses, and increasing the number of shots. A larger collection aperture of f/1 together with filtered photomultiplier detection can be employed to increase collection by a factor of 16 times compared to the f/4 light collection employed in the present system. Higher energy ablation and probe pulses can also be employed to increase the number of atoms ablated and probed though this would require larger laser systems and reduce the portability of such systems. Longer excitation probe pulses could also be employed to obtain multiple emission photons from the re-excitation of single Pb atoms several times. However, this gain is severely limited by trapping of most of the atoms in metastable states. Finally, increasing the number of shots would help achieve bet-

ter sensitivity based on the expected $N_{shot}^{1/2}$ scaling. With the use of customized fiber laser systems operating at 1-10 kHz repetition rate, the measurement could still be achieved in short measurement times. Overall, the results look promising for the development of such a portable system for on-line monitoring of lead contamination in drinking water.

4.4.1 LA-LIF of Pb using a PMT and a Multi-Pixel Photon Counter

Fig.4.13 shows the fluorescence signal measured for a LA-LIF experiment on a 1 ppm solution of Pb using a f/0.7 imaging lens and a PMT (Hamamatsu R7518) with a line filter centered at 405.8 and a bandwidth of 2 nm. The SNR obtained for a 100 shot accumulation was 43 leading to a 3σ detection limit of 70 ppb. The PMT was operated at 900 V bias voltage which corresponded to an electron gain of 10^6 .

Using the same f/0.7 imaging system and filter used in the PMT experiment we measured the fluorescence signal with the MPPC at 405.8 nm for 1 ppm lead solution corresponded to a detection of approximately 880 photons for a 100 shot sum. This corresponds to a 3σ detection limit of 101 ppb for a 100 shot accumulation. Fig.4.14 shows the output signal from the MPPC detecting the LA-LIF emission from a 1 ppm Pb solution for an ablation laser energy of 260 μJ and a excitation laser energy of 8 μJ for a sum of 100 shots. For a 10,000 shot accumulation based on SNR scaling as the square root of number of shots our projected 3σ LOD using the PMT would be 7 ppb and for the MPPC would be 10.1 ppb. The comparison of the three detectors namely the ICCD, PMT and the MPPC is shown in Table.4.4. A comparison of the solid angle of collection in steradians is made. For the ICCD system the solid angle of collection was 4.8×10^{-2} , the ICCD was operated at a gain of 200. The N_{count} obtained by the ICCD can be related to the N_{fl} , number of fluorescence photons. The transmission of the spectrometer is simple the reflectance (90 % at 405 nm) of the three Al mirrors at 405 nm (the Pb fluorescence wavelength) in the spectrometer multiplied together times the grating efficiency of 60 %. Thus the transmission of the spectrometer is $(0.9)^3$ and the quantum efficiency of the ICCD at 405 nm is 15 %. The number of photons detected for 100 shots by the ICCD detector is ≈ 215 .

The number of fluorescence photons collected in each collection geometry, f/4 for

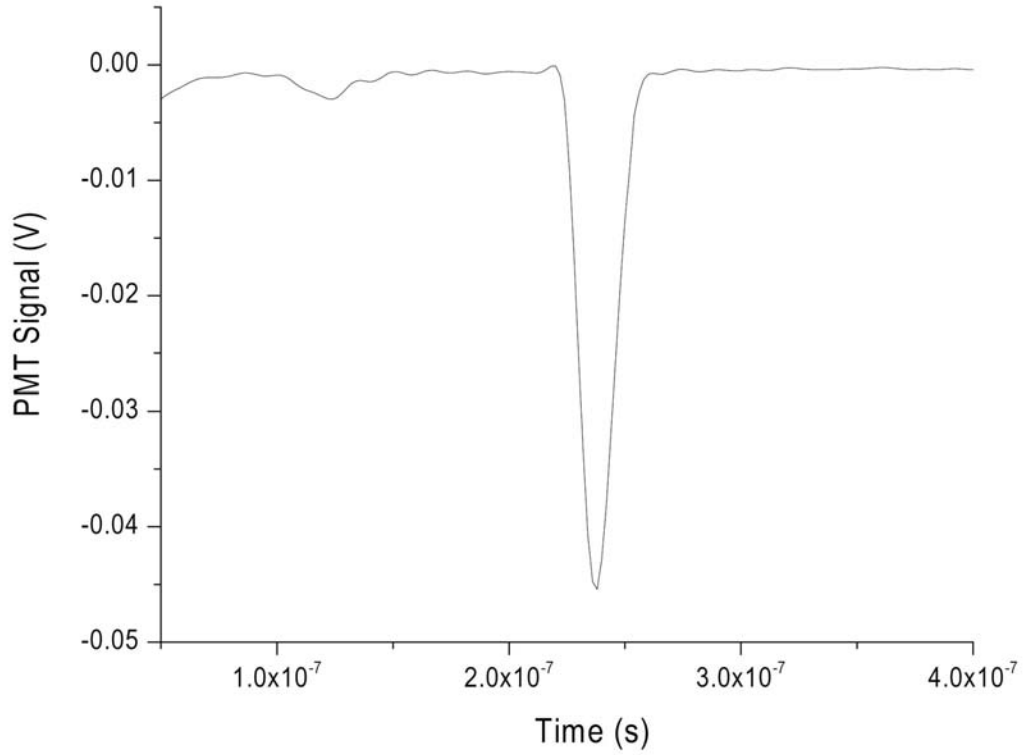


Figure 4.13: Pb emission signal measure using a PMT for an accumulation of 100 shots. The ablation laser energy was 260 μJ the probe laser energy was 8 μJ . The interpulse separation was 300 ns.

Detector	Collection	Photons Detected	Q.E	LOD (100 shots)
ICCD	f/4 0.0485 sr	215	0.2	353 ppb
PMT	f/0.7 1.17 sr	4060	0.25	70 ppb
APD	f/0.7 1.17 sr	880	0.45	103 ppb

Table 4.4: Comparison of three different detectors, ICCD, PMT and the MPPC on the basis of the 100 shot LOD's for 1 ppm Pb in water using different collection apertures. The photons detected represent the sum of the photoelectrons detected for 100 shots.

the ICCD and f/0.7 for the PMT and APD can be calculated by using Eq.3.3. If we move to the f/0.7 collection system with the PMT the number of collected improves to ≈ 4060 for 100 shots. The same collection system is employed for the APD but the APD has a much smaller active detection area which is 1 mm^2 whereas the beamsize of the imaged emission region was 8 mm^2 thus the number of photons detected were

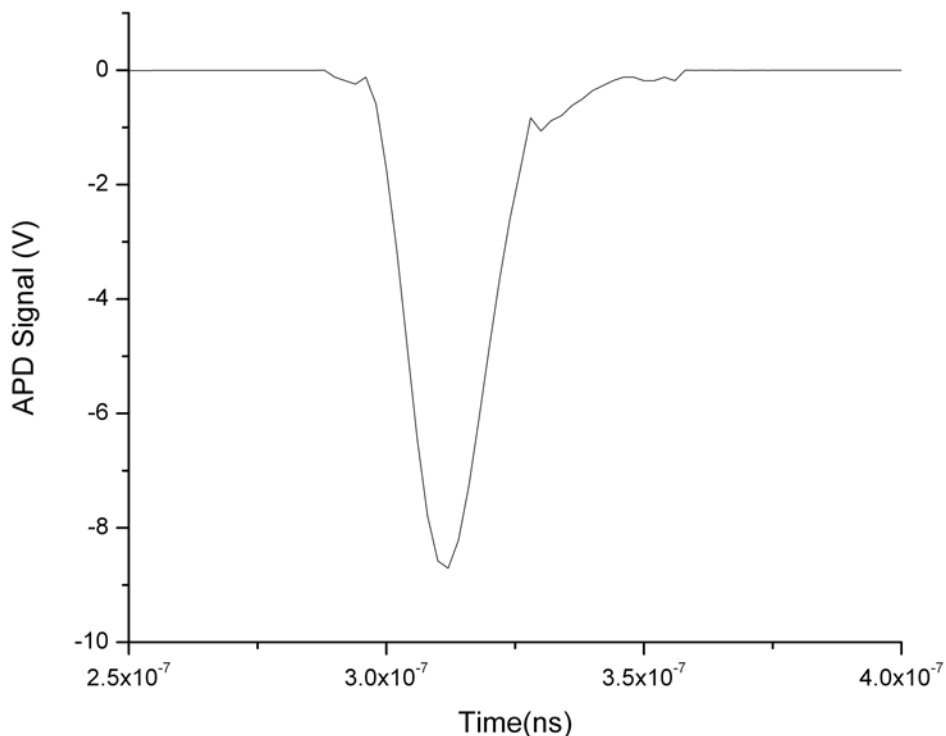


Figure 4.14: Pb emission signal measure using a MPPC for an accumulation of 100 shots. The ablation laser energy was 260 μJ the probe laser energy was 8 μJ . The interpulse separation was 300 ns.

lower in the case of the APD. One advantage with the APD is the high quantum efficiency (45%) which leads to a higher signal compared to the ICCD and the PMT. Another advantage in using the APD over the PMT is the lower power requirements for the APD for the same gain. Thus the APD or a series of APD's would be ideal in a portable water monitoring system for Pb. In the above experiment we did not focus the light into the APD. If we focus all the light into the APD we should be able to measure eight times the number of photons currently measured by the APD and the LOD would thus scale by $N_{shots}^{1/2}$ scaling law yielding a lower sensitivity of 36 ppb for the 100 shot LOD which would be ideal for water quality monitoring.

Fig.4.15 shows the theoretically estimated fluorescence photons emitted versus the experimentally determined number of fluorescence photons emitted for the LA-LIF experiment as a function of the probe pulse energy. For the number of counts ob-

tained with the ICCD based on our collection geometry we can estimate the total number of photons emitted. In Fig.4.15 the theoretical estimate for the number of photons emitted for a 1 ppm solution of Pb is shown. The estimate was made using the equations shown in appendix A for a starting atomic density of 10^{21} m^{-3} and a electron temperature of 0.2 ev. The estimate shown is for a 1000 shot accumulation. This theoretical estimate is compared to the estimated total photons emitted from the number of counts obtained using the ICCD. The total number of emitted photons predicted theoretically do not match with the total number of photons emitted determined experimentally. One reason for this could be that the model in Appendix A is a simple rate equation model which does not take collisional coupling of different atomic levels into consideration. The solution plotted for the rate equations is a steady state solution assuming the integration time and the spectral energy density in the probe laser are sufficiently large enough. Nevertheless the theoretical and experimental results predict the saturation behaviour of the signal fairly well.

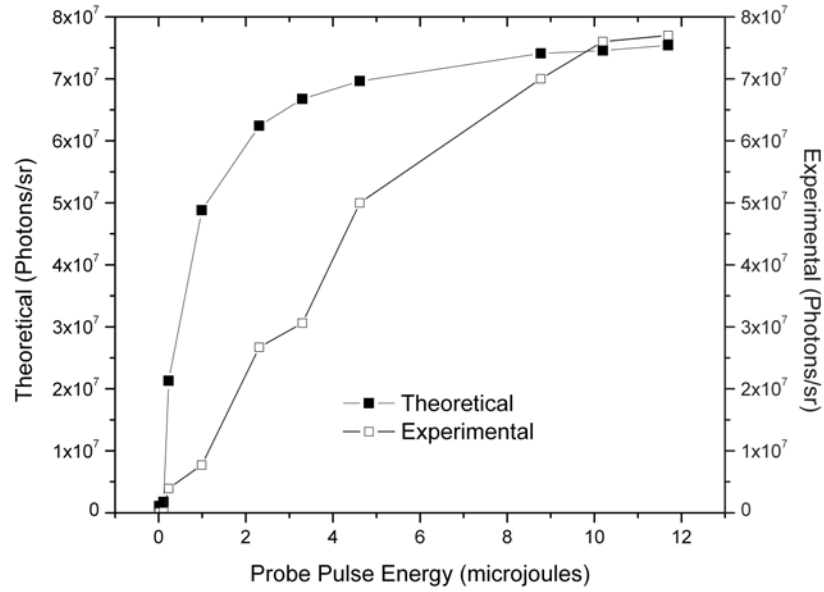


Figure 4.15: A comparison of the theoretical (closed squares) to the experimentally (open squares) determined values for the fluorescence signal emitted. The concentration of Pb was 1 ppm and the ablation pulse energy was 260 μJ the excitation pulse energy was varied. The theoretical results presented are for a sum of 1000 shots assuming a temperature of 0.2 eV and atomic density of 10^{21} m^{-3} and a 30% overlap factor between the probe pulse and the plasma (i.e) assuming the probe beam only samples 30% of the plasma plume. The delay between the two pulses was 300 ns. The detector gain was 200. Details of the calculation are given in Appendix A.

Chapter 5

μ LIBS on Microfluidic platform

There is great merit in integrating sensitive analytical technologies onto microfluidic platforms for portability to perform testing at remote locations. A potential application of μ LIBS is the detection of low concentration elemental species in fluids either for simple chemical analysis or for analysis of cell contents in a fluidic stream which have thus far not been explored. The feasibility of detecting and quantifying sodium and potassium in single human red blood cells using LIBS has been reported earlier [106]. Though impressive, this demonstration makes use of a fluidic jet as a sample source, which we believe is suitable for use in a laboratory rather than a portable setting. Analysis of single isolated droplets by sampling a droplet stream has been previously reported using LIBS where an improvement over probing bulk liquids was reported [107]. Droplet dispensers using the microfluidic chip format have recently found applicability to several fields [107] but have not yet been applied to LIBS. Using μ LIBS to analyze the content of a monodispersed droplet allows us to retrieve both qualitative and quantitative information of a sample while requiring low laser energies, the key aspect that needs to be dealt with to realize a portable system. An important implication of making use of μ LIBS on monodispersed droplets emanating from microfluidic chips is the possibility of integration of several analytical techniques that have already been demonstrated within microfluidic platforms and eventually direct this work towards life-science technologies. In this chapter the results of our experiments of applying μ LIBS and LA-LIF to analyse the elemental contents of microdroplets are presented. First we do a systematic study of the behaviour of the μ LIBS and LA-LIF signal intensities as a function of the size of the

microdroplets and the laser pulse energies. These results are then compared to those obtained using the waterjet system. We also present our results from applying μ LIBS to a microfluidic system.

5.1 μ LIBS and LA-LIF on Microdroplets: Piezoelectric Pulser Approach

In this study, measurements were based on fundamental approaches for quantitative analysis using the setup described in section 3.4. Monodisperse microdroplets with diameters ranging from 8 to 25 μm were generated for LIBS and LA-LIF analysis. Sensitivity of this new method using an inkjet system was compared to the conventional technique of employing a bulk waterjet using LIBS and LA-LIF measurements.

5.1.1 μ LIBS emission Intensity as a function of Gate Delay and Laser Pulse Energy

The piezoelectric microdroplet dispenser was included in the μ LIBS setup. The analyte used here was Na which was NaCl dissolved in water to obtain a concentration of 100 ppm of Na by weight. In order to obtain complete ablation of the microdroplet the spatial and temporal position of the microdroplet and the laser focal spot were matched. As shown in Fig.3.37 for an ablation pulse energy of 192 μJ a focal spot scan was done for a fixed microdroplet size and the best focusing conditions were obtained based on the maximum Na signal intensity. With the microdroplet position and the laser focal spot overlapping in space, a parametric study of LIBS emission as a function of the detector gate delay was carried out for different laser pulse energies in the range of 50 to 470 μJ .

Fig.5.1 summarizes the data obtained for the LIBS emission intensity for Na for different laser pulse energies with the detector gate delay varied from 80 ns to 1.2 μs . As can be observed the LIBS emission for pulse energies ranging from 50 to 190 μJ is maximum at a gate delay of 80 to 100 ns a similar trend was observed for μ LIBS studies using the waterjet for Pb as indicated in section 4.2 where a gate delay of 70 ns was observed in the case the μ LIBS of Pb for a pulse energy of 260 μJ . As the pulse energies were increased from 200 - 460 μJ the LIBS emission was maximum for

most of the energies at a gate delay of 200 ns. For the rest of the analysis for μ LIBS of Na the gate delay was fixed at 200 ns and the laser pulse energy was set to 200 μ J.

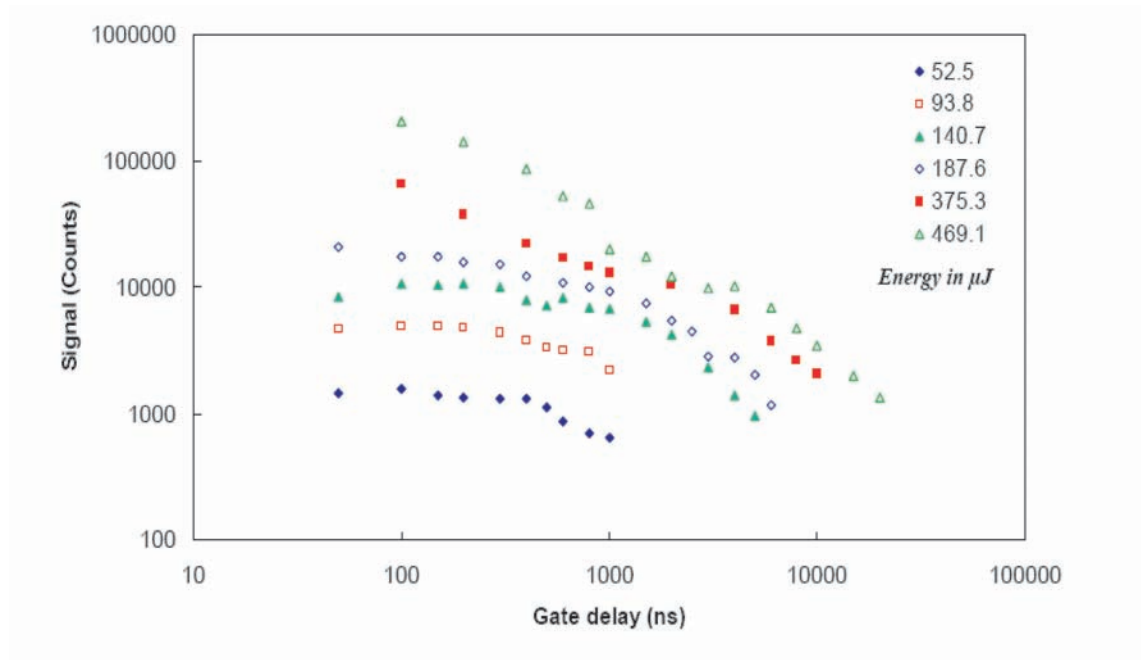


Figure 5.1: LIBS emission intensity as a function of detector gate delay for different laser pulse energy . The size of the microdroplet was constant at $\approx 20 \mu\text{m}$. The gate delay was varied from 80 ns to 10 μs . The laser pulse energy was varied from 50 μJ to 470 μJ . Each data point is an average of 100 laser shots. The detector gain was set at 200 and the gatewidth was 1 μs .

5.1.2 μ LIBS emission Intensity as a function of Microdroplet Size

To study how the LIBS emission changes as a function of the droplet size and thus as a function of analyte volume, microdroplets of different diameters were generated by varying the voltage pulses applied to the piezoelectric dispenser. The laser pulse energy was also varied to study the best laser conditions for ablation of a microdroplet of a particular size.

Fig.5.2 summarizes the LIBS signal intensity for microdroplets ranging from 8 - 23 μm and the laser pulse energy ranging from 50 to 500 μJ . The Na signal intensity was significantly lower for the 8 μm microdroplet as it is harder to spatially overlap the 12 μm ablation pulse with the 8 μm pulse. Higher pulse energies give better LIBS

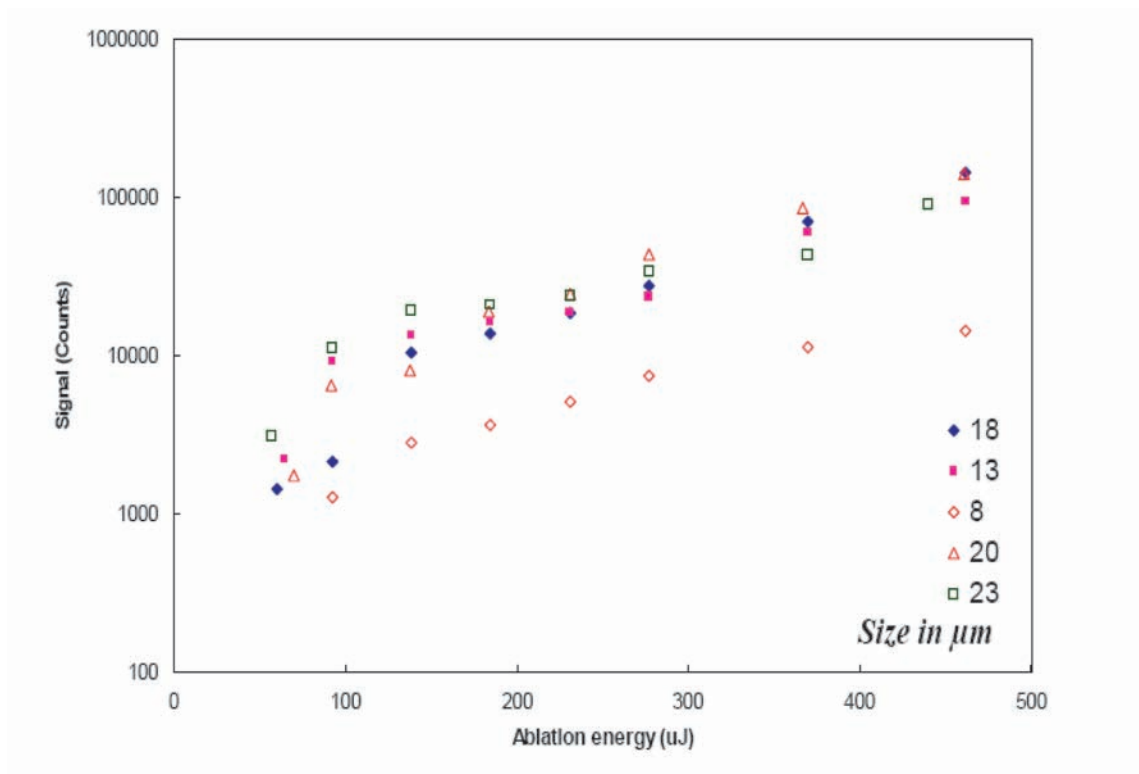


Figure 5.2: LIBS emission intensity as a function of laser energy for different sizes of the microdroplet for different gate delays. The laser pulse energy was varied from 50 - 450 μJ . The size of the microdroplets was varied from 8-23 μm . The detector gate delay was set at 100 ns and the gate width was 1 μs . The gain of the detector was set to 200 and the slit width of the spectrometer was 300 μm .

emission intensities, but the main goal of this experiment was to optimize the focus conditions and study the emission from the ablation of a ultralow volume of amount of analyte at $\approx 200 \mu\text{J}$ of laser pulse energy.

5.2 LA-LIF of microdroplets

Once the focusing conditions, camera parameters were optimized for the microdroplet a series of experiments were carried out to determine how the re-excitation of the plasma generated by the microdroplet compares to the bulk systems like the waterjet and what is our absolute limit of detection using LA-LIF for Pb. Using the setup described in Fig.3.33 in the previous chapter, the LA-LIF emission dependence on the size of the microdroplet was studied.

5.2.1 LA-LIF emission as a function of Microdroplet Size

Fig.5.3(a) shows the μ LIBS emission and the SNR as a function of droplet size and Fig.5.3(b) shows the LA-LIF signal and SNR as a function of microdroplet size. In both cases a 100 ppm of Pb dissolved in water was used as the analyte. The ablation pulse energy was 130 μ J in both cases, and the gate delay was 300 ns and gate width was 50 ns. In the LA-LIF case the inter-pulse separation was set to 300 ns and the probe pulse energy of the re-excitation laser pulse was 8 μ J. The results shown are an average of 200 single shot events captured. The SNR and signal for the μ LIBS case increase up to a droplet size of $\approx 18 \mu\text{m}$ and remains the same for larger sizes. The saturation in signal probably occurs due to the limited first pulse energy. When we examine the LA-LIF signal emission and the SNR as a function of the size of the microdroplet we can see the SNR and signal increase and level off after a droplet size of 18 μm as compared to the μ LIBS case there is a 11 fold increase in the SNR for Pb. The roll off in the SNR is probably due to the limited first pulse energy. Even if the first pulse energy is increased in this case the LA-LIF signal maybe limited by the diameter of the resonant probe pulse which was 218 μm .

The spectra shown in Fig.5.5 shows a comparison of the μ LIBS and LA-LIF spectra obtained from the ablation of an 18.5 μm droplet under similar conditions. As the LOD of our system is too low the μ LIBS emission signal for Pb is not visible in this case. The LA-LIF spectrum on the other hand clearly shows that as soon as the resonant pulse intersects the plasma 300 ns after the ablation pulse the Pb emission appears. Ten individual ablation events were captured and integrated for both the μ LIBS and the LA-LIF emission cases. Fig.5.4 shows the plasma images for the μ LIBS case and the LA-LIF case, the LA-LIF plasma clearly looks brighter indicates that the brightness is due to the re-excitation of the plasma by the probe pulse.

5.2.2 Effect of Probe pulse energy on LA-LIF of Microdroplets

To study the scaling of LA-LIF emission for Pb as a function of the probe pulse energy the energy of the resonant laser was varied from 1-7 μ J. Fig.5.6 shows the Pb emission intensity and the SNR as a function of the probe pulse energy. As the

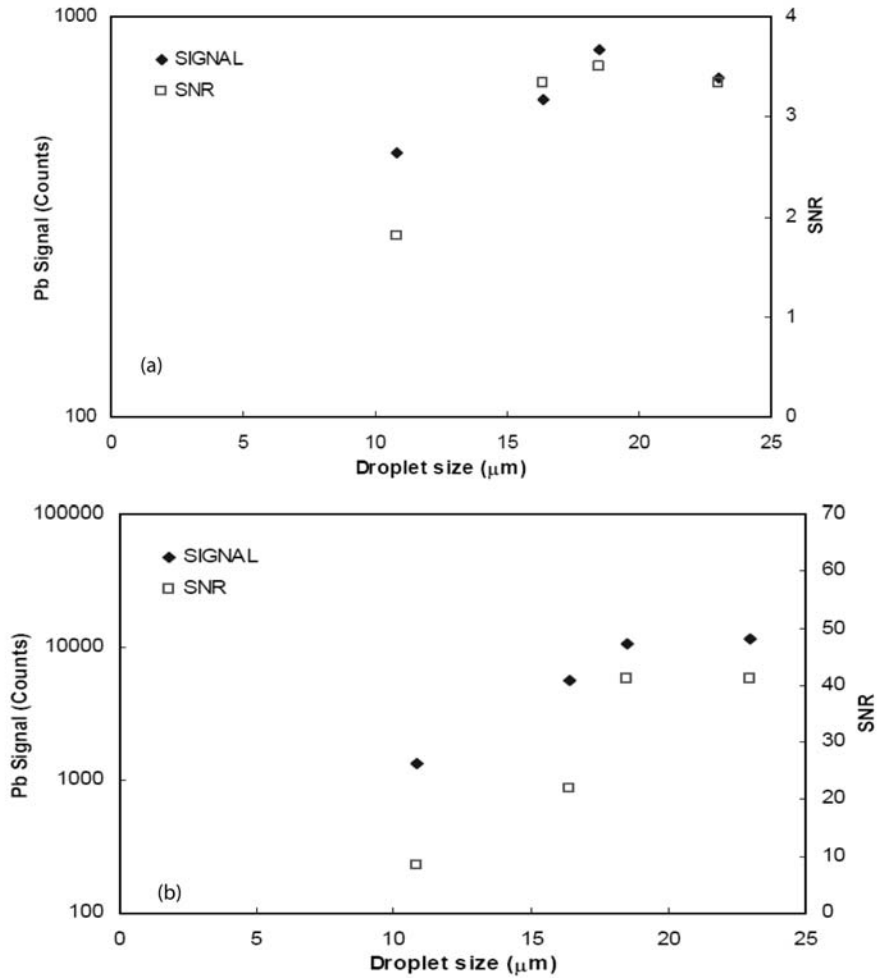


Figure 5.3: (a) Figure shows the variation of the μLIBS signal and SNR as a function of the size of the microdroplet. (b) Is the variation of the LA-LIF emission signal and the SNR as a function of the size of the microdroplet for a 100 ppm sample of Pb. In both the experiments the ablation pulse energy was $130 \mu\text{J}$ the gate delay was set to 300 ns and the gate width was 50 ns. For the LA-LIF case the energy of the probe pulse was $8 \mu\text{J}$. All data shown is an accumulation of 200 shots.

energy of the probe laser increased the emission intensity linearly increases as we could not increase the energy of the probe laser further due to technical issues we could not obtain a probe energy strong enough to saturate the emission. However the behaviour observed is similar to that of the waterjet and the emission intensity saturates for a probe laser energy greater than at $8 \mu\text{J}$ for a microdroplet size of $18 \mu\text{m}$ and a ablation energy of $130 \mu\text{J}$.

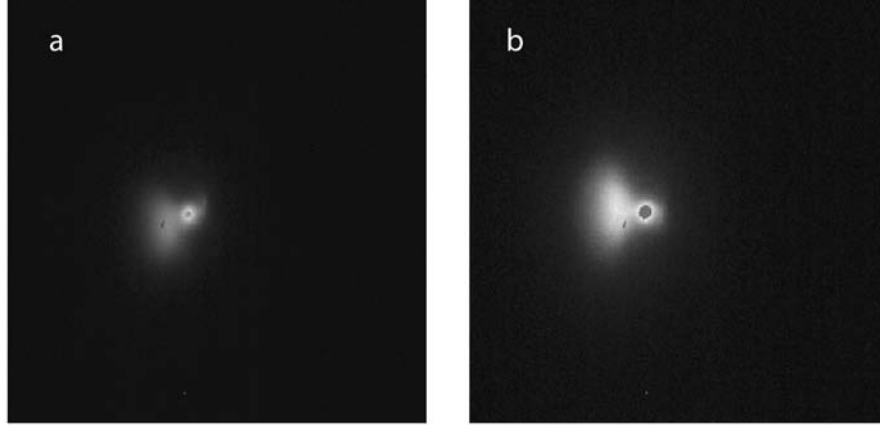


Figure 5.4: (a) Shows the 10 shot accumulation of μ LIBS emission from $20\ \mu\text{m}$ droplets. (b) Shows the 10 shot accumulation of LA-LIF emission from the microdroplet. The LA-LIF emission appears brighter indicating the resonant re-excitation of the plume. The ablation energy used in both cases was $195\ \mu\text{J}$ and the probe pulse energy in the LA-LIF case was $10\ \mu\text{J}$. The inter-pulse separation was $300\ \text{ns}$ and the gate width was $100\ \text{ns}$.

5.2.3 Comparison of LA-LIF of Microdroplets and LA-LIF for waterjet

If we examine the distribution of signal height for a large number of shots we can determine how effectively the microdroplet can be ablated, the fluctuation in the Pb emission signal was observed for 10,000 individual shots. There is a wide distribution in the data. The laser completely missed the microdroplet for 3.4 % of the shots as indicated in Fig.5.7. In order to increase the probability of ablation of the microdroplet the experimental setup should be modified to include a tracking laser similar to the one used in reference [154]. The tracking system would trigger the ablation laser only when the microdroplet is within the focal volume of the ablation laser. A comparison of the standard deviations of the signals from 1000 different acquisitions from the waterjet and the microdroplet are shown in Fig.5.8. The distributions are very similar with the standard deviations of the signal fluctuations in the same range. The average of the waterjet distribution is higher than that of the microdroplet. The reason being the variation in the spatial position of the microdroplet may cause incomplete ablation of the microdroplet. Also with the ablation of the microdroplet the plasma expands spherically as compared to a hemispherical expansion for the waterjet so in case of the microdroplet possibly only a fraction (down to a half) the

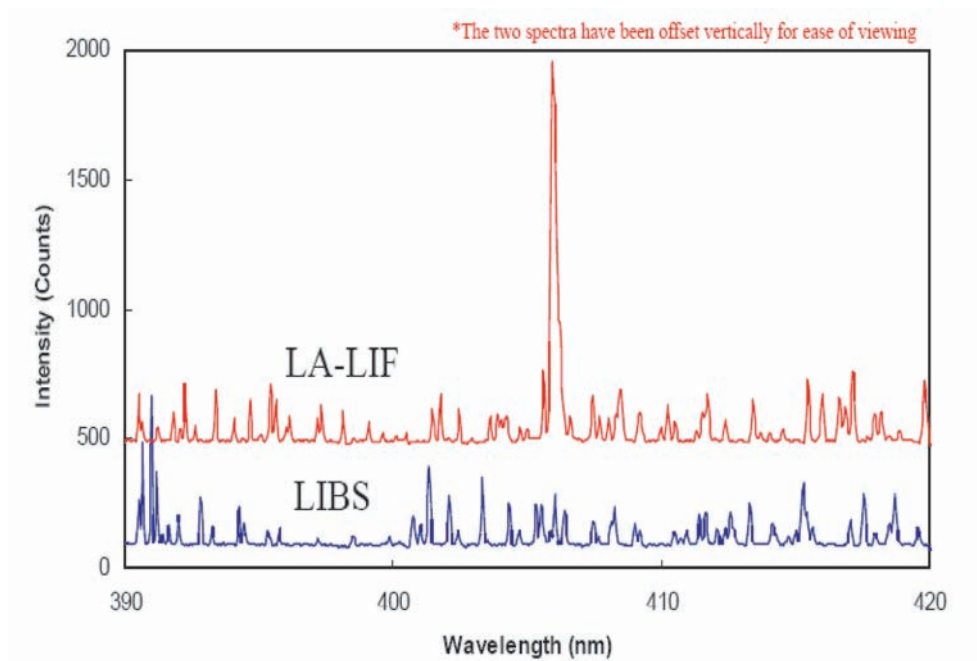


Figure 5.5: A comparison of the spectral emission for Pb obtained with μ LIBS and with LA-LIF. The μ LIBS laser pulse energy is 130 μ J the gate delay was set at 300 ns and the detector gate width was 50 ns the spectrometer slit width is 300 μ m the size of the microdroplet is 18 μ m the detector gain was set at maximum the concentration of Pb in the solution was 100 ppm. For the LA-LIF case the experimental conditions were the same, the energy of the resonant laser pulse was 8 μ J and the delay between the two pulses was 300 ns. The Pb emission is not visible for the μ LIBS case as it is below the detection limit of the system but the Pb emission at 405 nm is clearly visible for the LA-LIF case. Both spectra represent a 100 shot accumulation.

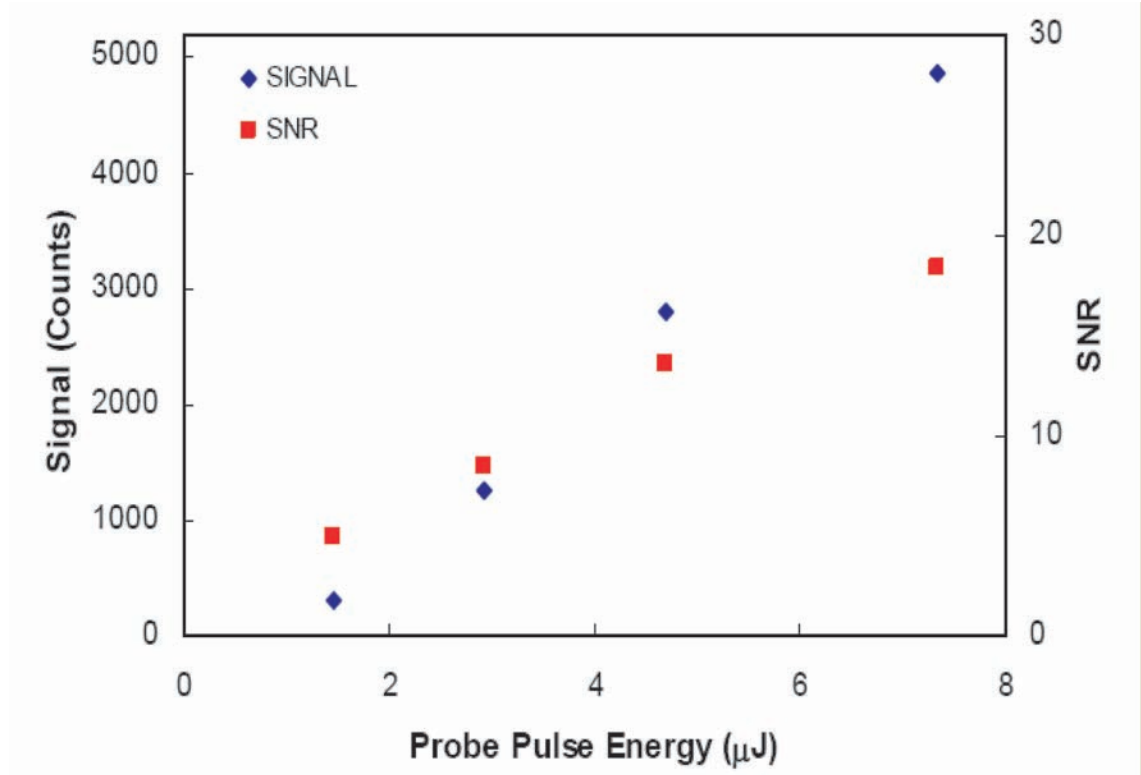


Figure 5.6: LA-LIF signal emission intensity and SNR as a function of the probe pulse energy. The ablation laser energy was 130 μJ the probe pulse was varied from 2-8 μJ . The delay between the two pulses was 300 ns. The detector gate delay was set at 300 ns and the integration time was set to 50 ns. The spectrometer was centered at 405 nm, the grating used was a 2400 1/mm and the slit width was 300 μm .

emission is collected by the imaging setup as compared to the waterjet.

5.3 Demonstration of μLIBS on a Microfluidic Platform

The spectral emission lines of interest for Na are the 588/589 nm doublet lines which involve transitions from ${}^3P_{1/2}$ upper states and ${}^3P_{3/2}$ to the ${}^3S_{1/2}$ lower states [155]. The sample tested here contained 200 ppm by weight of Na as an analyte in the form of NaCl dissolved in distilled water. LIBS was applied on the hemispherical microdroplet which was generated as described in the methods section. The gate width of the ICCD detector was set to 1 μs at maximum gain while the gate delay varied. The single shot Na 589 nm doublet spectra with different gate delay times are shown in Fig.5.9.

The signal is defined as the normalized intensity under the Na doublet with the

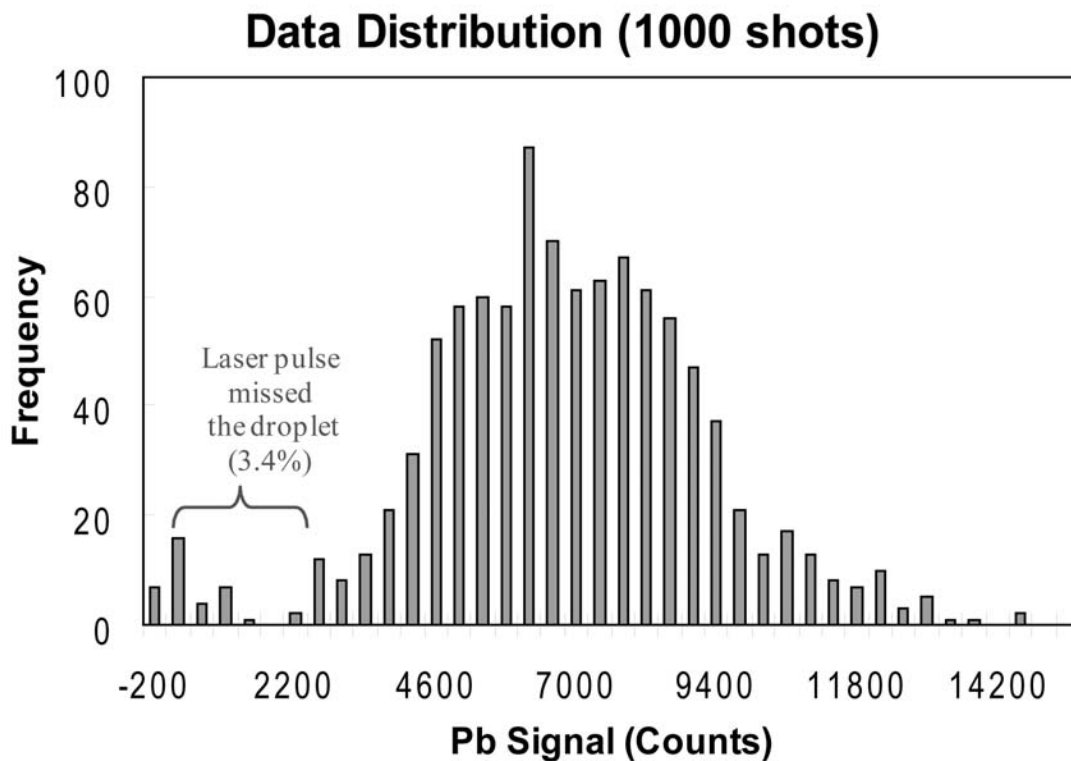


Figure 5.7: The signal distribution for 1000 shots for the LA-LIF emission for a 20 μm microdroplet.

average background subtracted, and the noise as the standard deviation of the background scaled to a bandwidth equivalent to that used to measure the line emission taking neighboring channel pixel correlations into account. Initially, at 100 ns gate delay in addition to the sodium lines many photons are detected across the full spectrum range viewed due to continuum emission from the plasma. When the plasma cooled down, the doublet could still be resolved but the line intensity also dropped significantly. The Na lines completely disappeared by 800 ns. The SNR of the spectrum with a gate delay of 100 ns was 10 resulting in a 3σ limit of detection LOD of 60 ppm.

However, certain applications may require a better LOD. To improve the SNR, an average of 100 shots were accumulated resulting in SNR of 100 with the same gate delay of 100 ns (Fig.5.10) and corresponding to a 3σ LOD of 6 ppm corresponding to a mass within the hemispherical droplet of 360 fg. Janzen et al. [156] using 100 shot average detection with much higher laser energies found a 3σ LOD of 0.2

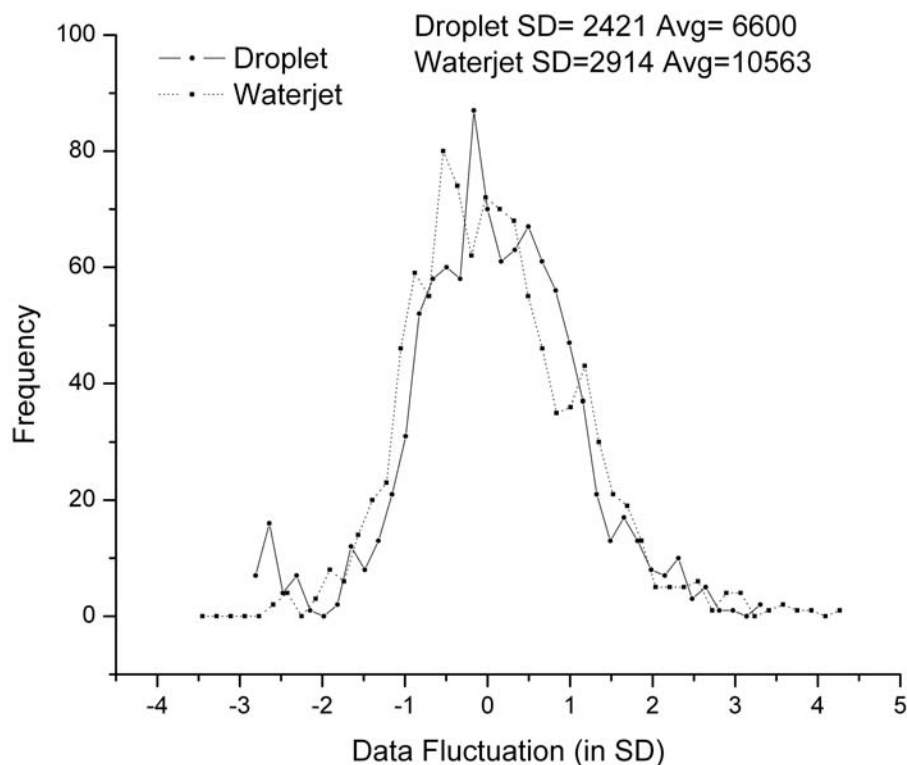


Figure 5.8: Comparison of the fluctuation in data of Na μ LIBS emission for 1000 shots for a waterjet target and a 20 μ m microdroplet target for a laser energy of 170 μ J. As can be observed the relative signal fluctuation is almost the same for both the microdroplet and the waterjet.

ppm for Na using the same emission lines. We attribute this increased sensitivity to the fact that they used a higher energy 25 mJ, 266 nm, laser pulse and a larger 80 μ m droplet. However, using larger laser pulse energies limits the portability of their system. The SNR distribution for 100 single shot data shows that majority of the spectra have a signal to noise ratio SNR between 10 and 20, and the standard deviation of the SNR for the 100 data set is 3. The fluctuations in the SNR were due primarily to the variations in droplet size ($\pm 15\%$) and in laser pulse energy ($\pm 10\%$), leading to a change in the initial ablation, the sampling volume, and the plasma conditions. Overall, we demonstrated 3σ LOD of 60 ppm and 6 ppm for single or 100 shot detection of sodium in water with 200 μ J laser pulses under the current conditions. A microfluidic-based LIBS system suitable for inexpensive and portable

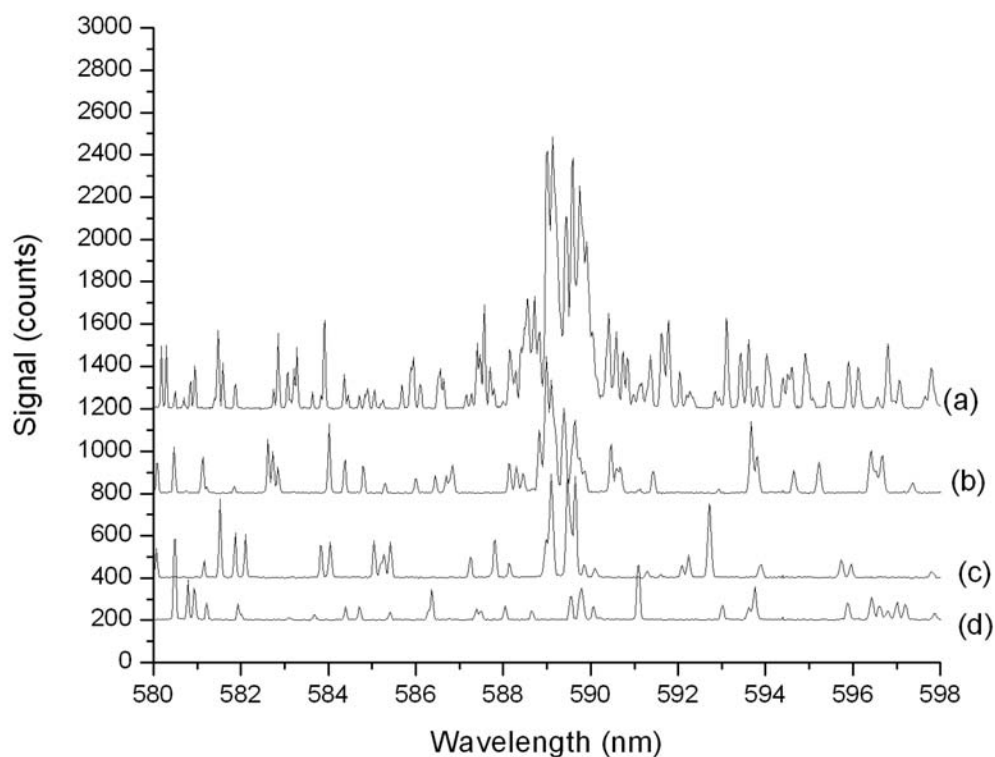


Figure 5.9: Single shot LIBS spectra on a micro-droplet. The pulse energy for ablation was 200 μJ , and the spectra were obtained at a gate width of 1 μs with gate delay varied: (a) 100 ns; (b) 200 ns; (c) 500 ns; and (d) 800 ns. The corresponding SNR are 11, 4, 2, and 0 respectively.

elemental detection/analysis devices has been demonstrated. LIBS will potentially have important applications in elemental analysis for monitoring of water quality for public health and biomolecule detection in point-of-care diagnostics. Our results indicate that μLIBS can be integrated with a microfluidic platform for such non-labeled analysis. This extension of LIBS could be implemented by integrating compact laser sources and filtered photomultiplier tubes PMT or avalanche photodiode arrays's these are more compact and hence appropriate for portable platforms. Such fully integrated systems will require further miniaturization of lasers and detector systems that is occurring naturally due to increasing demand to use spectroscopic techniques in numerous applications. The statistical spectral analysis results for 100 micro-droplets suggest that the reproducibility of the platform needs to be addressed if high

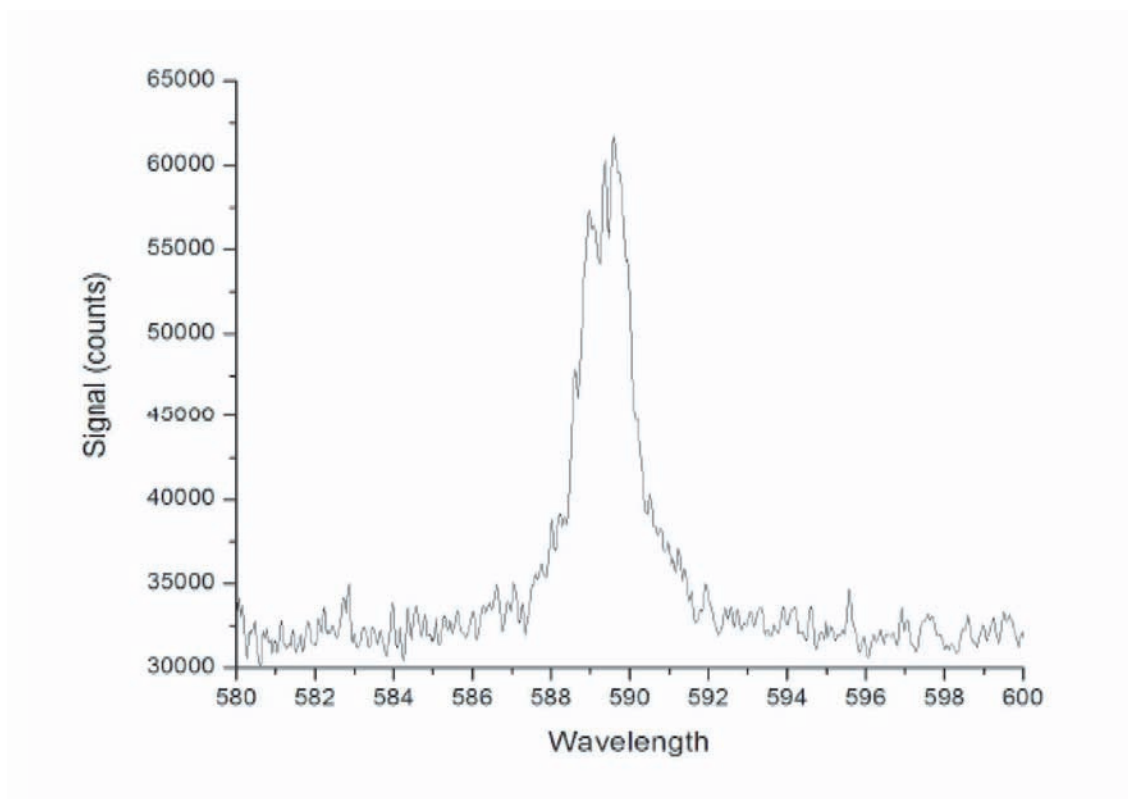


Figure 5.10: Multiple shot accumulation μ LIBS spectra on microdroplets. 100 shot accumulation μ LIBS spectra on micro-droplet. The gate delay was set at 100 ns.

precision single droplet measurements are required. The fluctuation of the SNR in the data in part is due to the instability in the microdroplet size and the microdroplet generation that resulted in varying degrees of ablation from shot to shot. Further, we are also currently characterizing the bubble retracting post ablation and the effect of debris. Even though we show the feasibility of using this technique with Na, this technique can potentially be used for less sensitive elements such as Ca by integrating a larger number of laser shots while keeping the detection time short by making use of microchip lasers which are capable of multi-KHz. repetition rates and also by making use of larger collection apertures coupled to large aperture sensitive detectors such as PMT's.

Chapter 6

Modelling of Laser Interaction

6.1 Introduction

The study of the Laser induced plasma is fundamental to an understanding of not only the LIBS process but many other applications concerning laser-matter interaction such as : Pulsed Laser Deposition (PLD) [157], Laser Cleaning [158] and Laser Shock Processing [159]. For further development of these fields, one needs a better understanding of basic ablation mechanisms. The complexity of the involved physical processes still does not allow a complete analytical description. Colonna et al. [160, 161] developed a theoretical model to study the characteristics of thin films deposited by laser ablation. Their model did not include laser-surface interaction mechanisms so it was a partial model. Their main intent was to study the expansion of the LIBS plasma. Itina et al. [162] developed a hybrid model to study the dynamics of laser plume expansion in vacuum or into a background gas. They studied high-repetition rate laser ablation for different background pressures. The model mainly studied laser plume interactions with the background gas. Their results mainly indicated the spatial maps of reaction products formed during the plume expansion into a reactive background gas. The Medusa103 hydrocode for modelling the laser ablation and emission dynamics was recently used by Dr. Martin Richardson's group at the University of Central Florida [163, 164] to study extreme ultraviolet (EUV) generation from the ablation of liquid microdroplet sources.

6.2 Analytical Models for laser absorption and expansion

A one dimensional planar model for the absorption of laser light by a plasma was developed by Mora in 1982 [165]. In his analytical model, the main absorption mechanism is inverse bremsstrahlung. The problem is studied as a function of laser intensity I , the laser pulse duration τ , target material, geometry of expansion and laser wavelength. The electron density is assumed to be a function of axial distance in the absorption region and is described by the density gradient length L , the density profile is assumed to be exponential.

$$n_e = n_c \exp(-x/L) \quad (6.1)$$

where n_c is the critical density associated with the wavelength and the frequency ω , $n_c = \epsilon_0 m_e \omega^2 e^{-2}$. The electron temperature T_e is estimated by equating the absorbed energy flux AI to the energy necessary to maintain self similar isothermal expansion from the critical density to vacuum

$$I = 4n_c T_e c_s \quad (6.2)$$

where c_s is the ion acoustic velocity $c_s = (ZT_e/m_i)^{1/2}$. The assumption here being that at steady state the outward heat flux is $q_{out} = n_c T_e c_s$ and the inward heat flux is $q_{in} = 3n_c T_e c_s$. The inverse bremsstrahlung absorption in the density profile is given by

$$A = 1 - \exp\left(2 \int_c Im(k) dx\right) \quad (6.3)$$

where the integral extends over the entire light path in the plasma, k is the wavenumber of the light $k = \omega \epsilon^{1/2}$ where ϵ is the complex dielectric constant given by

$$\epsilon \approx 1 - n_e/n_c - i(n_e/n_c)^2 v_c/\omega \quad (6.4)$$

where v_c is the electron ion collision frequency at the critical density

$$v_c = 2/3(2/\pi)^{1/2} \frac{\bar{Z} n_c e^4 \ln(\Lambda)}{8\pi m_e^{1/2} \epsilon_0 T_e^{3/2}} \quad (6.5)$$

$\ln(\Lambda)$ is the coulomb logarithm and \bar{Z} is the ion charge for a simple plasma and $\bar{Z} = \langle z^2 \rangle / \langle Z \rangle$ for an ionic mixture. using Eq.6.1 and Eq.6.4 in Eq.6.3 we obtain

$$A = 1 - \exp(-8/3v_c L/c) \quad (6.6)$$

For a planar case $L=c_s\tau$ if the other parameters are constant the light absorption is a function of $I^{-2/3}\lambda^{10/3}$. From Eq.6.6, A is a function of $v_c L$, where v_c scales as $n_c T_e^{-3/2}$ and L as $c_s\tau$. Thus $v_c L$ scales as $n_c T_e^{-1}$. When we equate the absorbed energy to the energy of the self similar expansion we obtain $T_e \approx (AI/n_c)^{2/3}$ and thus $v_c L$ scales as $(AI)^{-2/3} n_c^{5/3}$ or as $(AI\lambda^5)^{-2/3}$ which exhibits a $I^{-2/3}\lambda^{10/3}$ dependence for the absorption exponential parameter. One can define a transition flux where absorption starts to fall off by :

$$I^* = \lambda^{-5} \mu^{5/4} (\bar{Z}\Lambda\tau)^{3/2} \quad (6.7)$$

in this equation the various physical quantities have been normalized $\lambda = \lambda(\mu\text{m})/1.06$, $\mu = 2Z/A$, $\bar{\Lambda} = \ln\Lambda/6$, $\tau = \tau(\text{ps})/100$, $I = I(W/cm^2)/4.8 \times 10^{11}$. Thus we can determine equations for the electron temperature and pressure for this characteristic intensity for bremsstrahlung absorption.

$$\bar{T}_e = 0.55(I\lambda^{1/2})(\mu)^{-1/8}(\bar{Z}\Lambda\tau)^{1/4} \quad (6.8)$$

where $\bar{T}_e = T_e(\text{ev})/110$ The characteristic pressure is given by

$$\bar{P} = 1.3I^{3/4}\lambda^{-1/4}\mu^{-7/16}(\bar{Z}\bar{\Lambda}\tau)^{-1/8} \quad (6.9)$$

6.3 Blast wave theory

The classical blast wave theory in a gas [119] has been extended to the microscale laser-induced explosions and plasma expansion models by various authors [119, 122]. The models that have been mainly considered are two distinct one-dimensional treatments of the explosion problem, that assume constant and variable explosion energy, respectively. The constant energy model considers the instantaneous release of a finite energy E_o , occurring in a certain spatial point, on a line or on a surface, in an ambient gas with a scaling law depending on the dimensionality of the explosion geometry. No further hypothesis on the nature of the explosion or on the origin of the expanding

shock wave is required. The solutions that can be derived from these assumptions are useful to fit the observed shock wave behavior at times much longer than the real laser pulse duration and on propagation distances greater than the size of the original irradiation volume. At the same time the solution is only valid for a period when the energy released is much larger than the energy contained in the background gas swept up by the blast wave. In the spherical geometry the radius of the shock front is given by

$$R(t) = s(\gamma)t^{2/5}E^{1/5}\rho^{-1/5} \quad (6.10)$$

$R(t)$ is the radius of the shock front, E is the energy deposited in the plume, $s(\gamma)$ is a constant on the order of unity which is a function of the ratio of the specific heats of the background gas and ρ is the mass density of the ambient gas.

Laser pulses can induce a laser driven detonation wave into the ambient gas. The short laser pulses can induce an optical detonation when the laser intensity is high enough to generate in the close proximity of the target surface a plasma which directly absorbs a large fraction of the laser radiation in a thin layer. The strongly overcompressed and overheated gas forces a supersonic expansion of the shock front that produces the ionization of the surrounding unperturbed gas and increases the volume of the plasma region. Let us consider a laser pulse of time duration τ_L with top-hat spatial and temporal distributions, focused in air onto the target surface with a spot of diameter d and an intensity I_L the absorbed fluence is given by $F_{abs} = I_D\tau_D$ where τ_D is the laser pulse duration and the absorbed energy is

$$E_{abs} = (\pi/4)d^2I_L\tau_L \quad (6.11)$$

The limiting formulas for the density jump at the shock front is given by

$$\rho_1 = \rho_0(\gamma + 1)/(\gamma - 1) \quad (6.12)$$

The pressure of the shockfront p_f can approximately be expressed as $\rho_0(E/\rho_0)^{2/5}t^{-6/5} \approx E/R^3$

6.3.1 Dyer's Stagnation Model

The plume stagnation distance has been studied by Dyer and Sidhu [122] for ablation studies using pulsed lasers. They developed an empirical relation for the length of

the plume, L along the normal to the target when a pellet is irradiated with a KrF laser pulses of different intensities with low pressure oxygen gas as background. For a adiabatic expansion of the plasma with a conical expansion geometry the stagnation distance was reported to be

$$L = A[(\gamma - 1)E]^{1/3\gamma} P_o^{-1/3\gamma} V_i^{(\gamma-1)/3\gamma} \quad (6.13)$$

Here A is a geometric factor which depends on the expansion geometry of the plume. It is assumed here that at the end of the laser pulse the ablation products occupy a volume V_i and P is the ambient pressure, E is the absorbed laser energy. In the case of the study the plume has been assumed to expand as a cone with an angle θ which is capped with a hemispherical tip.

$$A = (1 + 1/\tan\theta)[3\tan\theta/(\pi + 2\pi\tan\theta)]^{1/3} \quad (6.14)$$

For a laser energy of 260 μJ and atmospheric pressure for an expansion cone angle of 25 degrees using Eq.6.14 and Eq.6.13 we obtain a stagnation distance of 2.06 mm.

6.3.2 Laser and Target Parameters

In this thesis the MEDUSA103 hydrocode was used to study the laser-plasma interaction dynamics in order to model the electron density, velocity, electron temperature, pressure as a function of space and time for our experimental parameters. All the physics of the laser-plasma coupling processes can be included using this model. The accuracy as discussed in Chapter 2 and in Appendix B depends on the mesh size and the convergence criterion. Theoretical calculations and simulation tools like MEDUSA 103 are important tools for gaining deeper insight into the plasma dynamics and their effect on the atomic physics that takes place during the irradiation of target materials with high intensity laser light. The simulations were performed for a laser with a wavelength of 266 nm and a gaussian pulse shape. The full width at half maximum FWHM of the laser pulse is 5 ns. The properties of the plasma expansion are analyzed using the computational hydrocode for a laser pulse intensity of $\approx 1.25 \times 10^{12} \text{ W/cm}^2$. The laser intensity is deposited on a microdroplet of water 40 μm in diameter and the plasma expands into a background gas which is taken as nitrogen in

our case which it extends up to 4 mm. The geometry of the simulation was set to be spherical giving to a total energy of 314 mJ. This energy is significantly higher than in our experiments but it was found that simulations at lower intensities led to numerical difficulties in the simulation. Even at this intensity the simulation could only be run until 200 ns before numerical difficulties emerged. The hydrocode Med103 is usually used for high density materials. In order to model our conditions we had to reduce the initial temperature settings to 50 K to avoid excessive contributions from the initial stored energy in the system.

6.4 Simulation Results

The propagation of the plasma and its hydrodynamic characteristics were studied. The density, electron and ion temperatures were plotted at various instances in time with respect to the laser pulse. the temporal profile of the laser pulse is shown in Fig.6.1. The overpressure at the liquid target surface leads to a shockwave propagating outwards into the undisturbed background gas and a shockwave inwards into the high density liquid.

The density profile is shown at various times in Fig.6.2. Due to the compression of the material we see the density jumps to 10 g/cc at 19 ns which is 1 ns after the peak of the laser pulse. As the material ionizes we see a density jump at the boundary of the liquid gas interface. At 30 ns (12 ns after the peak of the laser pulse) we see a shockwave traveling outwards through the system. The electron and ion temperature profiles are shown in Fig.6.3 and Fig.6.4 respectively. The peak temperature rises to 100 ev at the peak of the laser pulse and then falls to tens of ev later after the laser pulse duration is over. Fig.6.5 to Fig.6.7 show the density and electron temperature profiles at later times up to 200 ns. The propagation of the leading shockwave into the ambient gas slows down as expected. As for earlier times a number of shockwaves propagate back and forth in the plasma reflecting from the inner and outer boundaries. After 200 ns the low density and pressure values produce numerical instabilities in the present code and further simulation results could not be obtained.

The jump in ambient gas density observed at time 19 ns is 5 times while that predicted using the strong shockwave theory from Eq.6.12 is 6 times for a value of

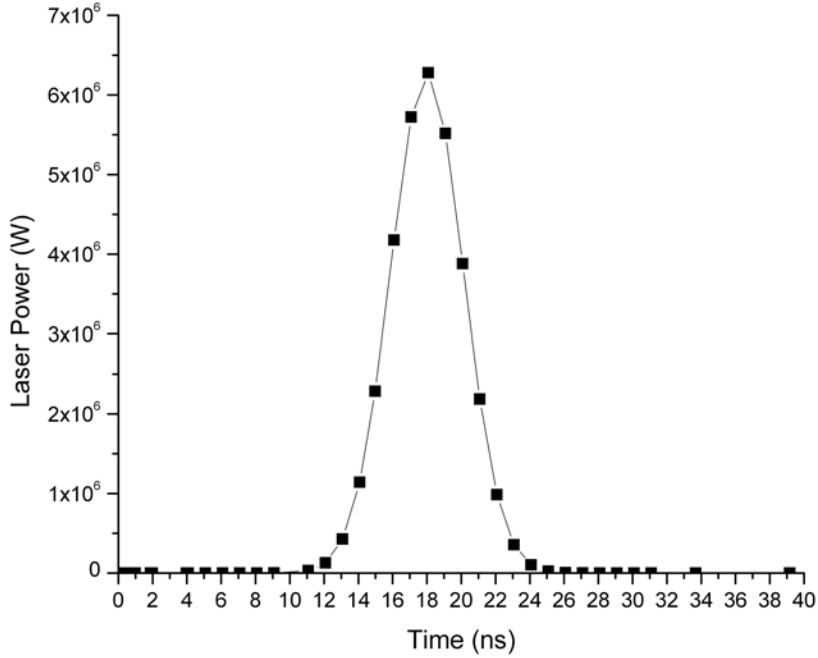


Figure 6.1: The temporal profile of the laser pulse as simulated by MED103 hydrocode.

$\gamma=1.2$. Using the theoretical formulas from the blast wave theory the radius of the shockfront can be plotted for the same energy absorbed as in the case used in Medusa, with respect to time as shown in Fig.6.8. We also plot the value of the position of peak density of the shock front from the Medusa simulation for times upto 200 ns on the same figure for comparison. The simulation contains the large mass of the 40 μm diameter water droplet which takes more energy to heat than the ambient gas alone. Thus it is expected that the simulated expansion will be slower than the ideal blast wave. Using Eq.6.7,Eq.6.8, Eq.6.9 from Mora's model as described earlier in this chapter we can calculate the electron temperature and pressure for a peak intensity of $1.25 \times 10^{12} \text{ W/cm}^2$ of laser intensity for a 5 ns laser pulse width we obtain a pressure of 0.4 Mbar and an electron temperature of 158.6 ev for a planar case. The temperature is in approximate agreement with the peak temperature of 120 ev observed in the simulation.

Fig.6.9 shows the experimentally determined LA-LIF spatial emission intensity as a function of the probe pulse delay and spatial position in the plasma for an ablation

energy of 260 μJ equivalent to an intensity of $6.6 \times 10^{10} \text{ W/cm}^2$ in a 10 μm diameter irradiation spot. In Fig.6.9 we can observe that the emission region has stagnated at a distance of approximately 1 mm by 500 ns with the leading edge of the plasma plume reaching 1mm by 200 ns. Using the ideal blast wave theory we can calculate the limiting distance of expansion where the strong shock is dissipated to be 0.65 mm. . Fig.6.10 shows the radius of the shockwave calculated for an absorbed energy of 260 μJ at different for times up to 2 μs . The predicted expansion appears slower than experimentally observed. However in reality the energy absorbed is channeled into gas expansion into a much smaller cone angle than the 4π sr rad assumed in the ideal blast wave model. Thus it is expected that the real expansion should be faster than the blast wave model estimate. For the same parameters if we apply Dyer's empirical formulas Eq.6.14 and Eq.6.13 for an energy of 260 μJ we obtain a stagnation distance of 2.06 mm. Thus the stagnation length is expected to be in the range of 0.65 to 2.06 mm which is consistent with the observed length of 1 mm. The peak temperature obtained with Medusa is in approximate agreement with Mora's scaling law predictions with Medusa values of 120 ev and Mora's self regulating model predicting an electron temperature of 158.6 ev. There is also an approximate agreement for up to 200 ns between the radii of the shock front predicted by the ideal blast wave theory and those predicted by Medusa. The discrepancy is because the Medusa simulations take the mass of the target into account so the radii predicted by Medusa are smaller than those from the ideal blast wave theory. The numerically predicted plasma parameters are in reasonable agreement with those predicted by analytical scaling models for a self regulating plasma model and the evolution of a strong blast wave into the ambient gas.

6.5 Conclusion

A preliminary investigation of the capabilities of the MEDUSA hydrocode for the one dimensional simulations of the plasma expansion and temperature predictions has been conducted. These results can be used in the future to theoretically determine the number of fluorescent photons emitted by the Pb atoms in the plume. However further work is needed to extend the hydrocode simulations to a longer time period and also

extend the simulations to a two dimensional geometry. Once the simulation code is extended then additional radiation physics routines can be included to calculate the predicted line emission for LIBS as well as LA-LIF.

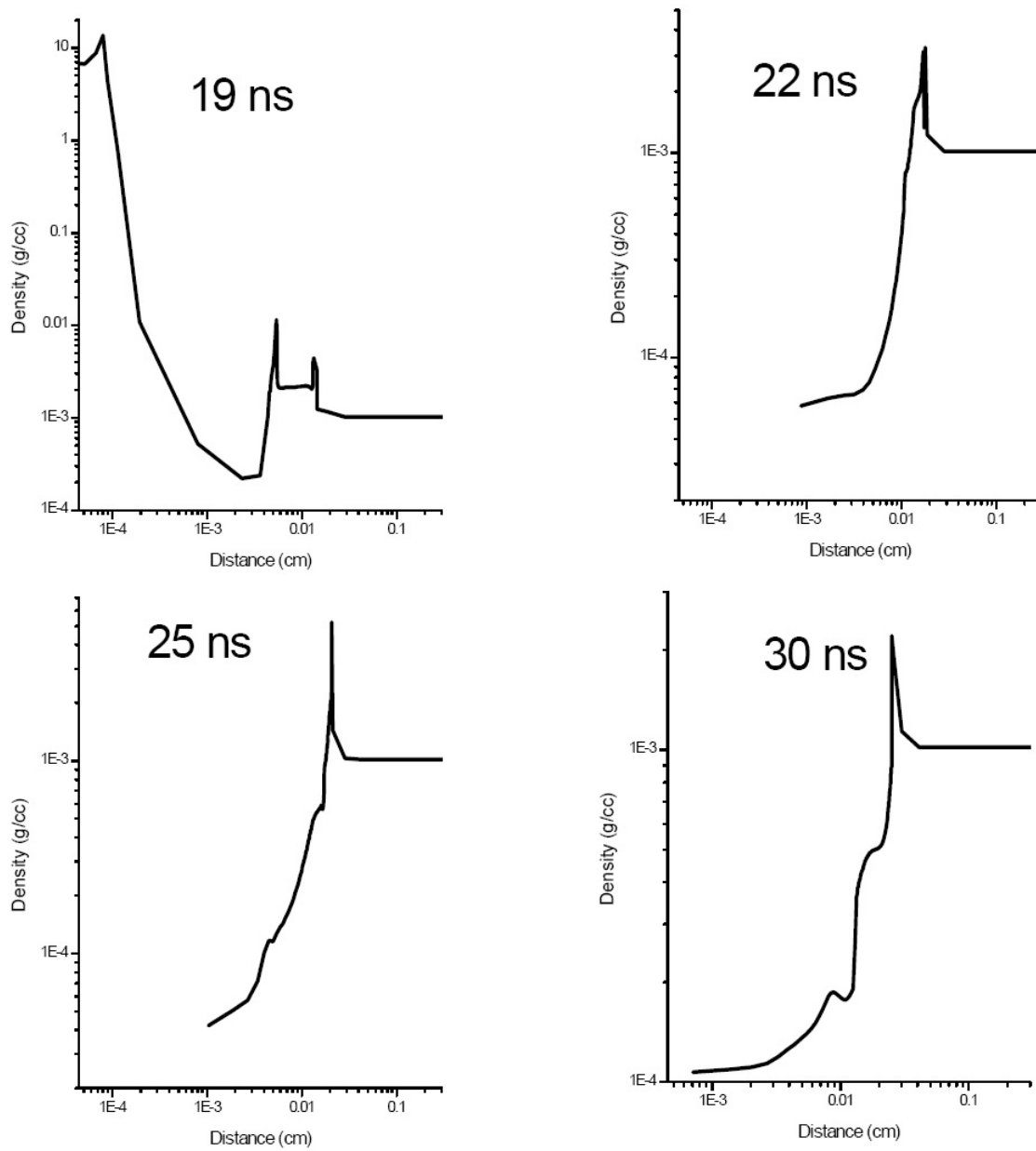


Figure 6.2: The spatial variation of the density profiles at different instances in time. The microdroplet is 40 μm in diameter.

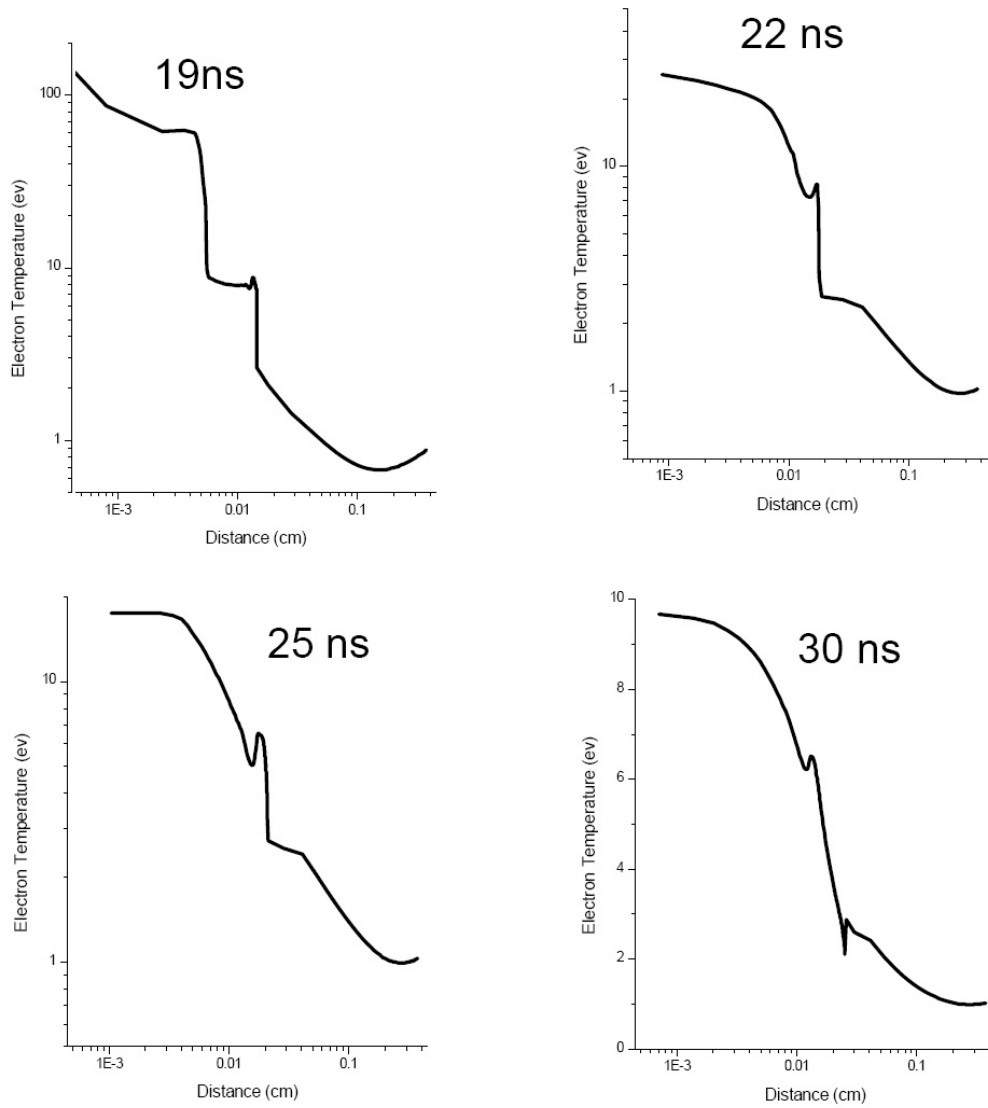


Figure 6.3: The spatial variation of the electron temperature profiles at different instances in time. The microdroplet is 40 μm in diameter.

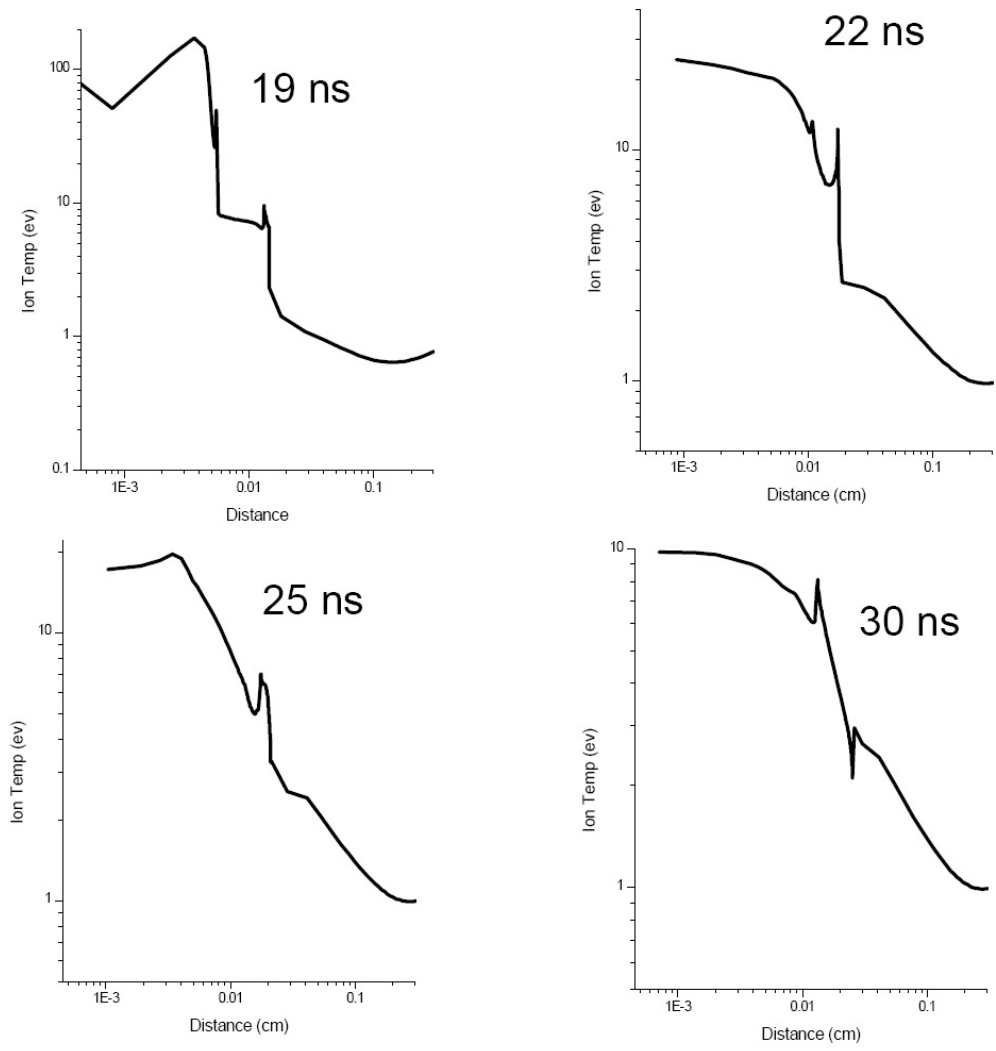


Figure 6.4: The spatial variation of the ion temperature profiles at different instances in time. The microdroplet is 40 μm in diameter.

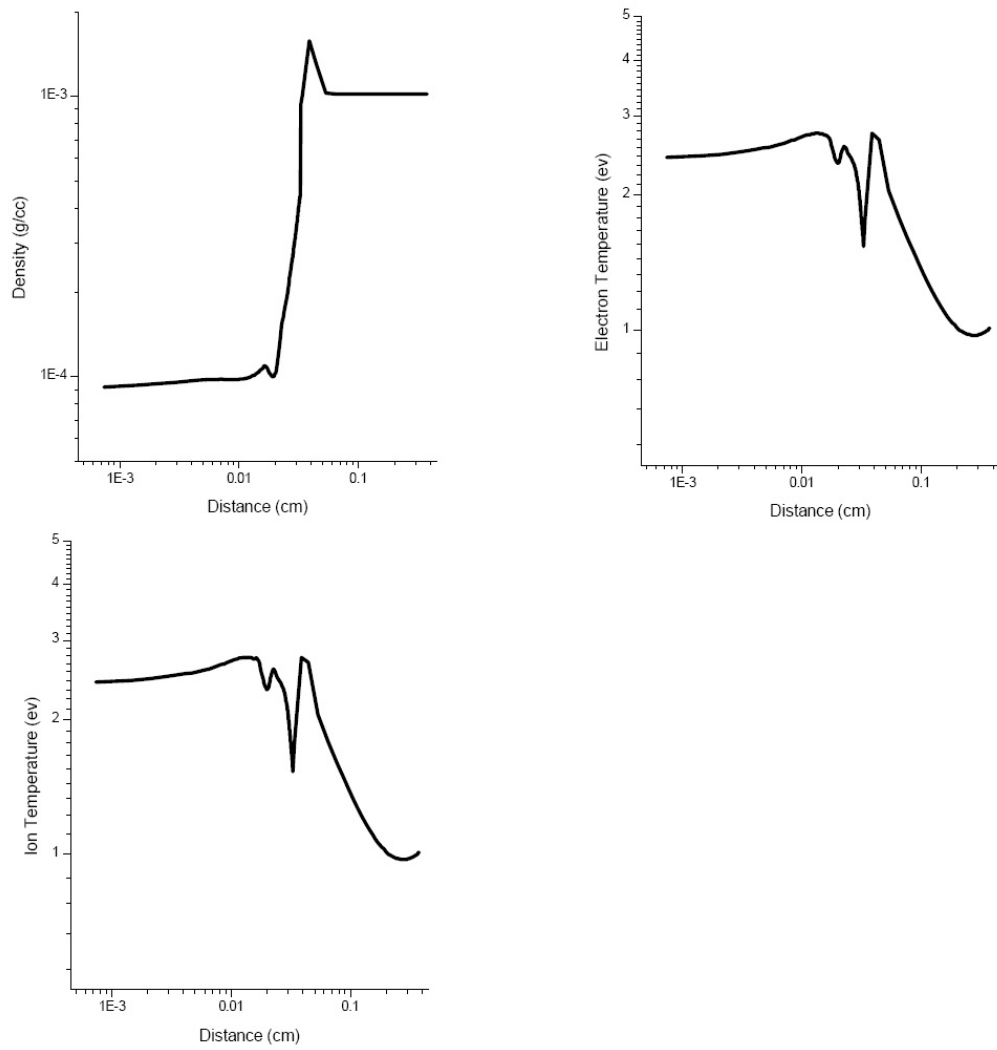


Figure 6.5: The spatial variation of the density, electron and ion temperature profiles 50 ns. The microdroplet is $40 \mu\text{m}$ in diameter.

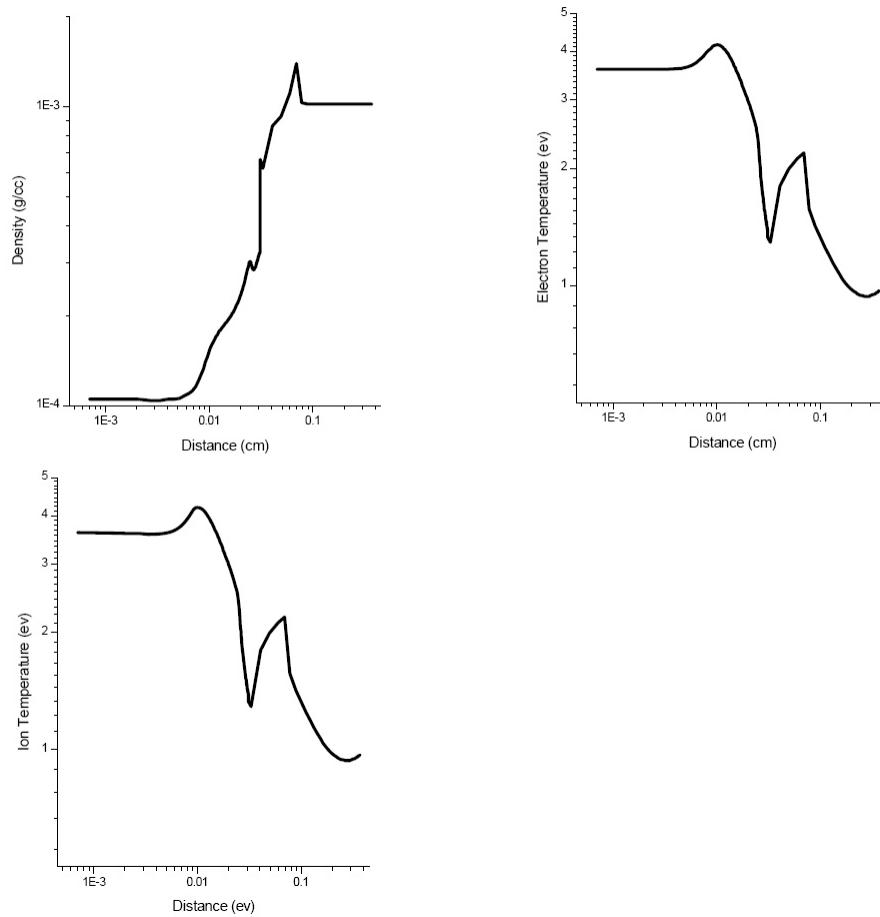


Figure 6.6: The spatial variation of the density, electron and ion temperature profiles at 100 ns. The microdroplet is $40 \mu\text{m}$ in diameter.

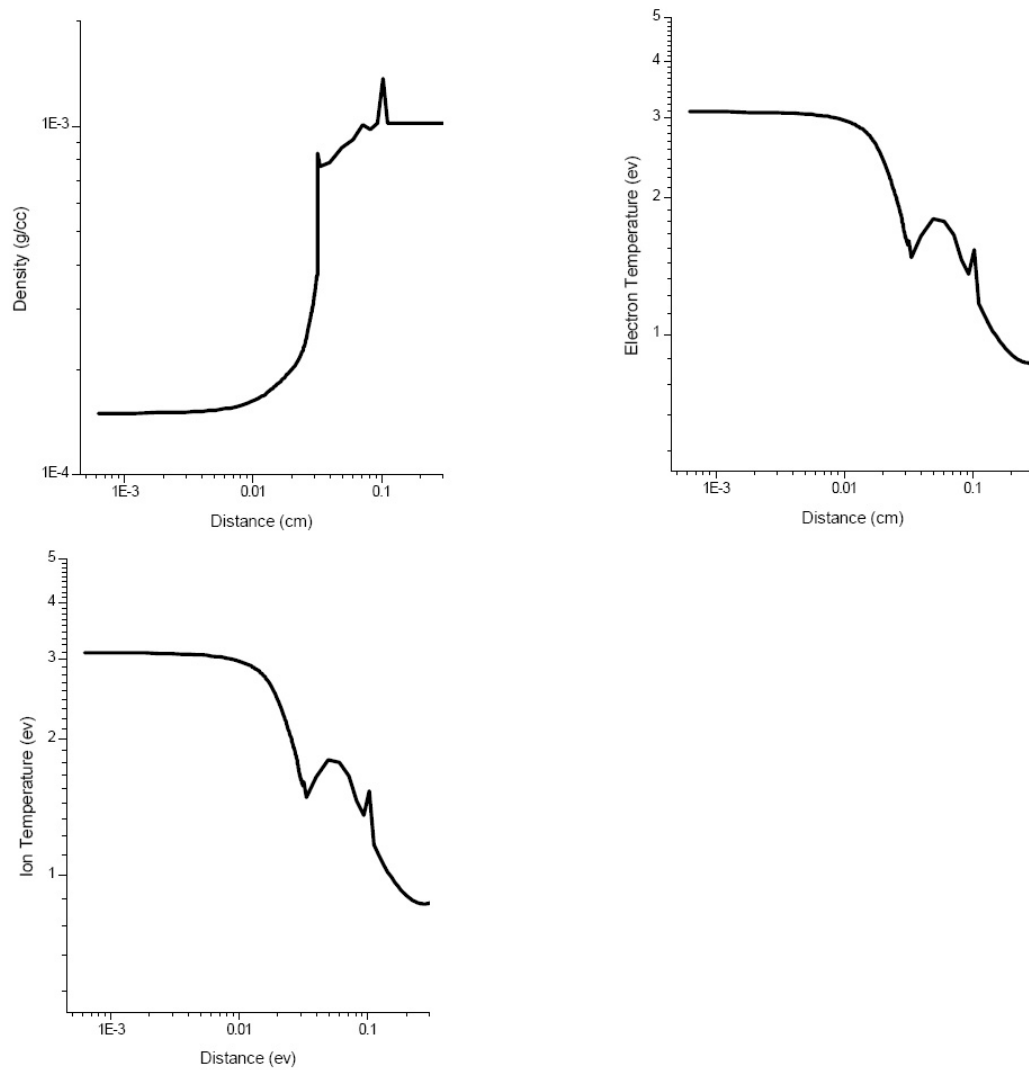


Figure 6.7: The spatial variation of the density, electron and ion temperature profiles at 200 ns. The microdroplet is 40 μm in diameter.

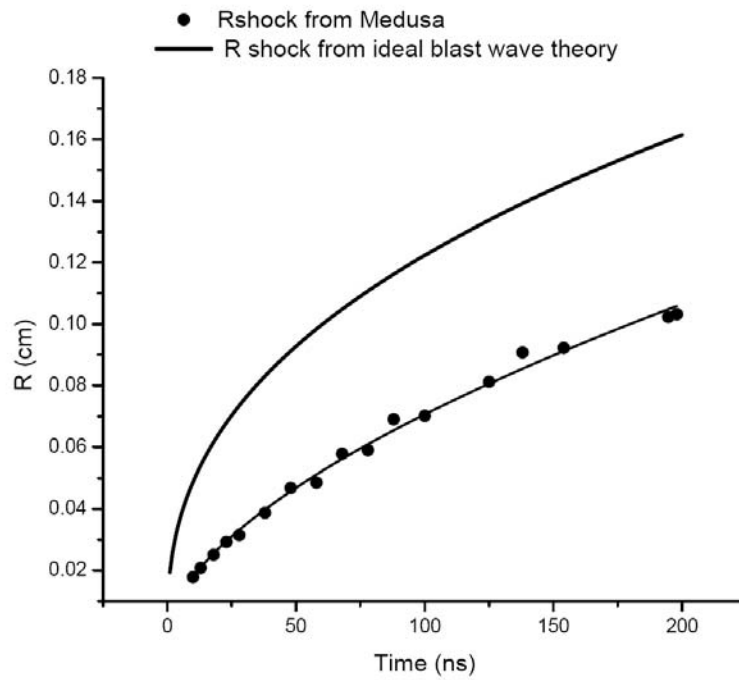


Figure 6.8: The radius of the shockwave as predicted by ideal blast wave theory (squares) into ambient 1 atm nitrogen and by the Medusa103 hydrocode (circles) for an absorbed energy of 300 mJ. The microdroplet is 40 μm in diameter.

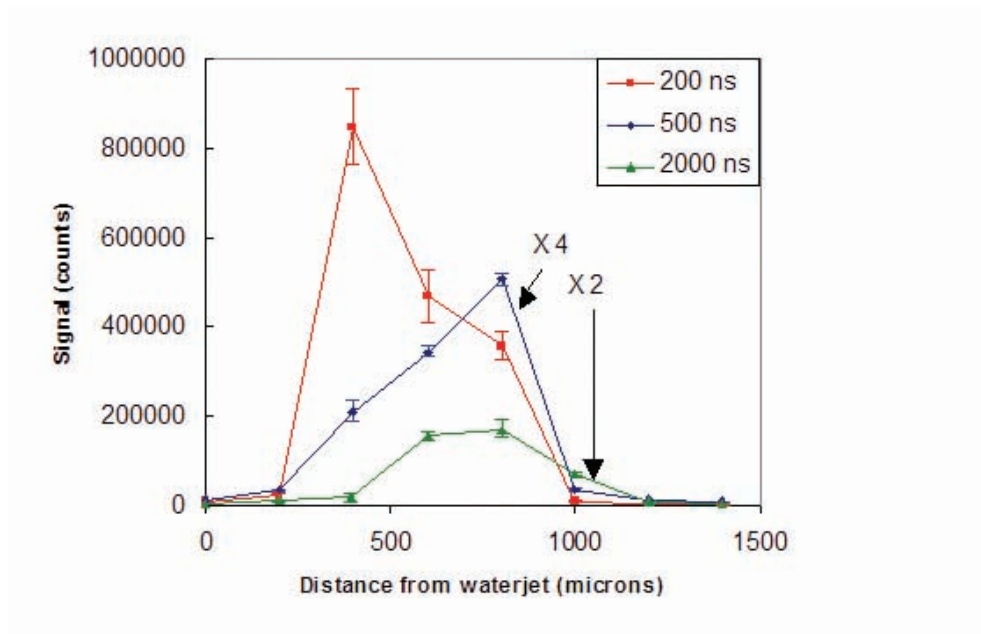


Figure 6.9: Emission signal versus the resonant excitation probe position as a function of distance from the waterjet surface. The probe beam (2nd beam) is 238 μm in diameter. Three different ΔT are compared: 200 ns, 500 ns, and 2000 ns.

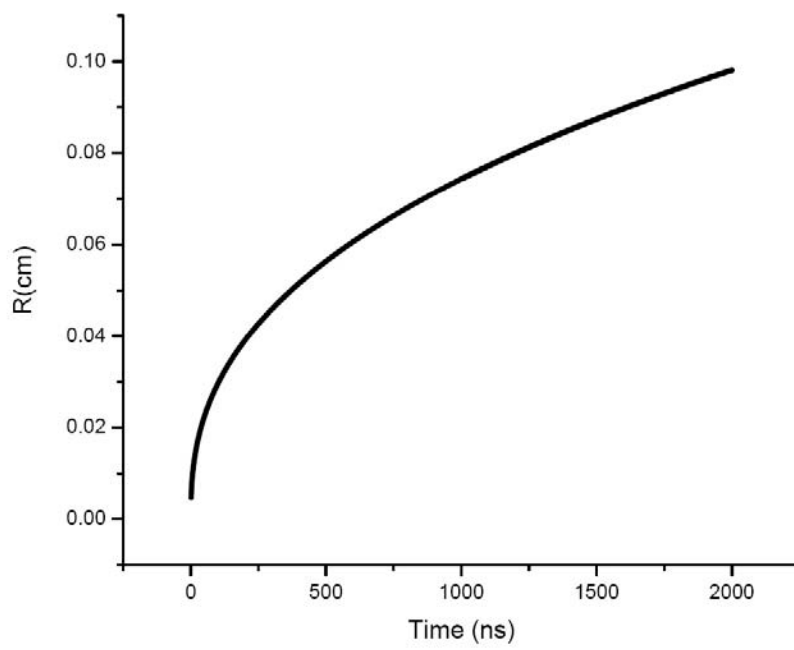


Figure 6.10: The radius of the shock wave as a function of time calculated using the ideal blast wave theory for an absorbed energy of $260 \mu\text{J}$.

Chapter 7

Preliminary studies on preconcentration for μ LIBS

7.1 Preconcentration for LIBS of Liquid Samples

μ LIBS has the potential to make LIBS a more widely acceptable analytical technique. The sensitivities reported by research groups [87, 166, 167] using μ LIBS have been shown to be comparable to those obtained using conventional LIBS. LIBS is probably the most versatile method of elemental analysis that is currently practiced but still its use is limited to the laboratory because the sensitivities for most elements are still in the ppm range. To improve the LOD's obtained using LIBS a sample preparation technique can be used to transform water samples into solid samples such as bulk ice [168] and calcium hydroxide [169], absorbed coatings to solid absorbers such as wood slices [170, 171], carbon substrates [172], filter paper [173, 174] or even by attracting ions onto membranes [175] and electrode plates [176]. For the method using freezing into ice, plasma quenching is still fast; for that using calcium hydroxide, the sample preparation is complicated; for that using filter paper, wrinkles form on the paper surface once it is dry, which makes the paper difficult to scan; the ion exchange membranes depend on the pH of the solution and the characteristics of different ions, which introduce new problems in chemical analysis. However, the wood slices and carbon substrates are both easy to handle and are capable of achieving a low LOD. It has been reported that, by use of wood substrates, different types of heavy metal, such as lead, chromium, copper, and cadmium in water can be detected to an LOD at the sub-ppm level using single laser pulses of 1064nm with an energy of 100mJ [170].

We have focused on investigating this technique with orders of magnitude lower laser pulse energies (≤ 5 mJ) , which is favorable for portable LIBS systems for in situ analysis. By use of aqueous samples that contain lead salt, the characteristic line emission signal intensity and signal-to-noise ratio SNR dependence on laser pulse energy, laser wavelength, and number of accumulated shots are studied. We determined that the same level of LOD can also be obtained with a low pulse energy, and the SNR can be further improved by accumulating emission from a greater number of shots. Some of our initial results for detecting Pb in water using the wood slice as a pre-concentrator are presented in the section below. One more pre-concentration technique we have considered that in the near future can be a very useful technique for ultrasensitive analysis of liquid samples for metal ion concentrations is electroplating preconcentration. We are currently developing a simple electroplating technique to transfer heavy metals in water to a thin film layer on the surface of an aluminum foil [2]. We can carry out LIBS on such samples to detect heavy metals in water using a diode pumped microchip laser system with pulse energy as low as $4\mu\text{J}$ at 1064nm. The initial results using this preconcentration technique are also given in the following sections.

7.2 Pb detection in water samples using LIBS of wood slice samples

In this section a summary of the major results of our experiments published in [171] are presented. These experiments were carried out in collaboration with another graduate student Zhijiang Chen. The experimental setup used to detect heavy metal in water by use of wood substrates as absorbers is shown in Fig.7.1. The laser used for LIBS was the same Nd:YAG laser used for the earlier experiments, in this experiment all three wavelengths : 1064nm fundamental output, 532nm second harmonic, and 266nm fourth harmonic output at a repetition rate of 10 Hz and pulse duration of 10 ns was used to induce the breakdown on wood surfaces. The laser pulses of the selected wavelength were focused by a $10 \times$ microscope objective onto the sample, and the diameter of the irradiation spot was approximately $11 \mu\text{m}$ for 266nm pulses, determined by a knife-edge measurement. The size of the ablated spots varied from

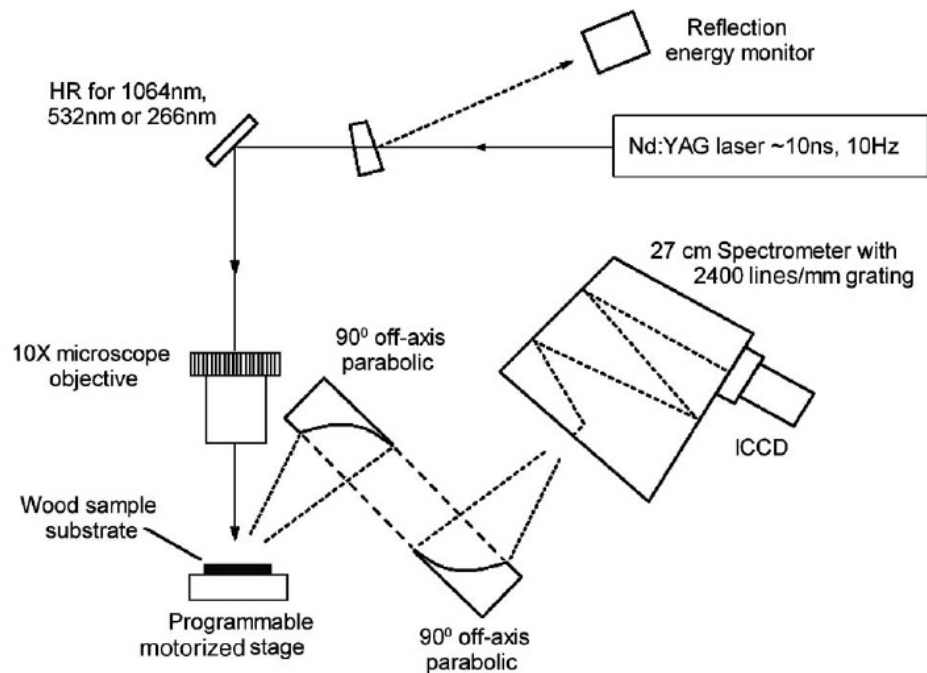


Figure 7.1: Illustration of our experimental setup. Only one of the three wavelengths (1064, 532, or 266 nm) was used at a time.

15 to 50 μm , which depend on the energy and wavelength of laser pulses. The wood substrate was mounted on a two-dimensional motorized stage (Physik Instrumente H218), the accuracy of which was better than 100 nm. The speed of the motorized stage was set to 1.2 mm/s, which corresponds to a distance of 120 μm between two consecutive spots to guarantee no overlapping spots. The 405.78nm line of lead was measured with integration of the emission in a 0.75nm bandwidth region around the peak. The background noise was measured in the same spectral region with the wood substrates that were dipped into distilled water.

7.2.1 Sample Preparation

The wood substrates were wood chips (wooden stirring sticks) approximately 18 cm long, 6.5 mm wide, and 1.5 mm thick. Each wood chip was cut into three parts, each approximately 6 cm long, two of which were used for the experiment. One part was dipped into an aqueous solution containing a known concentration of Pb, which was used to obtain the signal; the other was dipped into distilled water and was

used to obtain the background signal and noise. The sample signal was obtained by subtracting the emission signal of the first part from that of the second part. The lead solutions were prepared by dissolving lead nitrate in de-ionized water, and the solutions were homogenized by a magnetic stirrer before use. We prepared solutions with concentrations from 0.2 to 50 ppm. The wood substrate was dipped into the deionized water or the solution containing lead for 15 min. It was then taken out and put on a hot plate for approximately 10 minutes until the absorbed water evaporated before it was mounted on the motorized stage. Since the wood chips are easy to handle, the entire sample preparation can be completed within 30 min without any difficulty.

7.3 Results and Discussion

7.3.1 LIBS signal intensity as a function of Laser Pulse Energy

As a first step, we investigated the Pb emission intensity at 405.7 nm when the sample was ablated by laser pulses of different energies and wavelengths. Continuum emission was observed at the beginning of the breakdown process, and, thus, a suitable gate delay was required to optimize the sensitivity. To optimize the gate delay, the emission signal intensity was measured when the gate delay was varied from 500 ns to 3 μ s with the gate width of the detector set at 3 μ s. While the continuum emission decays rapidly, the detected line emission signal intensity decays more slowly as the gate delay increases as shown in Fig.7.2. Next we compared the Pb signal emission intensities for each wavelength as a function of pulse energies. For this experiment the gate delay was fixed at 500 ns and the gate width was fixed at 3 μ s. The energies were varied for all three wavelengths from 100 μ J to 4 mJ depending on the output pulse energy of the laser at the particular wavelength. The samples were wood substrates that were dipped into a lead solution with 50 ppm concentration, and the ICCD gain was set to 100, with 255 as the maximum gain setting, to avoid saturation of the detector for high pulse energy cases. Fig.7.3 shows the Pb signal emission intensity as a function of pulse energies for the three different wavelengths.

From the experimental measurements, we found that the LIBS emission threshold

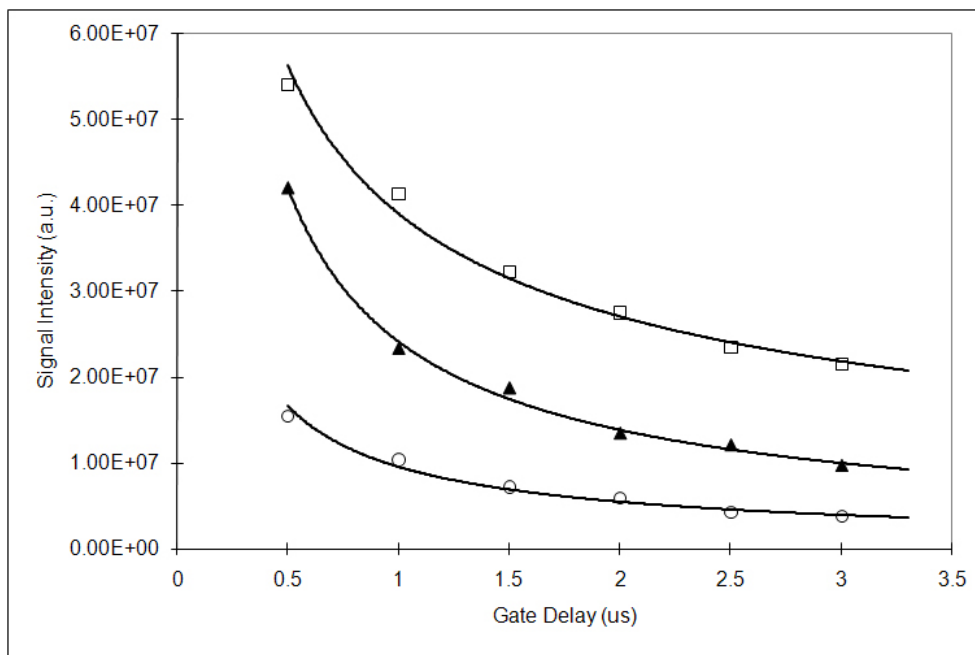


Figure 7.2: Detected Pb emission signal intensity at 405.7 nm as a function of detector gate delay. Three different wavelengths of laser pulses were used: 266 nm 1.8 mJ (open circles), 532 nm 3.46 mJ (filled triangles), 1064 nm 4 mJ (open squares). The detector gate delay was varied from 0.5 to 3 μ s, the gate width was set at 3 μ s, the detector gain setting was 100, the grating used was 2400 l/mm, centered at 405.7 nm and the slit width of the spectrometer was 100 μ m.

for 266, 532, and 1064nm wavelengths were 13 and 800 μ J and 1.9 mJ, respectively, as determined by the onset of observable line emission. For laser pulses with shorter wavelengths, the photon energy is higher and the breakdown threshold is lower. It is worth mentioning that, when we used 1064nm pulses, the probability of breakdown decreased with decreased pulse energy. Only approximately 60 % of the pulses induce a breakdown process when 2.2mJ is used, but, after breakdown occurs, a large amount of energy is absorbed into the sample. This breakdown mechanism leads to a high value of standard deviation of signal intensity when the breakdown threshold is approached and thus increases the measurement uncertainty. However, when 266 and 532nm pulses were used, the higher photon energy made the breakdown threshold more deterministic; thus the threshold was much sharper and the uncertainty did not come into play. The relative standard deviation RSD of signal intensity variation at different pulse energies for different wavelengths is shown in Fig.7.4. It can be seen that, for 1064nm pulses, when the pulse energy is above 3 mJ, the RSD is less

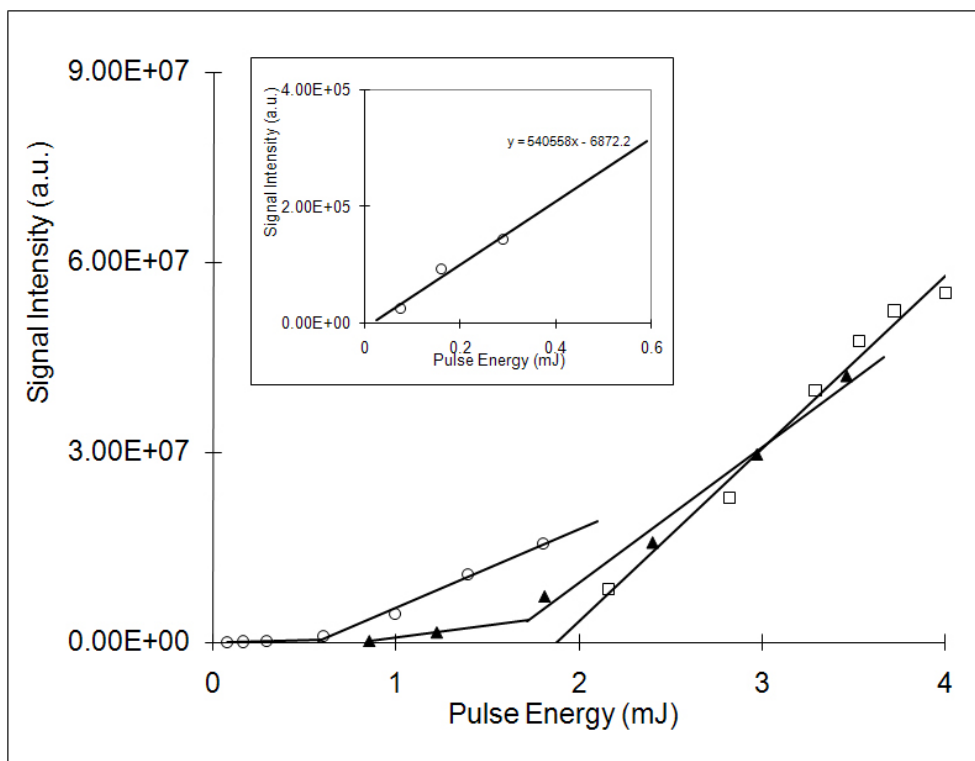


Figure 7.3: Detected Pb emission signal intensity at 405.7 nm as a function of detector gate delay. Three different wavelengths of laser pulses were used: 266 nm (open circles), 532 nm (filled triangles), 1064 nm (open squares). The detector gate delay was 500 ns, the gate width was set at 3 μ s, the detector gain setting was 100, the grating used was 2400 l/mm, centered at 405.7 nm and the slit width of the spectrometer was 100 μ m. The inset shows the magnification of the regime of 266 nm close to the ablation threshold.

than 4%. However, this value increases significantly when the pulse energy is below 3 mJ, where breakdown occasionally does not occur and the breakdown probability becomes a contributing factor.

In contrast, when 266nm pulses were applied, the RSD dropped to below 1% when the pulse energy was lower than 500 μ J. This is because the breakdown is more deterministic using ultraviolet laser light and, at a 500 ns gate delay with this low pulse energy, there was almost no continuum emission detected. At higher energy continuum emission, more variable plasma heating and substrate variations contribute to the increased variation of detected signals. At 532 nm, breakdown occurs for each laser shot but the stronger plasma created shows variations in emission from shot to shot because of the variable plasma heating and sample variations. Another

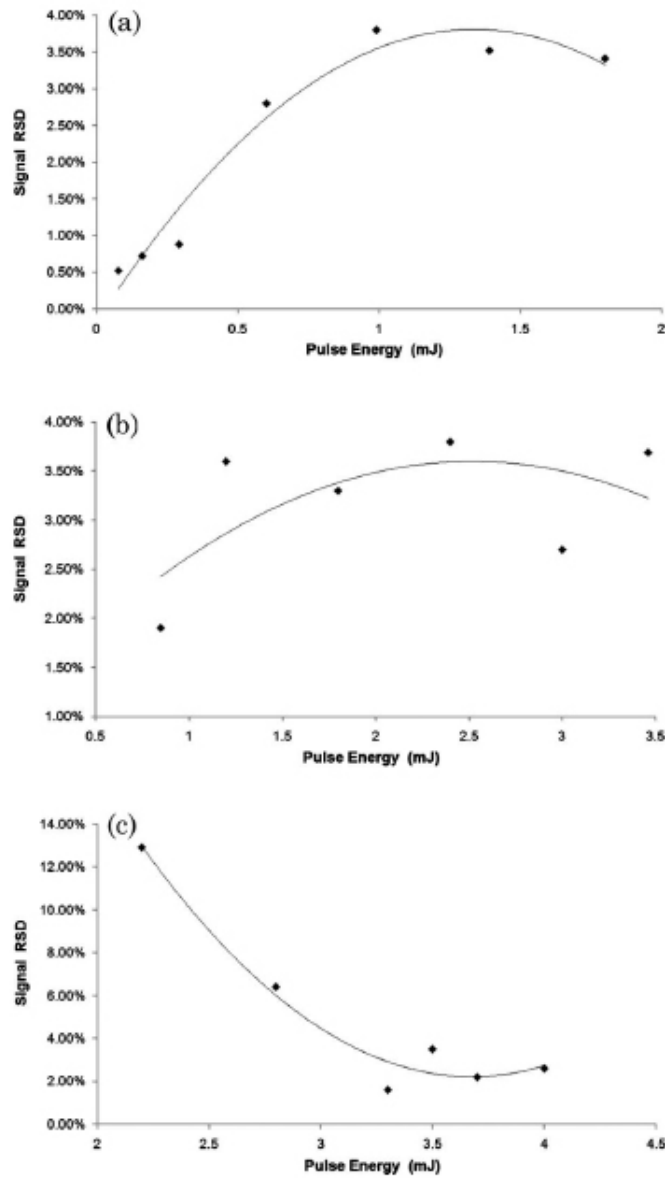


Figure 7.4: RSD of signal intensity versus pulse energies for three wavelengths: (a) 266 nm, (b) 532 nm, (c) 1064 nm. The RSD of each data point was measured based on five sets of signals with an accumulation of 100 shots in each set. The curves are visual fits to guide the eye.

important result is that two regimes of signal emission were found when the pulse energy was close to breakdown threshold with both 266 and 532nm pulses. This corresponds to a weak ablation regime near threshold that had been observed in previous experiments [141,177,178], where the scaling of plasma emission or ablation

with pulse energy is slower than in the high pulse energy regime. Although the emission intensity is low in this regime, the advantage is that the continuum emission is low and has a short lifetime, so that a nongated detector could be used in this regime.

7.3.2 SNR as a function of number of shots

The scaling of the SNR as a function of the number of shots, N , has a \sqrt{N} dependence. In order to study the SNR as a function of the number of shots accumulated by ablating the wood sample. The SNR variations for different numbers of accumulated shots from 10 to 1000 with different wavelengths are given in Fig.7.5. Solutions with 20 ppm concentration of Pb were used. For three different wavelengths, 266, 532, and 1064 nm, the pulse energies were 1.8, 3.5, and 4 mJ, respectively; the gate delays were set to 1.5, 1.8, and 2.3 μs . In all cases the gate width was fixed at 3 μs . In this experiment, a power law scaling of 0.57, 0.56, and 0.54 was observed for 266, 532, and 1064 nm, respectively as a function of the number of shots. For a statistically randomly fluctuating background noise a power law scaling of 0.5 is expected, and the current results are fairly close to the expected value. This scaling with number of shots is important when lasers with a higher repetition rate but low pulse energy are employed, such as self-Q-switched fiber lasers and microchip lasers.

7.3.3 Calibration Curves and L.O.D

To determine the LOD that can be achieved using this preconcentration technique, calibration curves versus sample concentration for laser pulses of three different wavelengths were plotted based on a 100 shot accumulation. The pulse energy, gate delay, and gate width were the same as in the experiment to determine the relation between SNR and number of shots. Aqueous solutions with different concentrations from 200 ppb to 50 ppm were used in this experiment. The calibration curves are shown in Fig.7.6, and the coefficient of linear regression R^2 values for all three are above 0.97. Ten, 100 shot accumulations were carried out on the same sample stick. The deviation of the calibration points from a perfectly linear variation with the concentration could be because of the slight differences in density, structure, and surface roughness from wood chip to wood chip, a subject that is under investigation in our lab. There

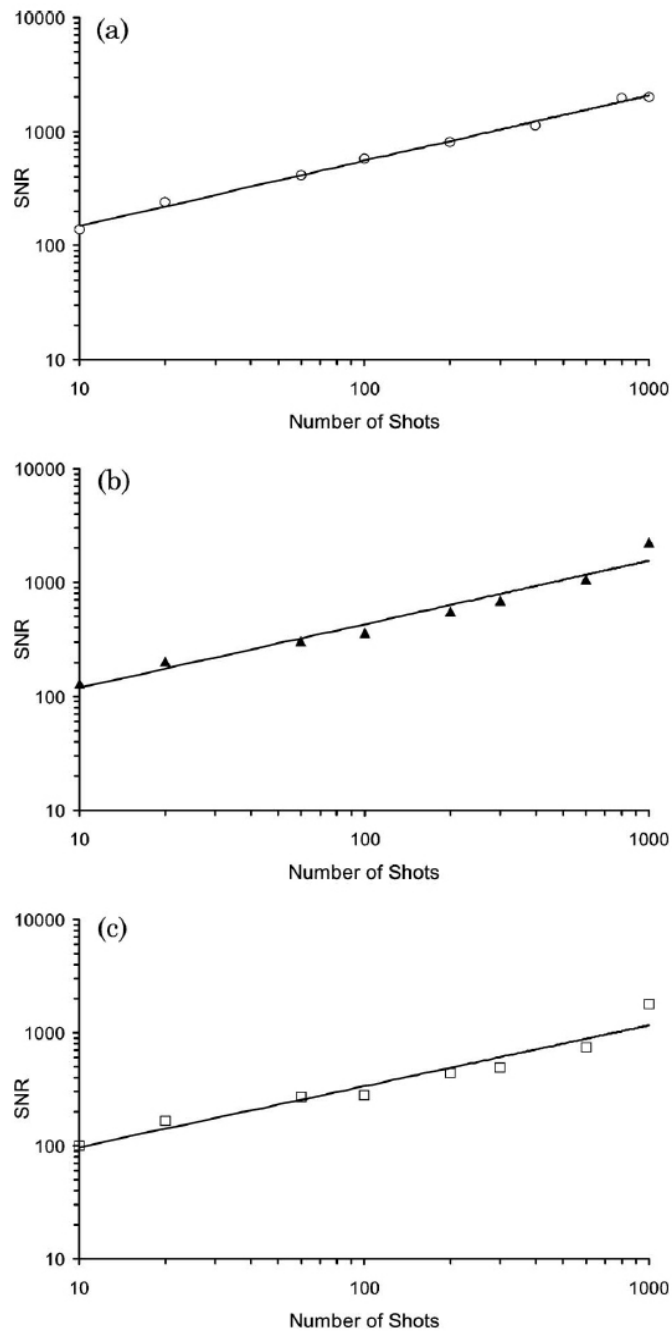


Figure 7.5: Relation between the SNR and the number of shots for pulses of three different wavelengths: (a) 266 nm, (b) 532 nm, (c) 1064nm for accumulations of 10 to 1000 shots on a wood slice sample preconcentrated for a 20 ppm concentration of Pb in water.

could also be some contribution from saturation of signal from optical opacity for the highest sample concentration with irradiation at 1064 nm. However, further studies

at higher concentrations would be required to establish whether this truly is the case. The LOD can be determined by the method described in Section 3.2.5 of chapter 3.

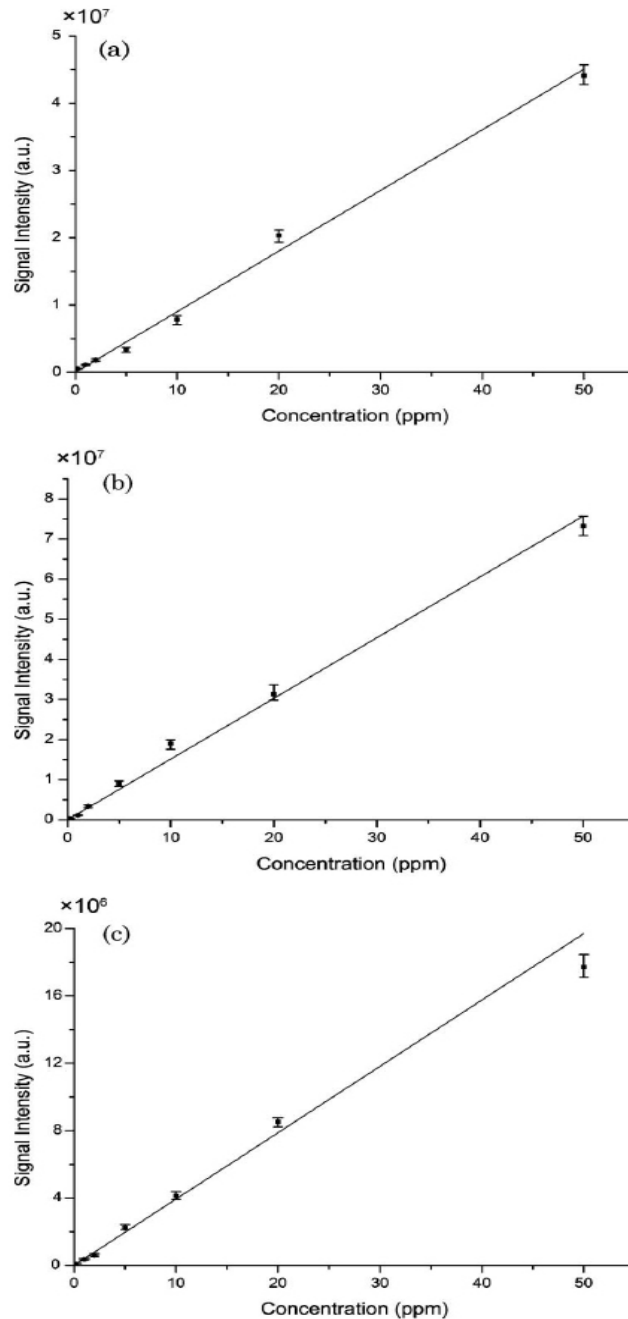


Figure 7.6: Calibration curves for pulses of three different wavelengths: (a) 266 nm, (b) 532 nm, (c) 1064 nm, with lead solutions with concentrations from 200 ppb to 50ppm. The error bars are based on the standard deviation of ten sets of measurements for 100 shots/measurement. Laser energies of 1.8, 3.5, and 4:0mJ were used for irradiation wavelengths of 266, 532, and 1064 nm, respectively.

For each concentration, pieces of a wood chips were used to measure the emission intensity, the average of the background signal, and standard deviation for a given sample set. The calculation of LOD is listed in Table.7.1.

Wavelength (nm)	266	532	1064
Energy (mJ)	1.8	3.5	4.0
Background, σ (counts)	43899	56548	63405
Slope (ppm^{-1})	895668	1507303	1455121
LOD(ppb)	147	113	131
Expected 1000 shot LOD (ppb)	45	36	41
1000 shot LOD of 20 ppm samples (ppb)	33	35	34

Table 7.1: Pulses of three different wavelengths using a 100 shot accumulation from the calibration curves with sample concentrations ranging from 200 ppb and 50 ppm. Scaling of the 100 shot data to the expected LOD for the 1000 shot accumulation and the 1000 shot LODs were determined from Fig.7.5.

The best LOD is obtained with the 532 nm laser pulse, the reason for this is that it has a relatively high pulse energy, which was close to that of 1064nm pulses and twice that of 266nm pulses, was employed, while its ablation threshold is much lower than that of 1064nm pulses. Fig.7.7 shows the emission signal from a wood substrate that was dipped into a 200 ppb solution of lead and ten measurements of background emission from another part of the same wood substrate that was dipped into de-ionized water and 532nm laser pulses were used. The range of fluctuations in the measurement, which was used to derive the background, can be observed. From the measurement of the sample that had been dipped into lead solution, the continuum emission (baseline) and line emission of other elements such as Fe (404.5 nm) are all in the background variation range. However the lead line is clearly much higher than the fluctuation level in its wavelength region. The background emission around the lead emission line (405.7 nm) also contains weak contributions from the manganese lines at 405.55 and 405.89 nm. By subtracting the mean value of background emission from the lead line emission signal, the residual signal yields a SNR of 6. If the wood chips have lower or no background emission around 405.8 nm, the background fluctuations could be further minimized, and the SNR could be further improved. If we consider the scaling effect of the number of shots accumulated, a better SNR and thus a lower LOD could be obtained. From the expected statistical power law, when 532nm

pulses are used, if we use the \sqrt{N} power law with a 1000 shot accumulation of the signal, the LOD can be improved to 36 ppb. This is comparable with the measured 10 to 1000 shot 3-sigma LOD's from the 20 ppm sample of lead shown in Fig.7.5 of 33, 35, and 44 ppb for wavelengths of 266, 532, and 1064 nm, respectively, for 1000 shots. This value is also comparable with the scaled 1000 shot LOD of 32 ppb that would be obtained from the measurement of the 200 ppb sample shown in Fig. 7.6. From the above results it is clear that wood slice sampling can be used as a easy and effective method for analysis of water samples. Although it can easily give sensitivities in the hundreds of ppb range we do sacrifice the speed of measurement as it adds the sample preparation step to the whole process. There is also the problem of background interference from trace metals in the wood sample as well. These issues need to be addressed with accurate background subtraction techniques or moving to purer porous substrates for sampling.

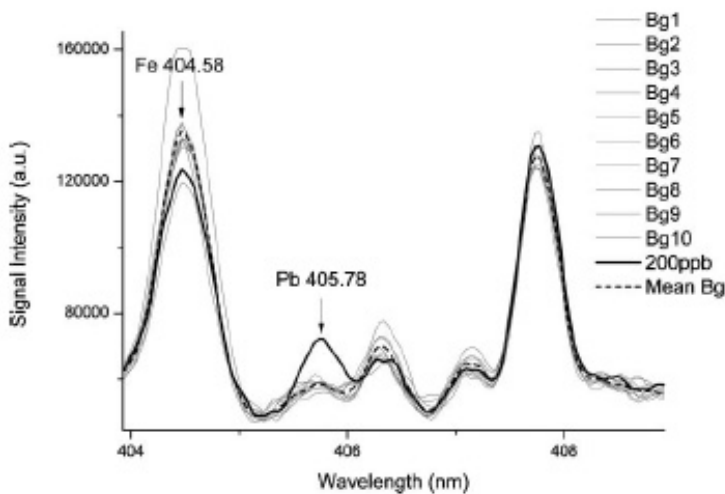


Figure 7.7: Measurement of the background emission of 10 different runs (grey line) and the emission from the wood substrate that has been dipped in 200 ppb lead solution (solid back line) by 100 shots accumulation with 532 nm pulses at an average energy of 3.5 mJ. The average of background signal is given by the black dashed line. An SNR of 6 is obtained

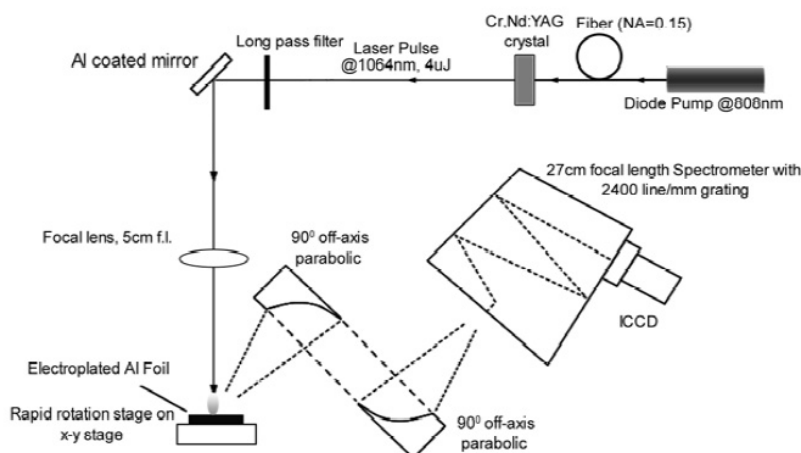


Figure 7.8: Experimental setup of the μ LIBS setup using electrolytic preconcentration. The microchip laser at 1064nm , 4 μ J is shown in the diagram.

7.4 Preconcentration using Electroplating

A second technique was also explored for sample preconcentration. In this technique an electrical deposition method was used to realize sample pre-concentration and eliminate the interference of the water matrix. This technique coupled with LIBS was first used by Z.Chen et al. [176] in 2008. They demonstrated sub-ppb LOD's for elements such as Cr,Cu,Mn,Zn,Cr and Pb. The trace metal atoms were electrically deposited on the surface of a high purity aluminium plate for a few minutes and quantitatively analyzed by LIBS. For ultrahigh purity testing this technique can be very effective as the preconcentration is very sensitive to the dissolved ions in the water and also for a given plating voltage we can in principle find out the deposited mass of the material and thus determine absolute sensitivities. To potentially make this a portable technique we have used this pre-concentration technique along with a microchip laser for the analysis of Pb in water. We have used this simple electroplating technique to transfer the heavy metals in water to a thin film layer on the surface of an aluminum foil , and then we can carry out μ LIBS to detect heavy metals in water using a diode pumped microchip laser system with pulse energy as low as 4 μ J 1064nm. In our experiment, lead (Pb) was used as an example of heavy metal. The experimental setup is illustrated at Fig.7.8. The output of an 808nm CW diode pump laser (Apollo Instrument, Inc. Model F20-108-1) is coupled into a fiber (diameter=100

μm , $\text{NA}=0.15$) to pump a codoped Cr, Nd:YAG crystal of 1.1mm thickness (Nd is 1% in weight, and Cr^{4+} is about $2 \times 10^{17} \text{cm}^{-3}$) which is coated with 1064nm high reflectivity coating on at one side (90%), and a dichroic coating on the other side with high reflectivity at 1064nm (99.8%) and high transmission at 808nm (95%) to form a cavity. The output pulse energy of the crystal was $4\mu\text{J}$, and the repetition rate could be varied from 1.7 kHz to over 10 kHz with increasing pump energy. A long pass filter blocked the 808nm light and let the 1064nm pulses pass through. The laser pulses were focused onto the plated Al foil by a lens of 5mm focal length. Heavy metal is collected onto the aluminum foil by electroplating from 100 ml lead solution in a small beaker at 15 volts in 30 minutes. The laser ablated spot was approximately 12 μm in diameter. For a high repetition rate of 8 kHz, stage running at 9.6cm/s is required to give a fresh ablation spot for each shot. A computer hard drive motor running at 5400 rpm was used to mount the sample, and the motor was mounted on a linear motion stage (Physik Instrument H218) running at 90 μm per second, so the track of the laser scanning was a spiral path. The optical emission from the sample was collected into a spectrometer couple to an ICCD (Andor iStar ICCD DH720-25). The acquisition time of the ICCD was set at 20ms, each spectra was taken with an accumulation of 1000 acquisitions, which required 20 seconds total accumulation time.

Fig.7.9 shows the signal and the background obtained using the setup with electroplating pre-concentration for a sample containing 30 ppb Pb dissolved in water. The concentration of the sample was verified using ICP-MS. The SNR of this spectrum was 14 which corresponds to a 3σ LOD of 6.4 ppb which is lower than the EPA required LOD of 15 ppb. This initial result indicates this technique has great potential to increase the sensitivities of μLIBS and make it a more widely acceptable technique. However during these measurements we observed that if the solution contained high concentrations of the heavy metals, more gas bubbles would be generated. The gas bubbles attached onto the surface of the aluminium plate and thus interfered of the deposition of metals. A similar observation was reported by [176]. One way to overcome this problem can be by diluting the samples to lower concentrations in case measurements on higher concentration samples are required.

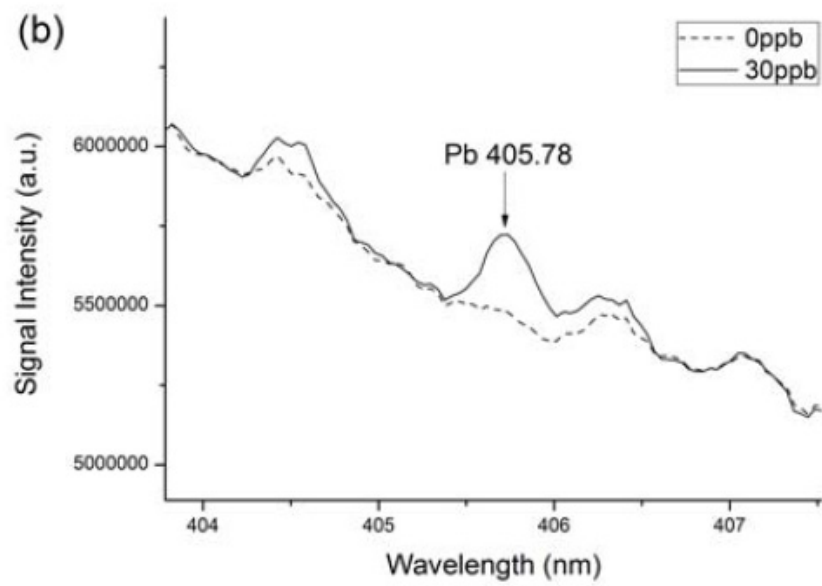


Figure 7.9: Pb spectra for two different concentrations, 0 ppb and 30 ppb. The spectra were obtained using the microchip LIBS setup described earlier. The concentrations were verified using ICPMS.

Chapter 8

Conclusions

8.1 Summary of Thesis Results

Conventionally in LIBS the laser pulse energies are in the range of 10 - 100 mJ which require large laser systems and thus limit the portability of this technique. Generally the sensitivities for most elements are in the ppm range. This has tended to limit LIBS systems to research purposes in a lab environment. To address the portability issue this thesis has focused on using LIBS with laser pulse energies in the hundreds of microjoule range while keeping the sensitivities competitive with conventional LIBS systems. Using very low energy, 250 μ J pulses in our experiments we have the potential of obtaining high spatial resolution in the case of solid sample analysis and also minimize the laser system requirements. Under such conditions it was very important to maximize the signal detected to give the best possible result. One technique that was developed was to improve the signal to noise ratios by the use of dual pulse excitation with the first pulse creating a vapor plume and the second pulse tuned to a resonant absorption line of the species of interest which we termed as LA-LIF. We investigated the performance of dual-pulse LIBS at low pulse energies for the detection of Pb as a contaminant in water. In our case, the second pulse was resonant, tuned to an atomic transition for the element of interest. This technique allows reasonable performance compared to high energy single-pulse LIBS, but at a much reduced total energy expenditure. This allowed LOD's well below the several ppm range which typically cannot be obtained with low energy single pulse probing of the systems. A systematic study of the detector conditions was made for the system for the detection of Pb. Scaling laws for the LOD in terms of the pump and

probe energies were measured and also the effect of detector gain, the gate delay and the gate width were studied. The LOD scaling for our system was measured for scaling the LOD for the number of shots integrated by the detector. Three different detectors : ICCD, PMT and a MPPC were tested to study the scaling of the LOD's based on the solid angle of collection and the quantum efficiency of the detector. The best LOD was obtained using the PMT with a similar performance from the MPPC under similar conditions. The MPPC though can give better sensitivities with better design of light collection optics due to its high quantum efficiency at the Pb emission wavelength. Using this technique this thesis has provided a detailed background study for a potential online drinking water monitoring system for Pb or a online industrial effluent monitoring system. The feasibility of using μ LIBS on ultralow volumes of analyte was also studied and the detection of Na was demonstrated in picolitres of analyte solution using a stand-alone microdroplet dispenser. A study of the μ LIBS emission versus microdroplet size (analyte volume), detector gate width, detector gate delay was carried out for Na as a analyte in monodispersed microdroplets in air. A rapid thermal heater based microfluidic μ LIBS system was developed for portable detection and analysis. The channel and the orifice for microdroplet extrusion were patterned on a PDMS layer using laser micromachining. Nucleation studies for bubble formation in the microfluidic chip were conducted. The Detection of Na as low as 360 femtograms was demonstrated for 100 shots integration using this device. To study the laser interaction with the water targets the MEDUSA one dimensional hydrocode was used. The various parameters in the code were studied to adapt it to use for our particular case. The propagation of the shockwave and plume dynamics were studied using this software. The expansion of the plume was studied and compared to experimentally measured values. Two preconcentration techniques were studied, one which used a wood-chip as a substrate to absorb the analyte liquid and wick the salt on the surface for analysis and the other was using an electroplating technique to plate the analyte metal as a thin film on a substrate metal used as a cathode. Our preliminary studies indicate that LOD's in the hundreds of ppb range can be obtained with 100 shot accumulation using the wood chip substrates as a preconcentration method with energies in the 1-3 mJ range.

8.2 Future Work: Outlook

8.2.1 μ LIBS Capabilities

The LOD capabilities of μ LIBS are comparable with those of traditional LIBS. With high repetition rate fiber or microchip lasers we can integrate a large number of shots and improve the sensitivity of μ LIBS using filtered PMT's or solid state multipixel photon counter MPPC to obtain sub-ppm levels of sensitivities for most elements. The advantage of using fiber or microchip lasers for sampling and MPPC's or PMT's as detectors can be that the system can have high sensitivities and also be portable which is still a major challenge for conventional LIBS systems. Another aspect and capability which is a niche for μ LIBS is the capability of assembling the systems with microfluidic chips. In this thesis ultralow volumes of analyte were sampled either from a standalone piezoelectric microdroplet dispenser or a microfluidic chip based on a rapid thermal heater as an actuator. An LOD of 7 ppm for the piezoelectric dispenser with 130 μ J of energy for an accumulation of 100 shots for Na was demonstrated and an LOD of 6 ppm for 100 shots was obtained using a microfluidic chip. The LOD's in these two cases can be improved by moving to higher collection apertures as opposed to the f/4 system used for these studies along with filtered MPPC's which can be easily coupled with microfluidic systems. To address the low sensitivity issue of LIBS or μ LIBS compared to other more mature techniques around a study of two preconcentration techniques were made for testing liquid samples. Although this technique gives sensitivities in the hundreds of ppb range we do sacrifice the speed of measurement as it adds the sample preparation step to the whole process. There is also the problem of background interference from trace metals in the wood sample as well. These issues need to be addressed with more work and investigations using purer porous substrates for sampling. This technique can be a useful tabletop technique and it is expected that a portable sample preparation and measurement system can be developed for quick chemical analysis of water samples. The electroplating method for preconcentration was also studied using a microchip laser and a LOD of 6.4 ppb for Pb in water was obtained for an accumulation of 200,000 shots. The initial data suggests that by using this technique highly sensitive measurements can be obtained at much lower ablation energies ($\approx 4 \mu$ J in our case). It is expected that

a small portable sample preparation system can be developed allowing for use of the technique in the field. Further work should be carried out on both techniques to characterize other heavy metal contaminants in water.

8.2.2 LA-LIF Capabilities

Laser Ablation - Laser Induced Fluorescence for the detection of Pb in water as a technique for online drinking water monitoring was studied. An LOD of ≈ 300 ppb was obtained for an accumulation of 100 shots with the ablation laser pulse energy of 250 μJ and an excitation laser pulse energy of 8 μJ . An improvement of the LOD was obtained by using a larger collection aperture and filtered detectors such as PMT's and MPPC's. Using the filtered PMT as the detector the 100 shot LOD for Pb was improved to 70 ppb this light collection could be further improved using the higher quantum efficiency APD detector to yield even better sensitivities. By using high repetition rate fiber lasers for the ablation laser and custom made fiber lasers with fiber bragg gratings for excitation along with the MPPC as a detector it is expected that a real-time Pb monitor for drinking water can be built. LA-LIF capabilities for probing ultralow volume samples in the form of microdroplets was also studied. The complexity of such a system is somewhat greater as the microdroplet and the ablation laser have to be coordinated in space and time and the excitation laser has to excite the microplasma at a specific time to obtain the best sensitivities. An LOD of 7 ppm for the detection of Pb for 100 shots accumulation was demonstrated using the LA-LIF technique on a 18 μm diameter microdroplet using 130 μJ as the ablation laser. It is expected that the sensitivities can be improved further using higher optical collection apertures rather than the f/4 system used in our current setup.

8.3 LIBS Modelling and Physics

To improve our understanding of LIBS and the physical processes involved further work needs to be done in modelling the various phenomena. the hydrodynamic simulation code MEDUSA gives a reasonable idea about the shockwave dynamics and the electron temperature for the LIBS plasma for certain cases. Further work needs to be done to incorporate line emission models and also models for double pulse LIBS

into such simulations. These results can be compared with other hydrocodes such as MULTI and MULTI 2D which also include radiative energy transport effects.

8.4 Conclusion

This thesis has helped improve the sensitivities of the μ LIBS technique by coupling it with fluorescence spectroscopy and developing scaling laws in terms of the use of energy for both the pump and probe laser systems. Also different detector geometries have been examined towards the eventual use of this system, as a in-situ water monitor. As one scales to microjoule levels of excitation energy efficient and sensitive detection system are required. These results have paved the way to the development of portable μ LIBS or LA-LIF systems using fiber or microchip laser along with filtered PMT's or Avalanche Photodiodes in the near future.

Appendix A

LA-LIF simulation using Mathcad

In this section screen captures of a mathcad simulation for the fluorescence signal for our LA-LIF experiment for Pb. Initially an LTE plasma is considered and the ionization fraction for Pb is calculated for a temperature range of 0 to 1 eV and a certain electron density.

Once we calculate the ionization fraction for Pb for a range of temperatures and for different number densities we can calculate the number of atoms that were created by the ablation process and then the ionization fraction will give us the number of atoms available for excitation by the probe laser beam.

$k := 1.38065812 \cdot 10^{-23}$	J/K Boltzmann constant
$h := 6.626075540 \cdot 10^{-34}$	m ² kg / s Plank constant
$c := 3 \cdot 10^8$	m/s Speed of light
$e_0 := 1.602 \cdot 10^{-19}$	coulombs Electron charge
$\epsilon_0 := 8.854 \cdot 10^{-12}$	A.s/(v*m) Permittivity constant
$m_e := 9.109 \cdot 10^{-31}$	Kg Electron mass
$m_{pb} := 3.43952 \cdot 10^{-25}$	Kg Pb mass
$G_{pb} := 8.9 \cdot 10^7$	S ⁻¹ Einstein transition constant (405.8nm)
$\lambda_{405} := 405.7807 \cdot 10^{-9}$	m 405.8 nm spectral line
$N_0 := 1$	
$n := 1 \cdot 10^{20}, 2 \cdot 10^{20} .. 10^{21}$	m ⁻³

Figure A.1: Definitions of physical constants in mathcad.

Partition function of PbI (Atomic energy level table)

A := 1 .. 22

$j_A :=$	$u_A :=$
0	0
1	7819.263
2	10650.327
2	21457.798
0	29466.830
0	34959.908
0	35287.224
1	42918.643
1	44400.890
0	44674.986
1	44809.364
2	45443.171
2	46328.667
3	46060.836
2	46068.438
1	48188.630
2	49439.616
1	48686.934
1	52101.660
2	52312.325
3	52311.315
2	52499.639
1	

$$Z_{\text{PbI}}(T) := \sum_{i=1}^{22} (2 \cdot j_i + 1) \cdot e^{-h \frac{c \cdot u_i \cdot 100}{T \cdot e_0}}$$

Figure A.2: Partition function matrix for PbI from NIST tables.

Partition function of PbII (atomic energy level table)

B := 23 .. 40

$j_B :=$	$u_B :=$
0.5	0
1.5	14081.074
0.5	57910.480
1.5	66124.530
2.5	73905.708
0.5	59448.560
2.5	68964.310
1.5	69739.603
0.5	74458.990
1.5	77272.570
2.5	88972.160
0.5	89180.180
3.5	92515.240
2.5	92530.66
1.5	94284.580
2.5	95304.250
4.5	108969.580
3.5	108969.670

$$\max(u) = 1.09 \cdot 10^5$$

$$Z_{\text{PbII}}(T) := \sum_{i=23}^{40} (2 \cdot j_i + 1) \cdot e^{-h \frac{c \cdot u_i \cdot 100}{T \cdot e_0}}$$

Figure A.3: Partition function matrix for PbII from NIST atomic energy level tables.

Saha Equation for Pb

$$F_{\text{Pb}}(T, n) := (2 \cdot \pi \cdot m_e \cdot e_0)^{\frac{3}{2}} \cdot h^{-3} \cdot \left(T^{\frac{3}{2}} \cdot e^{-\frac{7.4167}{T}} \cdot n^{-1} \right)$$

Debye Radius Calculation

$$D(T, n) := \left(\frac{\epsilon_0 \cdot T}{2 \cdot e_0 \cdot n} \right)^{\frac{1}{2}}$$

I := 1 .. 2

t_I :=

1
2

f_I :=

7.41663
15.03248

f = ionization potential of PbI(z=1) and PbII(z=2) respectively.

Figure A.4: Calculation of the Debye length and Saha equation for Pb.

Reduction of ionization Energy of PbI

$$\Delta_{\text{PbI}}(T, n) := \frac{t_1 \cdot e_0}{4 \cdot \pi \cdot \epsilon_0 \cdot D(T, n)}$$

Reduction of ionization energy of PbII

$$\Delta_{\text{PbII}}(T, n) := \frac{t_2 \cdot e_0}{4 \cdot \pi \cdot \epsilon_0 \cdot D(T, n)}$$

Figure A.5: Reduction in ionization energies.

Hydrogenic Approximation of Partition function of PbI

$$Y_{\text{PbI}}(T, n) := \frac{2}{3} \cdot \left[(t_1)^2 \cdot \frac{13.61}{\Delta_{\text{PbI}}(T, n)} \right]^{\frac{3}{2}} \cdot e^{-\left(\frac{f_1 - \Delta_{\text{PbI}}(T, n)}{T} \right)}$$

$$z_{\text{PbI}}(T, n) := Z_{\text{PbI}}(T) + Y_{\text{PbI}}(T, n)$$

Figure A.6: Approximation for partition function of PbI.

Hydrogenic Approximation of Partition function of PbII

$$Y_{\text{PbII}}(T, n) := \frac{2}{3} \cdot \left[(t_2)^2 \cdot \frac{13.61}{\Delta_{\text{PbII}}(T, n)} \right]^{\frac{3}{2}} \cdot e^{-\left(\frac{t_2 - \Delta_{\text{PbII}}(T, n)}{T} \right)}$$

$$z_{\text{PbII}}(T, n) := Z_{\text{PbII}}(T) + Y_{\text{PbII}}(T, n)$$

Figure A.7: Approximation for partition function of PbII.

Population of PbI Gr. state over Population of PbI

i.e. Probability that PbI at Gr.state

$$g_{\text{GrPbI}} := 1$$

$$E_{\text{GrPbI}} := 0$$

$$P_{\text{GrPbI}}(T, n) := \frac{g_{\text{GrPbI}} e^{-\frac{E_{\text{GrPbI}}}{T}}}{z_{\text{PbI}}(T, n)}$$

Population of PbII Gr. state over Population of PbII

$$g_{\text{GrPbII}} := 1$$

i.e. Probability that PbII at Gr.state

$$E_{\text{GrPbII}} := 0$$

$$P_{\text{GrPbII}}(T, n) := \frac{g_{\text{GrPbII}} e^{-\frac{E_{\text{GrPbII}}}{T}}}{z_{\text{PbII}}(T, n)}$$

Figure A.8: Probability that PbI or PbII are in ground state.

****Degree of Ionization α ****

$$\alpha_{\text{Pb}}(T, n) := \frac{1}{1 + \frac{1}{F_{\text{Pb}}(T, n)} \frac{P_{\text{GrPbI}}(T, n)}{P_{\text{GrPbII}}(T, n)}}$$

Population of PbI

$$\text{Pop}_{\text{PbI}}(T, n) := (1 - \alpha_{\text{Pb}}(T, n)) \cdot N_0$$

****Population of PbI Gr.state and PbI excited state****

$$\text{Pop}_{\text{GrPbI}}(T, n) := \text{Pop}_{\text{PbI}}(T, n) \cdot P_{\text{GrPbI}}(T, n)$$

Figure A.9: Calculation of degree of ionization.

****Population of PbI Gr.state at different T****

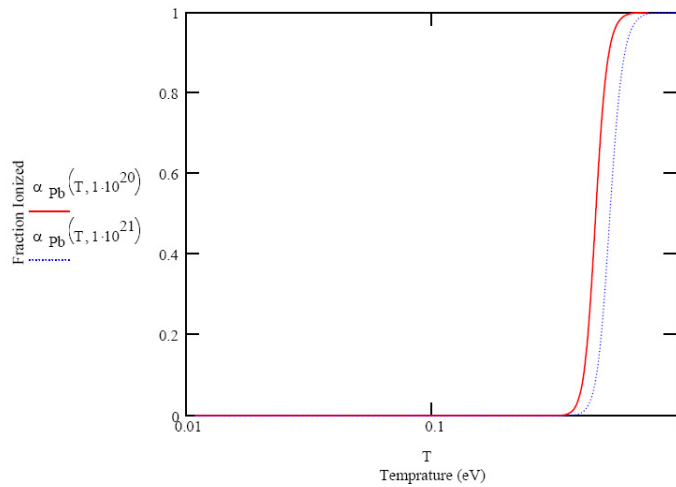


Figure A.10: Plot of degree of ionization for PbI from 0-1 eV at number densities of 10^{20} and 10^{21} m^{-3}

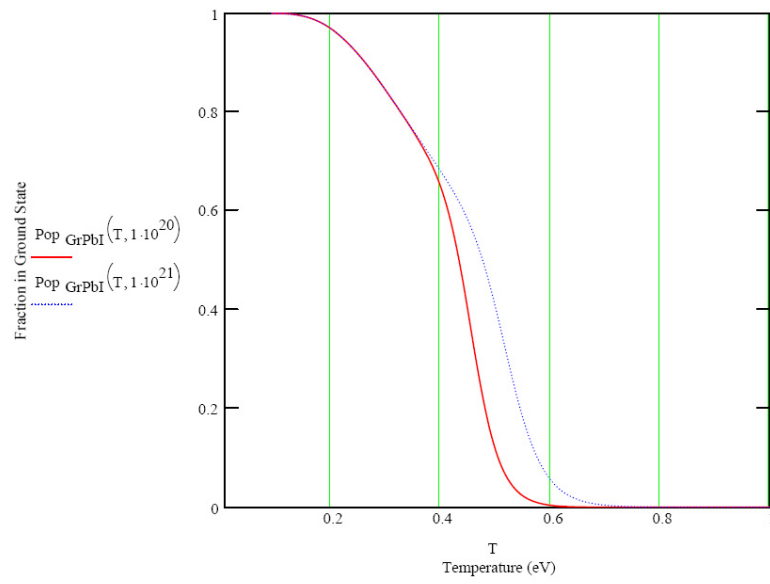


Figure A.11: Plot of fractional ground state population for PbI from 0-1 eV at number densities of 10^{20} and 10^{21} m^{-3}

Pbconc := 1 ppm concentration of Pb
 Pbmass := 207.19 amu
 Beam := $5 \cdot 10^{-6}$ m beam radius
 D := $1 \cdot 10^{-6}$ Estimated ablation depth of 1 μm
 t := $5 \cdot 10^{-9}$ Pulse width = 5 ns
 A21 := $5.8 \cdot 10^7$ s⁻¹
 g1 := 1
 A23 := $8.9 \cdot 10^7$ s⁻¹
 g2 := 3 g3 := 5
 c := $3 \cdot 10^8$ m/s

$$h := \frac{6.63}{2\pi} \cdot 10^{-34}$$
 h = $1.055197 \cdot 10^{-34}$ J.s
 $\lambda_{21} := 283.306 \cdot 10^{-9}$ m
 $\lambda_{23} := 405.783 \cdot 10^{-9}$ m
 E2p := $10 \cdot 10^{-6}$ microjoules

Figure A.12: Initial conditions and physical constants definitions. The energy of the probe laser beam was 10 μJ .

$$\text{BeamArea} := 0.5 \cdot 0.216 \cdot 10^{-3} \cdot 0.5 \cdot 0.334 \cdot 10^{-3} \cdot \pi$$

$$\text{BeamArea} = 5.666177 \cdot 10^{-8} \quad \text{m}^2$$

$$\text{linewidth} := 1.5 \cdot 10^{11} \quad \text{in s}^{-1}$$

Concentration of Pb Atom per m-3:

$$\text{Nconc} := \frac{\text{Pbconc} \cdot 6.02 \cdot 10^{23}}{\text{Pbmass}}$$

$$\text{Nconc} = 2.905546 \cdot 10^{21} \quad \text{in m}^{-3}$$

Volume of water being ablated:

$$V := \pi \cdot \text{Beam}^2 \cdot D$$

$$V = 7.853982 \cdot 10^{-17} \quad \text{in m}^{-3}$$

Number of atom available:

$$N := V \cdot \text{Nconc}$$

$$N = 2.28201 \cdot 10^5 \quad \text{in m}^{-3}$$

Figure A.13: Calculating the number of Pb atoms available based on the ablation laser spot size and concentration of the solution.

Obtained from Pb_faction.mcd, number of Pb at ground state at $T \sim 0.2\text{eV}$, $n=10\text{e}21$:

$$N_{\text{ground}} := 0.97 \cdot N$$

$$N_{\text{ground}} = 2.21355 \cdot 10^5 \quad \text{in } \text{m}^{-3}$$

$$\omega_{21} := 2 \cdot \pi \cdot \frac{c}{\lambda_{21}}$$

$$B_{21} := A_{21} \cdot \pi^2 \cdot \frac{c^3}{h \cdot \omega_{21}^3} \quad B_{21} = 4.973038 \cdot 10^{20} \quad \text{in } \text{m}^3 \text{J}^{-1} \text{Hzs}^{-1}$$

$$B_{12} := B_{21} \cdot \frac{g_2}{g_1} \quad B_{12} = 1.491911 \cdot 10^{21} \quad \text{in } \text{m}^3 \text{J}^{-1} \text{Hzs}^{-1}$$

$$g := 1 + \left(\frac{g_1}{g_2} \right)$$

$$\rho := \frac{E_{2p}}{\text{linewidth} \cdot \text{BeamArea}}$$

$$\rho = 1.176572 \cdot 10^{-9} \quad \text{in } \text{m}^{-3} \text{JHzs}^{-1}$$

Figure A.14: Calculating the number of atoms available in the ground state based on the ionization fraction and fractional ground state population from above.

$$N_{\text{emit}} := N_{\text{ground}} \cdot \rho \cdot B_{12} \cdot A_{23} \cdot \frac{t}{(A_{21} + A_{23} + \rho \cdot B_{12} \cdot g)}$$

$$N_{\text{emit}} = 7.387259 \cdot 10^4 \quad \text{photons}$$

Figure A.15: Calculation of the number of emitted photons.

$$\begin{aligned}
N_{\text{collect}} &:= N_{\text{emit}} \cdot 0.0475 && \text{photons collected by an f/4 system} \\
N_{\text{collect}} &= 3.508948 \cdot 10^3 && \text{photons} \\
N_{\text{collectK}} &:= 1000 \cdot N_{\text{collect}} && \text{photons for 1000 shots} \\
\text{for 1000} &&& \\
N_{\text{collectK}} &= 3.508948 \cdot 10^6 &&
\end{aligned}$$

Figure A.16: Calculation of the number of photons collected by the f/4 imaging system.

**Mirror reflectivity in the spectrograph = 0.9 @400nm;
Quantum efficiency of CCD = 15% @400nm;
At Gain=250, count per photon = 120;
Slit width =300um, ~15% of the plasma emission entering the slit (a wider slit will increase the noise and lead to poorer SNR);
Grating reflectivity at 400=0.6
1000 shot accumulation;
Spatial Scan suggested that we re-excited onl;y 1/3 of the plasma thus only 1/3 of Nground were used:**

$$\begin{aligned}
&&& \text{number of counts for the CCD} \\
\text{Count} &:= N_{\text{collect}} \cdot 0.9^3 \cdot 120 \cdot 0.15 \cdot 0.60 \cdot 1000 \cdot 0.15 \cdot 0.3 \\
\text{Count} &= 1.243199 \cdot 10^6
\end{aligned}$$

Figure A.17: Calculation of the number of counts observed using an f/4 collection system with an intensified CCD.

Appendix B

Medusa hydrocode parameter settings

The MEDUSA 103 hydrocode [179] is written and developed in Fortran. To run MEDUSA103 an input data file is needed. An example of a data file is given in Fig.B.1 this specifies an Al target irradiated by a 100 fs laser pulse. The meaning of the input parameters important to our particular experiment are explained in detail in this section as taken from reference [175].

XAMDAL is the laser wavelength (m).

NGEOM, this variable sets the geometry of the problem; 1 is planar, 2 is cylindrical and 3 is spherical.

GAUSS, this sets the laser pulse, GAUSS=1.0 sets a gaussian pulse given by $P(t) = P_{MAX} \times \exp(-((t-PMULT*PLENTH)/PLENTH)^2)$ GAUSS = -1.0 gives a triangular pulse given by $P(t) = P_{MAX} \times (TOFF-t)/(TOFF-PLENTH)$ for $0 \leq t \leq TOFF$ TON (R), defines the turn-on time of the laser (in s). This is normally set to 0.0.

TOFF (R), defines the turn-off time of the laser (in s). This is normally set to a large value such as 1.0. This does not mean that the simulation time is 1 second as other control factors will stop the run well before this.

PMAX is the peak power of the laser in units of $W m^{-2}$ for planar targets, $W m^{-1} rad^{-1}$ for cylindrical targets and $W ster^{-1}$ for spherical targets.

PLENTH , case of one Gaussian pulse, this is the time from the peak of the laser pulse to the value at which the laser is only e^{-1} of its maximum value (in s). This may be approximated to $PLENTH=0.6 \times FWHM$.

PMULT, in the case of a gaussian pulse, this is the number of PLENTH times at

```

AL100FS: A1 TARGET PLANAR GEOM 0.268UM
2 PULSES: 100 FS, 1.E17 W/CM^2 ON TOP OF 1NS 1.E11 W/CM2 ASE
DEGENERATE GAS, E BALANCE, ANABS=0.25
*****
$NEWRUN
XAMDA1=0.268E-6, TON=0., TOFF=1.,
GAUSS=1.0, ANPULS=2.0,
PMAx=1.E15, PLENTH=0.6E-09, PMULT=1.666666667,
XASER1(38)=1.E21, XASER1(42)=60E-15, XASER1(46)=16666.66667,
NGEOM=1, PIQ(55)=2.0,
MESH= 65, RINI=4.5E-6, RHOGAS=2700., RF1=0.9999,
XZ=13., XMASS=27., FNE=1.0,
ZGLAS= 20., DRGLAS=-.5000E-06, ROGLAS=2700., RF2=0.8711,
XZ2=13.0, XMASS2=27.00, FNE2=1.0,
ZPLAS=00., DRPLAS=0.00E-06, ROPLAS=2700., RF3=0.9999,
XZ1=13., XMASS1=27., HYDROG=0.0,
TEINI=11604.5000, PIQ(86)=11604.50, PIQ(89)=11604.50,
TIINI=11604.500, PIQ(87)=11604.50, PIQ(90)=11604.50,
PIQ(92)=1., PIQ(93)=1., PIQ(94)=1.,
PIQ(85)=1., PIQ(88)=1., PIQ(91)=1.,
NLHF=T, NLTNL=T, NLOMT3(10)=T, FLIMIT=10.,
NLBRMS=T,
NLCRI1=T, ANABS=0.25, FHOT=0.0, FTHOT=-1.0, RHOT=1.0,
NLPFE=F, STATE=0.0, SAHA=2.0,
ICXRL=0, ISTANCE=1,
IFRSTA=1, ILOSTA=0, IHISTA=3,
IDRFLG=0, DRMUL=1.0,
NLRES=F,
NPRNT=100., TSTOP=1.1E-9, NRUN=999999, DTMAX=1.E-11,
NP3=1, NLEMP=F,
$END

```

Figure B.1: An example of a MEDUSA 103 input file is shown. Details of the logical switches and the variables are explained in the text.

which the run starts before the peak of the pulse. The larger the number the slower the turn-on of the laser, this helps avoid shocks at the beginning. However, the larger the number, the longer the code will have to run and the more CPU time it will use. ANPULS (R) D=0.0 When using Gaussian pulses (GAUSS=1.), this sets the number of Gaussian pulses. Set this to 1.0, 2.0, 3.0, 4.0 or 5.0. Each of the additional 4 pulses is determined by specifying the peak power, width and time of peak, in a way similar to specifying (PMAx, PLENTH and PMULT) for the first pulse.

MESH (I) D= 40 : This controls the total number of cells used in all three layers. This number cannot exceed 200. The larger this number is, the more accurately the layer will be modelled but the longer the code will take to run. A typical value for

MESH is 60.

ZGLAS (R) D=0.0 This controls the number of cells in the second layer or glass layer.

ZPLAS (R) D=0.0 This controls the number of cells in the third layer or plastic layer.

RINI (R) D=4.8E-4 This sets the thickness of the inner layer or gas fill(m). Each cell will then be RINI/(MESH-ZGLAS-ZPLAS) thick, e. g. if RINI=10.0 E-6 and MESH= 60, ZGLAS= 20 and ZPLAS = 20.0 then the cell thickness in the inner layer will be 0.5E-6 meters.

DRGLAS (R) D=0.0 This sets the thickness of the second layer(m). The thickness of the individual zones is then DRGLAS/ZGLAS.

DRPLAS (R) D=0.0 This sets the thickness of the third layer(m). The thickness of the individual zones is then DRPLAS/ZPLAS.

RHOGAS (R) D=124.0 This is the density of the inner layer or gas fill. Units are kg/m³.

ROGLAS (R) D=0.0 This is the density of the middle layer or glass shell. Units are kg/m³.

ROPLAS (R) D=0.0 This is the density of the outer layer or plastic shell units are g/cc

XZ (R) D=1.0 This is the atomic number of the inner layer or gas fill material.

XZ2 (R) D=14.0 This is the atomic number of the middle layer or glass shell material.

XZ1 (R) D=6.0 This is the atomic number of the outer layer or plastic shell material.

XMASS (R) D=1. This is the atomic mass number of the inner layer or gas fill material.

XMASS2 (R) D=28.0855 This is the atomic mass number of the middle layer or glass shell material.

XMASS1 (R) D=12.011 This is the atomic mass number of the outer layer or plastic shell material.

FNE (R) D=0.0 This is the fraction of the material specified by XZ, XMASS and RHOGAS that is used in the inner layer. The remaining fraction is divided equally between deuterium and tritium. This is really only useful for modelling ICF targets, to fill the inner layer entirely with a specified material set FNE=1.0.

FNE2 (R) D=0.0 This is the fraction of the material specified by XZ2, XMASS2 and ROGLAS that is used in the middle layer. The remaining fraction is set to be silicon.

RF1 (R) D=0.99999 This controls the arithmetic gridding in the gas fill or inner layer.

RF2 (R) D=0.99999 This controls the arithmetic gridding in the glass or middle layer.

RF3 (R) D=0.99999 This controls the arithmetic gridding in the plastic or outer layer.

TEINI (R) D=1.0E3 This is the initial temperature of the electrons, normally set to a value of, typically, 300 K. It is possible to specify a different initial electron temperatures for each layer if desired.

TIINI (R) D=1.0E3 This is the initial temperature of the ions, normally set to the same value as TEINI, typically, 300 K. It is now possible to specify a different initial ion temperature in each layer if desired.

ANABS (R) D=0.0 This is the amount of laser energy that having reached critical density (i. e. having been to some extent depleted by inverse bremsstrahlung absorption) is deposited in the plasma by resonance absorption.

FHOT (R) D=0.0 This is the fraction of laser energy absorbed by resonance absorption that gets converted to hot electrons, typically 0.1. This is not the same as setting the amount, of laser energy deposited by resonance absorption.

FTHOT (R) D=0.0 This determines the way in which the code calculates the hot electron temperature. If $FHOT \geq 0.0$ then $T_H = FTHOT \times T_{ec}$, where T_{ec} , is the electron temperature at critical density. The transport of energy of hot electrons is handled by splitting the Maxwellian distribution into 10 groups and performing a dE/dx calculation for each group.

RHOT controls the transport of hot electron energy after the electrons have made a single pass through the target. If RHOT=1.0 the energy remaining at this time is deposited throughout the target uniformly. Typical value of RHOT is 1.0.

FLIMIT (R) D=0.0 This is the control of the flux limiter where classical free streaming limit desired flux limit $FLIMIT = \text{classical free streaming limit}/\text{desired flux limit}$
A typical value of FLIMIT is 10.0 (i. e. the desired flux limit is 0.1)

PIQ(27) (R) D=0.0 It is possible to vary the thermal conductivity of the electrons, $K_e \text{ using } K_e = K_{(Spitzer)} \times (1.0 + PIQ(27))$ AS all elements of the PIQ array

default to zero the conductivity will be the Spitzer value by default .

STATE (R) D=O.O The ions always have a perfect gas equation of state regardless of the value of NLPFI (see next section). If NLPFE=T then the electrons also use the perfect gas equation of state. If NLPFE=F then the equation of state is decided by the value given to STATE. Typically, STATE=3.0 is reasonable when using SAHA=1.0. If NLPFE=T, this will save CPU time but the physics may not be strictly applicable to your specific situation. The values of STATE are

* 0.0 Fermi Dirac

* 1.0 Thomas Fermi

* 2.0 Thomas Fermi with quantum corrections

* 3.0 Thomas Fermi with modified corrections to give correct solid density.

SAHA (R) D=O.O SAHA determines whether or not to calculate ionization equilibrium.

If SAHA=O.O, the material is assumed to be fully ionized.

If SAHA=1.0 then the ionization is calculated from Saha's equation ($Z \leq 18$) or the Thomas - Fermi model for higher Z values.

If SAHA=2.0 then the ionization is calculated from the time-dependent solution of the a.lrrera.g atom rate equations.

NLTNL (L) D=F This controls whether tunnel ionization is included in the average atom rates.

NLABS (L) D=T This controls whether the absorption of laser radiation by inverse bremsstrahlung is included in the calculation.

NLHF (L) D=F This controls whether a high field correction is applied to the absorption of laser radiation by inverse bremsstrahlung.

NLBRMS (L) D=T This controls whether radiation from bremsstrahlung in the plasma. is included in the calculation.

NLBURN (L) D=T This controls whether burning of fusion fuel is included in the calculation.

NLCRII (L) D=T This controls whether any laser energy is dumped at critical density in the calculation.

NLDEPO (L) D=T This controls whether any energy from fusion products is included in the calculation.

NLECON (L) D=T This controls whether electron heat conduction is included in the calculation.

NLICON (L) D=T This controls whether ion heat conduction is included in the calculation.

NLMOVE (L) D=T This controls whether fluid motion is included in the calculation.

NLPFE (L) D=T This controls whether the equation of state for electrons is the perfect gas EOS.

NLPFI (L) D=T This controls whether the equation of state for ions is the perfect gas

NLX (L) D=T This controls whether ion-electron collisional relaxation is included in the calculation.

TSTOP (R) D=1.OE-6 This is the time in the simulation at which the calculation stops (units are seconds).

NRUN (I) D=100 This is the maximum number of time steps that the code is allowed to run for. Set this to something large (e. g. 80000) so that the code will always terminate because of TSTOP rather than NRUN - this makes it easier to terminate the run exactly when required.

NPRNT (R) D=100.0 This is the number of time steps between printer (and restart and graphics files) dumps.

NLEMP (L) D=T This controls whether you receive reams of diagnostic print-out when the code falls over. Probably best set to FALSE

DELTAT (R) D=1.OE-18 This is the initial timestep, the code will automatically choose its own value for this after a few time steps. Something small, typically 10-18s (the default) is recommended.

DTMAX (R) D=1.E00 This is the maximum time step that the code is allowed to use. AKO (R) D=5.0 This is the maximum allowable ratio of successive time steps. Set AIiO to something large (e. g. 100.0) if message time centering is damaged appears.

AK1, AK2, AK3, AK4, AK5 (R) D=0.25,0.25,0.25,0.25,0.0 These numbers control the choice of timestep by the code. Ak1 controls the CFL condition.

AKS, AKQ, (R) D=0.25,0.25 These numbers also control the choice of timestep by the code when used the average atom model (SAHA=2.). AK9 was introduced to control

the change in average ionization state (useful when tunnel ionization is switched on).
AK8 was introduced to control the change in energy input in a given computational cell (useful when simulating high peak power short pulses).

NLITE (L) D=T This is a logical switch that controls iterations on T_i , T_e , and U (the internal energy). Since the thermal conductivity is non-linear it is best to iterate. Calculations which have electron thermal conduction switched off could set NLITE=F.

DUMAX, DTEMAX, DTIMAX (R) D=0.1,0.1,0.1 The maximum fractional change in U, T_i , and T_e which represent acceptable convergence.

NITMAX (I) D=5 The maximum number of iterations before code stops due to the iterations failing to converge.

Appendix C

Code for ICCD parameter optimization

```
cls()
t0 = time() // acquire starting time
print "Reading..."

nameroot$ = "D:\yogesh\2006\jun\jun14\dat_"
dat_des$ = "D:\yogesh\2006\jun\jun14\dat_desc.txt"
setAcquisitionType(0) // set to acquire signal
setAcquisitionMode(3) // set to kinetic
setTriggerMode(1) // set to external trigger
setDataTypes(1) // set to Counts

filenumber = 1000
repeat = 5
gatewidth = 50000
maxwidth = 450000
startgain = 0
endgain = 250
startdelay = 105000
delaystep = 20000
gainstep = 50
widthstep = 50000
```

```

while gatewidth <= maxwidth
print(time$())
SetDDG(3, 0, startdelay, gatewidth, delaystep)
setTriggerMode(1)
gain=startgain
while gain <= endgain
setgain(gain)
count = 1
while count <= repeat
run()
filename$ = nameroot$ + str$(filenumber) + ".sif"
Save(#0, filename$)
CloseWindow(#1)
print (filename$; "  gain: "; gain; "
Gatewidth: "; gatewidth; "  Repeat: "; count)
write(dat_des$, filename$, gain, gatewidth, count)
count = count + 1
filenumber = filenumber + 1
wend
gain = gain + gainstep
wend
gatewidth = gatewidth + widthstep
print(time$())
input("Clean the cover slip, input any number to continue", anyn)
wend

print ""
print "Final Filenumber:";
print filenumber
print ""

```

```
t1 = time()
telapsed = t1-t0
print "Total Run Time: ";
print telapsed;
print " seconds."
print ""
```

Appendix D

Matlab Code for Microheater temperature simulation

```
%Material parameters:%  
clear all;  
Tamb=298; %room temp%  
Pamb=1.01e5; %pressure in Pascals%  
Mw=18e-3; %molecular weight of water kg/mol%  
Tb=373; %normal boiling point of water%  
Tc=647; %critical temperature of water%  
Ha=55.336;  
Hb=-6869.5;  
Hc=-5.115;  
Hd=1.05;  
rho=998; %density of water kg/m3%  
sig=0.0728; %surface tension N/m%  
Na=6.022e23; %Avogadros number%  
Kb=1.3807e-23; %boltzmann constant%  
k=0.606; %thermal conductivity of water W/m/K  
c=4.186e3; %J/kg/K  
Dmin=rho*c/k;  
a1=1/Dmin;  
rho1=21.45e3; %??%  
rb=50e-6; %radius of bubble?%
```

```

tfinal=200e-6;

%Heater parameters%
Wh=100e-6; %width of the heater%
lh=100e-6; %length of the heater%

V=30; %voltage applied to the heater%
tL=40e-6;
Rh=50:10:700; %resistance of heater in ohms%
xn=5e-6;

for m=1:length(Rh)
    Q(m)=((V/Rh(m))^2)*Rh(m)/Wh/lh;
end

dt=1e-6; %time step 1us%
ndt=(tfinal-0)/dt;

%%%%%%%%%%%%%%%%%%%%%%%%%%%%%%%%%%%%%%%%%%%%%%%%%%%%%%%%%%%%%%%%%%%%%%%%
%SOLVING FINITE DIFFENCE EQUATIONS
%figure(2)
for m=1:length(Rh)

    for i=1:ndt,
        t(i)=dt*i;
        chi(i)=xn/2/sqrt(a1*t(i));
        %Assume rectangular heat pulse with pulse lasts for tL
        if t(i)<tL
            T(i,m)=Tamb+ 2*Q(m)*sqrt(t(i)/k/c/rho)*(1/sqrt(pi)
                *exp(-chi(i)*chi(i))-chi(i)*erfc(chi(i)));
        else

```

```

        chi1(i)=xn/2/sqrt(a1*(t(i)-tL));
        T(i,m)=Tamb+ 2*Q(m)*sqrt(t(i)/k/c/rho)
        *(1/sqrt(pi)*exp(-chi(i)*chi(i))-chi(i)
        *erfc(chi(i)))-2*Q(m)*sqrt((t(i)-tL)/k/c/rho)*(1/sqrt(pi)
        *exp(-chi1(i)*chi1(i))-chi1(i)*erfc(chi1(i)));
    end
    %plot(t(1:i),(T(1:i,m)-273),'b-')
    % hold on
    end
    plot(Rh(m),max((T(i,m)-273)),'rx')
    hold on;
end
%m=1:length(Rh);
%plot(Rh(m),max((T(i,m)-273)),'b-')
%hold on;

%Graph output
%plot(t(1:i),(T(1:i)-273),'b-'); hold on
% plot(tt(1:j),(Ta(1:j)-273),'r-');
title('Max. temp (at 5um) vs resistance at different
voltage/pulse width');
xlabel('Resistance (ohm)');
ylabel('Surface Temperature (C)');

```

To get a theoretical estimate on the heater surface and above the heater surface in the chamber the code shown above was run for two different voltages of 12 and 14 volts and the temperature distribution is as shown in the Fig.D.1 and Fig.D.2.

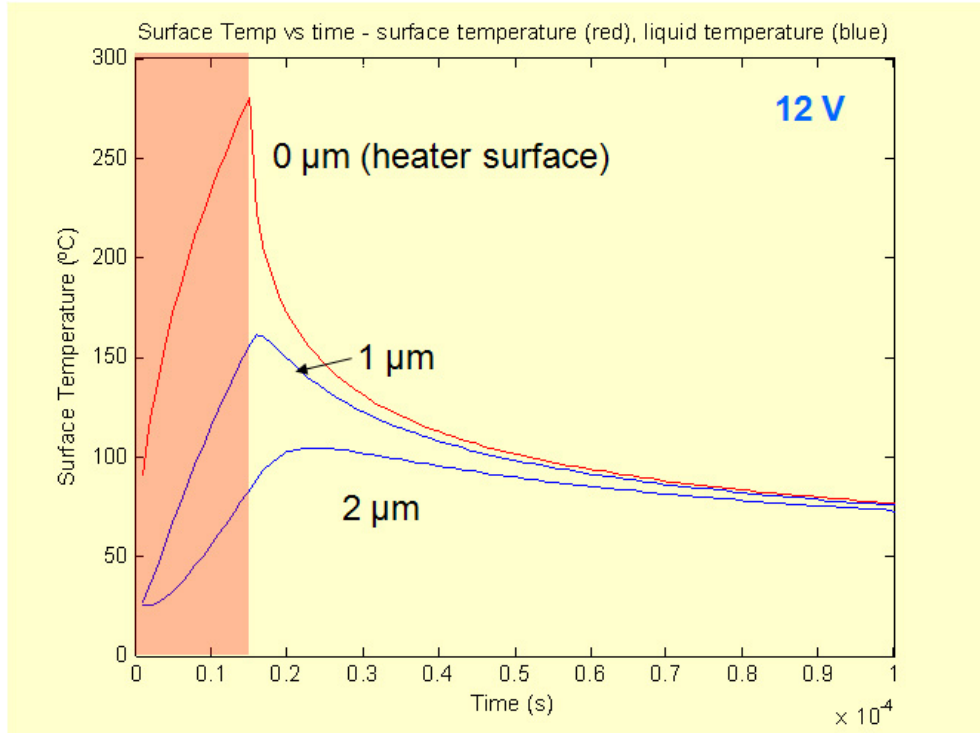


Figure D.1: Simulation of surface temperature profile for the Pt microheater for a 12 V 5 μs pulse on the surface and 2 and 5 μm above the surface.

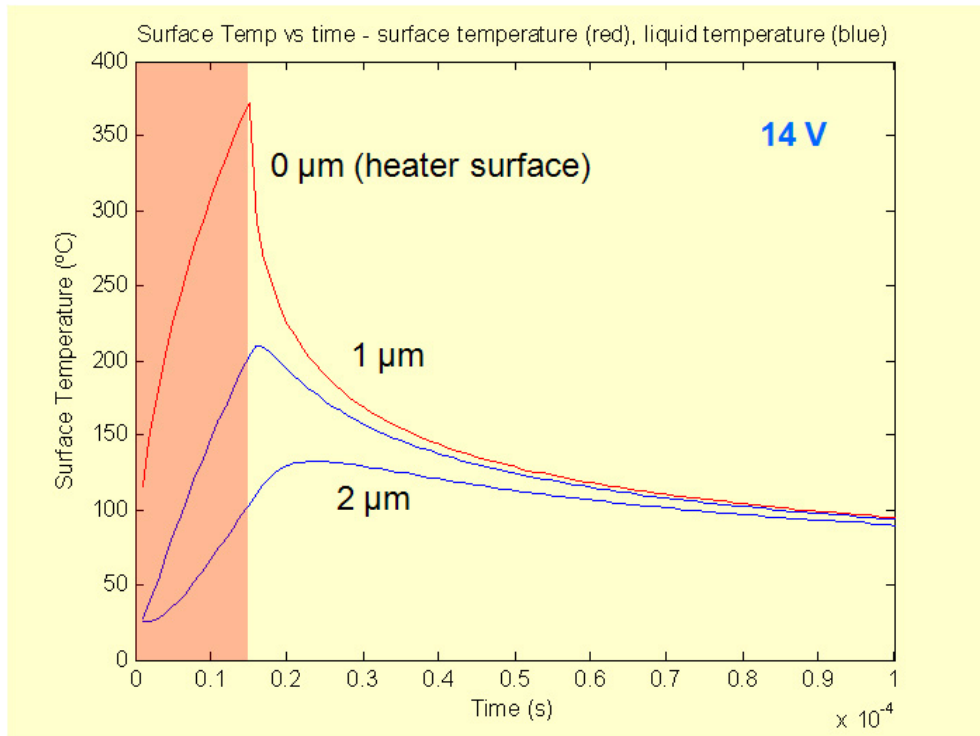


Figure D.2: Simulation of surface temperature profile for the Pt microheater for a 14 V 5 μs pulse on the surface and 2 and 5 μm above the surface.

Bibliography

- [1] Lucas M. C. Silva Celio Pasquini, Juliana Cortez and Fabiano B. Gonzaga. Laser induced breakdown spectroscopy. *J. Braz. Chem. Soc.*, Vol. 18:463–512, 2007.
- [2] M. Taguchi T. Nakaya M. Yokoyama, . T. Nobuhara. Development of multi-pixel photon counters. *SNIC Symposium, Stanford, California*, 2006.
- [3] F. Brech, L. Cross. Optical microemission stimulated by ruby maser. *Applied Spectroscopy*, Vol. 16:59, 1962.
- [4] L.J. Radziemski, T.R. Loree. Laser-Induced Breakdown Spectroscopy: Time-Resolved Spectrochemical Applications. *Plasma Chemistry and Plasma Processing*, Vol. 1:281 – 293, 1981.
- [5] Majidi V. and Joseph M.R. Spectroscopic Applications of Laser-Induced Plasmas . *Critical Reviews in Analytical Chemistry* , 23:143–162, 1992.
- [6] D.A. Cremers and L.J. Radziemski. *Handbook of Laser-Induced Breakdown Spectroscopy*. John Wiley & Sons, Ltd., 2006.
- [7] K. Song, Y.I. Lee, J. Sneddon. Applications of Laser-Induced Breakdown Spectroscopy. *Applied Spectroscopy Reviews*, Vol. 32:183 – 235, 1997.
- [8] S.S. Mao, X. Mao, R. Grief, R.E. Russo. Breakdown of equilibrium approximation for nanosecond laser-induced electron emission from silicon. *Applied Physics Letters*, Vol. 73:1331 – 1333, 1998.
- [9] L.M. Cabalin and J.J. Laserna. Experimental determination of laser induced breakdown thresholds of metals under nanosecond Q-switched laser operation. *Spectrochimica Acta B*, Vol. 53:723 – 730, 1998.

- [10] I.B. Gornushkin, B.W. Smith, H. Nasajpour and J.D. Winefordner. Identification of Solid Materials by Correlation Analysis Using a Microscopic Laser-Induced Plasma Spectrometer. *Analytical Chemistry*, Vol. 71:5157 – 5164, 1999.
- [11] X. Liu, D. Du, and G. Mourou. Laser Ablation and Micromachining with Ultrashort Laser Pulses. *IEEE JOURNAL OF QUANTUM ELECTRONICS*, Vol. 33:1706 – 1716, 1997.
- [12] J. P. Colombier, P. Combis, F. Bonneau, R. L. Harzic, and E. Audouard. Hydrodynamic simulations of metal ablation by femtosecond laser irradiation. *Phys. Rev. B*, Vol. 33:165406, 2005.
- [13] V. Margetic, A. Pakulev, A. Stockhaus, M. Bolshov, K. Niemax, R. Hergenröder. A comparison of nanosecond and femtosecond laser-induced plasma spectroscopy of brass samples. *Spectrochim. Acta, Part B*, Vol. 55:1771 – 1785, 2000.
- [14] B. Le Drogoff, J. Margot, M. Chaker, M. Sabsabi, O. Barthemlemy, T.W. Johnston, S. Laville, F. Vidal, Y. von Kaenel. Temporal characterization of femtosecond laser pulses induced plasma for spectrochemical analysis of aluminum alloys. *Spectrochimica Acta B*, Vol. 56:987 – 1002, 2001.
- [15] R. Le Harzic, D. Breitling, M. Weikert, S. Sommer, C. Fohl, S. Valette, C. Donnet, E. Audouard, and F. Dausinger,. Pulse width and energy influence on laser micromachining of metals in a range of 100 fs to 5 ps. *Appl. Surf. Sci.*, 249:322–331, 2005.
- [16] S. Preuss, A. Demchuk, and M. Stuke. Sub-picosecond UV laser ablation of metals. *Appl. Phys. A*, 61:33, 1995.
- [17] A. Semerok, C. Chaleard, V. Detalle, J-L. Lacour, P. Mauchien, P. Meynadier, C. Nouvellon, B. Salle e,P. Palianov, M. Perdix, G. Petite. Experimental investigations of laser ablation efficiency of pure metals with femto, pico and nanosecond pulses. *Applied Surface Science*, Vol. 138-139:311 – 314, 1999.

- [18] K. Furusawa, K. Takahashi, H. Kumagai, K. Midorikawa and M. Obara. Ablation characteristics of au,ag, and cu metals using a femtosecond ti:sapphire. *Appl. Phys. A*, Vol. 69:S359 – S366, 1999.
- [19] S. Nolte, C. Momma, H. Jacobs, A. Tunnermann, B. N. Chichkov, B. Welleghausen, and H. Welling. Ablation of metals by ultrashort laser pulses. *J. Opt. Soc. Am. B*, Vol. 14:2716–2722, 1997.
- [20] E. L. Gurevich and R. Hergenroeder. Femtosecond laser-induced breakdown spectroscopy: physics, applications, and perspectives. *Appl. Spectrosc.*, Vol. 61:233A – 242A, 2007.
- [21] V. Margetic, M. Bolshov, A. Stockhaus, K. Niemax, R. Hergenröder. Depth profiling of multi-layer samples using femtosecond ablation. *J. Anal. At. Spectrom.*, Vol. 16:616 – 621, 2001.
- [22] K.L. Eland, D.N. Stratis, D.M. Gold, S.R. Goode, S.M. Angel. Energy Dependence of Emission Intensity and Temperature in a LIBS Plasma Using Femtosecond Excitation. *Appl. Spectrosc.*, Vol. 55:286 – 291, 2001.
- [23] M. Baudelet, J. Yu, M. Bossu, J. Jovelet, J. P. Wolf, T. Amodeo, E. Frejafon, and P. Laloi,. Discrimination of microbiological samples using femtosecond laser-induced breakdown spectroscopy. *Appl. Phys. Lett.*, Vol. 89:163903, 2006.
- [24] P. Pouli, K. Melessanaki, A. Giakoumaki, V. Argyropoulos, and D. Anglos. Measuring the thickness of protective coatings on historic metal objects using nanosecond and femtosecond laser induced breakdown spectroscopy depth profiling. *Spectrochim. Acta, Part B*, Vol. 60:1163, 2005.
- [25] M.T. Taschuk and Y.Y. Tsui and R. Fedosejevs. Detection and Imaging of Latent Fingerprints by Laser-Induced Breakdown Spectroscopy. *Appl. Spectrosc.*, 60:1322 – 1327, 2006.
- [26] P. Rohwetter, J. Yu, G. Mejean, K. Stelmaszczyk, E. Salmon, J. Kasparian, J.-P. Wolf, and L. Woeste,. Remote libs with ultrashort pulses: characteristics in

- picosecond and femtosecond regimes. *J. Anal. At. Spectrom.*, Vol. 19:437–444, 2005.
- [27] O. Barthelemy, J. Margot, M. Chaker, M. Sabsabi, F. Vidal, T. W. Johnston, S. Laville and B. LeDrogoff. Influence of the laser parameters on the space and time characteristics of an aluminum laser-induced plasma . *Spectrochimica Acta Part B-Atomic Spectroscopy*, 60:905, 2005.
- [28] D. Menut, P. Fichet, J-L. Lacour, A. Rivoallan, and P. Mauchien. Micro-laser-induced breakdown spectroscopy technique: a powerful method for performing quantitative surface mapping on conductive and nonconductive samples. *Appl. Opt.*, 42:6063 – 6071, 2003.
- [29] I.B. Gornushkin, K. Amponsah-Manager, B.W. Smith, N. Omenetto, J.D. Winefordner. Microchip Laser-Induced Breakdown Spectroscopy: A Preliminary Feasibility Investigation. *Applied Spectroscopy*, Vol. 71:762 – 769, 2004.
- [30] Y. Godwal, S.L. Lui, M.T. Taschuk, Y.Y. Tsui and R. Fedosejevs. Determination of lead in water using laser ablation laser induced fluorescence. *Spectrochimica Acta Part B*, Vol.62:1443–1447, 2007.
- [31] V. Detalle, M. Sabsabi, L. St-Onge, A. Hamel, R. Hoon. Influence of Er:YAG and Nd:YAG Wavelengths on Laser-Induced Breakdown Spectroscopy Measurements Under Air or Helium Atmosphere. *Applied Optics*, Vol. 42:5971, 2003.
- [32] J. Gruber, J. Heitz, J. Strasser, H. Bauerle, N. Ramaseder. Elemental analysis of steel scrap metals and minerals by laser-induced breakdown spectroscopy. *Spectrochimica Acta Part B*, Vol. 56:685, 2001.
- [33] Ralf Nyga and Walter Neu. Double-pulse technique for optical emission spectroscopy of ablation plasmas of samples in liquids. *Optics Letters*, pages 747–749, 1993.
- [34] B. Le Drogoff, M. Chaker, J. Margot, M. Sabsabi, O. Barthelemy, T. W. Johnston, S. Laville, and F. Vidal . Influence of the laser pulse duration on spec-

- trochemical analysis of solids by laser-induced plasma spectroscopy. *Applied Spectroscopy*, Vol. 58:122 – 129, 2001.
- [35] R. Niessner G.A. Petrucci P. Cavalli R.E. Neuhauser, U. Panne and N. Omenetto. On-line and in situ detection of lead aerosols by plasma spectroscopy and laser-excited atomic fluorescence spectroscopy. *Anal. Chim. Acta*, pages 37 – 48, 1999.
- [36] Doug Body and Bruce L. Chadwick. Simultaneous elemental analysis system using laser induced breakdown spectroscopy. *REVIEW OF SCIENTIFIC INSTRUMENTS*, Vol. 72:1625 – 1629, 2001.
- [37] R. E. Neuhauser, B. Ferstl, C. Haisch, U. Panne, and R. Niessner. Design of a low-cost detection system for laser-induced plasma spectroscopy. *REVIEW OF SCIENTIFIC INSTRUMENTS*, Vol. 70:3519 – 3522, 1999.
- [38] M. Sabsabi, R. Hon and L. St-Onge. Critical evaluation of gated CCD detectors for laser-induced breakdown spectroscopy analysis. *Spectrochim. Acta, Part B*, Vol.60:1211, 2005.
- [39] Thomas W. Barnard, Michael I. Crockett, Juan C. Ivaldi and Peter L. Lundberg. Design and Evaluation of an Echelle Grating Optical System for ICP-OES. *Anal. Chem.*, Vol. 65:1225 – 1230, 1993.
- [40] L. Hiddemann, J. Uebbing, A. Ciocan, O. Dessenne and K. Niemax. Simultaneous multi-element analysis of solid samples by laser ablation-microwave induced optical emission spectroscopy. *Analytica. Chimica. Acta*, Vol.283:152 – 159, 1993.
- [41] G.R.Harrison. The production of diffraction gratings II: The Design of echelle gratings and spectrographs. *J.Opt. Soc. Am.*, Vol. 39:522 – 528, 1949.
- [42] R. George, J. A. Harrison, E. Archer and Jean Camus. A Fixed-Focus Broad-Range Echelle Spectrograph of High Speed and Resolving Power. *JOURNAL OF THE OPTICAL SOCIETY OF AMERICA*, Vol. 42:706 – 712, 1952.

- [43] H.E. Bauer, F. Leisb, K. Niemax. Laser induced breakdown spectrometry with an echelle spectrometer and intensified charge coupled device detection. *Spectrochimica Acta Part B*, Vol. 53:1815 – 1825, 1998.
- [44] C. Haisch,U. Panne,R. Niessner. Combination of an intensified charge coupled device with an echelle spectrograph for analysis of colloidal material by laser-induced plasma spectroscopy. *Spectrochim. Acta, Part B*, Vol. 53:1657 – 1667, 1998.
- [45] Peter Lindblom. New compact Echelle spectrographs with multichannel time-resolved recording capabilities. *Analytica Chimica Acta*, Vol. 380:353–361, 1999.
- [46] M. Sabsabi, R. Heon, V. Detalle, L. St-Onge and A. Hamel. Comparision between intensified CCD and non-intensified gated CCD detectors for LIPS analysis of solid samples. In *Laser Induced Plasma Spectroscopy and Applications*, volume 81 of *OSA Trends in Optics and Photonics (TOPS)*, 2002.
- [47] Dimitra N. Stratis, Kristine L. Eland,J. Chance Carter,Samuel J. Tomlinson, and S. Michael Angel. Comparison of Acousto-optic and Liquid Crystal Tunable Filters for Laser-Induced Breakdown Spectroscopy. *APPLIED SPECTROSCOPY*, Vol. 55:1297 – 1303, 2001.
- [48] Andrew K. Knight, Nancy L. Scherbarth, David A. Cremers and Monty J. Ferris. Characterization of Laser-Induced Breakdown Spectroscopy (*LIBS*) for Application to Space Exploration. *Applied Spectroscopy*, Vol. 54:331–340, 2000.
- [49] D. Bertuccelli J.M. Gomba, C. D Angelo and G. Bertuccelli. Spectroscopic characterization of laser induced breakdown in aluminiumlithium alloy samples for quantitative determination of traces. *Spectrochimica Acta Part B*, Vol. 56:695–705, 2001.
- [50] Tjia Kazuhiro Ikezawa Tadashi Maruyama Marincan Pardede, Hendrik Kurniawan and Kiichiro Kagawa. Spectrochemical Analysis of Metal Elements Electrodeposited from Water Samples by Laser-Induced Shock Wave Plasma Spectroscopy. *Applied Spectroscopy*, Vol. 55:1229–1236, 2001.

- [51] L.S. Huang J.S. Huang, C.B. Ke and K.C. Lin. The correlation between ion production and emission intensity in the laser-induced breakdown spectroscopy of liquid droplets. *Spectrochim. Acta Part B*, Vol. 57:3548, 2002.
- [52] Frank M. Pennebaker, David A. Jones, Chris A. Gresham, Robert H. Williams, Richard E. Simon, Michael F. Schappert and M. Bonner Denton. Spectroscopic instrumentation in the 21st Century: excitement at the horizon. *Journal of Analytical Atomic Spectrometry*, Vol. 13:821 – 827, 1998.
- [53] J.R. Janesick. *Scientific Charge-Coupled Devices*. SPIE Press, 2001.
- [54] Mohamad Sabsabi, Vincent Detalle, Mohamed A. Harith, Walid Tawfik, and Hisham Imam. Comparative study of two new commercial echelle spectrometers equipped with intensified CCD for analysis of laser-induced breakdown spectroscopy. *APPLIED OPTICS*, Vol. 42:6094, 2003.
- [55] C. Haisch and H. Becker-Ross. An electron bombardment ccd-camera as detection system for an echelle spectrometer. *Spectrochim. Acta, Part B*, Vol. 58:1351 – 1357, 2003.
- [56] J.E. Carranza, E. Gibb, B. Smith, D. Hahn, J. Winefordner. Comparison of nonintensified and intensified CCD detectors for laser-induced breakdown spectroscopy. *Applied Optics*, Vol. 42:6016–6021, 2003.
- [57] J.E. Carranza, D.W. Hahn. Sampling statistics and considerations for single-shot analysis using laser-induced breakdown spectroscopy. *Spectrochimica Acta Part B*, Vol. 57:779–790, 2002.
- [58] Gomez C, Costela, A, Garcia-Moreno, I, Sastre, R. Comparative study between ir and uv laser radiation applied to the removal of graffitis on urban buildings. *Applied Surface Science*, Vol. 252:2782–2793, 2005.
- [59] Katsuyoshi Yamasaki, Aki Tanaka, Tomoko Kimura, Okitsugu Kajimoto. An inexpensive handmade gated integrator. *Rev. Sci. Instrum.*, Vol. 66:4395–4396, 1995.

- [60] A. De Giacomo, V.A. Shakhmatov, O. De Pascale. Optical emission spectroscopy and modeling of plasma produced by laser ablation of titanium oxides. *Spectrochimica Acta B*, Vol. 56:753 – 776, 2001.
- [61] L.M. Cabalin and J.J. Laserna. Atomic emission spectroscopy of laser-induced plasmas generated with an annular-shaped laser beam. *J. Anal. Atomic Spectrom.*, Vol. 19:445, 2004.
- [62] G.W. Rieger, M. Taschuk, Y.Y. Tsui, and R. Fedosejevs. Laser Induced Breakdown Spectroscopy for Microanalysis using Sub-millijoule UV Laser Pulses. *Appl. Spectrosc.*, Vol. 56:689 – 698, 2002.
- [63]
- [64] Richard A. Myers, Arieh M. Karger, and David W. Hahn. Geiger photodiode array for compact, lightweight laser-induced breakdown spectroscopy instrumentation. *APPLIED OPTICS*, 42:6072, 2003.
- [65] D.A. Rusak, B.C. Castle, B.W. Smith, J.C. Winefordner. Recent Trends and the future of laser-induced plasma spectroscopy. *Trends in Analytical Chemistry*, Vol. 17:453 – 461, 1998.
- [66] Brian J. Marquardt, Scott R. Goode, and S. Michael Angel. In Situ Determination of Lead in Paint by Laser-Induced Breakdown Spectroscopy Using a Fiber-Optic Probe. *Analytical Chemistry*, 68:977–981, 1996.
- [67] Susumu Nakamura, Yoshiro Ito, Kazuhiro Sone, Hitoshi Hiraga and Ken-ichi Kaneko. Determination of an Iron Suspension in Water by Laser-Induced Breakdown Spectroscopy with Two Sequential Laser Pulses. *Analytical Chemistry*, 68:2981–2986, 1996.
- [68] P. Fichet, P. Mauchien, and C. Moulin. Determination of Impurities in Uranium and Plutonium Dioxides by Laser-Induced Breakdown Spectroscopy. *Appl. Spectrosc.*, Vol. 53:1111 – 1117, 1999.
- [69] V.I. Babushok, F.C. DeLucia Jr., J.L. Gottfried, C.A. Munson, and A.W. Miziolek. Double pulse laser ablation and plasma: Laser induced breakdown

- spectroscopy signal enhancement. *Spectrochim. Acta B*, Vol. 61:999 – 1014, 2006.
- [70] E.H. Piepmeier, H.V. Malmstadt. Q-Switched Laser Energy Absorption in the Plume of an Aluminum Alloy. *Analytical Chemistry*, Vol. 41:700 – 707, 1969.
- [71] R.H. Scott, A. Strasheim. Laser Induced Plasmas for Analytical Spectroscopy. *Spectrochimica Acta B*, Vol. 25:311 – 332, 1970.
- [72] D.A. Cremers, L.J. Radziemski and T.S. Loree. Spectrochemical analysis of liquids using the laser spark. *Applied Spectroscopy*, Vol. 38:721 – 729, 1984.
- [73] D.A. Cremers J. Scaffidi, S.M. Angel. Emission enhancement mechanisms in dual-pulse LIBS,. *Anal. Chem.*, Vol. 78:24 – 32, 2006.
- [74] J. Uebbing, J. Brust,W. Sdorra, F. Leis, K. Niemax. Reheating of a laserproduced plasma by a second pulse laser. *Applied Spectroscopy*, Vol. 45:1419 – 1423, 1991.
- [75] D.N. Stratis, K.L. Eland, S.M. Angel. Dual-pulse LIBS using a preablation spark for enhanced ablation and emission. *Appl. Spectrosc.*, Vol. 54:1270 – 1274, 2000.
- [76] C. Gautier, P. Fichet, D. Menut, J.L. Lacour, D.L Hermite and J. Dubessy. Quantification of intensity enhancements for double-pulse laser-induced breakdown spectroscopy in orthogonal beam geometry. *Spectrochimica Acta B*, Vol. 60:265 – 276, 2005.
- [77] J. Scaffidi, J. Pender, W. Pearman, S.R. Goode, B.W. Colston Jr., J.C. Varter, S.M. Angel. Dual-pulse laser-induced breakdown spectroscopy with combinations of femtosecond and nanosecond laser pulses. *Applied Optics*, Vol. 42:6099 – 6106, 2003.
- [78] J.C. Carter B.W. Colston Jr. S.M. Angel J. Scaffidi, W. Pearman. Temporal dependence of the enhancement of material removal in femtosecondnanosecond dual-pulse laser-induced breakdown spectroscopy,. *Applied Optics*, Vol. 43:6492 – 6499, 2004.

- [79] M. Sabsabi L. St-Onge, V. Detalle. Enhanced laser-induced breakdown spectroscopy using the combination of fourth-harmonic and fundamental nd:yag laser pulses. *Spectrochimica Acta B*, Vol. 57:121–135, 2002.
- [80] P.A. Benedetti, G. Cristoforetti, S. Legnaioli, V. Palleschi, L. Pardini, A. Salvetti, E. Tognoni. Effect of laser pulse energies in laser induced breakdown spectroscopy in double-pulse configuration,. *Spectrochimica Acta B*, Vol. 60:1392–1401, 2005.
- [81] V.N. Rai, F.Y. Yueh, J.P. Singh. Study of laser-induced breakdown emission from liquid under double-pulse excitation,. *Applied Optics*, Vol. 42:2085–2093, 2003.
- [82] N.H. Cheung S.Y. Chan. Analysis of solids by laser ablation and resonance enhanced laser-induced plasma spectroscopy. *Analytical Chemistry*, Vol. 72:2087 – 2092, 2000.
- [83] S.L. Lui, N.H. Cheung,. Resonance-enhanced laser-induced plasma spectroscopy: ambient gas effects. *Spectrochimica Acta Part B*, Vol.58:1613–1623, 2003.
- [84] H. Hakkanen, J. Houni, S. Kaski, and J.E.I. Korppi-Tommola. Analysis of paper by laser-induced plasma spectroscopy. *Spectrochim. Acta B*, Vol. 56:737 – 742, 2001.
- [85] I. Cravetchi, M. Taschuk, G.W. Rieger, Y.Y. Tsui, and R. Fedosejevs. Spectrochemical Microanalysis of Aluminum Alloys by Laser Induced Breakdown Spectroscopy: Identification of Precipitates. *Appl. Opt.*, Vol. 42:6138 – 6147, 2003.
- [86] I. Cravetchi, M. Taschuk, Y.Y. Tsui, and R. Fedosejevs. Scanning microanalysis of Al alloys by laser-induced breakdown spectroscopy. *Spectrochim. Acta B*, 59:1439 – 1450, 2004.

- [87] A. Freedman, F.J. Iannarilli Jr., and J.C. Wormhoudt. Aluminum alloy analysis using microchip-laser induced breakdown spectroscopy. *Spectrochim. Acta B*, Vol. 60:1076 – 1082, 2005.
- [88] J. Wormhoudt, F.J. Iannarilli Jr., S. Jones, K.D. Annen, and A. Freedman. Determination of Carbon in Steel by Laser-Induced Breakdown Spectroscopy Using a Microchip Laser and Miniature Spectrometer. *Appl. Spectrosc.*, Vol. 59:1098 – 1102, 2005.
- [89] H.S. Kwong and R.M. Measures. Trace Element Laser Microanalyzer with Freedom from Chemical Matrix Effect. *Anal. Chem.*, Vol. 51:428 – 432, 1979.
- [90] H.H. Telle, D.C.S. Beddows, G.W. Morris, O. Samek. Sensitive and selective spectrochemical analysis of metallic samples: the combination of laser-induced breakdown spectroscopy and laser-induced fluorescence spectroscopy. *Spectrochimica Acta B*, Vol. 56:947 – 960, 2001.
- [91] Frank Hilbk Kortenbrucka, Reinhard Noll, Peter Wintjensb, Heinz Falk, Christoph Becker. Analysis of heavy metals in soils using laser-induced breakdown spectrometry combined with laser-induced fluorescence. *Spectrochimica Acta B*, Vol. 56:933 – 945, 2001.
- [92] William. C. Pesklak and Edward. H. Piepmier. Laser-Induced Nonresonance Atomic Fluorescence in an Analytical Microprobe Plume. *Microchemical Journal*, Vol. 50:253 – 280, 1994.
- [93] I.B. Gornushkin, S.A. Baker, B.W. Smith, J.D. Winedordner. Determination of lead in metallic reference materials b laser ablation combined with laser excited atomic fluorescence. *Spectrochimica Acta B*, Vol. 52:1653 – 1662, 1997.
- [94] Sten Sjostrom. Laser-excited atomic fluorescence spectrometry in graphite furnace. *Spectrochimica Acta Reviews*, Vol. 13:407–465, 1990.
- [95] National Primary Drinking Water Standards. Publication No. EPA816F03016 Office of Water, United States Environmental Protection Agency, U.S. *Government Printing Office*, Washington DC, 2003.

- [96] DC 2006. United States Environmental Protection Agency, U.S. Government Printing Office: Washington. Lead and Copper Rule State File Review: National Report. *EPA*, Publication No. EPA816R06001, 2006.
- [97] R. Knopp et al. Laser induced breakdown spectroscopy (libs) as an analytical tool for the detection of metal ions in aqueous solutions. *Fresenius Journal of Analytical Chemistry*, Vol. 355:16 – 20, 1996.
- [98] R. L. Vander Waal, T. M. Ticich, J. R. West. Angle-resolved laser-induced breakdown spectrometry for depth profiling of coated materials. *Appl. Spectrosc.*, Vol. 53:1226 – 1236, 1999.
- [99] W.F. Ho, C.W. Ng and N.H. Cheung. Spectrochemical Analysis of Liquids Using Laser-Induced Plasma Emissions: Effects of Wavelength. *Applied Spectroscopy*, Vol. 51:87 – 91, 1997.
- [100] United States Environmental Protection Agency. Introduction to Hazardous Waste Identification; Publication No. EPA530K05012. *U.S Government Printing Office*, Washington DC, 2005.
- [101] J. Melin, H. Johansson, O. Soderberg, F. Nikolajeff, U. Landegren, M. Nilsson, and J. Jarvius. Thermoplastic microfluidic platform for single-molecule detection, cell culture, and actuation. *Analytical Chemistry*, Vol. 77:7122 – 7130, 2005.
- [102] S. Morel, N. Leone, P. Adam, and J. Amouroux. Detection of bacteria by time-resolved laser induced breakdown spectroscopy. *Appl. Opt.*, Vol. 42:6184 – 6191, 2003.
- [103] K. L. McNesby A. C. Samuels, F. C. DeLucia Jr. and A. W. Miziolek. Laser-induced breakdown spectroscopy of bacterial spores, molds, pollens and protein: initial studies of discrimination potential. *Appl. Opt.*, Vol. 42:6205 – 6209, 2003.
- [104] J. D. Hybl, G. A. Lithgow, and S. G. Buckley. Laser-induced breakdown spectroscopy detection and classification of biological aerosols. *Appl. Spectrosc.*, Vol. 57:1207–1215, 2003.

- [105] A. Kumar, F. Y. Yueh, S. Burgess, and J. Singh. Characterization of malignant tissue cells by laserinduced breakdown spectroscopy. *Appl. Opt.*, Vol. 43:5399–5403, 2003.
- [106] C. W. Ng and N. H. Cheung. Detection of sodium and potassium in single human red blood cells by 193 nm laser ablative sampling: A feasibility demonstration. *Anal. Chem.*, Vol. 72:247–250, 2000.
- [107] L. R. Allain, M. Askari, D. L. Stokes, and T. V. Dinh. Microarray sampling-platform fabrication using bubble-jet technology for a biochip system. *Fresenius J. Anal. Chem.*, Vol. 371:146–150, 2000.
- [108] M. Fujii, T. Hamazaki, and K. Ikeda. New thermal ink jet printhead with improved energy efficiency using silicon reactive ion etching. *J. Imag. Sci. and Technol.*, Vol. 43:332–338, 1999.
- [109] W. A. Buskirk, D. E. Hackleman, S. T. Hall, P. H. Kanarek, R. N. Low, K. E. Trueba, and R. R. van del Poll. Development of high-resolution thermal ink jet printhead. *Hewlett Packard Journal*, Vol. 127-129:55–60, 1988.
- [110] C. H. Lee, and A. Lal. Single microdroplet ejection using an ultrasonic longitudinal mode with pzt/tapered glass capillary. *IEEE Trans. Ultrason. Ferroelectr. Freq. Control*, Vol.51:1514–1522, 2004.
- [111] C. Ainsley N. Reis and B. Derby. Ink-jet delivery of particle suspensions by piezoelectric droplet ejectors. *Journal of Appl. Phys.*, Vol.97:094903, 2005.
- [112] P. L. Skipper S. J. Kim, Y. Song and J. Han. Electrohydrodynamic generation and delivery of monodisperse picoliter droplets using a poly(dimethylsiloxane) microchip. *Anal. Chem.*, Vol.78:8011–8019, 2006.
- [113] J.C. Miller, R.F. Haglund. *Laser Ablation and Desorption*. Academic Press, San Diego, California, 1998.
- [114] M. Von Allmen. *Laser-beam interactions with materials*. Springer Verlag, New York, 1987.

- [115] Annemie Bogaerts, Zhaoyang Chen, Renaat Gijbels and Akos Vertes. Laser ablation for analytical sampling: what can we learn from modeling? *Spectrochimica Acta Part B-Atomic Spectroscopy*, 58:1867 – 1893, 2003.
- [116] Laszlo Balazs, Renaat Gijbels, Akos Vertes. Expansion of laser-generated plumes near the plasma ignition threshold. *Analytical Chemistry*, Vol. 63:314–320, 1991.
- [117] R.E. Russo, X. L. Mao, J. H. Yoo and J. J. Gonzalez. Laser Ablation. In J.P. Singh, S.N. Thakur, editor, *Laser Induced Breakdown Spectroscopy*. Elsevier Science B.V., 2007.
- [118] S.K. Godunov, A.V. Zabrodin, G.P. Prokopov. Differential scheme for 2D non-stationary problems of gas dynamics and modeling of shock waves. *USSR Comput. Math. Math. Phys.*, 6:1020 – 1050, 1961.
- [119] Y. B. Zeldovich, Y. P. Raizer,. *Physics of Shock Waves and High Temperature Hydrodynamic Phenomena*,. *Academic Press, New York*, 1996.
- [120] G. Taylor. The formation of a blast wave by a very intense explosion I. Theoretical discussion. *Proceedings of the Royal Society of London. Series A, Mathematical and Physical Sciences*, Vol. 21:159–174, 1950.
- [121] L.I. Sedov. *Similarity and Dimensional Methods in Mechanics*. CRC Press, 10th edition edition, 1993.
- [122] P.E. Dyer and J. Sidhu. Spectroscopic and fast photographic studies of excimer laser polymer ablation. *Journal of Applied Physics*, Vol. 64:4657 – 4663, 1988.
- [123] Gustav Robert Kirchhoff. On the Law of Distribution of Energy in the Normal Spectrum. *Phil. Mag.*, Vol. 20:1–21, 1860.
- [124] Max Planck. On the Law of Distribution of Energy in the Normal Spectrum. *Annalen der Physik*, Vol. 4:553, 1901.
- [125] Ludwig Boltzmann. *Lectures on Gas Theory* translated by Stephen G. Brush. *University of California Berkeley Press*, 1965.

- [126] C.M. Guldberg and P. Waage. Studies Concerning Affinity. *C. M. Forhandlinger: Videnskabs-Selskabet i Christiana*, page 35, 1864.
- [127] M. Venugopalan. *Reactions under Plasma conditions*. Wiley-Interscience, New York, 1971.
- [128] G. Bekefi. *Principles of Laser Plasmas*,. Wiley-Interscience, New York, 1976.
- [129] Meghnad Saha. On a physical theory of stellar spectra. *Proceedings of the Royal Society of London, Series A*, Vol. 99, Issue. 697:135 – 153, 1921.
- [130] R.W.P. McWhirter. Spectral intensities. *Plasma Diagnostic Techniques, Academic Press*, Chapter 5, 1965.
- [131] H.R. Griem. *Principles of Plasma Spectroscopy*. Cambridge University Press, 1997.
- [132] J.P. Christiansen et al. Medusa: A one-dimensional laser fusion code. *Computer Physics Communications*, Vol. 7:271 – 287, 1974.
- [133] D.J. Rose and M. Clarke. *Plasmas and Controlled Fusion. John Wiley and Sons Inc.*, 1961.
- [134] L. Spitzer. Physics of fully ionized gases. *Interscience Publishers*, 2nd Ed., 1965.
- [135] R.E.Kidder. Interaction of intense photon and electron beams with plasmas. *Proceedings of International school of Physics Enrico Fermi, course XLVIII Academic Press*, 1971.
- [136] V. G. KOLOSHNIKOV M. A. BOLSHOV, A. V. ZYBIN and K. N. KOSHELEV. Some characteristics of laser excited atomic fluorescence in a three-level scheme. *Spectrochimica Acta B*, Vol. 32:279–286, 1977.
- [137] G.W. Rieger, M. Taschuk, Y.Y. Tsui, and R. Fedosjevs. Comparative study of laser-induced plasma emission from microjoule picosecond and nanosecond KrF-laser pulses. *Spectrochim. Acta B*, Vol. 58:497 – 510, 2003.

- [138] M.T. Taschuk, S.E. Kirkwood, Y.Y. Tsui and R. Fedosejevs. Quantitative emission from femtosecond microplasmas for laser-induced breakdown spectroscopy. *Journal of Physics: Conference Series*, (In Press), 2007.
- [139] C.J. Sansonetti J. Reader and J.M. Bridges. Irradiances of spectral lines in mercury pencil lamps. *Appl. Opt.*, Vol. 35:78 – 83, 1996.
- [140] Marc. L. Salit C.J. Sansonetti and Joseph Reader. Wavelengths of spectral lines in mercury pencil lamps. *Applied Optics*, Vol. 35:74–77, 1996.
- [141] Michael Thomas Taschuk. Quantification of Laser-Induced Breakdown Spectroscopy at low energies. *Ph.D. thesis University of alberta*, 2007.
- [142] M. Born and E. Wolf. *Principles of Optics*. Cambridge University Press, 7th (expanded) edition, 1999.
- [143] G.F. Knoll. *Radiation Detection and Measurement*. John Wiley & Sons, Inc., 3rd edition. edition, 2000.
- [144] Hamamatsu. Multi-pixel photon counters. *www.hamamatsu.com*.
- [145] V. Hoang. Thermal management strategies for microfluidic devices. *MSc. Thesis*, University of Alberta, 2008.
- [146] R. Penterman G. V. Kaigala, S. Ho and C. J. Backhouse. Rapid prototyping of microfluidic devices with a wax printer. *Lab on a Chip*, 7:384–387, 2007.
- [147] M. A. Argument. Laser micromachining of dielectrics. *MSc. Thesis*, University of Alberta, 2006.
- [148] Y. Godwal, M.T.Taschuk, S.L. Lui, Y.Y. Tsui and R. Fedosejevs. Development of laser-induced breakdown spectroscopy for microanalysis applications. *Laser and Particle Beams*, Vol.26:95–104, 2008.
- [149] S.L. Lui, Y. Godwal, M.T. Taschuk, Y.Y. Tsui, R. Fedosejevs. Detection of Lead in Water Using Laser-Induced Breakdown Spectroscopy and Laser-Induced Fluorescence. *Analytical Chemistry*, Vol.80:1995–2000, 2008.

- [150] K.M. Lo and N.H. Cheung. Arf laser-induced plasma spectroscopy for part-per-billion analysis of metal ions in aqueous solutions. *Applied Spectroscopy*, Vol. 56:682 – 688, 2002.
- [151] G. Arca, A. Ciucci, V. Palleschi, S. Rastelli, E. Tognoni. Detection of Pollutants in Liquids by Laser Induced Breakdown Spectroscopy Technique. *IEEE Geoscience and Remote Sensing Symposium*, pages 520 – 522, 1996.
- [152] M. Taschuk et al. Optimization of laser induced breakdown spectroscopy from water jet samples. *International Conference on Analytical Sciences and Spectroscopy 2003, June 1 - 4*, 2003.
- [153] X. Y. Pu and N. H. Cheung. ArF Laser Induced Plasma Spectroscopy of Lead Ions in Aqueous Solutions: Plume Reheating with a Second Nd : YAG Laser Pulse. *Applied Spectroscopy*, 57:588–590, 2003.
- [154] Joanna Pawlat Satoshi Ikezawa, Muneaki Wakamatsu and Toshitsugu Ueda. Evaluation of laser-induced breakdown spectroscopy quantitative sensing performance using a micro-droplet ejection system. *IEEE SENSORS 2007 Conference*, 1-4244-1262-5/07:407–410, 2007.
- [155] D. E. Kelleher A. E. Kramida A. Musgrove J. Reader W. L. Wiese Y. Ralchenko, F. C. Jou and K. Olsen. National institute of standards and technology, gaithersburg, md. *NIST Atomic Spectra Database (version 3.1.3)*.
- [156] R. Noll H. Schwenke W. Lahmann J. Knoth P. Beaven E. Jantzen A. Oest C. Janzen, R. Fleige and P. Koke. Analysis of small droplets with a new detector for liquid chromatography based on laser-induced breakdown spectroscopy. *Spectrochim. Acta Part B*, Vol. 60:993 – 1001, 2005.
- [157] C.K. Hubler (Ed.'s) D.B. Chrisey. Pulsed laser deposition of thin films. *Wiley, New York*, 1994.
- [158] Gao H Zhou Y, Zheng L. Cleaning of the first mirrors and diagnostic windows with a yag laser on hl2a. *Physics Scripta*, 9 T138 Article Number: 014066:Con-

- ference Information: 12th International Workshop on Plasma–Facing Materials and Components for Fusion Applications, MAY, 2009 Julich, GERMANY, 2009.
- [159] I. Smurov V.I.MAzhukin, V.V Nosov. Modeling of laser plasma dynamics at the air-water interface: Application to laser shock processing. *Journal of Applied Physics*, 90:607–617, 2001.
- [160] G. Colonna, A. Casavola, M. Capitelli. Modelling of libs plasma expansion. *Spectrochimica Acta B*, Vol. 56:567 – 586, 2001.
- [161] G. Colonna, L.D. Pietanza, M. Capitelli. Coupled solution of a time-dependent collisional-radiative model and boltzmann equation for atomic hydrogen plasmas:possible implications with libs plasmas. *Spectrochimica Acta B*, Vol. 56:587 – 598, 2001.
- [162] T.E. Itina, J. Hermann, Ph. Delaporte, M. Sentis. Combined continuous-microscopic modeling of laser plume expansion. *Applied Surface Science*, Vol. 208:27–32, 2003.
- [163] Martin C. Richardson, Chiew-Seng Koay, Kazutoshi Takenoshita, Christian Keyser. High conversion efficiency mass-limited sn-based laser plasma source for euv lithography. *Journal of Vacuum Science and Technology*, Vol.22:785–790, 2004.
- [164] Simi A. George, William Silvestro, Kazutoshi Takenoshita, Robert Bernath, Chiew-Seng Koay, Greg Shimkaveg, Martin Richardson. Euv generation from lithium laser plasma for lithography. *Proc. of SPIE*, Vol.6151:1–8, 2006.
- [165] P. Mora. Theoretical model of absorption of laser light by a plasma. *Physics of Fluids*, Vol. 25:1051 – 1056, 1982.
- [166] M.T. Taschuk, Y.Y. Tsui and R. Fedosejevs. Optimization of laser-induced breakdown spectroscopy for liquid samples at millijoule pulse energies. *2002 Laser Induced Breakdown Spectroscopy, Orlando, USA, Sept. 24 - 28th*, 2002.

- [167] Yogesh Godwal, Govind Kaigala, Viet Hoang, Siu-Lung Lui, Christopher Backhouse, Ying Tsui, and Robert Fedosejevs. Elemental analysis using micro Laser-induced Breakdown Spectroscopy (μ LIBS) in a microfluidic platform. *Optics Express*, Vol.16:12435–12445, 2008.
- [168] H. H. Telle J. O. Caceres, J. T. Lopez and A. G. Urena. Quantitative analysis of trace metal ions in ice using laser-induced breakdown spectroscopy. *Spectrochim. Acta Part B*, 56:831–838, 2001.
- [169] D. M. Diaz Pace, C. A. D’Angelo, D. Bertuccelli, and G. Bertuccelli. Analysis of heavy metals in liquids using laser induced breakdown spectroscopy by liquid-to-solid matrix conversion. *Spectrochim. Acta Part B*, 61:929–933, 2001.
- [170] Z. Chen, H. Li, F. Zhao, and R. Li. Fast and sensitive trace metal analysis in aqueous solutions by laser-induced breakdown spectroscopy using wood slice substrates. *Spectrochim. Acta Part B*, 63:64–68, 2008.
- [171] Zhijiang Chen, Yogesh Godwal, Ying Yin Tsui, and Robert Fedosejevs. Sensitive detection of metals in water using laser-induced breakdown spectroscopy on wood sample substrates. *Applied Optics*, 49:87–94, 2010.
- [172] T. M. Ticich R. L. Vander Wal and Jr. J. R. West. Laser induced breakdown spectroscopy of trace metals,. *NASA/CR 2004212980 (National Center for Microgravity Research)*, 212980, 2004.
- [173] A. Sarkar D. Alamelu and S. K. Aggarwal. Laser-induced breakdown spectroscopy for simultaneous determination of sm, eu and gd in aqueous solution. *Talanta*, 77:256–261, 2008.
- [174] P. Yaroshchyk, R. J. S. Morrison, D. Body, and B. L. Chadwick. Quantitative determination of wear metals in engine oils using libs: The use of paper substrates and a comparison between single- and double-pulse libs. *Spectrochimica Acta Part B*, 60:1482–1485, 2005.

- [175] N. E. Schmidt and S. R. Goode. Analysis of aqueous solutions by laser-induced breakdown spectroscopy of ion exchange membranes. *Applied Spectroscopy*, 56:370–374, 2002.
- [176] Z. Chen, H. Li, F. Zhao, and R. Li. Ultra-sensitive trace metal analysis of water by laser-induced breakdown spectroscopy after electrical deposition of the analytes on an aluminum surface. *Journal of Analytical Atomic Spectroscopy*, 23:871–875, 2008.
- [177] R. K. Al Dhahir, P. E. Dyer, and Z. Zhu. Photoacoustic studies and selective ablation of vascular tissue using a pulsed dye laser. *Appl. Phys. B*, 51:81–85, 1990.
- [178] S. Amoruso, X. Wang, C. Altucci, C. de Lisio, M. Armenante, R. Bruzzese, and R. Velotta. Thermal and nonthermal ion emission during high-fluence femtosecond laser ablation of metallic targets. *Appl. Phys. Lett.*, Vol.77:3728–3730, 2000.
- [179] A Djaoui. A user guide for the Laser-Plasma Simulation Code: MED103. *Technical Report RAL-TR-96-099*, 1996.